HOKKAIDO UNIVERSITY

Title	Synthesis and Femtosecond Laser Excited-Terahertz Wave Emission of Cu-based and ZnTe Nano/Micro Materials
Author(s)	Chau, Yuen Ting Rachel
Degree Grantor	北海道大学
Degree Name	博士(工学)
Dissertation Number	甲第15350号
Issue Date	2023-03-23
DOI	https://doi.org/10.14943/doctoral.k15350
Doc URL	https://hdl.handle.net/2115/93133
Type	doctoral thesis
File Information	Yuen_Ting_Rachel_Chau.pdf

Hokkaido University Collection of Scholarly and Academic Papers : HUSCAP

Synthesis and Femtosecond Laser Excited-Terahertz Wave Emission of Cu-based and ZnTe Nano/Micro Materials



CHAU Yuen Ting Rachel

Graduate School of Engineering

Hokkaido University

March 2023

A dissertation submitted to the Graduate School of Engineering, Hokkaido University,

for the degree of Doctor of Philosophy in Materials Science and Engineering

CONTENT

CHAPTER 1 Research Background

1.1	Nano/Micro Materials	1
1.1.1	Cu-based nano/micro materials	2
1.1.2	ZnTe nano/micro materials	9
1.2	Syntheses of Nano/Micro Materials	13
1.2.1	Bottom-up	13
1.2.2	Top-down	17
1.2.3	Selecting an appropriate method: Bottom-up or top-down?	22
1.3	Femtosecond Laser Technologies	24
1.3.1	Brief introduction of ultrashort pulsed laser: How it is happened?	24
1.3.2	X-ray emission from solid/liquid targets	28
1.4	Terahertz Wave Technologies	34
1.4.1	Terahertz wave generation	36
1.4.1.1	Nonlinear optics	37
1.4.1.2	Semiconductors	39
1.4.1.3	Water film	44
1.4.2	Terahertz wave detection	47
1.5	Summary	50
1.6	Research Objectives	51
1.7	References	52

CHAPTER 2 Facile Synthesis of Cu and Cu-Pd alloy Nanoparticles in Polymer Matrix by Magnetron Sputtering

2.1	Introduction	71
2.2	Experimental	73
2.2.1	Preparation of Cu NPs in PEG	73
2.2.2	Preparation of Cu-Pd NPs in PEG	74
2.2.3	Sputtering Cu-Pd NPs onto Al foil, glass slide, Si wafer and TEM grid	75
2.2.4	Characterization	76

2.3	Results and Discussion	79
2.3.1	Size change of Cu NPs dispersed in PEG after as-sputtered	79
2.3.2	Absorption peak of Cu NPs at 570 nm degraded due to oxidation	81
2.3.3	Formation of Cu-Pd alloy NPs	84
2.3.4	Size of Cu-Pd alloy NPs against sputtering currents	86
2.3.5	Particle Composition against Sputtering Currents	88
2.3.6	Oxidation of Cu in Cu-Pd alloy NPs in PEG	99
2.3.7	Crystallinity of the Cu-Pd alloy NPs in PEG	101
2.4	Conclusion	103
2.5	References	105

CHAPTER 3 Degradation of Shell Thickness-Tunable Au@Cu_2O Core-Shell Nanoparticles in Aqueous Solution

3.1	Introduction	111
3.2	Experimental	113
3.2.1	Materials	113
3.2.2	Synthesis of Au NPs	113
3.2.3	Synthesis of Au@Cu_2O core-shell NPs	114
3.2.4	Characterization	114
3.3	Results and Discussion	116
3.3.1	Formation of Au@Cu_2O core-shell NPs	116
3.3.2	Tunable Cu_2O shell thickness	118
3.3.3	Aggregations of Au@Cu_2O core-shell NPs	122
3.3.4	Optical properties of Au@Cu_2O core-shell NPs	123
3.3.5	Stability of Au@Cu2O core-shell NPs in water/ethanol mixed solvent	124
3.4	Conclusion	128
3.5	References	129

CHAPTER 4 Relation between Oxidative Temperature and Intensity of THz Wave Emission of Copper Thin Films

4.1	Introduction	131
4.2	Experimental	133
4.2.1	Materials	133
4.2.2	Preparation of oxidative annealed Cu/Si and Cu/Au/Si samples	133
4.2.3	Characterization	135
4.2.4	THz wave emission measurement	135
4.3	Results and Discussion	137
4.3.1	Optical properties of prepared samples	137
4.3.2	Oxidation degree of Cu layer at different annealing temperatures	137
4.3.3	Cu_2O in Cu layer	142
4.3.4	Cu_2O/Cu interface as THz wave source	146
4.3.5	Function of Au layer	152
4.3.6	No THz wave emission from the inverted double-layered structure	155
4.3.7	Suggestions of improving THz wave emission intensity	156
4.4	Conclusion	157
4.5	References	159

CHAPTER 5 Mechanistic Studies of ZnTe Microspheres formed in a PVP-contained Polyol System and their THz Wave Emission Availability

5.1	Introduction	163
5.2	Experimental	168
5.2.1	Materials	168
5.2.2	Preparation of precursor solution	168
5.2.3	Synthesis of ZnTe microspheres	169
5.2.4	Characterization of ZnTe microspheres	171
5.2.5	Preparation of ZnTe/Si	173
5.2.6	THz wave emission measurement	174
5.3	Results and Discussion	176
5.3.1	Effect of PVP to ZnTe microspheres at reaction time of 48 h	176

5.3.2 Structure and composition of ZnTe microspheres 180
5.3.3 Relation of PVP amount to the growth of ZnTe microspheres 186
5.3.4 Consideration of formation process of ZnTe microspheres 198
5.3.5 Effect of reaction temperature to the microspheres' formation 209
5.3.6 Effect of concentration of Na_2TeO_3 to the microspheres' morphologies 213
5.3.7 $Zn(CH_3COO)_2$ as the Zn precursor 215
5.3.8 Effect of en to the microspheres' morphologies 216
5.3.9 ZnTe microspheres as THz wave source 219
5.4 Conclusion 229
5.5 References 231
5.6 Supporting Information 240

CHAPTER 6 General Conclusion 243

LIST OF JOURNAL PUBLICATIONS 248
LIST OF CONFERENCES 250

LIST OF TABLES AND FIGURES

Table	Description	Page
1.1	Gain media of laser and their spectra range.	26
1.2	Difference between soft and hard X-rays.	29
1.3	Rules of Schottky/ohmic junction formation at metal/semiconductor interfaces. Φ_M: Work function of metal; Φ_S: Work function of semiconductor.	40
2.1	Sputtering currents used in the preparation of Cu-Pd alloy NPs.	75
2.2	Solid substrates used with their corresponding sputtering time and characterization methods.	76
2.3	Summary of the Pd content in samples I–V determined by Vegard's law using XRD patterns, quantitative analysis by XPS, mass measurement, and elemental mapping by STEM-EDS.	90
2.4	Binding energies of Pd^0 $3d_{5/2}$ and Cu^0 $2p_{3/2}$ peaks in samples I–V.	95
4.1	The estimated amount of Cu_2O (wt.%) in the Cu film annealed at 80, 110 and 140 °C.	139
5.1	Parameters used in preparing each sample. (Reaction temperature: 200 °C and stirring speed = 1,000 rpm)	170
5.2	Average crystalline sizes calculated from XRD peaks of sample.	180
5.3	Lattice spacing of different planes of cubic (zincblende) ZnTe. ***S***: measured from the SAED pattern of 518PVP(48h); ***R***: taken from JCPDS reference no. 15-0746.	181
5.4	Estimated relative content of ZnTe in samples synthesized at 0.2 h and 0.5 h based on XRD results in Figure 5.13.	192
5.5	ZnTe microspheres used for THz emission test and their synthesis parameters.	219
5.6	Thickness of ZnTe microspheres film of each sample and the estimated number of layers of ZnTe microspheres loaded on Si wafer via dividing the thickness by the diameter of ZnTe microspheres.	223

A5.1 Crystalline size calculated with (111) and (220) peaks; peak intensity of (220) to sum of peak intensities of (111) and (220), using X'Pert HighScore Plus (Malvern PANalytical, the Netherlands). 242

Figure **Description** **Page**

1.1 *Red fluorescence properties from Cu NPs*. Photographs of Cu NPs (a-b) aqueous solution and (c-d) powder under (a,c) visible and (b,d) UV-light of 365 nm. 3

1.2 *Cu-Pd NPs show blue fluorescence under UV-light irradiation.* Photograph of Cu-Pd alloy NPs at different compositions under room light (upper row) and under UV light of 365 nm (lower row). 4

1.3 *Ag@Cu_2O core-shell NPs as photocatalyst.* Absorption peaks in UV-vis spectra red shifted with increasing the Cu_2O shell thickness. 6

1.4 *Au NPs embedded in Cu_2O heterostructure as photocatalyst.* (a-d) Micrographs of the heterostructure. (e) HR-TEM micrographs with labeling *d*-spacing of Au (yellow) and Cu_2O (red). (f) EDS mapping to show the distribution of Au on Cu_2O. (Lower) Schematic diagram of the photocatalytic activity given by the heterostructure. 8

1.5 *Photoluminescence from ZnTe@ZnSe core-shell QDs.* Micrographs of (a) ZnTe cores and (b) ZnTe@ZnSe core@shell QDs. (c) UV-vis absorption spectra of ZnTe core (black), ZnTe@ZnSe core@shell QDs with 1.0 (violet), 1.4 (blue), 2.0 (green), 3.3 (orange), and 5.0 (red) monolayers of ZnSe shell. (d) Corresponding PL spectra with respect to different numbers of shell monolayers. 10

1.6 *Broadband THz pulse emitted and detected by ZnTe crystal.* (a) Temporal waveform of the THz pulse from 30 μm ZnTe emitter and measured by a 27 μm ZnTe sensor. (b) Power spectrum of the waveform in (a). 11

1.7 *ZnTe microspheres as photocatalysts for CO_2 reduction.* (a) Negative band position of ZnTe and reduction potential of products against CO_2. (b) Micrographs of mesoporous ZnTe microspheres. (c) Higher yield of 12

methane by using ZnTe mesoporous compared with ZnTe nanocrystals.
1.8 *Formation scheme of zerovalent metal colloids through bottom-up approach.* 14
1.9 Schematic diagram of sputtering process. 17
1.10 TEM micrographs and size distribution of NPs synthesized by sputter deposition. (a) Ag sputtered into pentaerythritol tetrakis(3-mercaptopropionate) (PEMP), sputtering current = 30 mA, sputtering time = 20 min. (b) Ag sputtered into PEG, sputtering current = 20 mA, sputtering time = 20 min. (c) Pt sputtered into PEG, sputtering current = 50 mA, sputtering time = 30 min. 19
1.11 (a) Schematic diagram of the double target sputtering chamber. (b) Cu content of Au-Cu alloy NPs against sputtering current for Cu target from 10-50 mA and sputtering current for Au target at 10 mA and 20 mA. Half-filled diamond data points represent the composition of alloy NPs sputtered by double head system using Au-Cu alloy target. (c) HAADF and EDS mappings [Au L (red), Cu K (green), and overlay] for nearly equimolar Au-Cu alloy NPs. 21
1.12 Scheme of laser light generated from Ti:sapphire as the gain medium. 26
1.13 Block diagram of resonant cavity of passive mode-locked laser. 27
1.14 Process of chirped pulse amplification for mode-locked laser. 28
1.15 (Top) Schematic diagram of the X-ray emission test from metal target. (Bottom) Corresponding X-ray emission spectra of (a) Ti, (b) stainless steel, (c) Ni, (d) Cu, (e), Ta targets. 30
1.16 (Left) Schematic diagram of the X-ray emission test from Ga liquid jet and (Right) X-ray emission spectrum of Ga jet target. 31
1.17 X-ray emission intensity against diameters of Au nanoparticles. Au concentration was 1.2×10^{-3} M in all samples. 33
1.18 Terahertz band in the electromagnetic wave spectrum. 34
1.19 Comparison of sensing capability of THz wave and X-ray. (a) Photographs of model objects. (b) X-ray radiographs. (c) THz wave imaging. (d) Differential THz wave (subtraction image between filled 36

jar and empty jar).

1.20 Crystal structure diagram of nonlinear crystals: (a) $LiNbO_3$ and (b) ZnTe. 38

1.21 Band diagrams showing Schottky barrier forms when metal and n-/p-type semiconductor are brought in contact. (E_F: Fermi energy, E_C: Energy level at conduction band edge, E_V: Energy level at valence band edge.) 41

1.22 THz wave generated from Cu_xO/Au structure. (Top left) TEM micrograph of Cu/Au film on Si wafer. (Top right) SAED pattern of oxidized Cu film. (Bottom) THz-TDS showing Cu/Au/Si heated at 110 ºC emits THz wave. 42

1.23 Transient polarization built from the diffusion of holes and electrons at different speeds in the region near to the surface of a semiconductor due to femtosecond laser irradiation. 43

1.24 (Left) Femtosecond laser irradiates the water film created by collision of two water jets. (Right, top) X-ray emission intensity against laser focal point along the z-axis. (Right, bottom) THz emission intensity against laser focal point along the z-axis in reflection and transmission pathway, respectively. 45

1.25 (Left) THz electric field emitted from aqueous film of ZnTe nanocolloids and bare water. (Right) The corresponding powder spectra. The laser intensity is 0.75 mJ/pulse. 47

1.26 Schematic illustration of a THz detection system (reflection mode: incident angle of pump beam to sample = 45º) 49

2.1 Schematic illustration of (a) single target sputtering system for metallic Cu NPs and (b) double target sputtering system for bimetallic Pd–Cu alloy NPs. 74

2.2 TEM images and size distributions of PEG-coated Cu NPs prepared by sputtering (current = 50 mA, time = 30 min, Pressure = 2 Pa, Temperature = 30 °C, substrate rotation speed = 80 rpm) at (a) 0 h, (b) 1 h, (c) 2 h, (d) 3 h, (e) 4 h, (f) 1 d, (g) 4 d, (h) 7 d. Scale bars in all 80

images are in 10 nm.
2.3 Particle sizes versus time from 0 d to 7 d. 81
2.4 (a) UV-Vis spectra from day 0 to day 10. (b) Absorbance at 570 nm from UV-Vis spectra versus time. Condition of cuvette indicated the colour faded out. 83
2.5 (a) UV-Vis absorbance onset of sealed cuvette (control) and opened cuvette at 1 hour. (b) SAED of the sample after 8 days from sputtering. 83
2.6 (a) UV-Vis absorption spectra of as-sputtered alloy samples I to V, monometallic Pd, monometallic Cu and vacuum dried PEG. (b) Dispersions of Pd-Cu alloy NPs (sample III), monometallic Pd NPs and monometallic Cu NPs in quartz cuvettes with a 1 mm optical path. 85
2.7 TEM images of samples I–V. Scale bar in all images is 10 nm. 87
2.8 Size distributions of the samples I–V. 87
2.9 XRD patterns of the Cu-Pd alloy sputtered on a glass slide for 30 min with the same sputtering current as samples (I–V). Below is the enlargement of the (111) peaks in the XRD patterns from 38° to 45°. Standard patterns of Cu (JCPDS no. 46-1043) and Pd (JCPDS no. 04-0836) for reference. 89
2.10 *d*-spacing determined from the (111) peak in the XRD patterns with respect to the Cu content calculated with Vegard's Law. 90
2.11 XPS spectra of Cu 2p (left) and Pd 3d (right) of samples I–V. The dotted black curves are the actual spectra. The blue and red curves are the fitting spectra with an asymmetric Gaussian–Lorentzian sum function (70% L–G) and a Shirley background. The dashed lines showing the reference peak positions of Cu and Pd are visual guides of the peak shifts. 92
2.12 TEM images of samples I–V directly sputtered on a TEM grid for 1 min. The scale bars in all images are 5 nm. 93
2.13 Shift of binding energies (ΔBE) of Pd^0 $3d_{5/2}$ (left y-axis) and Cu^0 $2p_{3/2}$ peak (right y-axis) with respect to the Cu content (at%) by quantitative analysis in XPS. 94

2.14	Masses of Pd and Cu obtained at the center area of the sputtering chamber with a diameter of 60 mm with respect to the sputtering currents from 10 to 50 mA.	98
2.15	op HAADF-STEM image and STEM-EDS mapping images of the overlapping of Pd and Cu, Cu, and Pd of a NP in PEG of sample III. Bottom HAADF and mapping images of Cu-Pd NPs sputtered on a carbon coated Mo microgrid (I_{Pd} = 50 mA, I_{Cu} = 50 mA). Yellow circle indicates the NPs of interest. Scale bar in all images is 3 nm.	98
2.16	HAADF-STEM images of Cu-Pd alloy NPs in samples II and III. The scale bars in all images are 2 nm.	99
2.17	UV-Vis spectra of samples (solid line) as-synthesized and (dashed line) at day 4 after synthesis: (A) II, (B) III and (C) IV.	100
2.18	HAADF-STEM images of NPs in sample III before and after STEM-EDS mapping for 60 s.	102
3.1	Procedure of synthesizing Au@Cu_2O core-shell NPs.	115
3.2	(a) TEM image with scale bar 100 nm. Inset is the photo of solution. (b) size distribution and (c) UV-Vis absorption spectrum as-synthesized Au NPs.	116
3.3	Color change in the synthesis of Au@Cu_2O NPs.	117
3.4	(a) HAADF-STEM and (b) TEM images of Au@Cu_2O core-shell NPs. (c) HRTEM image taken at the interface of Cu_2O shell and Au core labeled in (b). (d) Fast Fourier Transform (FFT) of the image in (c).	118
3.5	XRD patterns of as-synthesized Au@Cu_2O core-shell NPs and Cu_2O. Standard patterns of Cu_2O (JCPDS no. 05-0667) and Au (JCPDS no. 04-0836) for reference.	119
3.6	TEM images with scale bar 50 nm of as-synthesized Au@Cu_2O core-shell NPs named (a) Au@Cu_2O-100, (b) Au@Cu_2O-10, (c) Au@Cu_2O-2, and (d) Au@Cu_2O-1. The inset of each image shows the visual image of the solution with different Cu_2O shell thickness. (e-h) Size distributions of Cu_2O shell thickness correspond to (a-d).	121

3.7	DLS results of as-synthesized Au@Cu_2O core-shell NPs: (a) Au@Cu_2O-100, (b) Au@Cu_2O-10, (c) Au@Cu_2O-2, (d) Au@Cu_2O-1 (Concentration: 0.1 mM (based on Au); Solvent: ethanol).	122
3.8	UV-Vis absorption spectra of as-synthesized Au@Cu_2O-100, Au@Cu_2O-10, Au@Cu_2O-2, and Au@Cu_2O-1 core-shell NPs with decreasing Cu_2O shell thickness.	124
3.9	UV-Vis absorption spectra of Au@Cu_2O-100 core-shell NPs suspensions after synthesis for 1, 3, 5, 7, and 14 days stored in ethanol/water mixed solvents with different compositions (ethanol/water, vol %) of (a) 70:30 – #1, (b) 60:40 – #2, (c) 50:50 – #3, (d) 30:70 – #4, (e) 10:90 – #5.	125
3.10	TEM images of (a) as-synthesized Au@Cu_2O core-shell NPs, (b) after 5 days, and (c) after 14 days in an ethanol/water mixed solvent with composition of 30:70 in vol% (#4). The inset in (c) is the SAED pattern of the region labeled by dashed circle in (c).	127
3.11	UV-Vis absorption spectra of Cu_2O NPs stored in ethanol/water mixed solvent with composition of 30:70 in vol% (solvent #4).	127
3.12	TEM images of (a) as-prepared Cu_2O particles and (b) Cu_2O particles dispersed in ethanol/water mixed solvent with composition of 30:70 in vol% for 30 days at room temperature.	128
4.1	Reflectance spectra of Cu/Si and Cu/Au/Si samples at different annealing temperature.	140
4.2	XRD patterns of Cu films at conditions of (a) as-sputtered, annealed at (b) 80, (c) 110, (d) 140, (e) 170, (f) 200, (g) 250 and (h) 300 °C.	141
4.3	XRD patterns of (a) as-sputtered Cu film and (b) that being kept under ambient (25 °C) for one week.	141
4.4	(a) TEM image of the cross-sectional Cu/Au/Si structure annealed at 110 °C for 2.5 h. (b) and (d) are selected area of taking diffraction patterns of (c) Cu film and (e) interface of Cu and Au films.	144

4.5	(a-c) TEM image of Cu/Au/Si heated at 80 °C taken at different regions. Green line indicates the scan region of (d-e) corresponding EELS spectra. Only spectra that can identify Cu_2O thickness are displayed in the EELS spectra.	145
4.6	THz-TDS measurement of (a) bare Si wafer and (b) ZnTe <110> single crystal.	146
4.7	(a-h) THz-TDS and (i-p) corresponding FFT treated emission spectra of Cu/Si structures annealed at different temperatures.	148
4.8	(a-h) THz-TDS and (i-p) corresponding FFT treated emission spectra of Cu/Au/Si structures annealed at different temperatures.	149
4.9	Scheme and mechanism of using Cu_2O/Cu interface as the THz wave source under femtosecond laser excitation. Mobility of the holes is approximately one order lower than that of electrons.	150
4.10	Cross-sectional TEM images of Cu/Au/Si heated at (a) 80 °C, (b) 110 °C, and (c) 170 °C. Pink circle indicates the cavities inside of the Cu layer.	151
4.11	Total THz wave emission intensity of annealed Cu/Si and Cu/Au/Si structures against different annealing conditions.	154
4.12	UV-Vis spectra of Cu/Au/Glass and Cu/Glass annealed at 80 °C. A bare glass slide was used as the baseline.	155
4.13	THz wave emission intensity from Cu/Au/Si and Au/Cu/Si structures annealed at 110 °C.	156
5.1	Schematic diagram of the experimental setup of making ZnTe microspheres.	170
5.2	Block diagram of the experimental setup (top view).	175
5.3	SEM images of ZnTe microspheres from samples (a) 0PVP(48h), (b) 259PVP(48h), (c) 518PVP(48h), (d) 1036PVP(48h), and (e-h) the corresponding size distributions.	178
5.4	SEM images of rod structures in (a) 0PVP(48h) and (b) 259PVP(48h). (c) Region of sample 0PVP(48h) to perform EDS elemental mapping analysis of (d) Zn and (e) Te.	179

5.5	XRD patterns of sample (from bottom) (a) 0PVP(48h), (b) 259PVP(48h), (c) 518PVP(48h) (d) and 1036PVP(48h). Bar charts are reference patterns of ZnTe (Red, JCPDS No. 15-0746) and Te (Blue, JCPDS No. 36-1452).	179
5.6	Selected area electron diffraction (SAED) pattern of the ZnTe microsphere. Inset are the TEM images showing the area where the SAED pattern was taken.	181
5.7	(a) TEM micrographs of ZnTe microspheres in 518PVP(48h) in low magnification. (b) High magnification image of the region selected by the red square in (a). (c-e) Enlarged regions in (b), indicating the lattice spacing of ZnTe in (111), (200), (220) planes respectively.	183
5.8	(a) STEM bright field image of a ZnTe microsphere in 518PVP(48h). (b) Overlay image of elemental mapping of (c) Zn (K$\boldsymbol{\alpha}$ line) and (d) Te (L$\boldsymbol{\alpha}$ line).	184
5.9	SEM image of ZnTe microspheres in 518PVP(48h). (b) Overlay image of elemental mapping of (c) Zn and (d) Te.	185
5.10	Zn content (at. %) among 27 ZnTe microspheres detected by SEM-EDS point analysis.	185
5.11	SEM images of samples (a) 0PVP(0.5h), (b) 259PVP(0.5h), (c) 518PVP(0.5h), (d) 1036PVP(0.5h). (e) Size of ZnTe microspheres against amount of PVP at reaction time of 0.5 h.	188
5.12	(a) Length and (b) diameter of Te rods in samples synthesized for 0.5 h using 0 mg, 259 mg, 518 mg, and 1036 mg of PVP, respectively.	189
5.13	XRD patterns of sample (a) 0PVP(0.2h), (b) 259PVP(0.2h), (c) 518PVP(0.2h), (d) 1036PVP(0.2h), (e) 0PVP(0.5h), (f) 259PVP(0.5h), (g) 518PVP(0.5h), (h) 1036PVP(0.5h). Bar charts are reference patterns of ZnTe (JCPDS No. 15-0746) and Te (JCPDS No. 36-1452).	191
5.14	ZnTe particle sizes against reaction time of 0.2 h, 0.5 h and 48 h, respectively in sample (a) 0PVP, (b) 259PVP, (c) 518PVP and (d) 1036PVP.	194

5.15	XRD patterns of Te formed at reaction time of 3 min in the systems (a) 0PVP, (b) 259PVP, (c) 518PVP, (d) 1036PVP. Bar chart is a reference pattern of Te (JCPDS No. 36-1452).	196
5.16	(a) SEM image of Te rods synthesized for 3 min with 0 mg of PVP. TEM images of Te rods synthesized for 3 min with (b) 259 mg, (c) 518 mg and (d) 1036 mg of PVP, respectively.	197
5.17	(a) Indicating the target sites 'base1' and 'base2' of taken EDS spectra in Figure 5.16c. Inset is the SAED pattern taken from area indicated with a red circle. EDS spectra of (b) 'base1' and (c) 'base2' indicated in (a).	197
5.18	XRD patterns of samples 518PVP synthesized at (a) 0.2 h, (b) 0.5 h, (c) 1 h, (d) 2 h, (e) 6 h, (f) 12 h, (g) 24 h and (h) 48 h. Bar charts are reference patterns of ZnTe (JCPDS No. 15-0746) and Te (JCPDS No. 36-1452).	200
5.19	SEM images of samples 518PVP synthesized at (a) 0.2 h, (b) 0.5 h, (c) 1 h, (d) 2 h, (e) 6 h, (f) 12 h, (g) 24 h, and (h) 48 h. (i) Size of ZnTe microspheres against reaction time from 0.2 h to 48 h.	201
5.20	(a) STEM bright field image of a Te rod and ZnTe particle in 518PVP(0.5h). (b) Overlay image of elemental mapping of (c) Zn and (d) Te.	202
5.21	Te rod (dot) length, (square) diameter, (triangle) size of microspheres of samples 518PVP against reaction time from 0.2 h to 1 h.	202
5.22	(a-f) HVEM micrographs of 518PVP(0.5h). (b-c) Rapid destruction occurred at Te rods (indicated with arrows) in a second. (d) Regions with different contrast on Te rods: (e) High contrast region and (f) low contrast region. (g-i) TEM micrographs of cross-sectional specimens fabricated with the ultra-microtome from the resin embedded 518PVP(0.5h) sample. Voids at the Te rods region is due to the detachment of Te rods from the specimen. Dashed lines are guides for the eyes.	205

5.23	STEM-HAADF image of ZnTe microspheres in 518PVP(48h).	208
5.24	Schematic diagram of the formation process of ZnTe microspheres in PVP-contained EG.	208
5.25	A hexagonal pore appeared at the central region of the cross-section of ZnTe microspheres.	209
5.26	SEM images of products obtained at temperature (a-b) 160 ℃ for 48 h and 180 ℃ for (c-d) 6 h and (e-f) 48 h.	211
5.27	XRD patterns of products obtained at temperature (a) 160 ℃, (b) 180 ℃, and (c) 200 ℃ for 48 h.	212
5.28	SEM images of 518PVP(48h) synthesized using (a) 0.20 mmol and (b) 0.24 mmol of Na_2TeO_3 in the precursor solution. (c) The corresponding XRD patterns. Bar charts are reference patterns of ZnTe (JCPDS No. 15-0746) and Te (JCPDS No. 36-1452). Amount of $ZnCl_2$ = 0.20 mmol, reaction temperature = 200 ℃.	214
5.29	(a) SEM image (inset is the size distribution), TEM images (b) at low magnification and (c) at high magnification of the area marked in (b). (d) XRD pattern of the ZnTe microsphere sample 518PVP(48h) synthesized using $Zn(CH_3COO)_2$ (Amount of PVP = 518 mg, reaction time = 48 h, reaction temperature = 200 °C). XRD pattern of $ZnCl_2$ is attached for comparison. Bar charts are reference patterns of ZnTe (JCPDS No. 15-0746) and Te (JCPDS No. 36-1452).	216
5.30	SEM image (inset is the size distribution), TEM images (b) at low magnification (dashed line is a guide for eyes to identify a ZnTe microsphere) and (c) at high magnification of the area marked in (b). (d) XRD pattern of the ZnTe microsphere sample 518PVP(48h) synthesized using doubled amount (1.28 mL) of en in the precursor solution (Amount of PVP = 518 mg, reaction time = 48 h, reaction temperature = 200 °C). XRD pattern of using 0.64 mL of en is attached for comparison. Bar charts are reference patterns of ZnTe (JCPDS No. 15-0746) and Te (JCPDS No. 36-1452).	218

5.31 XRD patterns of (a) ZnTe-0.7, (b) ZnTe-0.8, (c) ZnTe-1.0, (d) ZnTe-1.6, and (e) ZnTe-1.9 loaded on Si wafer. Bar charts are reference pattern of ZnTe (JCPDS No. 15-0746). 220

5.32 (a) Sizes of crystals with (111) and (220) faces with respect to the ZnTe microspheres' diameter. (b) Content of (220) crystals determined from XRD peak intensities. 221

5.33 (a) THz-TDS of sample (a) ZnTe-0.7, (b) ZnTe-0.8, (c) ZnTe-1.0, (d) ZnTe-1.6, (e) ZnTe-1.9. Laser intensity is 0.4 mJ/pulse. (f) Summary of peak-to-peak intensities in TDS against average ZnTe microspheres' size with respect to different laser pulse intensity. 221

5.34 SEM image of stocked ZnTe microspheres before deposition on Si wafer for (a) ZnTe-1.9 and (d) ZnTe-0.8. Cross-sectional image of ZnTe microspheres layer deposited on Si wafer of (b) ZnTe-1.9 and (e) ZnTe-0.8. Pink circle indicates a bunch of ZnTe microspheres. Schematic diagram for explaining the induced dipoles in sample (c) ZnTe-1.9 and (f) ZnTe-0.8. 226

5.35 THz intensity (right y-axis) with respect to time with laser excitation at intensity 0.4 mJ/pulse (left y-axis). Total 80 data points were taken in between 10:00 am to 5:30 pm on 2022/05/04. 228

A5.1 3D diagram constructed by overlapping cross-sectional images of sample 518PVP(0.5h) using FIB-SEM. 240

A5.2 SEM images of (a) ZnTe-0.7 (746 $\pm$ 144 nm), (b) ZnTe-0.8 (854 $\pm$ 141 nm), (c) ZnTe-1.0 (1.0 $\pm$ 0.2 μm), (d) ZnTe-1.6 (1.6 $\pm$ 0.2 μm), and (e) ZnTe-1.9 (1.9 $\pm$ 0.5 μm). 241

A5.3 Diffuse reflectance spectra of ZnTe microspheres loaded on Si wafer. 242

ACKNOWLEDGEMENTS

I am deeply indebted to my supervisor, Prof. Tetsu Yonezawa for his dedicated support and guidance throughout these years. His ideas and knowledge in nanomaterials had inspired me a lot. He also gave me tremendous opportunities to become involved in many projects, that had expanded my research skills toward different subjects. Nothing can be done without his encouragement. Also, I would like to give my warmest thanks to my mentor Asst. Prof. Mai Thanh Nguyen. She continuously provided me feedbacks from different aspects. She encouraged me a lot during these years, even though she also had a tough time. I sincerely wished that she and her family could stay healthy. Special thanks to Asso. Prof. Masatoshi Sakairi for sharing his thoughts in both scientific research and daily conversations. I am also grateful to Asst. Prof. Yohei Ishida for giving comments to my works, as well as his warm greetings whenever I met him. Many thanks to Mr. Hiroki Tsukamoto for his expertise in different equipment that helped me a lot to continue research works. I am extremely grateful to the time and energy that they had contributed to me.

This thesis would not have been possible without Prof. Koji Hatanaka (Academic Sinica, Taipei) and his research staff Ms. Hsinhui Huang for conducting laser experiments in Taiwan. We had overcome lots of obstacles to continue the collaborating works during the COVID-19 pandemic. I am also thankful to Asst. Prof. Tomoharu Tokunaga (Nagoya Univ.) for his help in part of materials characterization. Sincerely thanks to Prof. Shigenari Hayashi and Prof. Toshihiro Shimada to be my examiners. Prof. Hayashi had evaluated my works since I was in master course. He can always give opinions from different aspects to let me improve my works. I am truly thankful for his comments in these years. My research work could not be done without the opinions given by Prof. Shimada. His expertise in applied physics also helped me to enrich my thesis. Also thanks to my thesis committees for their valuable comments.

Thanks to the following parties for their supports – Prof. Tamaki Shibayama, Ms. Minako Kondo, Asst. Prof. Takashi Endo, Ms. Yuko Mori for SEM-FIB support. Asso.

Prof. Norihito Sakaguchi for TEM advice. Mr. Takashi Tanioka, Mrs. Ryoko Yokohira, Mr. Ryo Ota, Mr. Ken-ichi Oukubo for TEM support. Ms. Naomi Hirai for STEM support. Mr. Keita Suzuki for XPS support. Ms. Suzuka Yoshida for microtome support. Asso. Prof. Tomobumi Mishina (Graduate School of Science) for experimental discussion. I would like to state my acknowledgement to the Hokkaido University Ambitious Doctoral Fellowship (Information Science and AI) for the support in my research works and daily expenses. I'd like to extend my sincere thanks to my labmates – Dr. Shilei Zhu, Dr. Zhong Huang, Dr. Kunihiro Narita, Mr. Shuichi Nukui, Dr. Haoran Liu, Mr. Li Li, Mr. Xiaole Han, Mr. Tong Shen, Mr. Wei Jian Sim. Special thanks to Dr. Min Jia Saw and Dr. Lianlian Deng. They had shared many experiences in studying at Hokkaido University and in job hunting processes. Many thanks to Ms. Zixuan Huang and Ms. Xinxin Liu for leaving me a good memory with happiness.

Words cannot express my gratitude to my former boss, Prof. Wallace Woon Fong Leung. I have always admired him for his passion in science and technology. I could not start any research without joining his group in 2017. Thanks should also go to my former supervisor Asso. Prof. Sai Wing Tsang (CityU HK). He gave me opportunities to step into research on nanomaterials. Special thanks to Ms. Maria Gan (PolyU HK), who always helps me out to search electronic copies of literatures and textbooks from PolyU HK. I am so glad to have Ms. Gan and other 'Materials Experts' as my classmates.

I'd also like to recognize some good friends located in different countries: Ka Hei Leung, Twinkle Lai, Allen Yip, Kate Ho, Daniel Chan, York Yeung, Tess Chiang, Nico Tam, Oi Yi Yip, Olivia Tsang, Ella Chow, Jesse Lam, Kwan Yin Cho, Cloey Wong, Karen Lam, Zoe Shaw, Hoi Ting Moyung, and others. I'd like to mention my father, Mr. Tony Chau, and his current spouse for their support. I would be remiss in not mentioning my aunt and uncle – Dr. Suet Fan Vicky McConnellogue and Mr. Charles McConnellogue for their unconditional love. Lastly, none of my life would be possible without my beloved mother Ms. Sui Ching Winnie Chung. Wherever you are, you are always in my thoughts.

Yuen Ting Rachel Chau

Abstract

Cu-based and ZnTe nano/micro materials are of interest due to their availability in tremendous applications such as broadband pulses emission in terahertz (THz) regime under femtosecond laser irradiation. Firstly, syntheses of these materials based on bottom-up and top-down approaches are discussed. In particular, Cu-based nanoparticles dispersion can be synthesized via sputter deposition, but the understandings to the sputtered nanoparticles are limited. ZnTe microstructures can be obtained via thermal decomposition, yet their formation mechanism remains unclear due to the unobservable characteristic of the solvothermal method. Secondly, with the development of ultrafast laser pulse technologies, the emission of X-ray and THz radiation as optical responses of materials to the laser excitation is concerned. Cu-based and ZnTe nano/micro materials are potential THz radiation sources as a semiconductor for Cu-based materials and as a nonlinear crystal for ZnTe. This dissertation focuses on the optical responses of Cu-based and ZnTe nano/micro materials to the ultrafast laser pulse excitation while elucidating their properties, structures, and formation mechanisms obtaining via different synthetic routes. The above research background and the objectives are given in chapter 1.

Chapter 2 presents the properties and structural characterization of Cu and Cu-Pd nanoparticles synthesized via sputter deposition onto a polymer matrix. Size of all nanoparticles obtained were less than 5 nm. Growth in size and the oxidation of monometallic Cu nanoparticles were monitored after synthesis. Cu-Pd alloy nanoparticles were synthesized by co-sputtering of each metal target. Compositions of Cu-Pd alloy nanoparticles obtained through alternating the sputtering currents were diversely

characterized using UV-vis, TEM, STEM-EDS, XRD and XPS. The findings revealed that co-sputter deposition is a facile method of having composition-tunable bimetallic alloy nanoparticles dispersion. Low crystallinity and degradation during storage of these nanoparticles were discussed. This chapter provided detail information of Cu and Cu-Pd alloy nanoparticles synthesized via sputter deposition.

Chapter 3 studies the stability of Au@Cu_2O core-shell nanoparticles synthesized via wet-chemical route and stored in water/ethanol mixed solvents. Thickness-tunable Cu_2O shells (2 to 40 nm) grew epitaxially on 16 nm-sized Au nanoparticles to give metal/semiconductor heterostructure. Shell thickness altered the absorption peak in UV-Vis region of the nanoparticles. The stability of Au@Cu_2O core-shell nanoparticles was poor in the solvents that contain > 50 vol % water content. This study showed the Au@Cu_2O core-shell nanoparticles dispersed in aqueous solvents was not an appropriate candidate for THz wave emission test due to their instability.

Chapter 4 presents THz wave emission from semiconductor/metal interface using aqueous free Cu and Cu/Au thin film (80nm-thick Cu, 55nm-thick Au) samples. Cu oxides as the semiconductor layer were obtained through oxidative annealing (80 to 300 ºC, 2.5 h). Samples were irradiated by femtosecond laser (35 fs, 800 nm). THz wave emission intensity with respect to the oxidation temperature for annealing Cu layer was discussed. Results showed that Cu_2O/Cu interface was the key feature of THz wave emission. The further THz wave emission enhancement can be achieved by underneath Au film as a reflector of laser light and THz wave. This chapter explained the THz wave emitting mechanism from Cu oxides and the function of Au film in the heterostructure.

Chapter 5 performs syntheses of ZnTe microspheres in a PVP contained polyol system via a hot injection method, with the investigation of their possibility as a THz wave emitting source. A retrospective study was conducted to evaluate the formation process of ZnTe microspheres from 0.2 to 48 h. It was found that the initially formed Te rods in the reaction system were sacrificial templates for the growth of ZnTe. Amount of PVP controlled dimensions of Te rods formed at the initial stage as well as the sizes of ZnTe microspheres by influencing the nucleation and growth rate of ZnTe. Although the ZnTe microspheres were polycrystalline, they emitted THz wave under ultrafast laser pulse irradiation. The larger ZnTe microspheres (> 1.0 μm) were prone to generate THz wave in higher intensity, which was originated from the nonlinear effect by ZnTe. This chapter discussed the formation of ZnTe microspheres and gave a preliminary report on THz wave emission from polycrystalline ZnTe microspheres.

Chapter 6 gives the general conclusion of the research topics covered by the dissertation, including the understanding on the properties of Cu-based and ZnTe nano/materials synthesized via different approaches, and the THz wave emission from these materials under ultrafast laser pulse excitation. The findings are significant to widen the availability of nano/micro materials for broadband THz pulse technologies.

CHAPTER 1

Research Background

1.1 Nano/Micro Materials

Nanomaterials are defined to have at least one physical dimension in the range of 1 to 100 nm. Micro materials are defined to have a physical dimension between 0.1 to 100 μm. Alternative physicochemical properties can be obtained through scaling down materials from bulk form due to the change in interatomic interaction and increasing surface-to-volume ratio. Nano/micro materials are in concerned because desired properties can be obtained through tuning the parameters in producing them. Nowadays, nano/micro materials have been emerged to medical diagnoses[1-3], drug delivery[4-6], optoelectronics[7-8], catalysis[9-11], and other interdisciplinary applications. The following sub-sections mainly list the unique properties and application examples of the Cu-based and ZnTe nano/micro materials.

1.1.1 Cu-based nano/micro materials

Cu metals. Cu is earth-abundant and thus inexpensive. Emerging Cu nano/micro materials can facilitate and enhance the practical use. Garg *et al.* have reported that the thermal conductivity of ethylene glycol as a coolant can be enhanced by dispersing 200 nm-sized Cu nanoparticles (NPs) into the ethylene glycol.[12] Park *et al.* have demonstrated direct ink-jet printing of ~50 nm-sized Cu NPs on a glass substrate, which had comparable conductivity with Au and Ag inks.[13] Yonezawa and his co-workers have took the advantages of lower melting point in nanomaterials and used different low temperature sintering processes to obtain a continuous Cu film with high conductivity.[14-18] Wang *et al.* have synthesized water-dispersible, red fluorescence ~3 nm-sized Cu NPs, that were used as probes for cellular imaging (**Figure 1.1**).[19] Venkatakrishnan *et al.* have synthesized air stable ~5 nm-sized Cu NPs under room temperature with catalytic function towards the reduction of nitro-aromatic compounds.[20] Several reports have also showed that Cu in nanowires form can be used as the transparent conducting electrode for optoelectronic devices.[21-26]

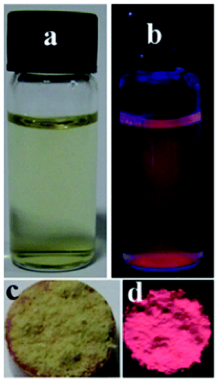


Figure 1.1 *Red fluorescence properties from Cu NPs*. Photographs of Cu NPs (a-b) aqueous solution and (c-d) powder under (a,c) visible and (b,d) UV-light of 365 nm. Reproduced with permission from ref. [19] Copyright 2014 Royal Society of Chemistry.

Cu-based alloys. Cu has been used as an alternative to the rare and expensive noble-metals. Particularly, alloying Cu with a noble metal in designing a catalyst can achieve cost reduction while maintaining a good catalytic performance. Xu *et al.* have improved the Pt monometallic catalysts on the oxidation of methanol by adapting nanotubular mesoporous Cu-Pt bimetallic catalyst.[27] Gong *et al.* also reported Cu-Pt alloy nanodendrites as catalyst for oxidation of methanol.[28] Jia *et al.* [29] and Huang *et al.*[30] have reported the catalytic functions of Cu-Au nanostructured alloy towards reduction of CO_2 to alcohols and reduction of CO to CH_4, respectively. The enhancement in catalytic activities is based on the higher activity of transition metals compared with noble metals [27] and Cu can be stabilized by alloying with noble metals to prevent degradation. Apart from catalytic function of Cu-based alloys, Chiba *et al.* have

synthesized Cu-Pd NPs at different compositions and stronger photoluminescence was observed from bimetallic NPs than that from single-metal NPs (**Figure 1.2**).[31] Chowdhury *et al.* have also conducted similar studies on compositional luminescence enhancement for the Cu-Ag alloys NPs.[32] Cu-Ag alloy NPs also served antibacterial functions by continuously releasing ions to suppress the bacterial activities.[33] Therefore, Cu-based alloy NPs can be used as the fluorescence probe for detecting and killing germs.

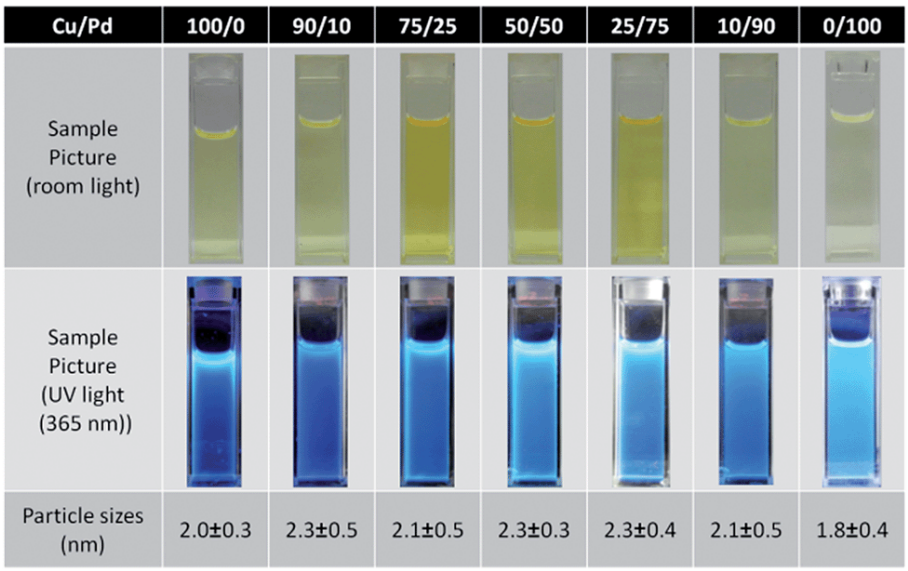


Figure 1.2 *Cu-Pd NPs show blue fluorescence under UV-light irradiation.* Photograph of Cu-Pd alloy NPs at different compositions under room light (upper row) and under UV light of 365 nm (lower row). Reproduced with permission from ref. [31] Copyright 2015 Royal Society of Chemistry.

Cu oxides. Cu has two types of oxides under atmospheric conditions – cuprous oxide (Cu_2O) and cupric oxide (CuO). Cu_2O is readily formed on Cu surfaces when exposing to ambient air at room temperature as a protective layer. Cu_2O is known to be a p-type semiconductor (direct bandgap 2.1 eV). CuO is formed when Cu_2O further interacts with oxygen at temperature above 250 ºC.[34-35] CuO is also a p-type semiconductor (indirect bandgap 1.35 to 1.5 eV). The semiconducting properties of Cu_2O and CuO provide photocatalytic functions.[36-37] CuO can also to be used in gas sensing application based on the change in electrical resistivity. For instance, the resistance of CuO was lowered by losing electrons when it contacted with NO_2 molecules [38] and increased by gaining electrons when it contacted with H_2 molecules [39]. Furthermore, the Cu_2O can be used as broadband pulse emission source under ultrafast laser excitation.[40]

Cu-based heterostructures. Heterostructures are referred to structures that contain an interface between different materials. Metal/semiconductor heterostructure has drawn attention because the interface of metal/semiconductor NPs provides outstanding properties for designing photovoltaic devices, catalysts and ion batteries.[41] Cu-based heterostructures are also having such characteristics without exception. Heterostructures

can be formed by, for instance, (1) core@shell nanoparticles, and (2) metal NPs embedded in host semiconductor NPs, and vice versa. In particular, Ag@Cu_2O core-shell NPs have better photocatalytic performance compared with Cu_2O NPs. It is because the Ag core can transfer plasmonic energy to the Cu_2O shell via plasmon resonance for the generation of electron-hole pairs in Cu_2O (**Figure 1.3**).[42] The electrons and holes in conduction and valance bands prone to react with the water molecules in the surrounding to form O_2^- (superoxide) and ·OH (hydroxyl radical) and thus resulting better photocatalytic performance. The metal core can also enhance the light absorption and tune the absorption spectra of the core@shell NPs so as to enhance photocatalytic activity over an extended wavelength range.[43]

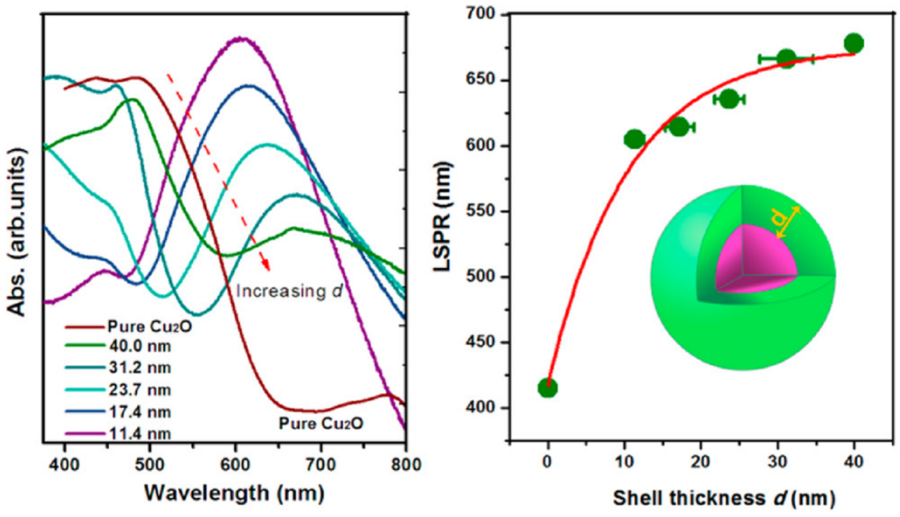


Figure 1.3 *Ag@Cu_2O core-shell NPs as photocatalyst.* Absorption peaks in UV-vis spectra red shifted with increasing the Cu_2O shell thickness. Reproduced with permission from ref. [42] Copyright 2013 The American Chemical Society.

Instead, electrons can be transferred to conduction band of semiconductor from the core metal as one of the photocatalytic mechanisms (also called '*hot electrons*').[44] However, the route of transferring electron from metal to semiconductor might be long for the core@shell structure.[45] Therefore, the heterostructure of metal NPs embedded in semiconductor microparticles was suggested. Ma *et al.* have synthesized a heterostructure with Au NPs embedded on Cu_2O microparticles.[46] The surface existed Au NPs exhibited strong plasmonic enhancement, which can promote the electron-hole pairs generation in Cu_2O. The structure was also benefits to the transfer of hot electrons from Au to the neighbor Cu_2O to facilitate the photocatalytic performance (**Figure 1.4**).[46] Moreover, metal/semiconductor interfaces are also used for designing semiconductor junction devices. When a semiconductor contacted to a metal, either ohmic or Schottky junction will be formed.[47] Each junction has its unique function for fabricating transistors, photovoltaic devices, etc. There are reports on low resistive Schottky junctions given by Au/Cu_2O interface [48-50]. Recent research have found the broadband pulse in terahertz (THz) frequency range emitted from Au/Cu_2O [51-54] and Ag/Cu_2O [55] interfaces under ultrafast pulse irradiation, making Cu-based heterostructures become applicable to more practical use (details in **section 1.4.1.2**).

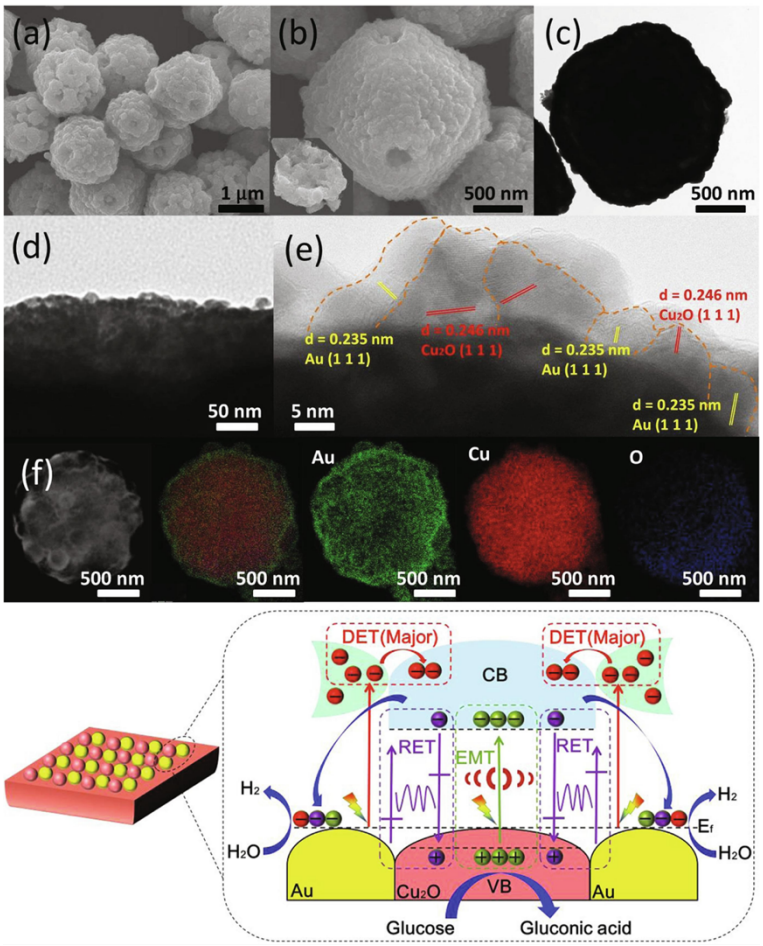


Figure 1.4 *Au NPs embedded in Cu_2O heterostructure as photocatalyst.* (a-d) Micrographs of the heterostructure. (e) HR-TEM micrographs with labeling *d*-spacing of Au (yellow) and Cu_2O (red). (f) EDS mapping to show the distribution of Au on Cu_2O. (Lower) Schematic diagram of the photocatalytic activity given by the heterostructure. Reproduced with permission from ref. [46] Copyright 2021, Elsevier, Ltd.

1.1.2 ZnTe nano/micro materials

ZnTe QDs. ZnTe is an II-IV semiconductor material with a wide and direct band gap of 2.26 eV (~ 548 nm) at room temperature. It has been considered as a prospective material for optoelectronic devices and green (λ = 550 nm) light-emitting-diodes (LEDs).[56-57] Like other quantum dots (QDs), ZnTe has special properties of narrow emission spectrum and wide excitation spectrum. It is usually emerged with other QDs by doping or in the form of core-shell structures to tune the energy band gap and achieve desired optical properties. **Figure 1.5** shows photoluminescence (PL) from ZnTe@ZnSe core@shell structure with 4.4 nm-sized ZnTe cores and different ZnSe shell thickness.[59] ZnTe itself can be used as heavy ions sensor to detect existence of heavy metals in aqueous media and anode materials for rechargeable Li-ion batteries through hybridizing with other conductive materials.[60-62] It can also be applied in solar cells such as enhance the photo-response to photoexcitation by tuning the energy bandgap through doping with other substances.[63]

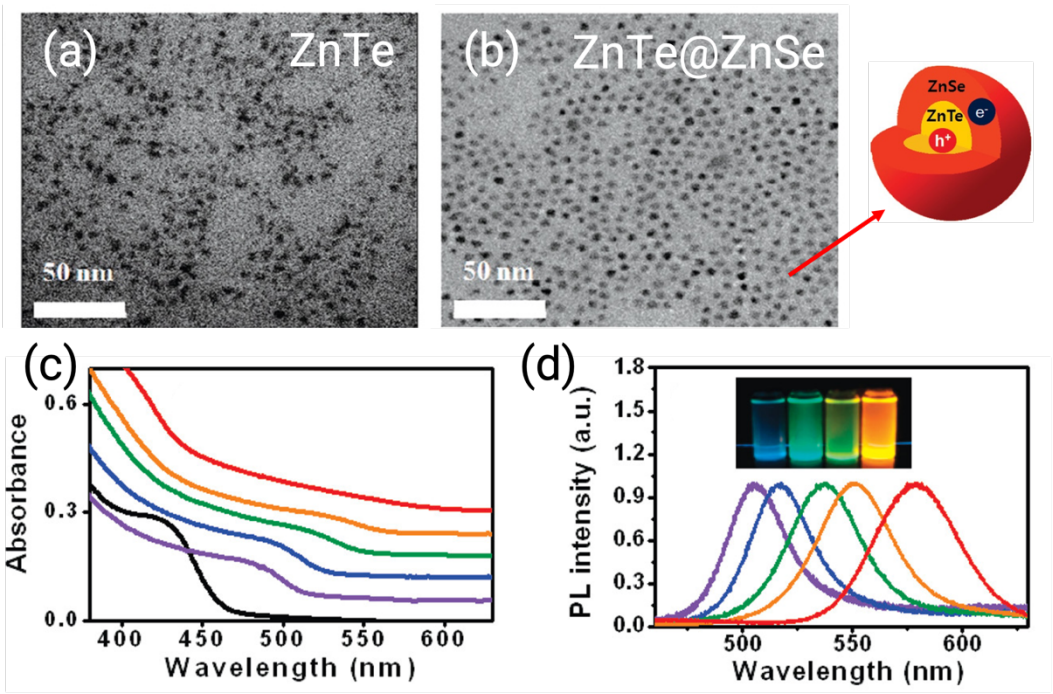


Figure 1.5 *Photoluminescence from ZnTe@ZnSe core-shell QDs.* Micrographs of (a) ZnTe cores and (b) ZnTe@ZnSe core@shell QDs. (c) UV-vis absorption spectra of ZnTe core (black), ZnTe@ZnSe core@shell QDs with 1.0 (violet), 1.4 (blue), 2.0 (green), 3.3 (orange), and 5.0 (red) monolayers of ZnSe shell. (d) Corresponding PL spectra with respect to different numbers of shell monolayers. Reproduced with permission from ref. [59] Copyright 2010, The American Chemical Society.

ZnTe single crystal. ZnTe belongs to the family of electro-optic (EO) crystals, those have non-centrosymmetrical crystal structure including GaAs, InP, ZnTe, CdTe, GaP, BBO and $LiTaO_3$. Zincblende structured ZnTe is particularly important among other EO crystals because it is suitable for both generation and detection of broadband THz pulses (**Figure 1.6**).[64] (details in **section 1.4.1.1**)

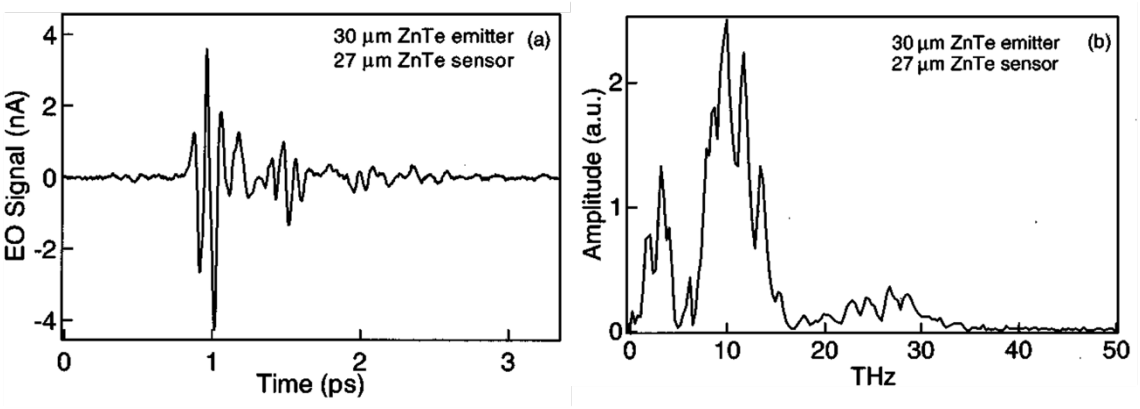


Figure 1.6 *Broadband THz pulse emitted and detected by ZnTe crystal.* (a) Temporal waveform of the THz pulse from 30 μm ZnTe emitter and measured by a 27 μm ZnTe sensor. (b) Power spectrum of the waveform in (a). Reproduced with permission from ref. [64] Copyright 1998, AIP Publishing.

ZnTe microspheres. ZnTe has negative conduction band position at –1.7 V vs NHE.[65] It can be used as the photocatalyst for CO_2 reduction and yielding CH_4.(**Figure 1.7**a) Ehsan *et al.* have found the mesoporous ZnTe microspheres [66] can provide more catalytic active sites for CO_2 reduction compared with ZnTe nanocrystals (**Figure 1.7**b-c)[67-70], but ZnTe nanocrystals serve better catalytic performance when they formed heterostructures with other n-type semiconductors such as TiO_2.[71]

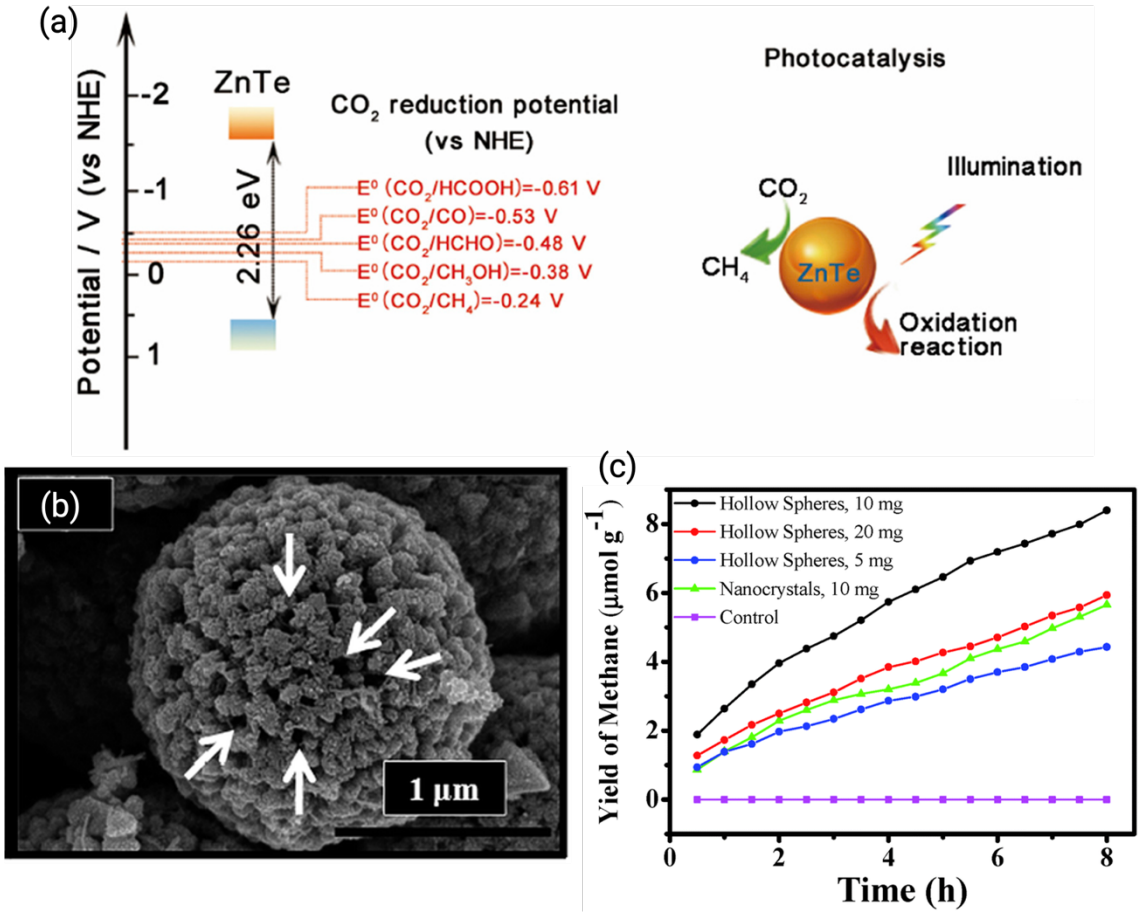


Figure 1.7 *ZnTe microspheres as photocatalysts for CO_2 reduction.* (a) Negative band position of ZnTe and reduction potential of products against CO_2. Reproduced with permission from ref. [70] Copyright 2019, Elsevier, Ltd. (b) Micrographs of mesoporous ZnTe microspheres. (c) Higher yield of methane by using ZnTe mesoporous compared with ZnTe nanocrystals. Reproduced with permission from ref. [69] Copyright 2014, Royal Society of Chemistry.

1.2 Syntheses of Nano/Micro Materials

There are two generic approaches for synthesizing nano/micro materials – Bottom-up and top-down. Bottom-up approach is to build up a larger structure from small components. Most of the materials are chemically synthesized with bottom-up approach. On the other hand, top-down approach is to break down a large structure to obtain smaller components.

1.2.1 Bottom-up

Wet-chemical synthesis. The method generally requires hydrolysis of the precursors (metal salts) followed with the addition of reducing agent. Nuclei/clusters of metal are then formed and proceed aggregation and coalescence to minimize their free surface energy, resulting in zerovalent metal nanomaterials in aqueous or organic media (**Figure1.8**).[72] This method is popular nowadays since it was firstly reported in 1857 by Faraday.[73] One of the most famous wet-chemical syntheses is the synthesis of 20 nm-sized gold colloids by reduction of $[AuCl_4]^-$ with sodium citrate, reported by Turkevich *et al*.[74] Cu colloids can also be synthesized by using wet-chemical methods. However, the limitation of synthesizing Cu colloids is that the colloids easily get oxidize during the after the reaction. So that, the methods are preferably performed in aqueous

free and under an inert atmosphere.[75] In case of compound formation, precursors for both cation and anion are required. Some precursors need special handling because they are not stable under ambient. For instance, telluride ion (Te^{2-}) has to be pre-prepared by dissolving semi-metallic Te into trioctylphosphone (TOP) solution, which stabilizes Te^{2-} for further reaction.[76] Generally, the average size of colloids increases with the increase of reaction temperature. A wide range of stabilizers and surfactants are used to control the growth of the nuclei and to prevent the agglomeration of nuclei, so as to yield nanomaterials with different sizes and morphologies.

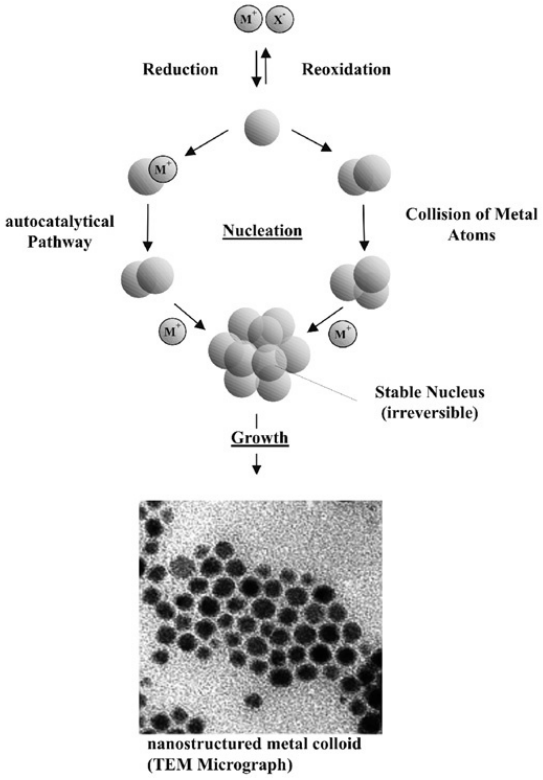


Figure 1.8 *Formation scheme of zerovalent metal colloids through bottom-up approach.* Reproduced with permission from ref. [72] Copyright 2001, WILEY.

The growth of colloids in the reaction system can be explained based on Ostwald ripening (OR) and oriented attachment (OA). OR refers to the larger particles grow to the detriment of the smaller particles because of smaller particles are having higher solubility. In case of no ligands are being adsorbed on the particles' surface, the smaller particles prone to dissolve into larger one for the latter to growth. OA refers to the self-organization of adjacent nanocrystals, which the crystals are sharing a common crystallographic orientation with each other, resulting in growth of colloids.[77-80] In OA mechanism, the primary particles are not necessary to be dissolved into others, but they likely assemble into larger agglomerates. The ZnTe microspheres given in **Figure 1.7** is one of the examples of particles formed via OA mechanism. Particles synthesized via OA mechanism are usually with mesoporous characteristic because the assembly of nanocrystals are not highly compact.

Thermal decomposition. This method uses a solvent under high pressure and temperature in a sealed vessel, that facilitates the interaction of precursors during synthesis. It is called 'hydrothermal synthesis' when water is used as solvent, otherwise it is called 'solvothermal synthesis'. Some inorganic materials synthesized via the hydro-/solvothermal method are predominantly having OA mechanism in their growth.[81]

Comparing with the conventional methods for making hollow structures, that require removable templates as the core and bring more procedures in the synthesis, hydro/solvothermal method can synthesize hollow/mesoporous structures in a template-free manner.[82-86] Although the operation of thermal decomposition method is relatively easy, parameters are hardly controlled. Inhomogeneous products are usually yielded due to unquantified pressure inside the reaction tank and/or the mixture is not stirred during the reaction. It is also difficult to observe the subsequent growth of particles at a certain time because of the sealing characteristics of this method.[87]

1.2.2 Top-down

Sputter deposition. Sputter deposition is a physical vapor depositions (PVD) technique. PVD techniques are traditionally referred to as a thin film deposition technique – the material goes from a condensed phase (solid) to a vapor phase and then back to a condensed phase on a solid substrate as the film structure with thickness in the range of a few nanometers to several micrometers. Sputter deposition has the advantage from traditional evaporation methods that materials which are difficult to evaporate can also be utilized for deposition. The inert ions, usually argon, create a plasma and accelerated in an electrical field. The kinetic energy of these ions is higher than the binding energy of the particles in the target material. The surface of the target material is then under bombardment by energetic gas ions and the particles on the surface are ejected due to the momentum transfer and relaxation processes (**Figure 1.9**).

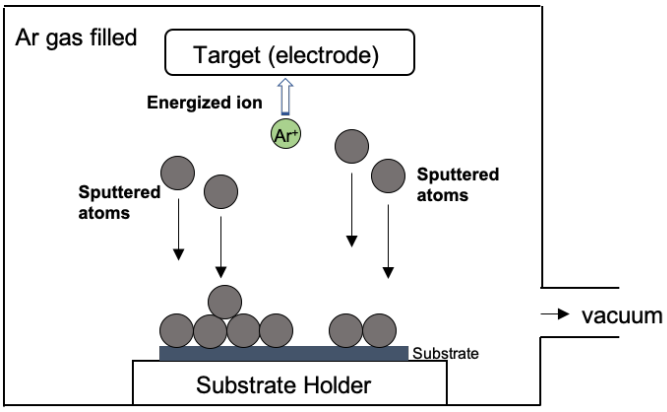


Figure 1.9 Schematic diagram of sputtering process.

Monometallic NPs dispersion via sputter deposition. Introducing liquid matrix as the substrate in the sputter deposition can easily generate NPs dispersion. Sputtering has advantages over using chemical reduction methods to synthesize NPs solution – it does not require high temperature for metal precursor reduction and free from contamination. Liquid media with low vapor pressure, e.g., silicon oil [88], ionic liquids[89], polymer[90], have been used in sputtering to make monometallic NPs. The liquid media are not only capturing NPs, but also provide steric effect to maintain the dispersiveness of NPs and control the sizes. The particle size is also tunable by varying (1) chamber pressure, (2) target-liquid distance, (3) applied voltage, (4) applied current, (5) existence of ligands in liquid matrix, (6) deposition time, (7) viscosity of liquid matrix, etc.[91] **Figure 1.10** shows the micrographs of Ag NPs and Pt NPs in polymer matrix synthesized via sputter deposition.

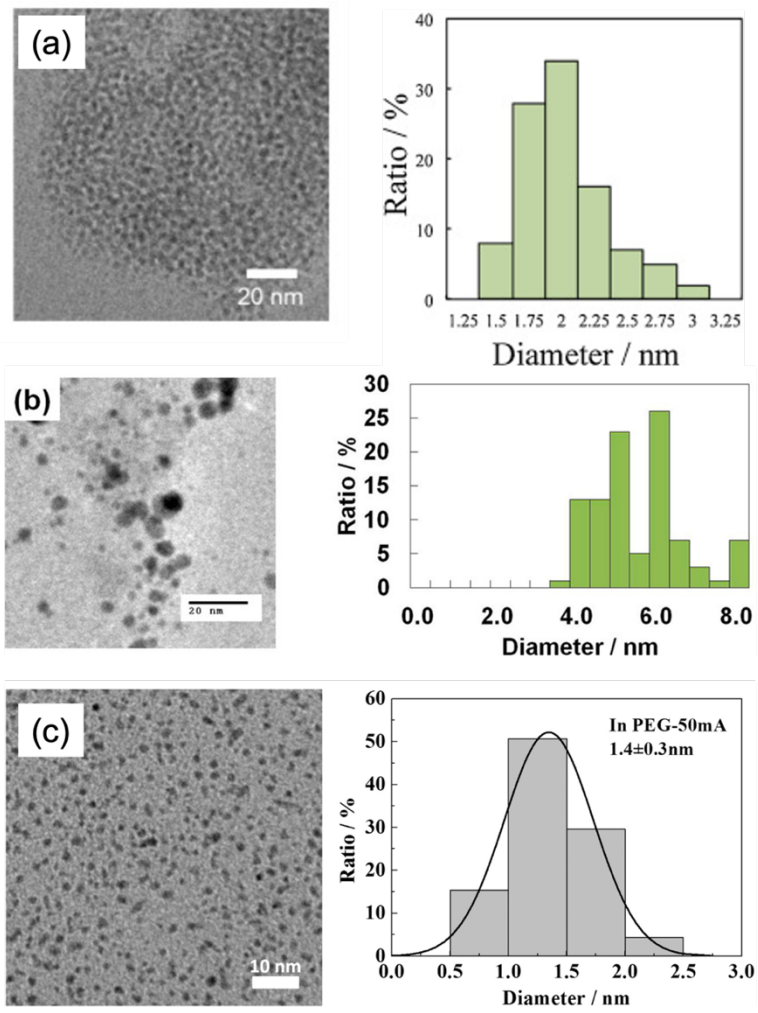


Figure 1.10 TEM micrographs and size distribution of NPs synthesized by sputter deposition. (a) Ag sputtered into pentaerythritol tetrakis(3-mercaptopropionate) (PEMP), sputtering current = 30 mA, sputtering time = 20 min.[92] Reproduced with permission from ref. [67] Copyright 2016 Elsevier Ltd. (b) Ag sputtered into PEG, sputtering current = 20 mA, sputtering time = 20 min. [93] Reproduced with permission from ref. [93] Copyright 2015 The America Chemical Society. (c) Pt sputtered into PEG, sputtering current = 50 mA, sputtering time = 30 min.[94] Reproduced with permission from ref. [69] Copyright 2018 The America Chemical Society.

Alloy NPs dispersion via sputter deposition. Alloy NPs can be synthesized by sputtering. One way is using tailor-made alloy targets for making alloy NPs in desired composition. However, the sputtered product might not have the same molar ratio as the target because the sputtering yield is dissimilar for different chemical elements, and thus the target needs long conditioning through trial and error to yield alloy NPs with desired composition. Another way is 'co-sputtering', which atoms are sputtered from various targets simultaneously. Co-sputtering does not require tailor-made alloy targets but a sputtering system with multiple heads is needed. Ludwig and his co-workers have synthesized Au-Cu[95], Fe-Al[96], Cu-Ru[97] alloy NPs in ionic liquids via double target sputtering. Yonezawa and his co-workers have performed double head target sputtering for making Au-Ag[98], Au-Cu[99], Pt-Au[100], Pt-Ag[101], Pt-Cu[102] alloy NPs in PEG. The composition of alloy NPs are tunable through adjusting the sputtering current for each metal targets (**Figure 1.11**).[99,101] Instead, there are reports on multiple-metallic alloy NPs. Garzón-Manjón *et al.* have used a high entropy alloy target of making Cr-Mn-Fe-Co-Ni NPs.[103] Zhu *et al.* have used a CuPt alloy target co-sputtered with Ag target to obtain CuPtAg alloy NPs dispersion with different composition.[104] From these findings, it is possible to synthesize multiple-metallic alloy NPs with different compositions if multiple sputtering heads are available.

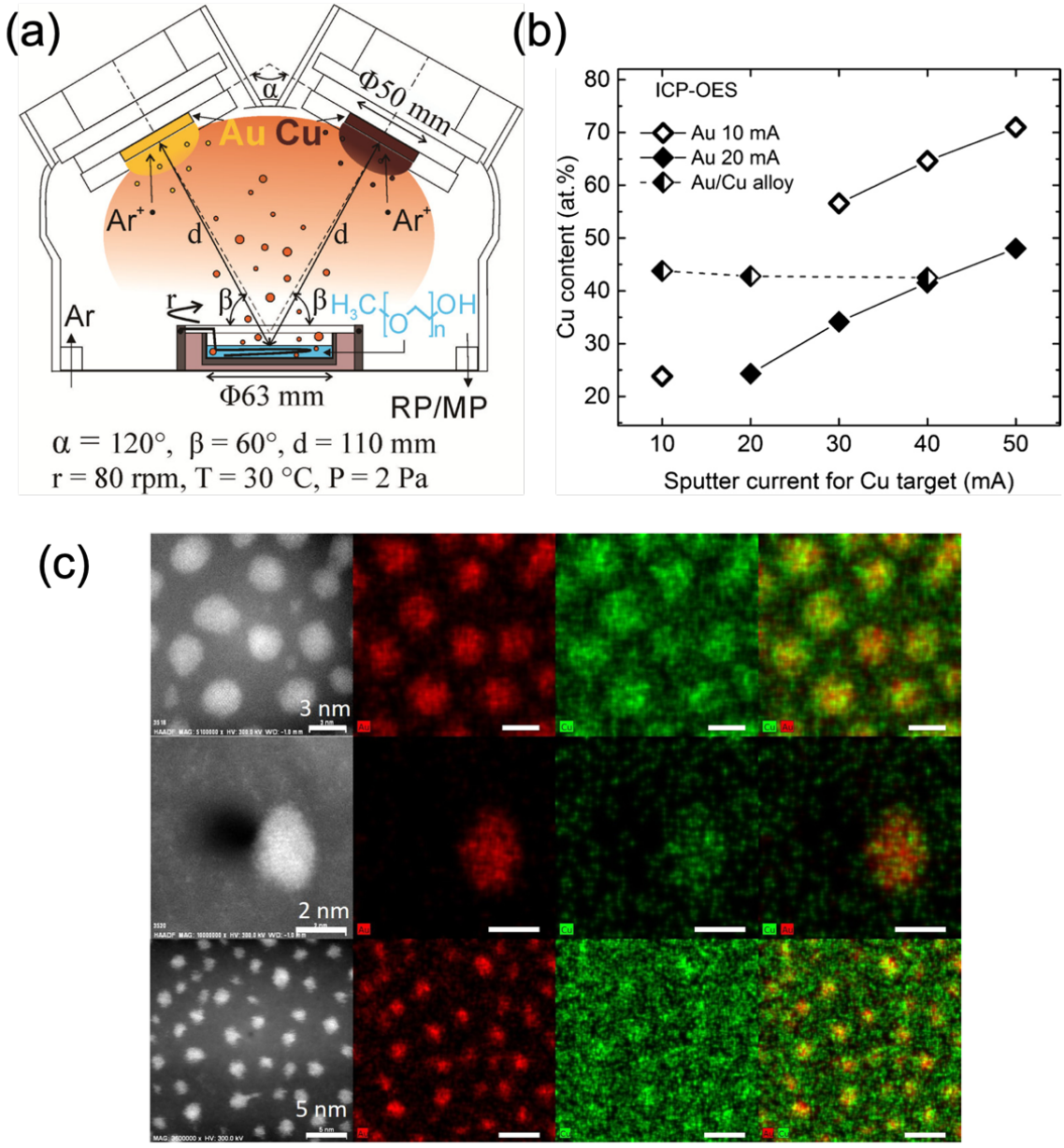


Figure 1.11 (a) Schematic diagram of the double target sputtering chamber. (b) Cu content of Au-Cu alloy NPs against sputtering current for Cu target from 10-50 mA and sputtering current for Au target at 10 mA and 20 mA. Half-filled diamond data points represent the composition of alloy NPs sputtered by double head system using Au-Cu alloy target. (c) HAADF and EDS mappings [Au L (red), Cu K (green), and overlay] for nearly equimolar Au-Cu alloy NPs. Reproduced with permission from ref. [99] Copyright 2017 The American Chemical Society.

1.2.3 Selecting an appropriate method: Bottom-up or top-down?

Nanomaterials with well-defined sizes and shapes can be synthesized using bottom-up approach. It is because the reaction temperatures, concentration of reagents, reaction environments, etc. can be controlled. The bottom-up process is also low-cost compared with the physical methods, which generally involve sophisticated equipment. However, there are some limitations of using bottom-up approach – (1) although the approach possibly proceeds large-scale syntheses for industrial-scale production of nanomaterials, trial-and-error tests are needed. It is because large-scale syntheses are not simply done by only scaling up all reagents and solvents. The different reaction volumes would affect the reaction kinetics of nuclei, causing different morphologies and sizes compared with the small-scale synthesis. (2) Separation of desired products from by-products is necessary. Product lost might happens during the purification steps. Also, the reagents used/by-products are possibly toxic to environment. (3) Making alloy nanomaterials is not as simply as reducing single element precursors. The difference in reduction potential should be taken into account when handling multiple metal precursors.[105-109] Galvanic reaction is preferably taken place when two metal precursors with large difference in reduction potential value, which forms a heterostructure instead of an alloy.

Top-down approach, such as sputter deposition, does not involve any toxic substance. It is a facile approach of making thin film on solid substrates. Multiple-layered thin film structures are also available by arranging the order of sputter deposition, and they are usually ready-to-use. The synthesis of NPs dispersion introduced in previous section has opened a new page for preparing NPs in an eco-friendly manner. Particularly it can synthesize alloy NPs with different compositions by simply alternating the sputtering current of the metal targets. Nevertheless, the method remains issues – (1) The volume of NPs dispersion is limited by the sputtering chamber, which is not suitable for large-scale production. Even though a large-scale chamber is available, high vacuum usage during the operation would consume much energy, and thus making the method is not eco-friendly in some extent. (2) Sputter deposition is likely producing solid NPs. Wire- and tube-liked morphologies and hollow structures synthesized by sputter deposition are not yet reported to the best of author's knowledge. (3) Only liquid substrates with low vapor pressure can be used. NPs dispersed in aqueous phase are not available by this approach because water molecules easily evaporate under high vacuum conditions. (4) The alloy NPs synthesized via sputter deposition are having low crystallinity.[103,104] This is a double-edged characteristic because some applications would require the use of highly crystallite materials (and some may not).

There are more ways to obtain precise nanomaterials, e.g., chemical vapor deposition, microwave-assisted synthesis, electrospinning, laser ablation, etc. However, there is no 'golden method' suits for synthesizing all kinds of nanomaterials. The properties of nanomaterials highly depend on the preparation method. Therefore, an appropriate method should be chosen with considering the desired characteristics.

1.3 Femtosecond Laser Technologies

1.3.1 Brief introduction of ultrashort pulsed laser: How it is happened?

"Laser" is an acronym for "**L**ight **A**mplification by **S**timulated **E**mission of **R**adiation". It is a spatial and temporal coherent light source, which allows lights to be focused to a tight spot and travels for long distances with very narrow spectrum. Unlike the continuous-wave that we commonly use in laser pointers, ultrashort pulsed laser has duration in nanosecond to femtosecond (10^{-15} s) scale and the pulses are emitted from the source periodically in certain rate. When nanosecond laser interacts with a solid target, thermal expansion of the target surface will happen because of the relatively long duration of laser pulse, which is known as laser ablation process. When shortening the pulse duration to femtosecond laser, the laser pulses are deposited into the solid target faster than the occurrence of laser ablation. The characteristics of femtosecond laser have

brought a new laser-solid interaction regime for new applications. Therefore, ultrashort pulsed lasers are of interest.

Q-switching and mode-locking are two mechanisms used for producing ultrashort laser pulses.[110] Q-switching usually generates nanosecond laser pulse, which is commonly used in precise laser beam machining. On the other hand, the mode-locking technique can reach to femtosecond level. Ultrafast mode-locked lasers usually consist of four components: (1) pump source, (2) reflector to form resonant cavity, (3) rare-earth-doped fibers, (4) mode-locked modulation device. Titanium-doped aluminum oxide (Ti:sapphire) is the predominant gain medium of femtosecond laser systems because of its high thermal conductivity, so the crystal can tolerate high optical pumping power to 20 W, and its short carrier lifetime (~3.2 ms). The mechanism of laser light generated from Ti:sapphire is illustrated in **Figure 1.12**. A green pump laser (~520 nm) excited the electrons, which then relax into lower and more stable states building up a population inversion and gives rise to stimulated emission near 800 nm. More examples of gain medium for femtosecond laser systems are listed in **Table 1.1**.[111] In the case of using Ti:sapphire as the gain medium, wavelength of femtosecond laser is not limited at 800 nm. The wavelength of the femtosecond laser pulse is tunable via nonlinear optical process. For instance, the wavelength is converted from 800 nm to 400 nm by second

harmonic generation (SHG) and even to about 250 nm by third harmonic generation. It can also be tuned to longer wavelength to about 1100 nm by optical parametric oscillator.

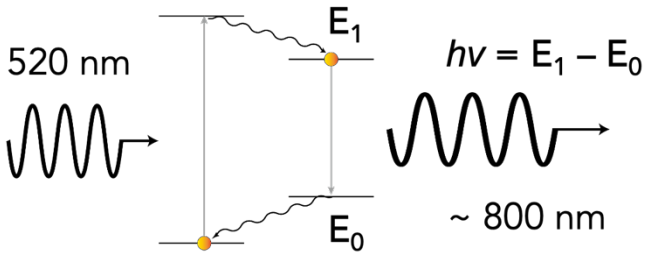


Figure 1.12 Scheme of laser light generated from Ti:sapphire as the gain medium.

Table 1.1 Gain media of laser and their spectra range.[111]

Gain medium	**Spectra range**
Rhodamine 6G	600-650 nm
Ti:sapphire	650-1100 nm
Cr:LiSAF	800-1000 nm
Nd:glass	1040-1070 nm

"Mode-locking" means the phase of all oscillating modes in the resonant cavity is locked, so it is able to generate short laser pulses. There are *active* and *passive* mode-locking methods. *Active* mode-locking needs an external periodic signal to control the parameters of resonant cavity. *Passive* mode-locking uses the intracavity mode-locked

device by installing a saturable absorber[112,113] into the resonant cavity and make use of its nonlinear absorption characteristics to generate ultrashort pulses (**Figure 1.13**). *Passive* mode-locking is more commonly used because the energy loss of pulse when it passes through the saturable absorber is low, and the loss of the low-intensity part of the two ends is large, which results in pulse narrowing.

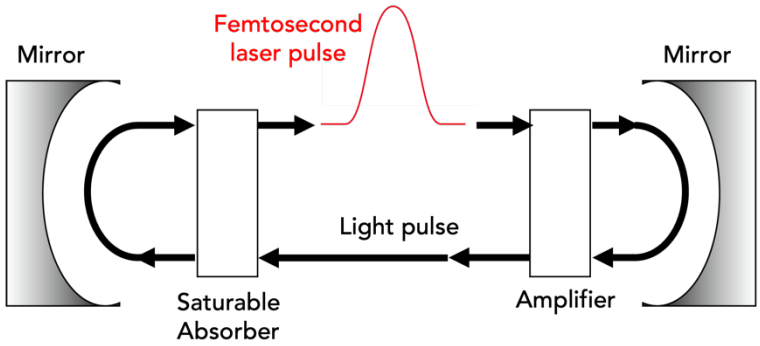


Figure 1.13 Block diagram of resonant cavity of passive mode-locked laser.

However, the output energy of mode-locked femtosecond laser is relatively weak (~1 nJ). Chirped pulse amplification (CPA) is the technique to enhance the output energy, which is invented by Mourou and Strickland (winners of The Nobel Prize in Physics 2018).[114] In CPA, the mode-locked laser pulse is used as a seed laser. The seed laser passes through a stretcher, which 'expands' the pulse and gives a broad peak with lower peak power. Then it passes to the gain medium, which enhances the peak power while the

peak was still broad. Finally, the broad peak passes to a compressor, which 'compresses' the peak so as to achieve a laser pulse with high peak power (**Figure 1.14**).

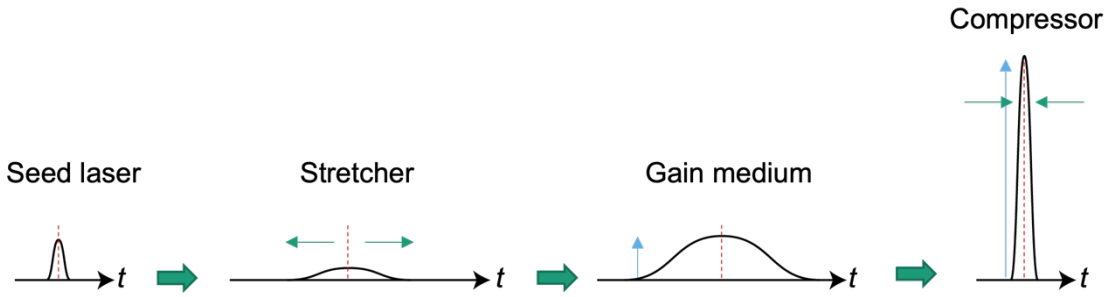


Figure 1.14 Process of chirped pulse amplification for mode-locked laser.

1.3.2 X-ray emission from solid/liquid targets

X-ray generation is one of the advanced photonic applications brought from the development of femtosecond laser. X-ray is categorized into hard and soft X-rays (**Table 1.2**). Hard X-ray has drawn more attention because it shows features similar to the conventional X-ray tubes. Especially the characteristic line radiation from different targets is of interest for applications due to the unique emission wavelength and the narrow spectral line width.

Table 1.2 Difference between soft and hard X-rays.

Item	**Soft X-ray**	**Hard X-ray**
Frequency	30 to 3000 PHz	3 to 300 EHz
Wavelength	10 to 0.1 mm	100 to 1 pm
Photon energy	< 0.2 keV	> 1 keV
Application	Mammography	Airport security, XRD

X-ray emission from bulk targets. Hard X-ray pulses can be generated through irradiating femtosecond laser to bulk metal targets (**Figure 1.15**), and polymers such as poly(vinyl chloride).[115-118] The X-ray generation is based on two phenomena – (1) laser-generated plasma and (2) hot electrons. Since the laser pulse energy is relatively high, ionization takes place when the laser pulse interacts with solid/gaseous atoms on the travelling path, forming plasma as the X-ray source. Then, electrons given from the plasma would penetrate into the solid target materials, knocking out bound *K*-shell electrons of target atom as another X-ray source. This latter process is also known as bremsstrahlung, i.e., kinetic energies of electron is converted to the photon energy.

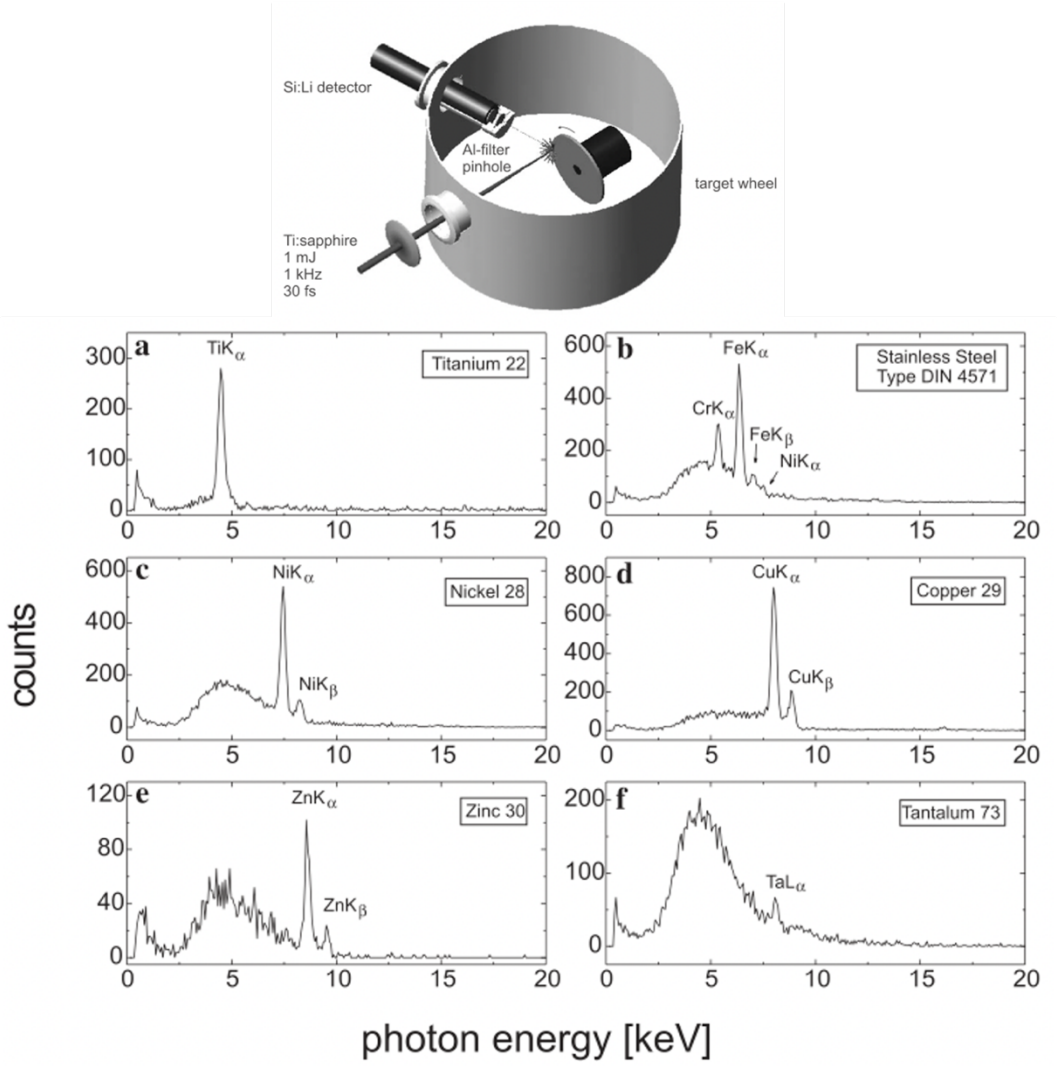


Figure 1.15 (Top) Schematic diagram of the X-ray emission test from metal target in ref. [116]. (Bottom) Corresponding X-ray emission spectra of (a) Ti, (b) stainless steel, (c) Ni, (d) Cu, (e), Ta targets. Reproduced with permission from ref. [116]. Copyright 2003 Springer.

X-ray emission from liquid targets. Additionally, liquid targets are used to generate hard X-ray. Tompkins *et al.* reported that the hard X-ray emission (5-20 keV) was observed from near-saturated aqueous copper nitrate solution and neat ethylene glycol.[119] Korn *et al.* has used the low-melting point property of Ga, making a liquid Ga jet as target and observed a broadband X-ray emission (4-14 keV) (**Figure 1.16**).[120]

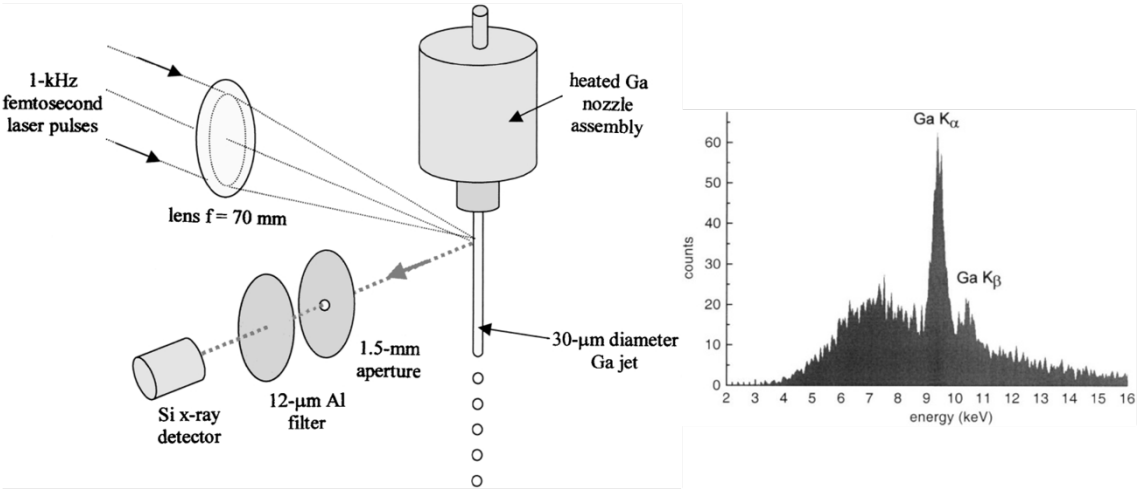


Figure 1.16 (Left) Schematic diagram of the X-ray emission test from Ga liquid jet in ref. [90] and (Right) X-ray emission spectrum of Ga jet target. Reproduced with permission from ref. [120] Copyright 2002 Optica Publishing Group.

Hatanaka *et al.* has extensively evaluated the X-ray emission through focusing femtosecond laser pulses onto Cesium chloride (CsCl) electrolyte in the aspect of laser intensity, solute concentration, solute atomic number, double-pulsed effect, and chirp

effect.[121-125] The X-ray intensity from CsCl solution increased with higher femtosecond laser power. It is because intense, high laser power causes multiphoton ionization.[121] The conductive electrons produced from the ionization collide with atoms and ions in the liquid target and knock out the inner shells' electron, resulting in X-ray emission. Increasing the CsCl concentrations and solute atomic numbers are also effective ways to enhance X-ray emission as the electron temperatures increased with more atoms existed in the solution.[122] Moreover, X-ray emission intensity increases almost four orders when using double pulse laser because the pre-pulse generates small droplets from the liquid target surface, enhancing the surface area for the main pulse irradiation.[123] Nanocolloid dispersion have been used as an alternative hard X-ray source. Masim *et al.* reported X-ray emission (15 keV) from Au nanoparticle suspension.[126] The X-ray emission intensity is the highest for Au nanoparticles in 40 nm of diameter, which have the strongest UV extinction (**Figure 1.17**). The X-ray intensity is driven by the absorbed energy and resonant absorption at the interface of water/air and Au/air. When Hsu *et al.* used double-pulse laser to irradiate the Au nanoparticles[127], the pre-pulse made the liquid surface became rough, and nanobubbles were generated, leading to a strong localization and absorption of light by Au nanoparticles. These resulted in higher electron temperature to achieve higher X-ray

emission intensity.

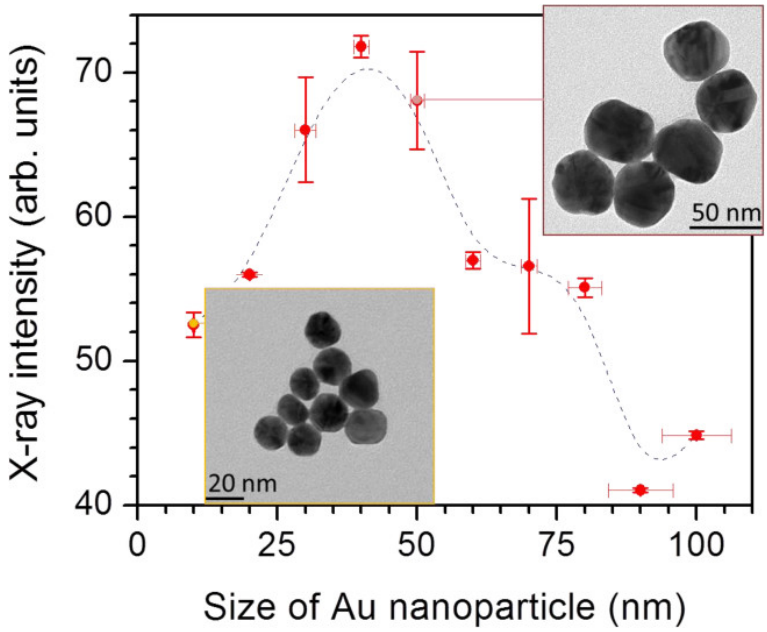


Figure 1.17 X-ray emission intensity against diameters of Au nanoparticles. Au concentration was 1.2 × 10^{-3} M in all samples. Reproduced with permission from ref. [126] Copyright 2016 The American Chemical Society.

X-ray emission from water. Instead of aqueous solution containing ions or nanocolloids with high atomic numbers, water itself can be a hard X-ray source. Huang *et al.* reported X-ray emission from a water film irradiated by femtosecond laser.[128-129] The major mechanism of X-ray emission from water film is related to laser-induced plasma formation. The X-ray emission intensity was increased with the increasing laser power due to the absorption of thermal energy by water, giving high electron temperature

as the X-ray source. The most interesting is that both X-ray and terahertz (THz) waves emission from water have been driven by femtosecond laser simultaneously.[128] In other words, with the use of femtosecond laser and specific targets, there is a potential of combining X-ray and THz wave for future applications.

1.4 Terahertz Wave Technologies

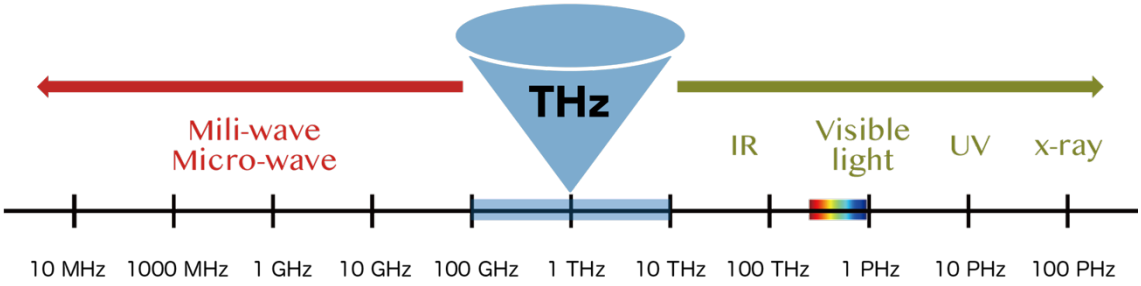


Figure 1.18 Terahertz band in the electromagnetic wave spectrum.

THz wave refers to those electromagnetic waves with frequency ranged between 0.1 and 10 THz (1 THz = 1 ps = 300 μm = 33.3 cm^{-1} = 4.1 meV = 47.6 K) (**Figure 1.18**). The spectral domain of THz hosts low frequency crystalline lattice vibrations, hydrogen-bonding stretches, and intermolecular vibrations of many chemical and biological molecules (e.g., proteins[130], DNA[131-132]), including explosives and related compounds and drugs. Similar to the Fourier Transform Infrared Spectroscopy (FTIR), the transmitted and reflected THz spectra of these materials contain THz absorption

fingerprints for us to distinguish the materials, but THz spectra can provide more information that is out of the detection range of FTIR and X-rays. Bessou *et al.* has compared the sensing capability of THz wave and X-ray for the same objects (**Figure 1.19**).[133] The THz wave provides more detailed image than X-ray does. Followings are some features of THz wave which motivate the development of THz technologies in the past decade for defense and security applications:

- Low photon energies (1 million times weaker than X-ray photons)
- Can penetrate through many nonpolar dielectric materials

  e.g., paper, cardboard, textile, plastic, wood, leather, ceramic, etc.
- Nondestructive and noninvasive

THz wave is categorized into (1) broadband pulses and (2) continuous-wave and the detection and generation have been focused in developing THz wave technologies. The generation and detection for each consist of different methods. This dissertation only discusses approaches related to THz broadband pulses.

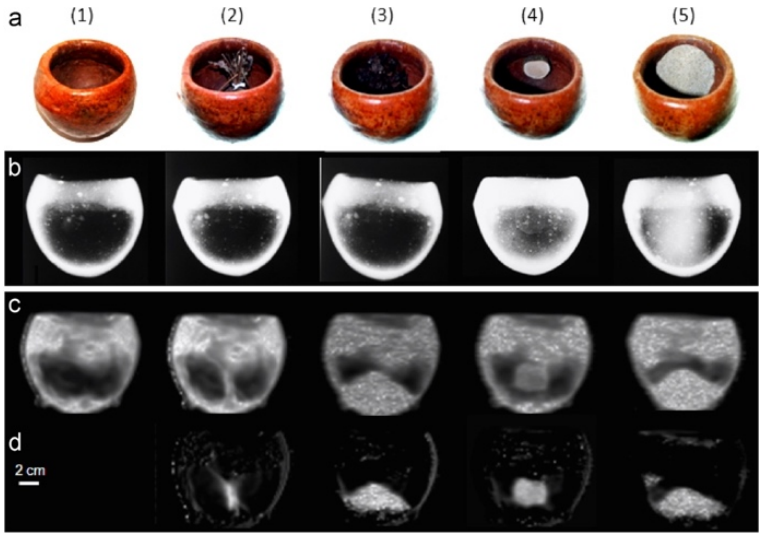


Figure 1.19 Comparison of sensing capability of THz wave and X-ray. (a) Photographs of model objects. (b) X-ray radiographs. (c) THz wave imaging. (d) Differential THz wave (subtraction image between filled jar and empty jar). Reproduced with permission from ref. [133] Copyright 2012 Elsevier Ltd.

1.4.1 Terahertz wave generation

The emission of THz only relies on the generation of a time-dependent polarization, varying on a short timescale. The emitted electric field is proportional to the second derivative of the induced polarization when the size of source is much smaller than the generated wavelength:

$$E(t) \propto \frac{\partial^2 P}{\partial t^2} \quad \text{...(Eq 1.1)}$$

The following sub-sections will introduce recent research on the materials used for generating THz wave pulse via femtosecond laser excitation.

1.4.1.1 Nonlinear optics

When electron interacts with incident light, both influence on the electrons' motion and magnetic fields of the materials are negligible. The optical response, such as THz wave emission, is counted only on the electric dipole oscillations of electrons. When an intense light passes through a *linear* crystal sinusoidally, amplitude of transient polarization change with the amplitude of incident light, the net transient polarization is zero, i.e., Electrons bound like a simple harmonic oscillator and the electric dipole moments are proportional to the amplitude of the applied optical field.

In case of a *nonlinear* crystal, the amplitude of transient polarization does not change with the amplitude of incident light, results in a time varying non-zero transient polarization. It should be noted that the spectral bandwidth (Tera = 10^{12}) of the radiation is roughly the inverse of the optical pulse duration (femto = 10^{-15}).This phenomenon is called optical rectification (OR). OR occurs in the crystals that lacking inversion symmetry (**Figure 1.20**). For instance, Yang *et al.* reported the generation of far-infrared radiation in $LiNbO_3$ via OR.[134] Auston *et al.* generated broadband pulses with frequency up to 4 THz in $LiTaO_3$.[135] THz pulses generation via optical rectification is also detected from GaAs [136], ZnTe [137], and dimethyl amino 4-*N*-methylstilbazolium tosylate (DAST) [138].

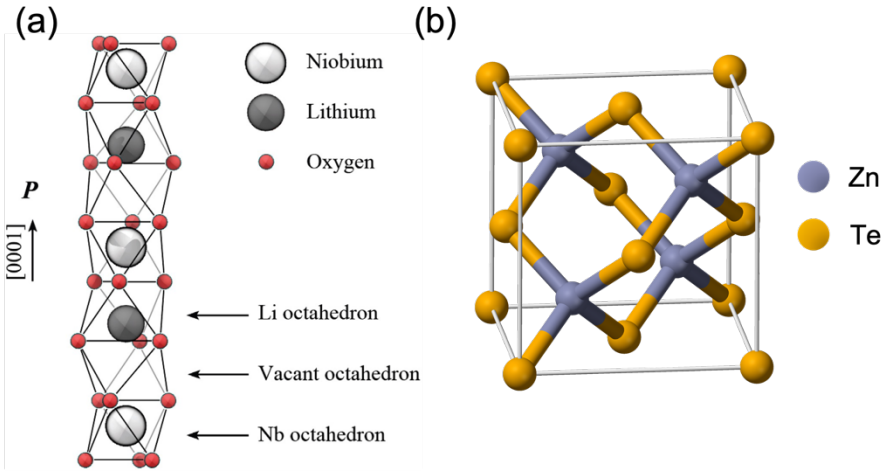


Figure 1.20 Crystal structure diagram of nonlinear crystals: (a) $LiNbO_3$ [139] , Reproduced with permission from ref. [139] Copyright 2017 IOP Publishing. (b) ZnTe.

All noncentrosymmetric crystals have non-zero second-order nonlinear susceptibility $\chi^{(2)}$. The relationship of applied electric field (ultrafast laser), $\boldsymbol{E}$, polarization (source of THz), $\boldsymbol{P}$, and the nonlinear susceptibility $\chi^{(2)}$ is given by

$$\boldsymbol{P}(t) = \epsilon_0 \chi^{(2)} \boldsymbol{E}^2(t) \quad \text{...(Eq 1.2)}$$

$$\text{where } \boldsymbol{E}(t) = \varepsilon \cos \omega t \quad \text{...(Eq 1.3)}$$

From **Eq 1.2**, the THz wave emission can be enhanced by using more powerful incident laser or using nonlinear crystals with higher susceptibility.

ZnTe. Among the THz generating crystals, ZnTe single crystal has drawn the most attention because it can be both emission and detection (details for detection part see **section 1.4.2**) medium for THz wave. THz wave emission from ZnTe via OR highly

depends on how the ultrafast laser pulse incident to the crystal. It is noteworthy that the intensity of THz emission is affected by the incident angle of laser pulse as well as the orientation of ZnTe crystal.[140-141] The THz intensity is maximum when the optical polarization lies on the {110} plane.[112] To achieve maximum intensity of THz wave emission from ZnTe, linearly polarized pulses are propagating along the [110] axis of ZnTe crystal and the angle of propagating direction of the pulses to the [001] axis of crystal should be 54º. Thus, ZnTe single crystal is used in THz wave technologies instead of polycrystalline ZnTe and the alignment of optical instruments are important.

1.4.1.2 Semiconductors

Auston and Lee applied a static electric field to amorphous Si and Cr-doped GaAs and observed THz pulse emission via ultrafast laser pulse from the materials.[142-144] Within the bulk semiconductor, electron-hole pairs are generated through photo-excitation and these carriers accelerate in a defined direction according to the applied electric field (bias). A transient photocurrent is induced during the process and thus resulting in THz wave emission.

Concepts of Schottky/ohmic junctions. Same effect can be given by 'built-in' bias in the Schottky interface created through bringing metal and semiconductor into

contact. For an isolated metal, the states below Fermi energy (E_F) are filled, while above E_F is empty. When it is contacted with a semiconductor, a Schottky barrier is given, which is quantified by the Schottky barrier height (ϕ_B). In n-type semiconductor, the barrier is against the electron flow, whereas it is against the hole flow in the p-type semiconductor. Electrons/holes tend to move toward to other side, but they are 'trapped' because of the barrier (**Figure 1.21**). Therefore, the build-in bias is formed at the interface. In fact, tendency of the charges move from one side to the other depends on the work function of materials. The Schottky only forms when the work functions of metal and semiconductor satisfy the conditions in **Table 1.3**. Otherwise, an ohmic contact forms, which has low resistivity and no voltage across it, thus no build-in bias. During the ultrafast pulse laser irradiation, excitation of electron-hole pairs in the depletion field forms a transient current to emit THz pulses.

Table 1.3 Rules of Schottky/ohmic junction formation at metal/semiconductor interfaces. Φ_M: Work function of metal; Φ_S: Work function of semiconductor.

	n-type semiconductor	p-type semiconductor
$\Phi_M > \Phi_S$	Schottky	Ohmic
$\Phi_M < \Phi_S$	Ohmic	Schottky

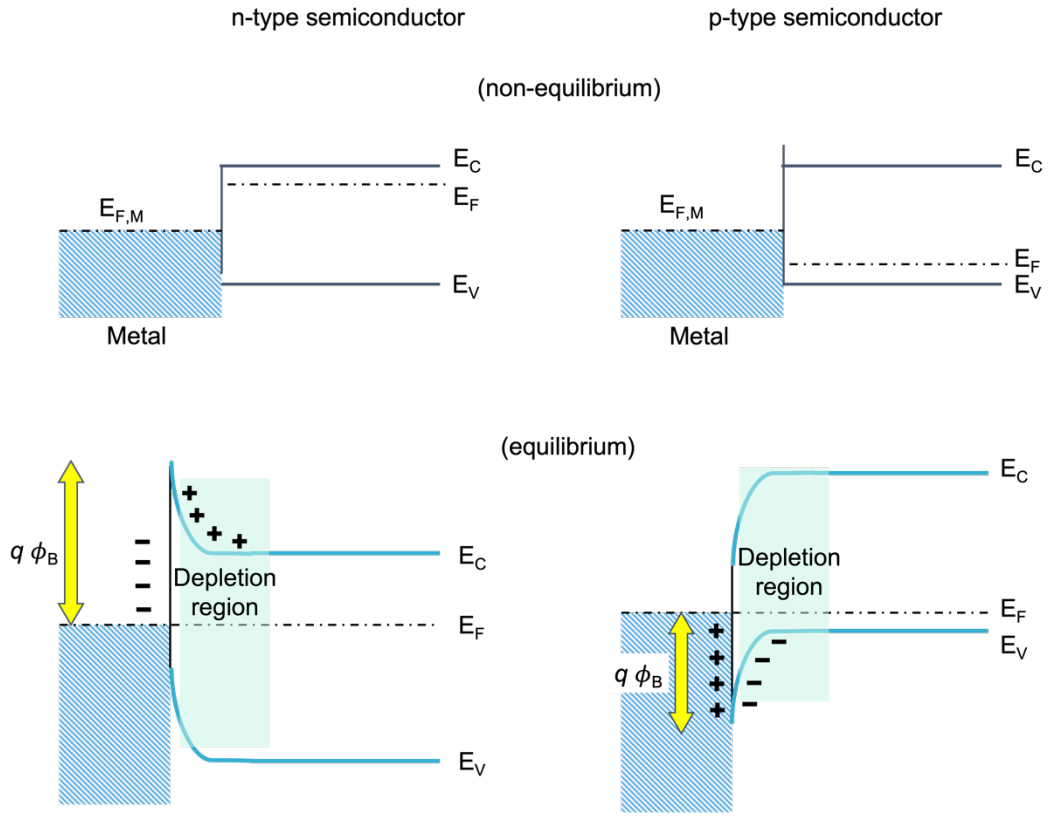


Figure 1.21 Band diagrams showing Schottky barrier forms when metal and n-/p-type semiconductor are brought in contact. (E_F: Fermi energy, E_C: Energy level at conduction band edge, E_V: Energy level at valence band edge.)

Jin *et al.* reported the THz pulse generation by exciting the Schottky interfaces formed by Cr and GaAs with femtosecond laser pulses.[144] THz wave emitted from the sample is relatively weak because the Cr on the surface has blocked the incident laser pulses, weakening the photoexcitation. Recently, THz wave emission from thin film Cu_2O/Au interface has been reported (**Figure 1.22**), which is more cost effective

compared with using Cr and GaAs.[145-148] The underlying Au film does not block the incident laser but works as a reflector of incident laser pulse to enhance the photo absorption for exciting carriers drift in the depletion field at Cu_2O/Au interface, and thus resulting in stronger THz wave emission.[148]

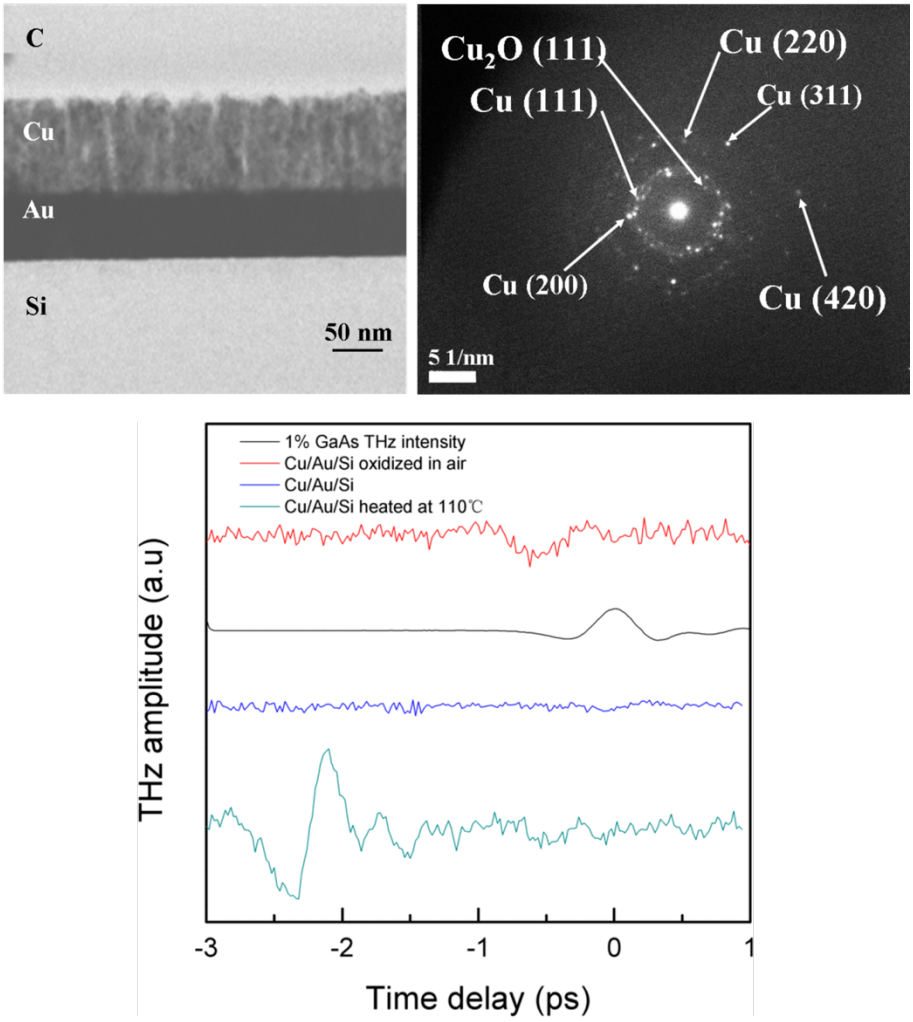


Figure 1.22 THz wave generated from Cu_xO/Au structure. (Top left) TEM micrograph of Cu/Au film on Si wafer. (Top right) SAED pattern of oxidized Cu film. (Bottom) THz-TDS showing Cu/Au/Si heated at 110 °C emits THz wave. Reproduced with permission from ref. [145] Copyright 2014 IEEE.

Photo-Dember effect. THz pulses via femtosecond laser excitation are also detected from the surfaces of semiconductors. The first one is known as photo-Dember effect, which happens to all semiconductors irrespective of the doping type.[149] Photo-Dember effect is based on the diffusive and drift motion of charge carriers due to the excitation by intense laser pulse.[150] Due to the difference in mass diffusivity of holes and electrons, the electrons move faster and diffuse away in longer distance than holes. In such a way, a transient polarization is built up as the THz wave source (**Figure 1.17**).

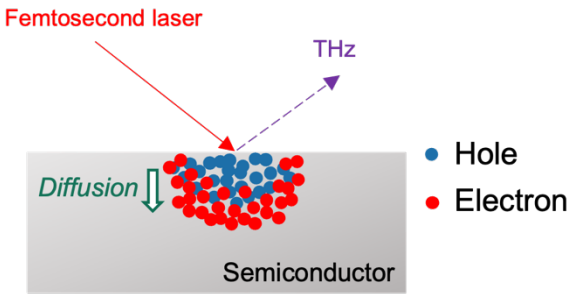


Figure 1.23 Transient polarization built from the diffusion of holes and electrons at different speeds in the region near to the surface of a semiconductor due to femtosecond laser irradiation.

Surface depletion field. Energy band bending also occurred for air-exposed surface of semiconductor. Similar to the Schottky barrier, the surface depletion field means depletion of free carriers near the surface of semiconductor. This phenomenon

particularly applicable to doped semiconductors or those contain impurities. When charge carriers are generated in the surface depletion field by ultrafast laser irradiation, the charges drift under the depletion field and result in a transient current. THz wave emission contributed by surface depletion field usually happens in semiconductors with small energy band gap since the laser light wavelength is usually at 800 nm (corresponding to a photon energy of 1.55 eV).

1.4.1.3 Water film

Although bulk liquid water is known as a strong THz wave absorber, recent research found the generation of broadband THz waves from liquid water film via femtosecond laser pulses excitation.[151] Water film with thickness less than 200 μm does not absorb THz as compared with bulk liquid water. Jin *et al.* did the experiments with different focal points of the laser and confirmed THz wave generation when laser focused near the water film.[151] Although they did not conclude the mechanism of such THz wave generation, their findings had turned the page in THz wave research on the universal solvent. Huang *et al.* set an experiment to show THz wave and X-ray emission happened simultaneously from a water film under femtosecond laser irradiation.[128] Although the highest intensity of X-ray can be generated when the laser tightly focuses

on the center of the water film, THz wave intensity in the transmission pathway was weakened (**Figure 1.24**). The author has assigned the THz wave generation from water is based on the laser-induced plasma at near surface of the water flow, but not at the center of the water film.[128] The author also reported using double-pulse excitation can enhance the THz wave emission.[152] The pre-pulse creates mist ejection from the water film, and the surface of water film becomes rougher, that creates interferometric effects spatially for THz wave emission by the main pulse.[152] The time delay between two pulses is also an important factor to achieve the highest THz wave emission from the water film and Huang *et al.* found that 4.7 ns of time delay is the optimal condition in their set up.[153]

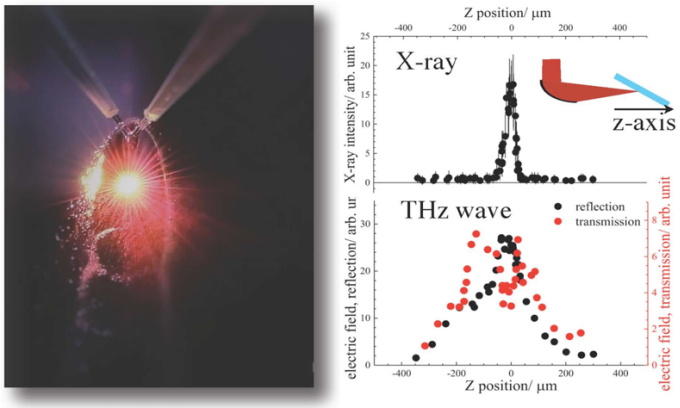


Figure 1.24 (Left) Femtosecond laser irradiates the water film created by collision of two water jets. (Right, top) X-ray emission intensity against laser focal point along the z-axis. (Right, bottom) THz emission intensity against laser focal point along the z-axis in reflection and transmission pathway, respectively. Reproduced with permission from ref. [128] Copyright 2018 MDPI.

Zhang *et al.* also attempted explaining the THz generation from water by irradiating near surface of a water line (thickness 200 μm) with femtosecond laser.[154] Similar to ref. [128], THz pulse generation has been observed if the focal point deviated from the center by 60 μm (both positive and negative directions). Experiments and computational simulations have been done to explain THz generation from the formation of nonzero net currents in the laser interactions with the water-column plasma.[154] Although the exact mechanism of THz emission from a water film is the fully elucidated yet, the above-mentioned research have confirmed that – (1) reducing thickness of water (from bulk to film) can prevent the water target absorbing THz wave; (2) THz emission is more significant when laser focuses at several micrometers from the central axis of the water film; (3) double-pulse excitation can enhance the THz emission from water film; (4) THz and hard X-ray emission can be achieved simultaneously.

Additionally, Huang *et al*. reported THz wave enhancement from ZnTe nano-colloidal aqueous dispersion compared with bare water film under femtosecond laser irradiation (**Figure 1.25**).[155] Their findings have risen an idea of making THz emitting materials (nonlinear crystals, semiconductors, etc.) in nanosized and merging them into aqueous-based suspension to provide stronger THz wave emission.

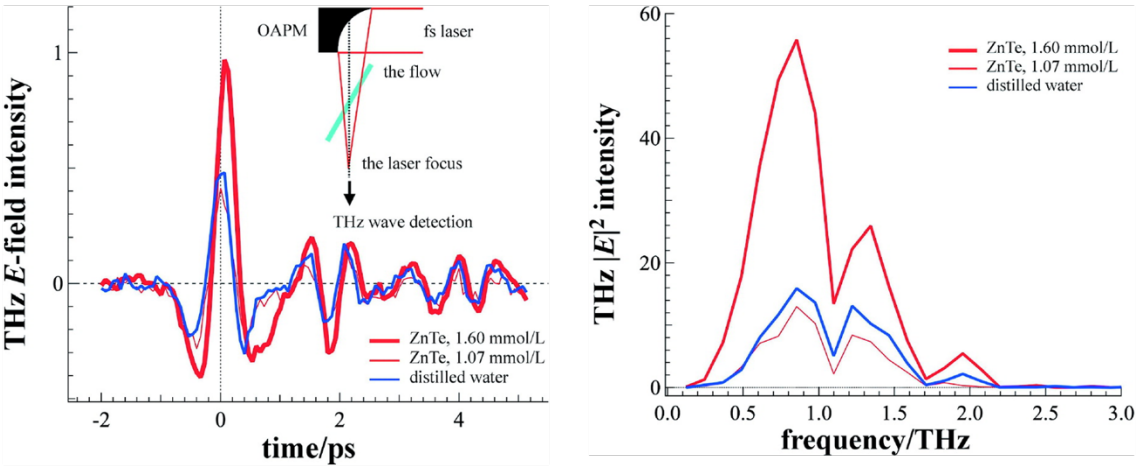


Figure 1.25 (Left) THz electric field emitted from aqueous film of ZnTe nanocolloids and bare water in ref. [155]. (Right) The corresponding powder spectra. The laser intensity is 0.75 mJ/pulse. Reproduced with permission from ref. [155] Copyright 2020 The Chemical Society of Japan.

1.4.2 Terahertz wave detection

Terahertz time-domain (THz-TDS) spectroscopy is used to detect broadband THz pulses. The THz pulse emitted from sample via femtosecond laser excitation is usually directed to an electro-optic sampling (EO) sampling crystal by parabolic mirrors. The THz pulse is directly detected as a function of time which gives the amplitude and phase of the THz pulse. The power spectrum of the THz pulse can be obtained through Fourier transforming the THz-TDS spectrum. EO sampling takes the advantages of Pockels effect in EO crystals. Pockels effect is a second-order nonlinear effect and only occurs in non-centrosymmetric crystals. The EO crystal is always being focused by a

probe beam and the THz pulse emitted from samples. Birefringence is induced when the THz pulse electric field interacts with the probe beam in EO crystal. Probe beam is elliptically polarized due to the THz pulse electric field and that is proportional to the THz electric field. The polarized probe beam is propagating to the differential detector diodes. Then, the nonzero differential signal as THz electric field is than digitalized and displayed on the THz-TDS software.

Figure 1.26 is a general set up of measuring THz pulse from sample (in reflection mode) by EO sampling. Since there is no absolute reference of time exists, the relative time delay between the pump and probe pulses is used as a temporal reference frame. The femtosecond laser beam is separated to two pathways by a splitter – probe beam and pump beam. Probe beam propagates through reflectors and mirrors and focused on the EO crystal. The relative time delay is adjusted by the translational stage that changes the path length of the pump line. With the excitation by the pump beam, the sample emits THz pulse, which is directed by set of parabolic mirrors and propagates toward to EO crystal. Finally, the electric field of THz pulse is recorded and displayed on THz-TDS.

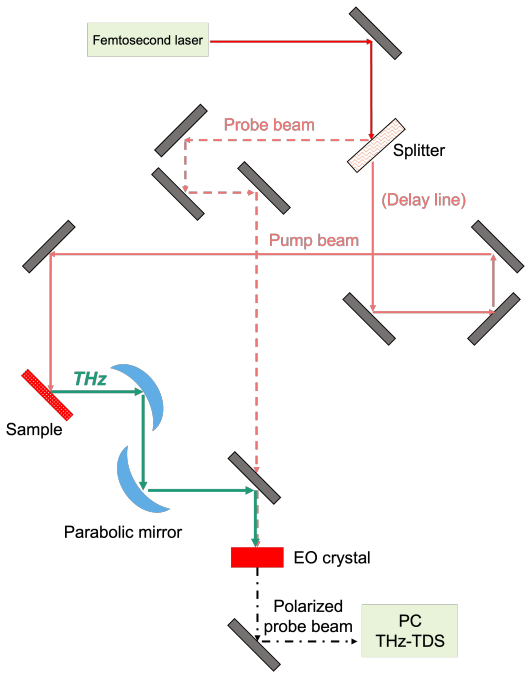


Figure 1.26 Schematic illustration of a THz detection system (reflection mode: incident angle of pump beam to sample = 45º)

Moreover, materials used for EO samplings are categorized by three types – (1) ionic crystals (e.g., $LiTaO_3$, $LiNbO_3$, $BaTiO_3$), (2) organic materials, (3) covalent crystals. However, ionic crystals show strong dispersion and absorption in THz regime, so the thickness of ionic crystals should be minimized as the THz sensor. Organic materials also have thermal stability problem. Therefore, covalent crystals are the best in all. The covalent crystals give higher frequency response than that in ionic crystals. Also, covalent zincblende materials have relatively low dielectric constant, moderate EO coefficients and zero intrinsic birefringence.[156] From that, <110>-directional ZnTe single crystal is a suitable candidate used for EO sampling.

1.5 Summary

Cu-based and ZnTe nano/micro materials are of interest because they have different characteristics with respect to oxidation states and/or sizes. Generally nano/micro materials are synthesized by top-down and bottom-up approaches. In the syntheses of NPs dispersion via sputter deposition, characterizations on products are still limited. On the other hand, bottom-up approaches such as wet-chemical method and thermal decomposition still remain unclear. For example, the formation scheme of microstructures synthesized using solvothermal method are not well elucidated, because the process is not observable during syntheses. Moreover, the interaction between ultrafast laser pulse and different nano/micro materials (nonlinear optics, semiconductors, water, etc.) have drawn attention since EM wave in X-ray and THz regime emission have been observed. Therefore, it is believed that the in-depth studies of synthesizing Cu-based and ZnTe nano/micro materials and their optical response to the ultrafast laser pulse are important to broaden the application of them.

1.6 Research Objectives

This dissertation focuses on synthesizing Cu-based and ZnTe nano/micro materials. With the concern of novel approach to synthesize nano/micro materials, monometallic Cu and bimetallic Cu-Pd alloy NPs are synthesized via sputter deposition in a polymer matrix. Characterizations on the NPs are carried out to evaluate their stability in the liquid polymer. Interaction between nano/micro materials and ultrafast laser pulse is also of interest. For this purpose, Au@Cu_2O core-shell structured NPs are synthesized and their stability in aqueous solvents are monitored as the potential candidate of THz wave emitter. Moreover, oxidized Cu thin film structures are fabricated for studying their THz wave emission mechanism from metal/semiconductor interfaces to avoid the influences due to the deterioration of Au@Cu_2O core-shell in aqueous solvent. On the other hand, ZnTe microspheres are synthesized using a hot injection method. Unlike the solvothermal method used in other studies, the method used in this dissertation allows us monitoring the formation mechanism of ZnTe microspheres. Lastly, a preliminary report on ZnTe microspheres as a THz wave emitter is given.

1.7 References

1. Agasti, S.S.; Rana, S.; Park, M.-H.; Kim, C.K.; You, C.-C.; Rotello, V.M. Nanoparticles for detection and diagnosis. *Adv. Drug Deliv. Rev.*, **2010**, *62*(3), 316-328.
2. Brigger, I.; Dubernet, C.; Couvreur, P. Nanoparticles in cancer therapy and diagnosis. *Adv. Drug Deliv. Rev.*, **2012**, *64*, 24-36.
3. Yezhelyev, M.V.; Gao, X.; Xing, Y.; Al-Hajj, A.; Nie, S.; O'Regan, R.M. Emerging use of nanoparticles in diagnosis and treatment of breast cancer. *Lancet Oncol.*, **2006**, *7*(8), 657-667.
4. Faraji, A.H.; Wipf, P. Nanoparticles in cellular drug delivery. *Bioorg. Med. Chem.*, **2009**, *17*(8), 2950-2962.
5. Couvreur, P. Nanoparticles in drug delivery: Past, present and future. *Adv. Drug Deliv. Rev.*, **2013**, *65*(1), 21-23.
6. Mitchell, M.J.; Billingsley, M.M.; Haley, R.M.; Wechsler, M.E.; Peppas, N.A.; Langer, R. Engineering precision nanoparticles for drug delivery. *Nat Rev Drug Discov.*, **2021**, *20*, 101-124/
7. Jeong, S.-H.; Choi, H.; Kim, J.Y.; Lee, T.-W. Silver-Based Nanoparticles for Surface Plasmon Resonance in Organic Optoelectronics. *Part Part Syst Charact.*, **2014**, *32*(2), 164-175.
8. Joyce, H.J.; Gao, Q.; Tan, H.H.; Jagadish, C.; Kim, Y.; Zou, J.; Smith, L.M.; Jackson, H.W.; Yarrison-Rice, J.M.; Parkinson, P.; Johnston, M.B. III-V semiconductor nanowires for optoelectronic device applications. Prog. Quantum. Electron., **2011**,
9. Wang, C.; Daimon, H.; Sun, S. Dumbbell-like Pt-Fe3O4 Nanoparticles and Their Enhanced Catalysis for Oxygen Reduction Reaction. *Nano Lett.*, **2009**, *9*(4), 1493-

1496.

10. Haruta, M.; Daté, M. Advances in the catalysis of Au nanoparticles. *Appl. Catal. A: Gen.*, **2001**, *222*(1-2), 427-437.
11. Gawande, M.B.; Goswami, A.; Asefa, T.; Guo, H.; Biradar, A.V.; Peng, D.-L.; Zboril, R.; Varma, R.S. Core-shell nanoparticles: synthesis and applications in catalysis and electrocatalysis. *Chem. Soc. Rev.*, **2015**, *44*, 7540-7590.
12. Garg, J.; Poudel, B.; Chiesa, M.; Gordon, JB.; Ma, J.J.; Wang, J.B.; Ren, Z.F.; Kang, Y.T.; Ohtani, H.; Nanda, J.; McKinley, G.H.; Chen G. Enhanced thermal conductivity and viscosity of copper nanoparticles in ethylene glycol nanofluid. *J. Appl. Phys.*, **2008**, *103*, 074301.
13. Park, B.K.; Kim, D.; Jeong, S.; Moon, J.; Kim, J.S. Direct writing of copper conductive patterns by ink-jet printing. *Thin Solid Films*, **2007**, *515*(19), 7706-7711.
14. Yong, Y.; Yonezawa, T.; Matsubara, M.; Tsukamoto, H. The mechanism of alkylamine-stabilized copper fine particles towards improving the electrical conductivity of copper films at low sintering temperature. *J. Mater. Chem. C*, **2015**, *3*(23), 5890–5895.
15. Qin, G.; Watanaka, A.; Tsukamoto, H.; Yonezawa, T. Copper film prepared from copper fine particle paste by laser sintering at room temperature: Influences of sintering atmosphere on the morphology and resistivity. *Jpn. J Appl. Phys.*, **2014**, *53*(9), 096501.
16. Yonezawa, T.; Tsukamoto, H.; Matsubara, M. Low-temperature nanoredox two-step sintering of gelatin nanoskin-stabilized submicrometer-sized copper fine particles for preparing highly conductive layers. *RSC Adv.*, **2015**, *5*(75), 61290–61297.
17. Yonezawa, T.; Tsukamoto, H.; Yong, Y.; Nguyen, M.T.; Matsubara, M. Low

temperature sintering process of copper fine particles under nitrogen gas flow with Cu^{2+}-alkanolamine metallacycle compounds for electrically conductive layer formation. *RSC Adv.*, **2016**, *6*(15), 12048–12052.

18. Huang, K.-M.; Tsukamoto, H.; Yong, Y.; Chiu, H.-L.; Nguyen, M.T.; Yonezawa, T.; Liao, Y.-C. Stabilization of the thermal decomposition process of self-reducible copper ion ink for direct printed conductive patterns. *RSC Adv.*, **2017**, *7*(40), 25095–25110.
19. Wang, C.; Wang, C.; Xu, L.; Cheng, H.; Lin, Q.; Zhang, C. Protein-directed synthesis of pH-responsive red fluorescent copper nanoclusters and their applications in cellular imaging and catalysis. *Nanoscale*, **2014**, *6*, 1775-1781.
20. Venkatakrishnan, S.; Veerappan, G.; Elamparuthi, E.; Veerappan, A. Aerobic synthesis of biocompatible copper nanoparticles: promising antibacterial agent and catalyst for nitroaromatic reduction and C–N cross coupling reaction. *RSC Adv.*, **2014**, *4*, 15003-15006.
21. Won, Y.; Kim, A.; Lee, D.; Yang, W.; Woo, K.; Jeong, S.; Moon, J. Annealing-free fabrication of highly oxidation-resistive copper nanowire composite conductors for photovoltaics. *NPG Asia Mater.* **2014**, *6*, e105.
22. Yoon, H.; Shin, D. S.; Babu, B.; Kim, T. G.; Song, K. M.; Park, J. Control of copper nanowire network properties and application to transparent conducting layer in LED. *Mater. Des.*, **2017**, *132*, 66-71.
23. Xiang, H.; Guo, T.; Xu, M.; Lu, H.; Liu, S.; Yu, G. Ultrathin Copper Nanowire Synthesis with Tunable Morphology Using Organic Amines for Transparent Conductors. *ACS Appl. Nano Mater.*, **2018**, *1*, 3754-3759.
24. Guo, H.; Lin, N.; Chen, Y.; Wang, Z.; Xie, Q.; Zheng, T.; Gao, N.; Li, S.; Kang,

J.; Cai, D.; Peng, D.-L. Copper Nanowires as Fully Transparent Conductive Electrodes. *Sci. Rep.*, **2013**, *3*, 2323.

25. Kang, C.; Yang, S.; Tan, M.; Wei, C.; Liu, Q.; Fang, J.; Liu, G. Purification of Copper Nanowires To Prepare Flexible Transparent Conductive Films with High Performance. *ACS Appl. Nano Mater.*, **2018**, *1*, 3155-3163.
26. Kumar, D. V. R.; Woo, K.; Moon, J. Promising wet chemical strategies to synthesize Cu nanowires for emerging electronic applications. *Nanoscale*, **2015**, *7*, 17195-17210.
27. Xu, C.; Wang, L.; Wang, R.; Wang, K.; Zhang, Y.; Tian, F.; Ding, Y. Nanotubular Mesoporous Bimetallic Nanostructures with Enhanced Electrocatalytic Performance. *Adv. Mater.*, **2009**,*21*(21), 2165-2169.
28. Gong, M.; Fu, G.; Chen, Y.; Tang, Y.; Lu, T. Autocatalysis and Selective Oxidative Etching Induced Synthesis of Platinum–Copper Bimetallic Alloy Nanodendrites Electrocatalysts. *ACS Appl. Mater. Interfaces*, **2014**, *6*(10), 7301-7308.
29. Jia, F.; Yu, X.; Zhang, L. Enhanced selectivity for the electrochemical reduction of CO_2 to alcohols in aqueous solution with nanostructured Cu–Au alloy as catalyst. *J. Power Sources*, **2014**, *252*, 85-89.
30. Guan, A.; Wang, Q.; Ji, Y.; Li, S.; Yang, C.; Qian, L.; Zhang, L.; Wu, L.; Zheng, G. Steric effect induces CO electroreduction to CH_4 on Cu–Au alloys. *J. Mater. Chem. A.*, **2021**, *9*, 21779-21784.
31. Chiba, M.; Nguyen M.T.; Hasegawa, Y.; Obora, Y.; Kwasaki, H.; Yonezawa, T. Synthesis of binary solid solution Cu–Pd nanoparticles by DMF reduction for enhanced photoluminescence properties. *J. Mater. Chem. C.*, **2015**, *3*, 514-520.
32. Chowdhury, S.; Bhethanabotla, V.R.; Sen, R. Effect of Ag−Cu Alloy Nanoparticle

Composition on Luminescence Enhancement/Quenching. *J. Phys. Chem. C.*, **2009**, *113*(30), 13016-13022.

33. Valodkar, M.; Modi, S.; Pal, A.; Thakore, S. Synthesis and anti-bacterial activity of Cu, Ag and Cu–Ag alloy nanoparticles: A green approach. *Mater. Res. Bull.*, **2011**, *46*(3), 384-389.
34. De Los Santos Valladares, L.; Hurtado Salinas, D.; Bustamante Dominguez, A.; Najarro Acosta, D.; Khondaker, S.I.; Mitrelias, T.; Barnes, C.H.W.; Albino Aguiar, J.; Majima, Y. Crystallization and electrical resistivity of Cu2O and CuO obtained by thermal oxidation of Cu thin films on SiO2/Si substrates. *Thin Solid Films*, **2012**, *520*(20), 6368-6374.
35. Njeh, A.; Wieder, T.; Fuess, H. Reflectometry studies of the oxidation kinetics of thin copper films. *Surf. Interface Anal.*, **2022**, *33*, 626-628.
36. Yang, H.; Ouyang, J.; Tang, A.; Xiao, Y.; Li, X.; Dong, X.; Yu, Y. Electrochemical synthesis and photocatalytic property of cuprous oxide nanoparticles. *Mater. Res. Bull.*, **2006**, *41*(7), 1310-1318.
37. Harish, S.; Archana, J.; Sabarinathan, M.; Navaneethan, M.; Nisha, K.D.; Ponnusamy, S.; Muthamizhchelvan, C.; Ikeda, H.; Aswal, D.K.; Hayakawa, Y. Controlled structural and compositional characteristic of visible light active ZnO/CuO photocatalyst for the degradation of organic pollutant. *Appl. Surf. Sci.*, **2017**, *418*, 103-112.
38. Li, Y.; Liang, J.; Tao, Z.; Chen, J. CuO particles and plates: Synthesis and gas-sensor application. *Mater. Res. Bull.*, **2008**, *43*(8-9), 2380-2385.
39. Nguyen, D.H.; Nguyen, V.Q.; Jung, H.; Kim, D.; Kim, H.; Hong, S.-K. Synthesis of porous CuO nanowires and its application to hydrogen detection. *Sens. Actuators B*

Chem., **2010**, *146*(1), 266-272.

40. Huber, R.; Schmid, B.A.; Shen, R.; Chemla, D.S.; Kaindl, R.A. Stimulated Terahertz Emission from Intraexcitonic Transitions in Cu_2O. *PRL*, **2006**, *96*, 017402.
41. Lv, Y.; Duan, S.; Wang, R. Structure design, controllable synthesis, and application of metal-semiconductor heterostructure nanoparticles. *Prog. Nat. Sci.*, **2020**, *30*(1), 1-12.
42. Li, J.; Cushing, S.K.; Bright, J.; Meng, F.; Senty, T.R.; Zheng, P.; Bristow, A.D.; Wu, N. Ag@Cu_2O Core-Shell Nanoparticles as Visible-Light Plasmonic Photocatalysts. *ACS Catal.*, **2013**, *3*(1), 47-51.
43. Cushing, S.K.; Li, J.; Meng, F.; Senty, T.R.; Suri, S.; Zhi, M.; Li, M.; Bristow, A.D.; Wu, N. Photocatalytic Activity Enhanced by Plasmonic Resonant Energy Transfer from Metal to Semiconductor. *J. Am. Chem. Soc.*, **2012**, *134*(36), 15033-15041.
44. Furube, A.; Du, L.; Hara, K.; Katoh, R.; Tachiya, M. Ultrafast Plasmon-Induced Electron Transfer from Gold Nanodots into TiO2 Nanoparticles. *J. Am. Chem. Soc.*, **2007**, *129*(48), 14852-14853.
45. Bai, S.; Ge, J.; Wang, L.; Gong, M.; Deng, M.; Kong, Q.; Song, L.; Jiang, J.; Zhang, Q.; Luo, Y.; Xie, Y.; Xiong, Y. A Unique Semiconductor–Metal–Graphene Stack Design to Harness Charge Flow for Photocatalysis. *Adv. Mater.*, **2014**, *26*(32), 5689-5695.
46. Ma, B.; Bi, J.; Lv, J.; Kong, C.; Yan, P.; Zhao, X.; Zhang, X.; Yang, T.; Yang, Z. Inter-embedded Au-Cu_2O heterostructure for the enhanced hydrogen production from water splitting under the visible light. *Chem. Eng. J.*, **2021**, *405*, 126709.
47. Sze, S.M.; Ng, K.K. Physics of Semiconductor Devices. **2006** Wiley, New York, USA.
48. Kafi, F.S.B.; Jayathilaka, K.M.D.C.; Wijesundera, R.P.; Siripala, W. Effect of pre-

surface treatments on p-Cu_2O/Au Schottky junctions. *J. Natn. Sci. Foundation Sri Lanka*, **2021**, *49*(1), 61-66.

49. Jiang, D.; Zhou, W.; Zhong, X.; Zhang, Y.; Li, X. Distinguishing Localized Surface Plasmon Resonance and Schottky Junction of Au–Cu_2O Composites by Their Molecular Spacer Dependence. *ACS Appl. Mater. Interfaces*, **2014**, *6*(14), 10958-10962.
50. Zhang, W.; Wang, B.; Hao, C.; Liang, Y.; Shi, H.; Ao, L.; Wang, W. Au/Cu_2O Schottky contact heterostructures with enhanced photocatalytic activity in dye decomposition and photoelectrochemical water splitting under visible light irradiation. J. Alloys Compd., **2016**, *684*, 445-452.
51. Lu, X.; Yonezawa, T. Terahertz emission from Cu_xO/Au thin film. 2014 *MWP/APMP* **2014**, 164-165.
52. Lu, X.; Ishida, Y.; Mishina, T.; Nguyen, M. T.; Yonezawa, T. Enhanced Terahertz Emission from Cu_xO/Metal Thin Film Deposited on Columnar-Structured Porous Silicon. *Bull. Chem. Soc. Jpn.* **2015**, *88*, 10, 1385-1387.
53. Ramanandan, G. K. P.; Adam, A. J. L.; Ramakrishnan, G.; Petrik, P.; Hendrikx, R.; Planken, P. C. M. Optical characterization of gold-cuprous oxide interfaces for terahertz emission applications. *Appl. Opt.* **2014**, *53*, 10, 1994-2000.
54. Ramakrishnan, G.; Ramanandan, G. K. P.; Adam, A. J. L.; Xu, M.; Kumar, N.; Hendrikx, R. W. A.; Planken, P. C. M. Enhanced terahertz emission by coherent optical absorption in ultrathin semiconductor films on metals. *Opt. Express* **2013**, *21*, 14, 16784-16798.
55. Lu, X.; Qin, M.; Wang, Y.; Zhou, J.; Zhu, Q.; Peng, P.; Zhang, Y.; Wu, H. Strong terahertz emission from copper oxides/silver micro thin film deposited on

nanoparticles aggregation substrate. *Appl. Surf. Sci.*, **2020**, *508*, 145219.

56. Ruda, H.E. Compensation and transport characteristics of n-ZnTe. *J. Phys. D: Appl. Phys.*, **1991**, *24*, 1158.
57. Chang, J.H.; Takai, T.; Godo, K.; Song, J.S.; Koo, B.H.; Hanada, T.; Yao, T. ZnTe-Based Light-Emitting-Diodes Grown on ZnTe Substrates by Molecular Beam Epitaxy. *Phys. Stat. Sol. (B)*, **2002**, *229*(2), 995-999.
58. Lakhal, L.; Mezrag, F.; Bouarissa, N. Quantum Confinement Effects on Physical Properties of ZnTe Spherical Quantum Dots. *Acta Phys. Pol.*, **2020**, *137*, 451-453.
59. Bang, J.; Park, J.; Lee, J.H.; Won, N.; Nam, J.; Lim, J.; Chang, B.Y.; Lee, H.J.; Chon, B.; Shin, J.; Park, J.B.; Choi, J.H.; Cho, K.; Park, S.M.; Joo, T.; Kim, S. ZnTe/ZnSe (Core/Shell) Type-II Quantum Dots: Their Optical and Photovoltaic Properties. *Chem. Mater.*, **2010**, *22*(1), 233-240.
60. Xing, X.; Wang, D.; Chen, Z.; Zheng, B.; Li, B.; Wu, D. ZnTe quantum dots as fluorescence sensors for the detection of iron ions. *J. Mater. Sci.: Mater. Electron*, **2018**, *29*, 14192-14199.
61. Seo, J.-U.; Park, C.-M. ZnTe and ZnTe/C nanocomposite: a new electrode material for high-performance rechargeable Li-ion batteries. *J. Mater. Chem. A*, **2014**, *2*, 20075-20082.
62. Ni, W.; Li, X.; Shi, L.-Y.; Ma, J. Research progress on ZnSe and ZnTe anodes for rechargeable batteries. *Nanoscale*, **2022**, *14*, 9609-9635.
63. Wang, W.; Lin, A.S.; Phillips, J.D. Intermediate-band photovoltaic solar cell based on ZnTe:O. *Appl. Phys. Lett.*, **2009**, *95*(1), 011103.
64. Han, P.Y.; Zhang, X.-C. Coherent, broadband midinfrared terahertz beam sensors. *Appl. Phys. Lett.*, **1998**, *73*, 3049.

65. Kaniyankandy, S.; Rawalekar, S.; Verma, S.; Ghosh, H.N. *J Phys Chem C*, **2010**, *115*, 1428-1435.

66. Ehsan, M.F.; Ashiq, M.N.; He, T. Hollow and mesoporous ZnTe microspheres: synthesis and visible-light photocatalytic reduction of carbon dioxide into methane. *RSC Advances*, **2015**, *5*(8), 6186-6194.

67. Ehsan, M.F.; He, T. In situ synthesis of ZnO/ZnTe common cation heterostructure and its visible-light photocatalytic reduction of CO_2 into CH_4. *Appl. Catal. B*, **2015**, *166-167*, 345-352.

68. Ehsan, M.F.; Khan, R.; He, T. Visible-Light Photoreduction of CO2 to CH4 over ZnTe-Modified TiO_2 Coral-Like Nanostructures. *ChemPhysChem*, **2017**, *18*(22), 3203-3210.

69. Ehsan, M.F.; Ashiq, M.N.; Bi, F.; Bi, Y.; Palanisamy, S.; He, T. Preparation and characterization of $SrTiO_3$–ZnTe nanocomposites for the visible-light photoconversion of carbon dioxide to methane. *RSC Advances*, **2014**, *4*(89), 48411-48418.

70. Wang, Y.; He, T. ZnTe-based nanocatalysts for CO_2 reduction. *Curr. Opin. Green Sustain. Chem.*, **2019**, *16*, 7-12.

71. Habisreutinger, S.N.; Schmidt-Mende, L.; Stolarczyk, J.K. Photocatalytic reduction of CO_2 on TiO_2 and other semiconductors. *Angew Chem, Int. Ed. Engl.*, **2013**, *52*, 7372-7408.

72. Bönnemann, H.; Richards, R.M. Nanoscopic Metal Particles – Synthetic Methods and Potential Applications. Eur. J. Inorg. Chem., **2001**, *10*, 2455-2480.

73. Faraday, M. X. The Bakerian Lecture. – Experimental relations of gold (and other metals) to light. *Philos. Trans. R. Soc. London*, **1857**, *147*, 145-153.

74. Turkevich, J.; Stevenson, P.C.; Hillier, J. A study of the nucleation and growth processes in the synthesis of colloidal gold. *Disc. Faraday Soc.*, **1951**, *11*, 55-75.

75. Mott, D.; Galkowski, J.; Wang, L.Y.; Luo, J.; Zhong, C.J. Synthesis of size-controlled and shaped copper nanoparticles. *Langmuir*, **2007**, *23*, 5740-5745.

76. Zhang, J.; Sun, K.; Kumbhar, A.; Fang, J. Shape-Control of ZnTe Nanocrystal Growth in Organic Solution. *J. Phys. Chem. C*, **2008**, *112*(14), 5454-5458.

77. Penn, R.L.; Banfield, J.F. Oriented attachment and growth, twinning, polytypism, and formation of metastable phases: Insights from nanocrystalline TiO_2. *Am. Mineral.*, **1998**, *83*, 1077-1082.

78. Penn, R.L.; Banfield, J.F. Morphology development and crystal growth in nanocrystalline aggregates under hydrothermal conditions: Insights from titania. *Geochim. Cosmochim. Acta*, **1999**, *63*, 1549-1557.

79. Penn, R.L.; Banfield, J.F. Imperfect oriented attachment: Dislocation generation in defect-free nanocrystals. *Science*, **1998**, *281*, 969-971.

80. Dalmaschio, C.J.; Ribeiro, C.; Leite, E.R. Impact of the colloidal state on the oriented attachment growth mechanism. *Nanoscale*, **2010**, *2*, 2336-2345.

81. Cölfen, H.; Antonietti, M. Mesocrystals: Inorganic superstructures made by highly parallel crystallization and controlled alignment. *Angew. Chem., Int. Ed.*, **2005**, *44*, 5576-5591.

82. Zou, G.; Liu, Z.; Wang, D.; Jiang, C.; Qian, Y. Selected-Control Solvothermal Synthesis of Nanoscale Hollow Spheres and Single-Crystal Tubes of PbTe. *EurJIC*, **2004**, *22*, 4521-4524.

83. Zhang, H.; Wu, J.; Zhai, C.; Du, N.; Ma, X.; Yang, D. From ZnO nanorods to 3D hollow microhemispheres: solvothermal synthesis, photoluminescence and gas

sensor properties. *Nanotechnology*, **2007**, *18*, 455604.

84. Zhu, L.-P.; Xiao, H.-M.; Zhang, W.-D.; Yang, G.; Fu, S.-Y. One-Pot Template-Free Synthesis of Monodisperse and Single-Crystal Magnetite Hollow Spheres by a Simple Solvothermal Route. *Cryst. Growth Des.*, **2008**, *8*(3), 957-963.
85. Zhang, Y.C.; Wang, G.L. Solvothermal synthesis of CdO hollow nanostructures from CdO_2 nanoparticles. *Mater. Lett.*, **2008**, *62*(4-5), 673-675.
86. Park, J.; Shen, X.; Wang, G. Solvothermal synthesis and gas-sensing performance of Co_3O_4 hollow nanospheres. *Sen. Actuators B Chem.*, **2009**, *136*(2), 494-498.
87. Li, S.; Xu, Y.; Zhang, L.; Zhong, B.; Yan, J. Controllable preparation and rapid photoelectric response of homogeneous ZnTe microspheres. *New J. Chem.*, **2022**, *46*, 3777-3785.
88. Ye, G.; Zhang, Q.; Feng, C.; Ge, H.; Jiao, Z. Structural and electrical properties of a metallic rough-thin-film system deposited on liquid substrates. *Phys. Rev. B*, **1996**, *54*, 14754.
89. Torimoto, T.; Okazaki, K.; Kiyama, T. Sputter deposition onto ionic liquids: Simple and clean synthesis of highly dispersed ultrafine metal nanoparticles. *Appl. Phys. Lett.*, **2006**, *89*, 243117.
90. Shishino, Y.; Yonezawa, T.; Udagawa, S.; Hase, K.; Nishihara, H. Preparation of Optical Resins Containing Dispersed Gold Nanoparticles by the Matrix Sputtering Method. *Angew. Chem. Int. Ed.*, **2011**, *50*(3), 703-705.
91. Nguyen, M.T.; Deng, L.; Yonezawa, T. Control of nanoparticles synthesized via vacuum sputter deposition onto liquids: a review. *Soft Matter*, **2022**, *18*, 19-47.
92. Ishida, Y.; Udagawa, S.; Yonezawa, T. Grwoth of sputtered silver nanoparticles on a liquid mercaptan matrix with controlled viscosity and sputter rate. *Colloids Surf. A*

Physicochem., **2016**, *498*, 106-111.

93. Sumi, T.; Motono, S.; Ishida, Y.; Shirahata, N.; Yonezawa, T. Formation and Optical Properties of Fluorescent Gold Nanoparticles Obtained by Matrix Sputtering Method with Volatile Mercaptan Molecules in the Vacuum Chamber and Consideration of Their Structures. *Langmuir*, **2015**, *31*(14), 4323-4329.
94. Deng, L.; Nguyen, M.T.; Yonezawa, T. Sub-2 nm Single-Crystal Pt Nanoparticles via Sputtering onto a Liquid Polymer. *Langmuir*, *34*(8), 2876-2881.
95. Corpuz, R.D.; Ishida, Y.; Nguyen, M.T.; Yonezawa, T. Synthesis of positively charged photoluminescent bimetallic Au–Ag nanoclusters by double-target sputtering method on a biocompatible polymer matrix. *Langmuir*, **2017**, *33*(36), 9144-9150.
96. König, D.; Richter, K.; Siegel, A.; Mudring, A.-V.; Ludwig, A. High-Throughput Fabrication of Au-Cu Nanoparticle Libraries by Combinatorial Sputtering in Ionic Liquids. *Adv. Funct. Mater.*, **2013**, *24(14)*, 2049-2056.
97. Schmitz, A.; Meyer, H.; Meischein, M.; Manjón, A.G.; Schmolke, K.; Giesen, B.; Schlüsener, C.; Simon, P.; Grin, Y.; Fischer, R.A.; Scheu, C.; Ludwig, A.; Janiak, C. Synthesis of plasmonic Fe/Al nanoparticles in ionic liquids. *RSC Adv.*, **2022**, *10*, 12891-12899.
98. Meischein, M.; Manjón, A.G.; Hammerschmidt, T.; Xiao, B.; Zhang, S.; Abdellaoui, L.; Scheu, C.; Ludwig, A. Elemental (im-)miscibility determines phase formation of multinary nanoparticles co-sputtered in ionic liquids. *Nanoscale Adv.*, **2022**, *4*, 3855-3869.
99. Nguyen, M.T.; Zhang, H.; Deng, L.; Tokunaga, T.; Yonezawa, T. Au/Cu bimetallic nanoparticles via double-target sputtering onto a liquid polymer. *Langmuir*, **2017**,

33(43), 12389-12397.

100. Deng, L.; Nguyen, M.T.; Mei, S.; Tokunaga, T.; Kudo, M.; Matsumura, S.; Yonezawa, T. Preparation and growth mechanism of Pt/Cu alloy nanoparticles by sputter deposition onto a liquid polymer. *Langmuir*, **2019**, *35*(25), 8418-8427.

101. Zhu, M.; Nguyen, M.T.; Chau, Y.R.; Deng, L.; Yonezawa, T. Pt/Ag Solid Solution Alloy Nanoparticles in Miscibility Gaps Synthesized by Cosputtering onto Liquid Polymers. *Langmuir*, **2021**, *37*(19), 6096-6105.

102. Deng, L.; Nguyen, M.T.; Shi, J.; Chau, Y.R.; Tokunaga, T.; Kudo, M.; Matsumura, S.; Hashimoto, N.; Yonezawa, T. Highly correlated size and composition of Pt/Au alloy nanoparticles via magnetron sputtering onto liquid. *Langmuir*, **2022**, *36*(12), 3004-3015.

103. Garzón-Manjón, A.; Meyer, H.; Grochla, D.; Löffler, T.; Schuhmann, W.; Ludwig, A.; Scheu, C. Controlling the Amorphous and Crystalline State of Multinary Alloy Nanoparticles in An Ionic Liquid. *Nanomaterials*, **2018**, *8*(11), 903.

104. Zhu, M.; Nguyen, M.T.; Sim, W.J.; Yonezawa, T. Co-sputtered CuPt/Ag alloy nanoparticles and comparative catalytic performance of mono-, bi-, and tri-metallic nanoparticles in the oxygen reduction reaction. *Mater. Adv.*, **2022** (in press).

105. Xu, J.; Zhao, T.; Liang, Z.; Zhu, L. Facile Preparation of AuPt Alloy Nanoparticles from Organometallic Complex Precursor. *Chem. Mater.*, **2008**, *20*(5), 1688-1690.

106. Toshima, N.; Yonezawa, T.; Kushihashi, K. Polymer-protected palladium–platinum bimetallic clusters: preparation, catalytic properties and structural considerations. *J. Chem. Soc., Faraday Trans.*, **1993**, *89*, 2537-2543.

107. Toshima, N.; Harada, M.; Yonezawa, T.; Kushihashi, K.; Asakura, K. Structural Analysis of Polymer-Protected Pd/Pt Bimetallic Clusters as Dispersed Catalysts by

Using Extended X-ray Absorption Fine Structure Spectroscopy. *J. Phys. Chem.*, **1991**, *95*, 7448-7453.

108. Yonezawa, T.; Toshima, N. Polymer- and micelle-protected gold/platinum bimetallic systems. Preparation, application to catalysis for visible-light-induced hydrogen evolution, and analysis of formation process with optical methods. *J. Mol. Catal.*, **1993**, *83*(1-2), 167-181.

109. Ferrando, R.; Jellinek, J.; Johnston, R.L. Nanoalloy: from theory to applications of alloy clusters and nanoparticles. *Chem Rev.*, **2008**, *108*(3), 845-910.

110. Han, Y.; Guo, Y.; Gao, B.; Ma, C.; Zhang, R.; Zhang. H. Generation, optimization, and application of ultrashort femtosecond pulse in mode-locked fiber lasers. *Prog. Quantum Electron*, **2020**, *71*, 100264.

111. Kartner, F.X.; Aus der Au, J.; Keller, U. Mode-Locking with Slow and Fast Saturable Absorbers-What's the Different. *IEEE J. Sel. Top. Quantum Electron*, **1998**, *4*(2), 159-168.

112. Keller, U. Recent developments in compact ultrafast lasers. *Nature*, **2003**, *424*(6950), 831-838.

113. Strickland, D.; Mourou, G. Compression of amplified chirped optical pulses. *Opt. Commun.*, **1985**, *56*(3), 219-221.

114. Lee, Y.-S. Generation and Detection of Broadband Terahertz Pulses. In: Principles of Terahertz Science and Technology. **2009** Springer. Boston, MA.

115. Jiang, Y.; Lee, T.; Li, W.; Ketwaroo, G.; Rose-Petruck, C.G. High-average-power 2-kHz laser for generation of ultrashort x-ray pulses. *Opt. Lett.*, **2002**, *27*(11), 963-965.

116. Hagedorn, M.; Kutzner, J.; Tsilimis, G.; Zacharias, H. High-repetition-rate hard X-ray generation with sub-millijoule femtosecond laser pulses. *Appl. Phys. B.*, **2003**, *77*,

49-57.

117.Hada, M.; Matsuo, J. Effects of ambient pressure on Cu Kα X-ray radiation with millijoule and high-repetition-rate femtosecond laser. *Appl. Phys. B*, **2010**, *99*, 173-179.

118.Hatanaka, K.; Yomogihata, K.; Ono, H.; Fukumura, H. Femtosecond laser induced X-ray emission from metal alloys, polymers, and color filters. *Appl. Surf. Sci.*, **2005**, *247*(1-4), 232-237.

119.Tompkins, R.K.; Mercer, I.P.; Fettweis, M.; Barnett, C.J.; Klug, D.R.; Porter, L.G.; Clark, I.; Jackson, S.; Matousek, O.; Parker, A.W.; Towrie, M. 5-20 keV laser-induced x-ray generation at 1 kHz from a liquid-jet target. *Rev. Sci. Instrum.*, **1998**, *69*(9), 3113.

120.Korn, G.; Thoss, A.; Stiel, H.; Vogt, U.; Richardson, M.; Elsaesser, T.; Faubel, M. Ultrashort 1-kHz laser plasma hard x-ray source. *Opt. Lett.*, **2002**, *27*(10), 866-868.

121.Hatanaka, K.; Miura, T.; Fukumura, H. Ultrafast x-ray pulse generation by focusing femtosecond infrared laser pulses onto aqueous solutions of alkali metal chloride. *Appl. Phys. Lett.*, **2002**, *80*(21), 3925.

122.Hatanaka, K.; Miura, T.; Fukumura, H. White X-ray pulse emission of alkali halide aqueous solutions irradiated by focused femtosecond laser pulses: a spectroscopic study on electron temperatures as functions of laser intensity, solute concentration, and solute atomic number. *Chem. Phys.*, **2003**, *299*, 265-270.

123.Hatanaka, K.; Ono, H.; Fukumura, H. X-ray pulse emission from cesium chloride aqueous solutions when irradiated by double-pulsed femtosecond laser pulses. *Appl. Phys. Lett.*, **2008**, *93*, 064103.

124.Hanataka, K.; Ida, T.; Ono, H.; Matsushima, S.; Fukumura, H.; Juodkazis, S.; Misawa,

H. Chirp effect in hard X-ray generation from liquid target when irradiated by femtosecond pulses. *Opt. Express*, **2008**, *16*(17), 12650-12657.

125. Hatanaka, K.; Fukumura, H. X-ray emission from CsCl aqueous solutions when irradiated by intense femtosecond laser pulses and its application to time-resolved XAFS measurement of I^- in aqueous solution. *X-Ray Spectrom.*, **2012**, *41*, 195-200.

126. Masim, F.C.P.; Porta, M.; Hsu, W.-H.; Nguyen, M.T.; Yonezawa, T.; Balčuytis, A.; Juodkazis, S.; Hatanaka, K. Au Nanoplasma as Efficient Hard X-ray Emission Source. *ACS Photonics*, **2016**, *3*, 2184-2190.

127. Hsu, W.-H.; Masim, F.C.P.; Balčytis, A.; Huang, H.; Yonezawa, T.; Kuchmizhak, A.A.; Juodkazis, S.; Hatanaka, K. Enhancement of X-ray emission from nanocolloidal gold suspensions under double-pulse excitation. *Beilstein J. Nanotechnol.*, **2018**, *9*, 2609-2617.

128. Huang, H.; Nagashima, T.; Hsu, W.; Juodkazis, S.; Hatanaka, K. Dual THz Wave and X-ray Generation from a Water Film under Femtosecond Laser Excitation. *Nanomaterials*, **2018**, *8*(7), 523.

129. Huang, H.; Juodkazis, S.; Hatanaka, K. Correlated emission of X-ray and sound from water film irradiated by femtosecond laser pulses. *Appl. Surf. Sci.*, **2019**, *480*, 665-670.

130. Yoshida, H.; Ogawa, Y.; Kawai, Y. Terahertz sensing method for protein detection using a thin metallic mesh. *Appl. Phys. Lett.*, **2007**, *91*(25), 253901.

131. Markelz, A.; Roitberg, A.; Heilweil, E. Pulsed terahertz spectroscopy of DNA, bovine serum albumin and collagen between 0.1 and 2.0 THz. *Chem. Phys. Lett.*, **2000**, *320*, 42-48.

132. Fischer, B.M.; Walther, M.; Uhd Jepsen, P. Far-infrared vibrational modes of DNA components studied by terahertz time-domain spectroscopy. *Phys. Med. Biol.*, **2002**, *47*, 3807-3814.

133. Bessou, M.; Duday, H.; Caumes, J.-P.; Salort, S.; Chassagne, B.; Dautant, A.; Ziéglé, A.; Abraham, E. Advantage of terahertz radiation versus X-ray to detect hidden organic materials in sealed vessels. *Opt. Commun.*, **2012**, *285*(21-22), 4175-4179.

134. Yang, K.H.; Richards, P.L.; Shen, Y.R. Generation of Far-Infrared Radiation by Picosecond Light Pulses in $LiNbO_3$. *Appl. Phys. Lett.*, **2003**, *19*(9), 320.

135. Auston, D.H.; Cheung, K.P.; Valdmanis, J.A.; Kleinman. Cherenkov Radiation from Femtosecond Optical Pulses in Electro-Optic Media. *Phys. Rev. Lett.*, **1984**, *53*, 1555.

136. Zhang, X.-C.; Jin, Y.; Yang, K.; Schowalter, L.J. Resonant nonlinear susceptibility near the GaAs band gap. *Phys. Rev. Lett.*, **1992**, *69*, 2303.

137. Rice, A.; Jin, Y.; Ma, X.F.; Zhang, X.-C. Terahertz optical rectification from 〈110〉 zinc-blende crystals. *Appl. Phys. Lett.*, **1994**, *64*(11), 1324.

138. Zhang, X.-C.; Ma, X.F.; Jin, Y.; Lu, T.-M.; Boden, E.P.; Phelps, P.D.; Stewart, K.R.; Yakymyshyn, C.P. Terahertz optical rectification from a nonlinear organic crystal. *Appl. Phys. Lett.*, **1992**, *61*(26), 3080.

139. Sanna, S.; Schmidt, W.G. $LiNbO_3$ surfaces from a microscopic perspective. *J. Phys.: Condens. Matter*, **2017**, *29*, 413001.

140. Chen, X.; He, S.; Shen, Z.; Zhao, F.L.; Xu, K.Y.; Wang, G.; Wang, R.; Dai, N. Influence of nonlinear effects in ZnTe on generation and detection of terahertz waves. *J. Appl. Phys.*, **2009**, *105*(2), 023106.

141. He, W.-Q.; Gu, C.-M.; Shen, W.-Z. Direct evidence of Kerr-like nonlinearity by femtosecond Z-scan technique. *Opt. Express*, **2006**, *14*(12), 5476-5483.

142. Auston, D.H. Picosecond optoelectronic switching and gating in silicon. *Appl. Phys. Lett.*, **1975**, *26*(3), 101.

143. Lee, C.H. Picosecond optoelectronic switching in GaAs. *Appl. Phys. Lett.*, **1977**, *30*(2), 84.

144. Jin, Y.; Ma, X.F.; Wagoner, G.A.; Alexander, M.; Zhang, X.-C. Anomalous optically generated THz beams from metal/GaAs interfaces. *Appl. Phys. Lett.*, **1994**, *65*, 682-684.

145. Lu, X.; Yonezawa, T. Terahertz emission from Cu_xO/Au thin film. 2014 *MWP/APMP* **2014**, 164-165.

146. Lu, X.; Ishida, Y.; Mishina, T.; Nguyen, M. T.; Yonezawa, T. Enhanced Terahertz Emission from Cu_xO/Metal Thin Film Deposited on Columnar-Structured Porous Silicon. *Bull. Chem. Soc. Jpn.* **2015**, *88*, 10, 1385-1387.

147. Ramanandan, G. K. P.; Adam, A. J. L.; Ramakrishnan, G.; Petrik, P.; Hendrikx, R.; Planken, P. C. M. Optical characterization of gold-cuprous oxide interfaces for terahertz emission applications. *Appl. Opt.* **2014**, *53*, 10, 1994-2000.

148. Ramakrishnan, G.; Ramanandan, G. K. P.; Adam, A. J. L.; Xu, M.; Kumar, N.; Hendrikx, R. W. A.; Planken, P. C. M. Enhanced terahertz emission by coherent optical absorption in ultrathin semiconductor films on metals. *Opt. Express* **2013**, *21*, 14, 16784-16798.

149. Dember, H. Photoelectromotive force in cuprous oxide crystals. *Phys. Z.*, **1931**, *32*, 554-556.

150. Kono, S.; Gu, P.; Tani, M.; Sakai, K. Temperature dependence of terahertz radiation from n-type InSb and n-type InAs surfaces. *Appl. Phys. B-Lasers O.*, **2000**, *71*, 901-904.

151. Jin, Q.; Yiwen, E.; Williams, K.; Dai, J.; Zhang, X.-C. Observation of broadband terahertz wave generation from liquid water. *Appl. Phys. Lett.*, **2017**, *111*, 071103.

152. Huang, H.; Nagashima, T.; Yonezawa, T.; Matsuo, Y.; Ng, S.H.; Juodkazis, S.; Hatanaka, K. Giant Enhancement of THz Wave Emission under Double-Pulse Excitation of Thin Water Flow. *Appl. Sci.*, **2020**, *10*(6), 2031.

153. Huang, H.; Juodkazis, S.; Gamaly, E.G.; Nagashima, T.; Yonezawa, T.; Hatanaka, K. Saptio-temporal control of THz emission. *Commun. Phys.*, **2022**, *5*, 134.

154. Zhang, L.-L.; Wang, W.-M.; Wu, T.; Feng, S.-J.; Kang, K.; Zhang, C.-L.; Zhang, Y.; Li, Y.-T.; Sheng, Z.-M.; Zhang, X.-C. Strong Terahertz Radiation from a Liquid-Water Line. *Phys. Rev. Applied*, **2019**, *12*, 014005.

155. Huang, H.; Chau, Y.R.; Yonezawa, T.; Nguyen M.T.; Zhu, S.; Deng, D.; Nagashima, T.; Hatanaka, K. THz wave emission from ZnTe nano-colloidal aqueous dispersion irradiated by femtosecond laser. *Chem. Lett.*, **2020**, *49*(6), 597-600.

156. Wu, Q.; Zhang, X.-C. Design and Characterization of Traveling-Wave Electroopic Terahertz Sensors. *IEEE Journal of Selected topics in quantum electronics, 2(3)*, 1996

CHAPTER 2

Facile Synthesis of Cu and Cu-Pd alloy Nanoparticles in Polymer Matrix by Magnetron Sputtering

2.1 Introduction

Alloy NPs are applied as catalysts widely because of their high surface-to-volume ratio.[1-9] Chowdhury *et al*. found the catalytic function of Pd NPs can be enhanced by alloying with Cu.[6] They synthesized bimetallic Cu-Pd alloy NPs with average particle diameters of 6-10 nm and reported that the Cu_4Pd_{96} gives the greatest electrocatalytic activity among other compositions of Cu-Pd alloy NPs as well as monometallic Cu and Pd.[6] Therefore, it is of interest to synthesize Cu-Pd alloy NPs with various compositions, which would help the future research on the mechanism of their catalytic function.

Cu-Pd alloy NPs are usually synthesized by chemical reduction strategies.[6-9] However, chemical reduction can give undesired by-products at the end of the synthetic route.[10] Magnetron sputtering, a physical deposition technique, has drawn attention in many research studies for making metal NP dispersions. NPs are knocked out from the metal target surface by excited argon atoms, and they fall into a liquid matrix substrate

during the sputtering deposition.[11] Monometallic Au,[12,13] Ag,[14] Cu,[15] and Pt[16] and bimetallic AuAg,[17] AuCu,[18] and PtCu[19] were successfully synthesized into ionic liquids[13,16] or polymers[12,14-16,18,19] via sputtering.

This chapter aimed at introducing the syntheses of monometallic Cu and Cu-Pd alloy NPs via sputtering deposition. For Cu NPs, Nakagawa *et al.* found that the sputtered Cu NPs in pentaerythritol ethoxylate (PEEL) were completely oxidized in a week from as-synthesized.[15] A weak localized surface plasmon resonance (LSPR) of Cu NPs was measured from the Cu NPs dispersed in PEEL sputtered with low sputtering current. The phenomenon was possibly caused by the changing of particle size and/or the oxidation of Cu NPs. In this chapter, discussions on the oxidation of Cu NPs suspended in pure PEG were included. Furthermore, synthesis of Cu-Pd alloy NPs dispersion by sputtering deposition was conducted. Compositions of Cu-Pd alloy NPs were varied by controlling the sputtering current. The relation of particle size and composition with the sputtering currents and the stability of Cu-Pd NPs with respect to oxidation were characterized.

2.2 Experimental

2.2.1 Preparation of Cu NPs in PEG

PEG (M.W. = 600, Junsei, Japan) was stirred at 700 rpm under vacuum in a silicon oil bath at 80 ºC for 2 h to remove moisture and gases. 10 mL of vacuum-dried PEG was then put into a Petri dish with an inner diameter of 60 mm. It was then located at the center of the sputtering chamber. Vertical distance from single head target and the surface of PEG was 6 cm. A stainless stirrer was immersed in the PEG. The stirring speed was kept at 80 rpm during sputtering. 20 cycles of gas exchange at a base pressure of 5 × 10^{-3} Pa were completed to remove ingredient molecules in PEG and oxygen in the sputtering chamber. Cu target (99.96 % in purity, 50 mm in diameter, Nilaco, Japan) was then sputtered in the argon gas filled environment with 2 Pa of chamber pressure. The target was firstly sputtered for 10 min for cleaning the surface. Cold ethanol at 0 °C was used for cooling the metal target during the experiment. Movable shutter was placed on top of the PEG to prevent the substance from dropping into the PEG during the cleaning process. Sputtering time and current were set to 30 min and 50 mA respectively. **Figure 2.1**a shows the schematic diagram of the sputtering process.

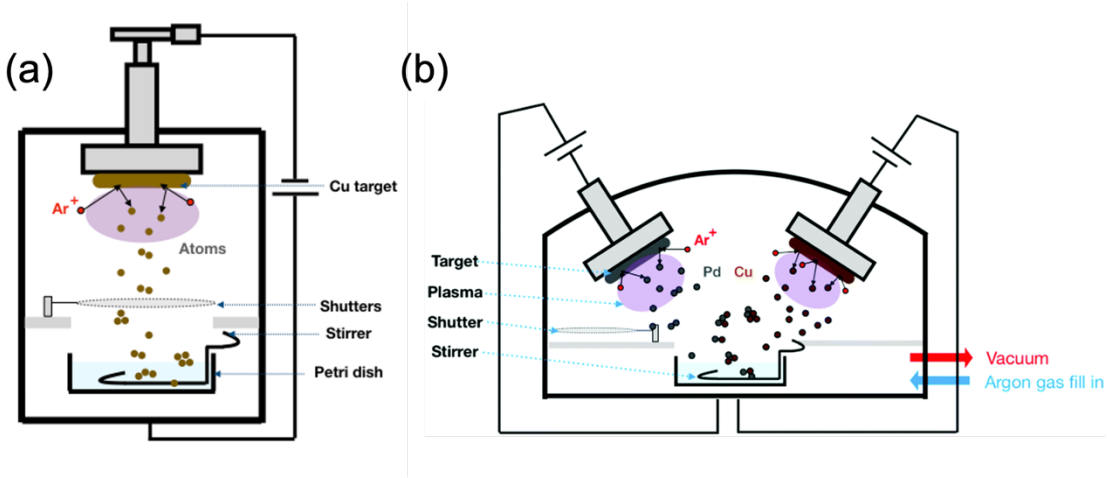


Figure 2.1 Schematic illustration of (a) single target sputtering system for metallic Cu NPs and (b) double target sputtering system for bimetallic Pd–Cu alloy NPs.

2.2.2 Preparation of Cu-Pd NPs in PEG

Same procedure was carried out to treat PEG before sputtering deposition, but double target sputtering system was used (**Figure 2.1**b). The distance between the metal target center and the center of the liquid PEG substrate was 110 mm. Similarly, Movable shutters were placed in front of the metal targets and above the PEG to prevent the substance from dropping into the liquid substrate during the cleaning process. Co-sputtering was performed to obtain Cu-Pd alloy NPs. The sputtering current combinations set in the experiments are listed in **Table 2.1**. Sputtering was conducted for 30 min in all experiments.

Table 2.1 Sputtering currents used in the preparation of Cu-Pd alloy NPs.

Sample	Sputtering current, I (mA)	
	I_{Cu}	I_{Pd}
I	50	10
II	50	30
III	50	50
IV	30	50
V	10	50

2.2.3 Sputtering Cu-Pd NPs onto Al foil, glass slide, Si wafer and TEM grid

Sputtering currents of 10, 20, 30, 40 and 50 mA were applied to either the Cu or Pd target for 30 min in each experiment using aluminum (Al) foil as the substrate. The mass of Al foil was recorded before and after sputtering for calculating the estimated composition of the obtained Cu-Pd alloy when using different current pairs. Sputtering currents listed in **Table 2.1** were used for co-sputtering of Cu and Pd on a TEM grid and a Si wafer for 60 s. Sputtering on a carbon-coated molybdenum (Mo) TEM grid for 1 s at 50 mA for both Pd and Cu targets was also conducted for confirming if the quantitative analysis of STEM-EDS is consistent with the results from XRD, XPS and mass measurement when PEG is not used. **Table 2.2** lists the sputtering time and the characterization methods used for different solid substrates. Each solid substrate was

located at the center of the Petri dish during sputtering.

Table 2.2 Solid substrates used with their corresponding sputtering time and characterization methods.

Substrate	Sputtering time	Characterization
Glass slide	30 min	XRD
TEM grid	1 s, 60 s	STEM, TEM
Si wafer	60 s	XPS

2.2.4 Characterization

The sputtered dispersions were filled into a quartz cuvette with a 1 mm optical path. Optical absorption onset in the UV-Vis region (300 to 1000 nm for Cu NPs, 200 to 800 nm for Cu-Pd alloy NPs) of the as-synthesized dispersions was obtained with a UV-Vis spectrometer (Shimadzu UV-1800). For Cu NPs, portion of the obtained dispersions were filled into a glass cuvette with 5 mm of optical path. The cuvette was placed in air with and without a plastic cap at room temperature, optical absorption onset in the UV-Vis region was then monitored time by time. For Cu-Pd alloy NPs, portions of the obtained dispersions were taken from the incubator 4 days after synthesis for measuring the UV-Vis spectra to determine the oxidation of the dispersion. Baseline correction was done by using an empty quartz cuvette before each measurement.

A collodion coated Cu grid (for transmission electron microscopy (TEM)) or a carbon coated Mo microgrid (for scanning TEM (STEM)) was dipped into the dispersion for 15 s, followed with dipping into ethanol for 15 min to remove excess PEG. The grid was then dried in air at room temperature. The size of NPs was obtained by measuring about 150 NPs from images taken using TEM (JEOL JEM-2000FX, 200 kV). Particularly for Cu-Pd alloy NPs, high-angle annular dark-field (HAADF)-STEM images were obtained with a JEOL JEM-ARM200F system operating at 200 kV. Composition of NPs was obtained by elemental mapping using energy-dispersive X-ray spectroscopy (EDS) coupled with STEM. TEM grids prepared by direct sputtering (**Table 2.2**) were observed by STEM (sputtering time of 1 s) and TEM (sputtering time of 60 s), respectively.

The values of mass difference of Al foil before and after sputtering were used to estimate the composition of Cu-Pd alloy NPs sputtered into PEG with the same sputtering current. m_{Pd} and m_{Cu} were the mass of Pd and Cu loaded on the Al foil with respect to the metal target and sputtering current used. w_{Pd} and w_{Cu} were the weight percent of Pd and Cu, respectively. The estimated Pd content of alloy NPs for each pair of sputtering currents was calculated by:

$$w_{\mathrm{Pd}} = \frac{m_{\mathrm{Pd}}}{m_{\mathrm{Pd}}+m_{\mathrm{Cu}}} \quad \ldots \textbf{(Eq. 2.1)}$$

$$\text{Number of Pd atoms } (n_{\mathrm{Pd}}) = w_{\mathrm{Pd}} \times \frac{N_{\mathrm{A}}}{106.420} \quad \ldots \textbf{(Eq. 2.2)}$$

$$\text{Number of Cu atoms } (n_{\mathrm{Cu}}) = w_{\mathrm{Cu}} \times \frac{N_{\mathrm{A}}}{63.546} \quad \ldots \textbf{(Eq. 2.3)}$$

$$\text{at\% of Pd} = \frac{n_{\mathrm{Pd}}}{n_{\mathrm{Pd}}+n_{\mathrm{Cu}}} \times 100\ \% \quad \ldots \textbf{(Eq. 2.4)}$$

where N_A is Avogadro's constant.

Crystal structure and composition of the CuPd alloys obtained by sputtering on glass substrates were also evaluated using X-ray diffraction (XRD, Rigaku MiniFlex II, Cu Ka radiation, λ= 1.5418 Å, scan speed = 0.1° min^{-1}, and scanning range = 30° to 70°). The electronic state of the samples was determined using a JEOL JPS-9200 X-ray photoelectron spectroscopy (XPS) device equipped with a monochromatic Al Ka X-ray source (1486.6 eV) operating at 100 W under ultrahigh vacuum ($< 5.0 \times 10^{-7}$ Pa) conditions. Charge correction was performed by referring to the binding energy (BE) of Si 2p from the Si wafer substrate.

2.3 Results and Discussion

2.3.1 Size change of Cu NPs dispersed in PEG after as-sputtered

The average size of as-sputtered Cu NPs was 3.1 ± 0.8 nm. This value is similar with the Cu NPs sputtered into PEEL with sputtering current of 50 mA.[15] **Figure 2.2** shows TEM images and size distribution curve of Cu NPs dispersed in PEG at different time from as-synthesized. The Cu NPs were observed growth to 3.4 ± 0.7 nm after the solution was transferred into the cuvette in ambient for 1 h. Further growth of Cu NPs to average size of 4.1 ± 0.8 nm were observed at 4 h after as-synthesized. The average size of Cu NPs at day 7 was 4.1 ± 0.8 nm. The sizes of Cu NPs did not have large variation from day 1 onwards. **Figure 2.3** has summarized the average size of Cu NPs against time. Agglomeration of Cu NPs was not observed for entire 7 days from as-synthesized. Hence, PEG is effective for restricting agglomeration of Cu NPs.

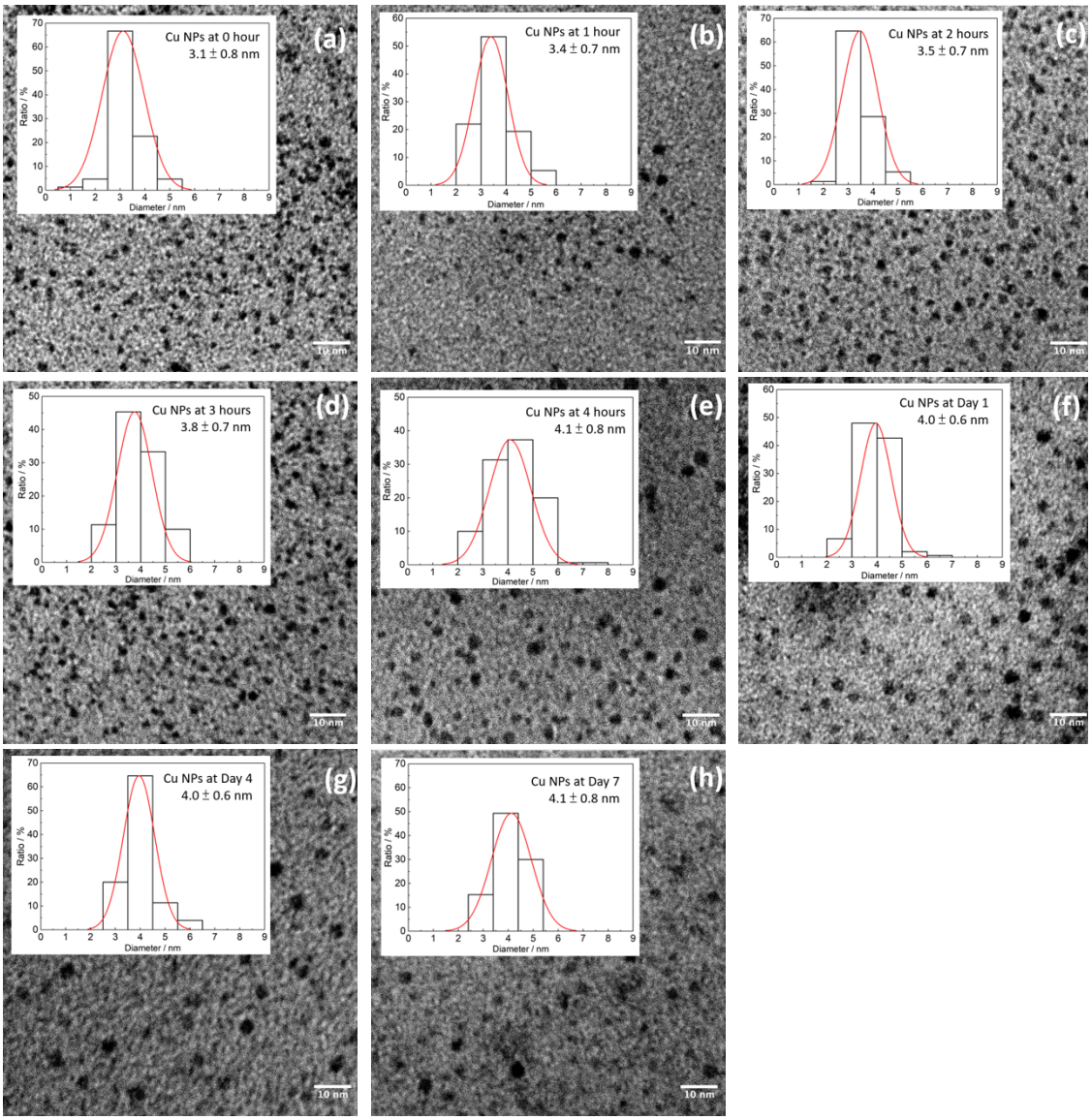


Figure 2.2 TEM images and size distributions of PEG-coated Cu NPs prepared by sputtering (current = 50 mA, time = 30 min, Pressure = 2 Pa, Temperature = 30 °C, substrate rotation speed = 80 rpm) at (a) 0 h, (b) 1 h, (c) 2 h, (d) 3 h, (e) 4 h, (f) 1 d, (g) 4 d, (h) 7 d. Scale bars in all images are in 10 nm.

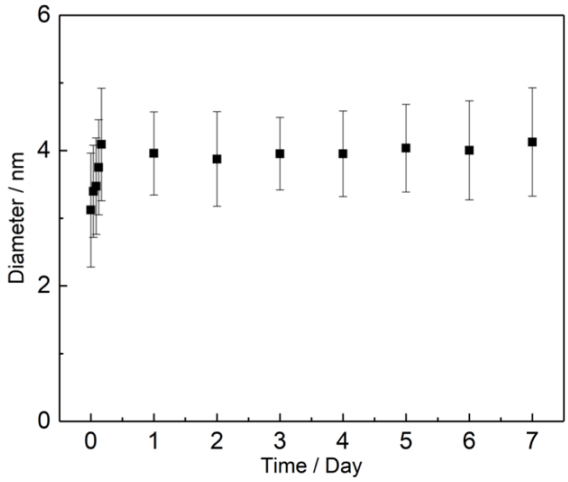


Figure 2.3 Particle sizes versus time from 0 d to 7 d.

2.3.2 Absorption peak of Cu NPs at 570 nm degraded due to oxidation

As-synthesized dispersion showed LSPR at about 570 nm in UV-Vis spectra of Cu NPs (**Figure 2.4**a). This confirmed that the sputtered NPs are metallic Cu. A slightly blue shift in the LSPR was found for the first 2 days. There was an increase in the absorbance of the dispersion at day 1 accompany with the shift in LSPR of Cu NPs. This attributes to the increase of particle size. The absorbance of the dispersion showed a decreasing trend from day 1 after synthesized. The decreasing in absorbance at 570 nm was almost linear with time (**Figure 2.4**b). Meanwhile, the visual colour of the dispersion faded out significantly from dark brown to pale yellow with respect to time and clear pale yellow colour was observed at day 10 after synthesized. The shrinkage of dark brown coloured region in the cuvette happened along with the decreasing absorbance of the

dispersion. These results are in good agreement showing the oxidation of Cu NPs.

To further confirm the oxidation of Cu NPs, UV-Vis spectra of the dispersion keeping in air without plastic cap and sealed with a plastic cap (as control) were measured. Cuvettes were kept in dark at room temperature. **Figure 2.5**a shows the opened cuvette resulted lower absorbance in the UV-Vis spectra when compared to the cuvette sealed with the plastic cap. It was considered that the solution in the opened cuvette oxidizes faster than the sealed cuvette. Until day 10 from as-synthesized, the colour of solution almost diminished. Since the plastic cap was not a perfect sealing, the dispersion in the sealed cuvette also experienced oxidation as shown in the visual images in **Figure 2.4**b but in slower rate. Selected area electron diffraction (SAED) image was taken for the sample synthesized for 8 days. **Figure 2.5**b shows the diffraction from (111) and (200) planes of CuO, suggested that the Cu NPs oxidized.

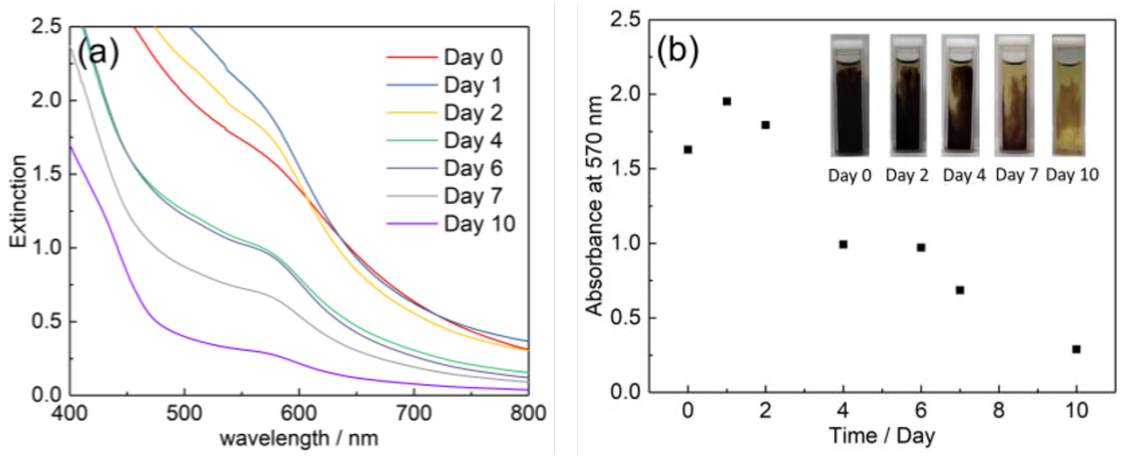


Figure 2.4 (a) UV-Vis spectra from day 0 to day 10. (b) Absorbance at 570 nm from UV-Vis spectra versus time. Condition of cuvette indicated the colour faded out.

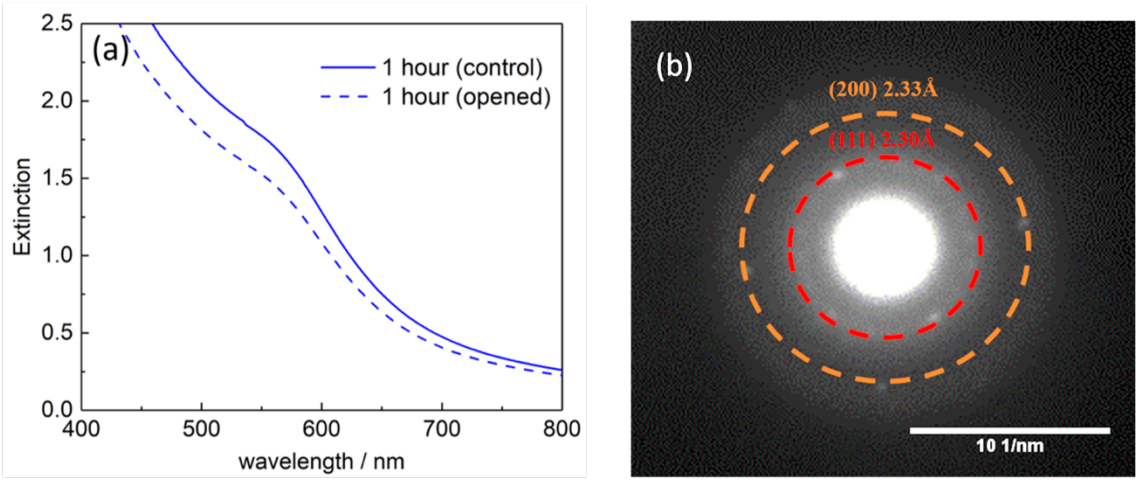


Figure 2.5 (a) UV-Vis absorbance onset of sealed cuvette (control) and opened cuvette at 1 hour. (b) SAED of the sample after 8 days from sputtering.

2.3.3 Formation of Cu-Pd alloy NPs

Cu-Pd alloy NPs were synthesized by sputtering deposition onto PEG. The UV-Vis spectra with range from 200 to 800 nm in **Figure 2.6**a illustrates dispersions containing metal had higher absorbance among the spectra than pure PEG, which showed negligible absorption above 250 nm and very weak absorption from 230 to 250 nm. Monometallic Cu in PEG had localized surface plasmon resonance (LSPR) at 570 nm which is typical for Cu.[15] Dispersion of monometallic Pd NPs gave an absorption shoulder in the short wavelength region (230-250 nm) and monotonically decreased at higher wavelength region. Similar phenomenon was observed for Pd NPs in ionic liquid and water.[20-21] All Cu-Pd alloy NPs (samples I to V) did not show LSPR peak at 580 nm and exhibited a decrease in absorbance from short to long wavelength. **Figure 2.6**b shows the dispersion in quartz cuvette with 1 mm of optical path, which was taken to the UV-Vis measurement. No precipitation was observed with the naked eyes. The UV-Vis spectra indicated that Cu and Pd can form alloy NPs instead of monometallic Pd NPs, Cu NPs, and Pd-Cu core-shell structure.[22] A decrease in the absorbance for the whole measurement range was observed when the sputtering current for Cu decreased from 50 mA to 10 mA and keeping the sputtering current of Pd was kept constant at 50 mA (samples III, IV, V). This can be explained by the lower amount of Cu in the alloys in the

dispersion when decreasing the sputtering current of Cu. Similar phenomenon occurred when keeping the sputtering current for Cu constant at 50 mA and decreasing the sputtering current of Pd from 50 mA (sample III) to 30 mA (sample II). However, the further decrease in the sputtering current of Pd to 10 mA did not result further decrease in the absorbance.

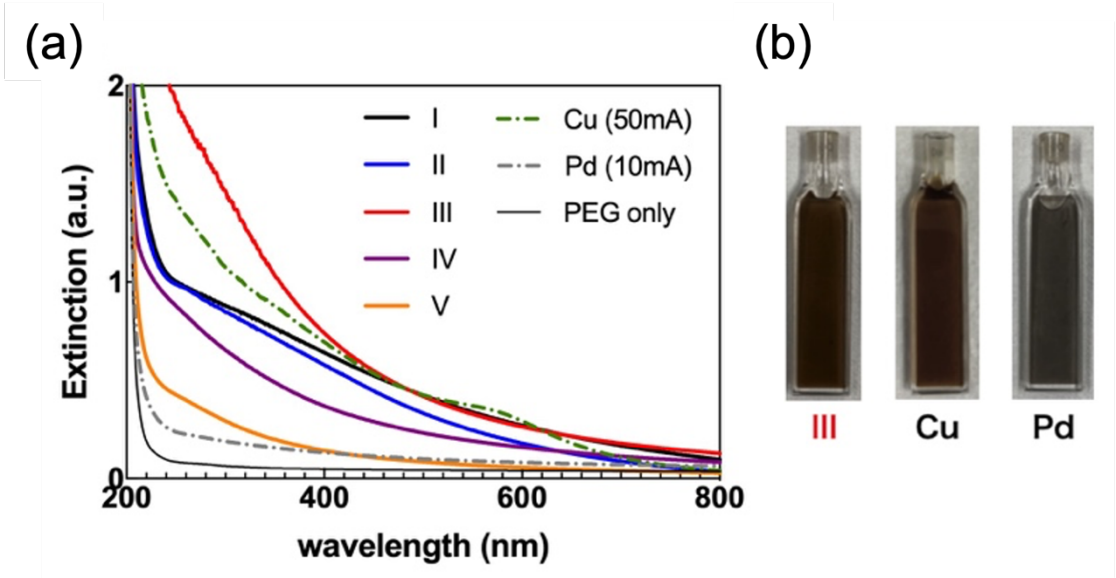


Figure 2.6 (a) UV-Vis absorption spectra of as-sputtered alloy samples I to V, monometallic Pd, monometallic Cu and vacuum dried PEG. (b) Dispersions of Pd-Cu alloy NPs (sample III), monometallic Pd NPs and monometallic Cu NPs in quartz cuvettes with a 1 mm optical path.

2.3.4 Size of Cu-Pd alloy NPs against sputtering currents

TEM images and the particle size distributions of samples I to V are given in **Figure 2.7** and **Figure 2.8**. The average size of CuPd alloy NPs was 2.4–2.5 nm despite the different combinations of sputtering currents. Research on monometallic NPs and alloy NPs in PEG synthesized by single target sputtering deposition had found a dependency of NP size on sputtering current.[15] It had been reported that bigger NPs were often observed for a higher sputtering current.[13,16] On the other hand, for alloy NPs prepared by double target sputtering, or sequential sputtering, the relation of particle size and sputtering currents is more complicated. Some researchers observed an increase in particle size of alloy NPs with increasing sputtering current, while others observed the opposite.[18,23] However, in the case of bimetallic Cu-Pd alloy NPs, particles in all samples had an average size of 2.4-2.5 nm despite the sputtering current (10-50 mA). In the case of Cu NPs synthesized via single target sputtering, the sizes of Cu NPs sputtered with sputtering current of 10-50 mA were about 2.7-3.9 nm in size. This suggested that the sputtering currents used in the double target sputtering system (10-50 mA) were not sufficient to show the effectiveness of increasing or decreasing particle size by increasing sputtering current of the Cu and Pd metal pair. No aggregation was found in all samples since PEG can act as a protective layer to the single particle and has the function of

suppressing NP aggregation.[16]

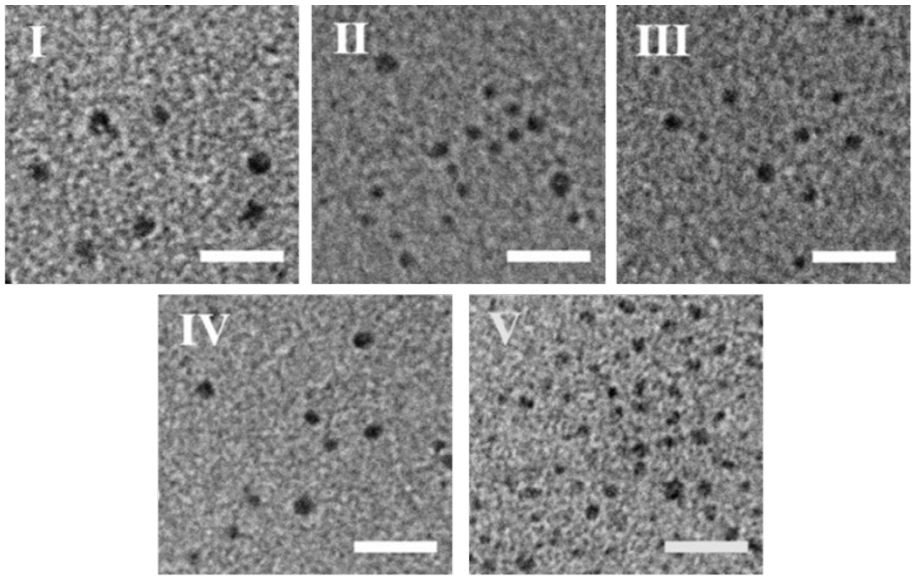


Figure 2.7 TEM images of samples I–V. Scale bar in all images is 10 nm.

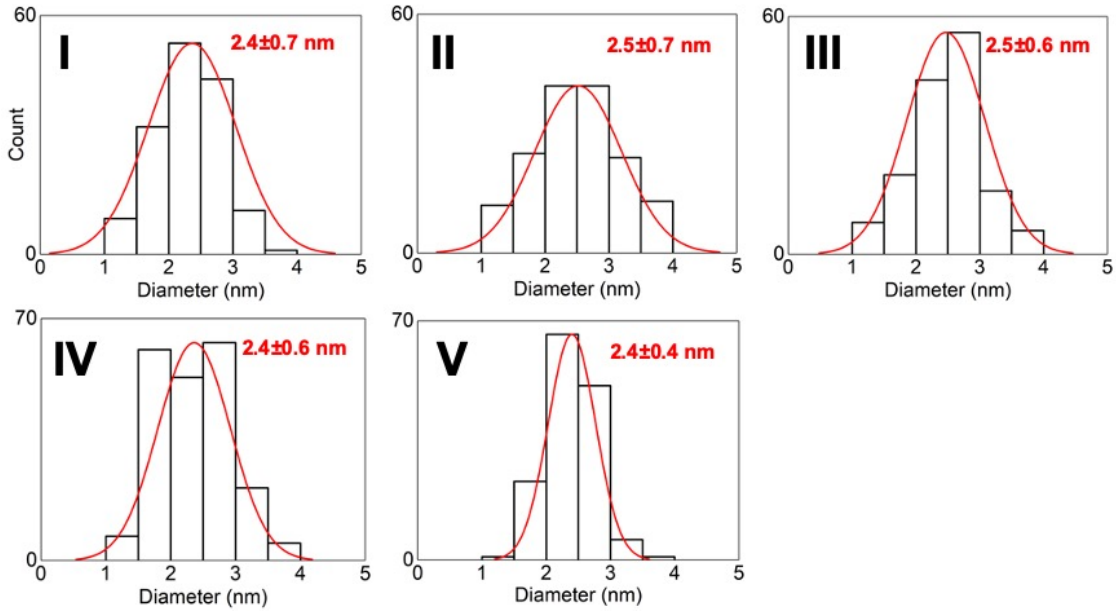


Figure 2.8 Size distributions of the samples I–V.

2.3.5 Particle Composition against Sputtering Currents

For the purpose of knowing the structure of the NPs and alloy formation, XRD and XPS were performed. The reason for performing the direct deposition on the solid substrate but not using the alloy NPs synthesized in PEG for XRD and XPS measurement was that the NPs were unable to be separated from the PEG even using ultra speed centrifugation. 30 min of sputtering time was used to make the sample for XRD measurement to obtain enough signal from the alloy structure.

The XRD patterns of the sputtered thin film on glass slide substrate are displayed in **Figure 2.9**. A single peak was located between the (111) peaks of pure Cu and Pd for all samples. The (111) diffraction peak in the XRD pattern were (I) 42.69°, (II) 41.75°, (III) 41.55°, (IV) 41.03 and (V) 40.46° respectively. The peak was shifted from Pd towards Cu with the increase of Cu content according to the change of sputtering current for Cu and Pd. The peak positions obtained for the (111) plane was used to determine the *d*-spacing for each sample via Bragg's law[24]: $d = n\lambda/(2\ sin\theta)$, whereas n is unity, λ = 1.5418 Å, θ is the angle of the peak located. The composition of the alloy was then calculated with the d-spacing via Vegard's Law.[25] **Table 2.3** lists Pd content interpreted from XRD result in sample I – V. **Figure 2.10** shows the *d*-spacing calculated using the (111) peak in the XRD patterns of all samples linearly decreased when Cu content

increased, which follows Vegard's law for a bimetallic solid solution. This suggested that a solid solution alloy of cubic structure was obtained for Cu-Pd sputtered on the solid substrate. Thus, we believed that the NPs sputtered into PEG were also a solid solution because they had a higher surface energy and atomic diffusion processes were more favourable in NPs dispersion compared with those of a thin film on a glass slide.

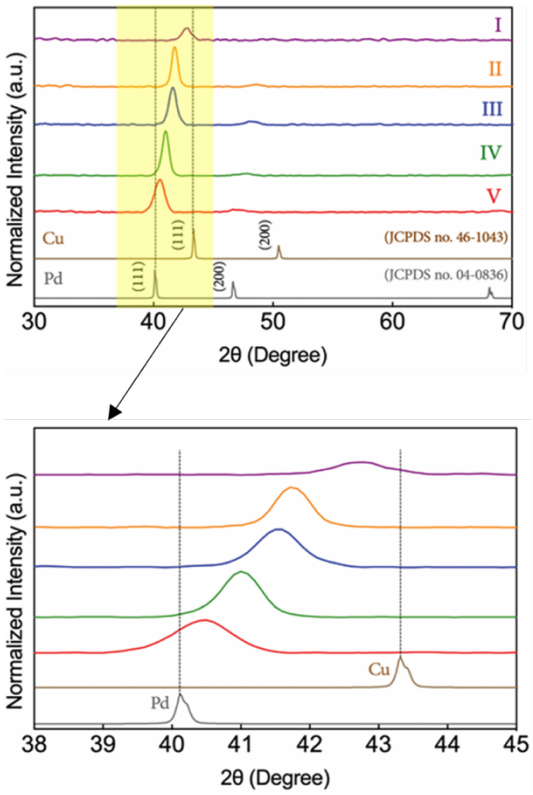


Figure 2.9 Left XRD patterns of the Cu-Pd alloy sputtered on a glass slide for 30 min with the same sputtering current as samples (I–V). Below is the enlargement of the (111) peaks in the XRD patterns from 38° to 45°. Standard patterns of Cu (JCPDS no. 46-1043) and Pd (JCPDS no. 04-0836) for reference.

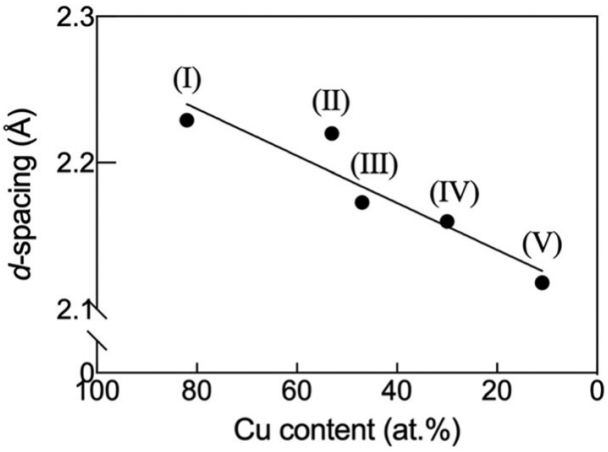


Figure 2.10 *d*-spacing determined from the (111) peak in the XRD patterns with respect to the Cu content calculated with Vegard's Law.

Table 2.3 Summary of the Pd content in samples I–V determined by Vegard's law using XRD patterns, quantitative analysis by XPS, mass measurement, and elemental mapping by STEM-EDS.

	Pd content determined by different methods (at %)			
Sample	**XRD**	**XPS**	**Mass measurement**	**STEM-EDS**
I	18	11	17	74 ± 2
II	47	45	45	66 ± 3
III	53	57	55	77 ± 3
IV	70	64	71	84 ± 5
V	89	86	88	89 ± 2

The binding energies of the Cu 2p level and Pd 3d level in samples I–V sputtered directly on the Si wafer for 1 min are shown in **Figure 2.11**. Since many reports mentioned that the particle size would affect the binding energies of core levels,[26-29] 1 min of sputtering time was used to avoid particle growth happening on the solid substrate. Direct sputtering was performed on the TEM grid and 150 NPs were taken for size measurement. The average size of alloy NPs in all samples sputtered for 1 min was 2.3–2.6 nm (**Figure 2.12**). In addition, 1 min of sputtering time was still not enough for the NPs to form a film structure although the NPs were very close to each other compared with those in the PEG. Thus, the XPS results, i.e., the electronic structure and composition, of the sample sputtered on Si wafer can be used for discussing the alloy formation in close relation to the Cu-Pd NPs obtained in PEG. The graph on the left of **Figure 2.11** shows the Cu $2p_{1/2}$ and Cu $2p_{3/2}$ peaks. The difference of the binding energies of these peaks was 19.8 eV in all spectra, which is typical for a Cu 2p spectrum.[30] For the Pd 3d level spectra (right of **Figure 2.11**), the Pd $3d_{3/2}$ and Pd $3d_{5/2}$ peaks had a binding energy difference of 5.3 eV, which is the same as the standard spectrum of Pd at the 3d core-level.[31] The composition of samples I–V was determined by quantitative analysis is given in **Table 2.3**.

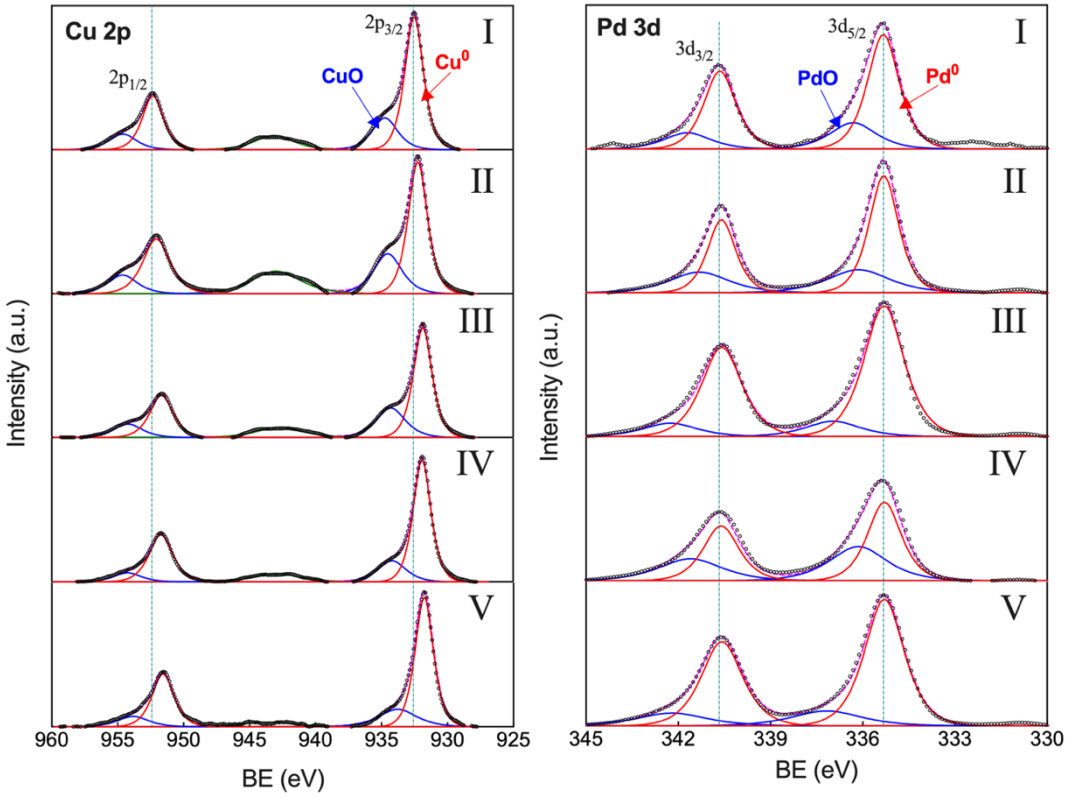


Figure 2.11 XPS spectra of Cu 2p (left) and Pd 3d (right) of samples I–V. The dotted black curves are the actual spectra. The blue and red curves are the fitting spectra with an asymmetric Gaussian–Lorentzian sum function (70% L–G) and a Shirley background. The dashed lines showing the reference peak positions of Cu and Pd are visual guides of the peak shifts.

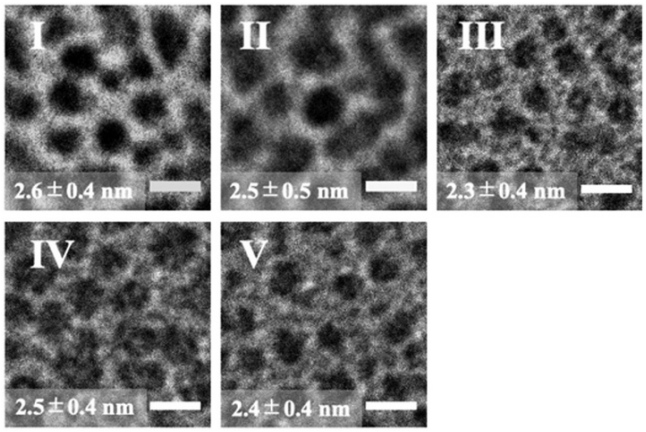


Figure 2.12 TEM images of samples I–V directly sputtered on a TEM grid for 1 min. The scale bars in all images are 5 nm.

Figure 2.13 shows the trend of binding energy shifting of the Pd $3d_{5/2}$ peak and Cu $2p_{3/2}$ peak against the Cu content. The core-level binding energy (BE) shifted from 335.30 to 335.33 eV for Pd $3d_{5/2}$, and from 931.76 to 932.50 eV for Cu $2p_{3/2}$ when the Cu content was increased by lowering the sputtering current for Pd and increasing the sputtering current for Cu. The BE shifting was observed in all samples compared with the BE of pure Cu (932.8 eV) and Pd (335.1 eV), whereas the BE shifted negatively for Cu $2p_{3/2}$ and positively for Pd $3d_{5/2}$ (**Table 2.4**).[32-35] BE shifting can be due to the size effect and alloying.[36] The size effect on BE shifting should be taken into account if the NP size difference was about 5 to 10 nm.[37] In our samples, the NP size difference was less than 1 nm. Therefore, it is considered that the BE shifting was due to alloy formation but not due to the size effect. The shifting of BE might be ascribed to the occurrence of

electron transfer between Pd and Cu within the alloy NPs.[38] The magnitude of BE shifting in Cu 2p was significantly higher than that in Pd 3d. A similar finding was reported elsewhere.[39] The results from XRD and XPS confirmed that the formation of the solid solution with different sputtering current pairs for Pd and Cu.

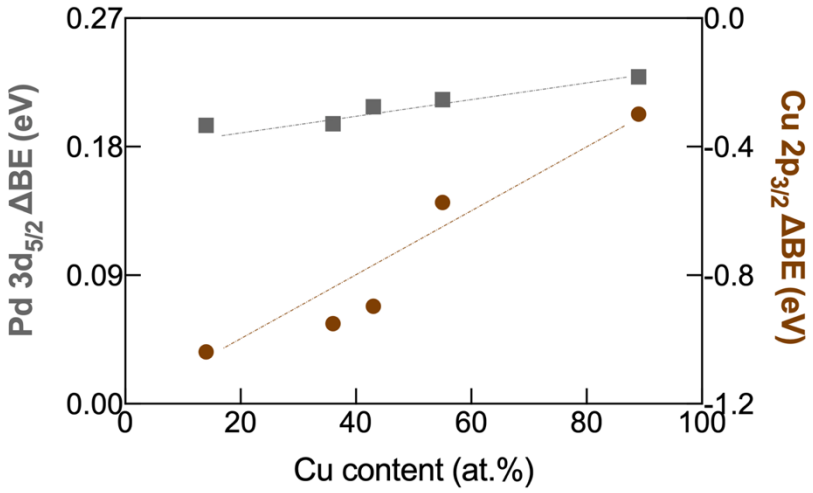


Figure 2.13 Shift of binding energies (ΔBE) of Pd^0 $3d_{5/2}$ (left y-axis) and Cu^0 $2p_{3/2}$ peak (right y-axis) with respect to the Cu content (at%) by quantitative analysis in XPS.

Table 2.4 Binding energies of Pd^0 $3d_{5/2}$ and Cu^0 $2p_{3/2}$ peaks in samples I–V.

	Binding energies (eV)	
Sample	**Pd^0 $3d_{5/2}$**	**Cu^0 $2p_{3/2}$**
I	335.33	932.50
II	335.31	932.23
III	335.30	931.90
IV	335.30	931.85
V	335.30	931.76

Masses of the sputtered Pd and Cu on Al foil were obtained from the mass differences of the Al foil before and after sputtering. The sputtered amounts of Pd and Cu were directly proportional to the sputtering current used (**Figure 2.14**). For Cu, 10 mA, 30 mA and 50 mA sputtering currents yielded 0.1 mg, 0.3 mg, and 0.6 mg of Cu; the same current conditions yielded 0.2 mg, 0.8 mg, and 1.2 mg of Pd, respectively. The estimated average amount of Pd in the Cu-Pd alloy obtained by co-sputtering was then calculated from the mass of Pd and Cu complying with **Eq. 2.1 – 2.4**. and the results are shown in **Table 2.3**. The compositions estimated from mass measurement can be considered as the theoretical composition of Cu-Pd alloy if they form a solid solution.

Composition of Pd in NPs of samples I–V was analyzed with STEM-EDS results. The Pd content in the samples was (I) 74 ± 2 at%, (II) 66 ± 3 at%, (III) 77 ± 3 at%, (IV)

84 ± 5 at% and (V) 89 ± 2 at%, respectively. STEM-EDS mapping in **Figure 2.15** shows that the particles from sample III have both Pd and Cu co-existing in the same place, suggesting the formation of the alloy structure. The content of Pd in the alloy NPs in PEG measured by STEM-EDS for all samples was higher than the estimated values from XRD peak position, XPS quantitative analysis and the mass measurement of the samples on solid substrates. The carbon coated Mo grid containing alloy NPs prepared by direct sputtering with the same sputtering current as that of sample III, *i.e.* I_{Pd} = 50 mA, I_{Cu} = 50 mA, was also subjected to STEM-EDS analysis. In contrast, the result showed that the sample has a Pd content of 58 ± 6 at%, which is very close to the estimated value determined by XRD (53 at%), XPS (57 at%), and mass measurement (55 at%). The increase in Pd at% with increasing sputtering current for Pd or lowering sputtering current for Cu so far was observed in STEM-EDS mapping for sputtered Cu-Pd alloy NPs in PEG as expected. This revealed the capability of varying the sputtering current to tailor the particle composition. However, it was found that the average Pd content in Cu-Pd NPs of all samples measured by STEM-EDS is higher than the value determined by other methods. This might be because some atoms/clusters were not included in NPs and stay as free atoms/clusters as in the HAADF-STEM images (**Figure 2.15**). The free atoms/clusters can be stabilized in PEG from collision and growth to form NPs but the

signal from very small NPs, clusters, and free atoms is too weak to be sorted out from the background signal and counted in STEM-EDS analysis. Furthermore, the measurement of STEM-EDS in this research was performed by detecting the signal from particles of narrow area but not the whole sample (yellow circle in **Figure 2.15**), while obtaining accurate compositions of the particles in the sample requires STEM-EDS mapping of all particles and sizes. Thus, we think that there were NPs/clusters with smaller sizes that maybe richer in Cu existing in the sample. For example, the composition of alloy NPs observed in **Figure 2.16** was calculated with Vegard's Law from their lattice spacing.[25] It was found that NPs in sample II have 37 at% Pd and the ones in sample III have 58 at% Pd.

Compared with the estimated content of Pd by mass measurement, the Pd content of NPs in sample III was close to the value obtained by XPS measurement (57 at%), whereas that of the NPs in sample II (37 at%) was lower than the value obtained by XPS (45 at%) and XRD (47 at%) measurement. As a result, it is also possible that there were some alloy NPs containing more/less Pd than the neighbour NPs and what we obtained for each pair of sputtering currents was a mixture of alloy NPs. The obtained NPs had a range of composition, wherein Pd and Cu contents were not uniform throughout all alloy NPs.

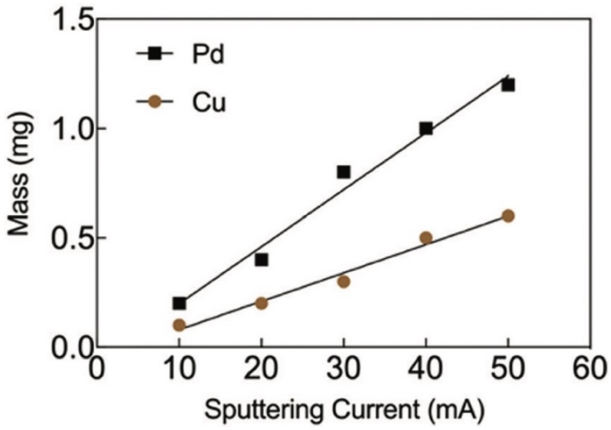


Figure 2.14 Masses of Pd and Cu obtained at the center area of the sputtering chamber with a diameter of 60 mm with respect to the sputtering currents from 10 to 50 mA.

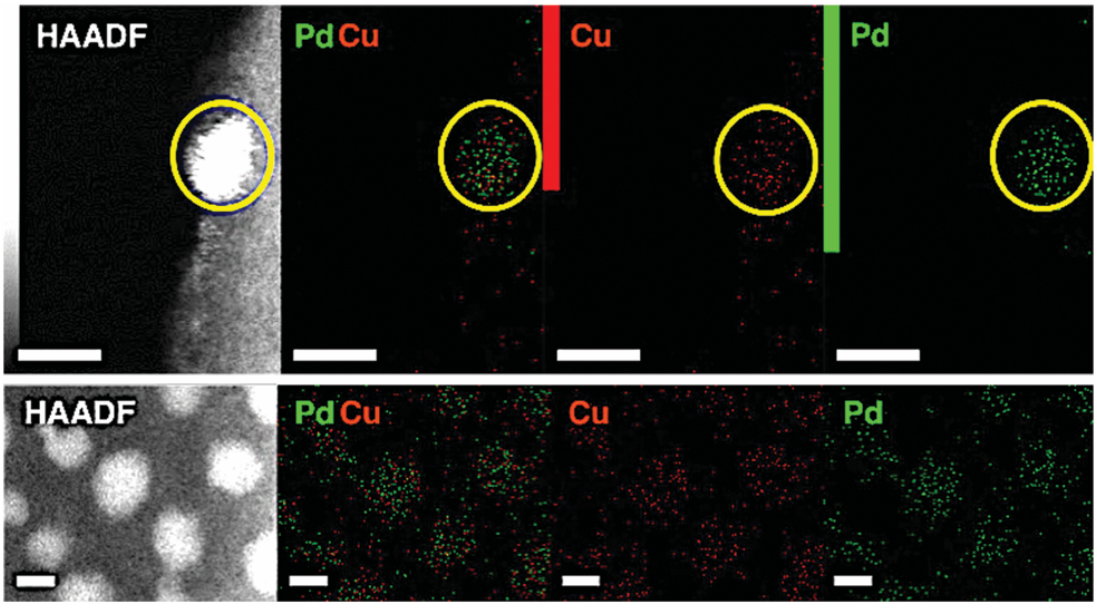


Figure 2.15 Top HAADF-STEM image and STEM-EDS mapping images of the overlapping of Pd and Cu, Cu, and Pd of a NP in PEG of sample III. Bottom HAADF and mapping images of Cu-Pd NPs sputtered on a carbon coated Mo microgrid (I_{Pd} = 50 mA, I_{Cu} = 50 mA). Yellow circle indicates the NPs of interest. Scale bar in all images is 3 nm.

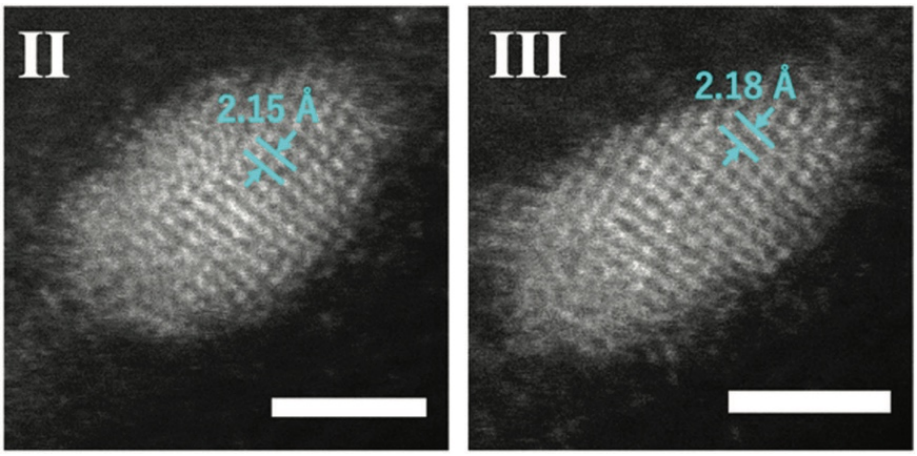


Figure 2.16 HAADF-STEM images of Cu-Pd alloy NPs in samples II and III. The scale bars in all images are 2 nm.

2.3.6 Oxidation of Cu in Cu-Pd alloy NPs in PEG

Because Pd rich Cu-Pd alloy NPs were often observed among the Cu-Pd alloy NPs in STEM-EDS mapping and Cu is prone to oxidation, we also suspected that Cu atoms from the formed Cu-Pd alloy NPs were also possibly oxidized. The Cu $2p_{3/2}$ XPS spectra (**Figure 2.11**) of all samples clearly show the existence of Cu_xO judging from the presence of the satellite peak (940–945 eV) and the high binding energy part near Cu^0. In addition, Gabrielli *et al*. suggested that the presence of PEG would increase the oxidation potential of Cu, causing Cu dissolution.[40] To check the oxidation of the dispersion, samples II, III and IV were subjected to UV-Vis measurement at day 4 after the synthesis. The UV-Vis spectra (**Figure 2.17**) show a decrease of absorbance of these samples at day 4 after the synthesis. This phenomenon was also found in the synthesis of monometallic

Cu in ionic liquids[41,42] by sputtering and this might be due to the formation of Cu_xO at the surface of Cu atoms/clusters in the dispersion. Furthermore, using the same sputtering configuration of sample III to synthesize Cu-Pd alloy NPs on the TEM grid without PEG resulted in a content of Pd (58 ± 6 at%) that is much closer to the content (57 at%) found by XPS measurement. Therefore, Cu atoms in the alloy NPs dispersed in PEG possibly oxidized and migrated into the liquid polymer due to weak chemical interaction between metal and polymer,[43] causing less Cu to be observed in the alloy NPs by STEM-EDS mapping. Although sputtering deposition is a direct top-down approach for producing NPs, which does not require the use of a variety of reducing agents, the problem of oxidation of Cu atoms in the alloy NPs and the dissolution should be solved before promoting the dispersion made by sputtering for catalytic reactions reported elsewhere.[6-9,44]

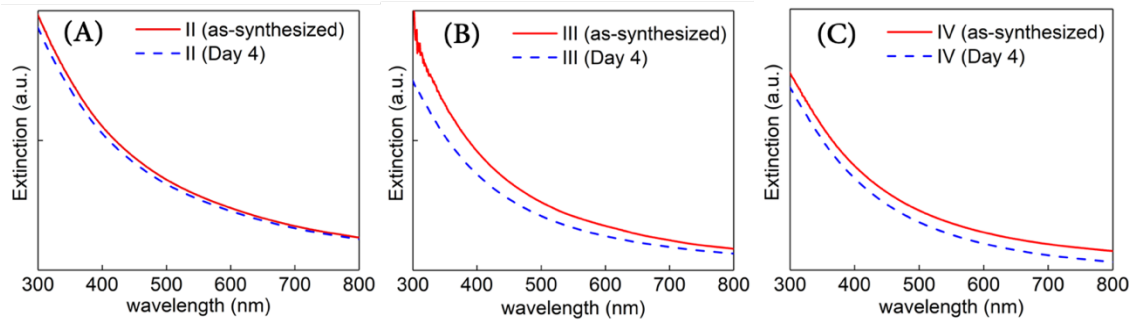


Figure 2.17 UV-Vis spectra of samples (solid line) as-synthesized and (dashed line) at day 4 after synthesis: (A) II, (B) III and (C) IV.

2.3.7 Crystallinity of the Cu-Pd alloy NPs in PEG

Under the observation of STEM, many of the NPs had very low crystallinity and do not show clear atomic columns in HAADF images. After the electron beam scanning by STEM-EDS mapping, crystallinity of the CuPd alloy NP was increased (**Figure 2.18**). Similar results were found by Garzón-Manjón *et al*. while they made Cr–Mn–Fe–Co–Ni alloy NPs by magnetron sputtering onto ionic liquid.[45] This indicates the impact of the focused electron beam on improving the crystallinity of the alloy NPs. Heat energy (temperature of 30 °C) of PEG for capturing the NPs was not sufficient for NPs to be well crystallized. Also, particles tended to aggregate and fuse together after EDS mapping for 1 min (**Figure 2.18**). Thus, post-treatment (electron irradiation, heat treatment, etc.) can be considered to improve the crystallinity of the sputtered NPs.

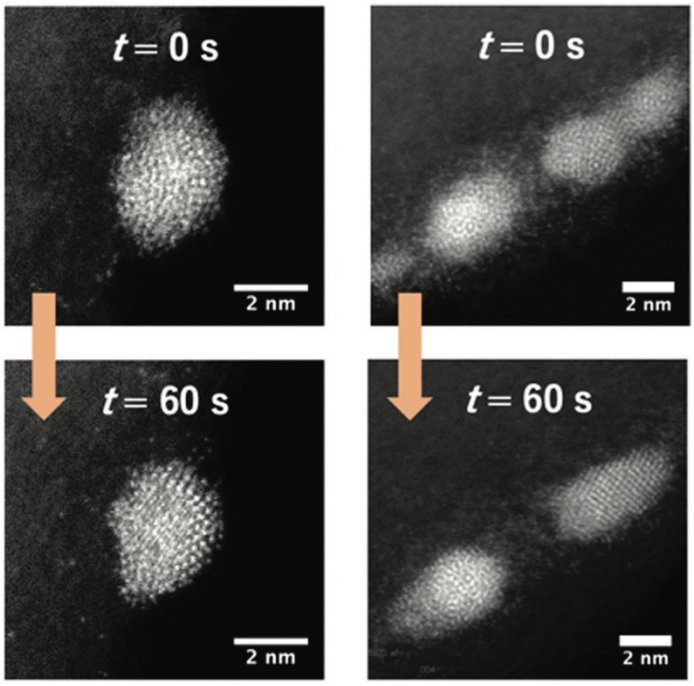


Figure 2.18 HAADF-STEM images of NPs in sample III before and after STEM-EDS mapping for 60 s.

2.4 Conclusion

Cu NPs sized less than 4 nm were synthesized in PEG by single target sputtering deposition. When PEG was used as the substrate, it could avoid aggregation of NPs. Shoulders at 570 nm in UV-Vis spectra assigned to the LSPR of metallic Cu NPs. Cu NPs oxidized in PEG after sputtered in few hours. If adopting Cu NPs in PEG by sputtering deposition in practical usage, oxidation and growth of particles are the major concerns. On the other hand, bimetallic Cu-Pd alloy NPs with size less than 3 nm were synthesized by double target sputtering deposition. No absorption shoulder/peak was found at 570 nm, indicated that the product contained Cu-Pd alloy NPs dispersion, but not the mixture of single element Cu and Pd. From the results of XRD and XPS, wherein alloy NPs were directly sputtered onto a solid substrate, the composition of the alloy NPs was found to vary with different combinations of the sputtering current for Cu and Pd targets. However, the composition of NPs sputtered onto PEG had an exceptionally high content of Pd compared with the results of XRD and XPS, and the estimated value by mass measurement. It is suspected that Cu atoms in the alloy NPs oxidized and dissolved into PEG, so that all alloy NPs were found to be Pd-rich under STEM-EDS. The further study regarding to the mobility of Cu atom in the alloy NPs dispersed in PEG is required to understand the reason of Pd-rich particles found in liquid polymer only but not on the

solid substrates. One of the uncertainties is that the sputtering deposition could yield alloy NPs with deviation in the composition. Therefore, in order to determine the catalytic properties of the sputtered NPs, composition should be controlled precisely, and this remained a challenge for using sputtering technique to synthesize nano-scaled catalyst.

2.5 References

1. King, M.E. and Personick, M.L. Iodide-induced differential control of metal ion reduction rates: synthesis of terraced palladium–copper nanoparticles with dilute bimetallic surfaces. *J. Mater. Chem. A*, **2018**, 6, 22179.
2. Toshima, N. and Yonezawa, T. Bimetallic nanoparticles—novel materials for chemical and physical applications. *New J. Chem.*, **1998**, 22, 1179–1201.
3. Yonezawa, T. and Toshima, N. Mechanistic consideration of formation of polymer-protected nanoscopic bimetallic clusters. *J. Chem. Soc., Faraday Trans.*, **1995**, 91, 4111–4119.
4. Yonezawa, T. and Toshima, N. Polymer- and micelle-protected gold/platinum bimetallic systems. Preparation, application to catalysis for visible-light-induced hydrogen evolution, and analysis of formation process with optical methods *J. Mol. Catal.*, **1993**, *83*(1–2), 167–181.
5. Yonezawa, T.; Cempel, D.; Nguyen, M.T. Microwave-Induced Plasma-In-Liquid Process for Nanoparticle Production. *Bull. Chem. Soc. Jpn.*, **2018**, *91*(12), 1781–1798.
6. Chowdhury, S.R.; Mukherjee, P.; Bhattachrya, S. Palladium and palladium–copper alloy nano particles as superior catalyst for electrochemical oxidation of methanol for fuel cell applications. *Int. J. Hydrogen Energy*, **2016**, *41*(38), 17072–17083.
7. Narayanan, R and El-Sayed, M.A. Effect of Catalysis on the Stability of Metallic Nanoparticles: Suzuki Reaction Catalyzed by PVP-Palladium Nanoparticles. *J. Am. Chem. Soc.*, **2003**, *125*(27), 8340–8347.
8. Jansat, S.; Gómez, M.; Philippot, K.; Muller, G.; Guiu, E.; Claver, C.; Castillón, S.; Chaudret, B. A Case for Enantioselective Allylic Alkylation Catalyzed by Palladium

Nanoparticles. *J. Am. Chem. Soc.*, **2004**, *126*(6), 1592–1593.

9. Zhao, H.; Yang, J.; Wang, L.; Tian, C.; Jiang, B.; Fu, H. Fabrication of a palladium nanoparticle/graphenenanosheet hybrid via sacrifice of a copper template and its application in catalytic oxidation of formic acid. *Chem. Commun.*, **2011**, *41*, 2014–2016.
10. Gao, W.; Guan, N.; Chen, J.; Guan, X.; Jin, R.; Zeng, H.; Liu, Z.; Zhang, F. Titania supported Pd-Cu bimetallic catalyst for the reduction of nitrate in drinking water. *Appl. Catal., B*, **2003**, *46*(2), 341–351.
11. Nguyen, M.T. and Yonezawa, T. Sputtering onto a liquid: interesting physical preparation method for multi-metallic nanoparticles. *STAM*, **2018**, *19*(1), 883–898.
12. Hatakeyama, Y.; Morita, T.; Takahashi, S.; Onishi, K.; Nishikawa, K. Synthesis of gold nanoparticles in liquid polyethylene glycol by sputter deposition and temperature effects on their size and shape. *J. Phys. Chem. C*, **2011**, *115*(8), 3279–3285.
13. Wender, H.; Oliveira, L.F.; Migowski, P.; Feil, A.F.; Lissner, E.; Prechtl, M.H.G.; Teixeira, S.R.; Dupont, J. Ionic Liquid Surface Composition Controls the Size of Gold Nanoparticles Prepared by Sputtering Deposition. *J. Phys. Chem. C*, **2010**, *114*(27), 11764–11768.
14. Ishida, Y.; Udagawa, S.; Yonezawa, T. Growth of sputtered silver nanoparticles on a liquid mercaptan matrix with controlled viscosity and sputter rate. *Colloids Surf.*, **2016**, *498*, 106–111.
15. Nakagawa, K.; Narushima, T.; Udagawa, S.; Yonezawa, T. Preparation of copper nanoparticles in liquid by matrix sputtering process. *J. Phys. Conf.: Ser.*, **2013**, *417*, 012038.

16. Deng, L.; Nguyen, M.T.; Yonezawa, T. Sub-2 nm single-crystal Pt nanoparticles via sputtering onto a liquid polymer. *Langmuir*, **2018**, *34*, 2876–2881.
17. Okazaki, K.; Kiyama, T.; Hirahara, K.; Tanaka, N.; Kuwabata, S.; Torimoto, T. Single-step synthesis of gold–silver alloy nanoparticles in ionic liquids by a sputter deposition technique. *Chem. Commun.*, **2008**, 691–693.
18. Nguyen, M.T.; Zhang, H.; Deng, L.; Tokunaga, T.; Yonezawa, T. Au/Cu bimetallic nanoparticles via double-target sputtering onto a liquid polymer. *Langmuir*, **2017**, *33*(43), 12389–12397.
19. Deng, L.; Nguyen, M.T.; Mei, S.; Yokunaga, T.; Kudo, M.; Matsumura, S.; Yonezawa, T. Preparation and growth mechanism of Pt/Cu alloy nanoparticles by sputter deposition onto a liquid polymer. *Langmuir*, **2019**, *35*(25), 8418–8427.
20. Hirano, M.; Enokida, K.; Okazaki, K.; Kuwabata, S.; Yoshida, H.; Yorimoto, T. Composition-dependent electrocatalytic activity of AuPd alloy nanoparticles prepared via simultaneous sputter deposition into an ionic liquid. *Phys. Chem. Chem. Phys.*, **2013**, *15*, 7286–7294.
21. Omidvar, A.; RashidianVaziri, M.R.; Jaleh, B.; PartoviShabestari, N.; Noroozi, M. Metal-enhanced fluorescence of graphene oxide by palladium nanoparticles in the blue–green part of the spectrum. *Chin. Phys. B*, **2016**, *25*(11), 118102.
22. Eberhardt, W.; Fayet, P.; Cox, D.M.; Fu, Z.; Kaldor, A.; Sherwood, R.; Sondericker, D. Photoemission from mass-selected monodispersed Pt clusters. *Phys. Rev. Lett.*, **1990**, *64*(7), 780–783.
23. Nguyen, M.T.; Yonezawa, T.; Wang, Y.; Tokunaga, T. Double target sputtering into liquid: A new approach for preparation of Ag–Au alloy nanoparticles. *Mater. Lett.*, **2016**, *171*, 75–78.

24. Bragg, W.L. The early history of intensity measurements. *Acta Crystallogr.*, **1969**, A25, 1–3.

25. Vegard, L. Zeitchrift for Physik a Hadrons and Nuclei. *Z. Phys.*, **1921**, *5*(1), 17–26.

26. Wertheim, G.K.; DiCenzo, S.B.; Youngquist, S.E. Unit charge on supported gold clusters in photoemission final state. *Phys. Rev. Lett.*, **1983**, *51*(25), 2310–2313.

27. Eberhardt, W.; Fayet, P.; Cox, D.M.; Fu, Z.; Kaldor, A.; Sherwood, R.; Sondericker, D. Photoemission from mass-selected monodispersed Pt clusters. *Phys. Rev. Lett.*, **1990**, *64*(7), 780–783.

28. Vijayakrishnan, V.; Chainani, A.; Sarma, D.D., Rao, C.N.R. Metal-insulator transitions in metal clusters: a high-energy spectroscopy study of palladium and silver clusters. *J. Phys. Chem.*, **1992**, *96*(22), 8670–8682.

29. Richter, B.; Kuhlenbeck, H.; Freund, H.-J.; Bagus, P.S. Cluster core-level binding-energy shifts: the role of lattice strain. *Phys. Rev. Lett.*, **2004**, *93*(2), 026805.

30. Deng, L.; Lin, F.; Yu, Q.; He, X.; Liu, A.; Shi, W.; Feng, J. Improved ferromagnetic behavior and novel near-infrared photoluminescence in Mg/Mn-codoped $CuCrO_2$ ceramics. *J. Mater. Sci.*, **2016**, *51*, 7491–7501.

31. Briggs, D. *Handbook of X-ray and ultraviolet photoelectron spectroscopy*, Heyden & Son Ltd, London, **1977**.

32. Sundaram, V.S.; Moraes, M.B.; Rogers, J.D.; Kleiman, G.G. X-ray photoemission lineshapes and energies in PdxCu1-x. *J. Phys. F: Met. Phys.*, **1981**, *11*, 1151–1157.

33. Chen, D.; Sun, P.; Liu, H.; Yang, J. Bimetallic Cu–Pd alloy multipods and their highly electrocatalytic performance for formic acid oxidation and oxygen reduction. *J. Mater. Chem. A*, **2017**, *5*, 4421–4429.

34. Castegnaro, M.V.; Gorgeski, A.; Balke, B.; Alves, M.C.M.; Morais, J. Charge transfer effects on the chemical reactivity of Pd_xCu_{1-x} nanoalloys. *Nanoscale*, **2016**, *8*, 641–647.

35. Olovsson, W.; Göransson, C.; Pourovskii, L.V.; Johansson, B.; Abrikosov, I.A. Core-level shifts in fcc random alloys: A first-principles approach. *Phys. Rev. B: Condens. Matter Mater. Phys.*, **2005**, *72*, 064203.

36. Harikumar, K.R.; Ghosh, S.; Rao, C.N.R. X-ray Photoelectron Spectroscopic Investigations of Cu−Ni, Au−Ag, Ni−Pd, and Cu−Pd Bimetallic Clusters. *J. Phys. Chem. A*, **1997**, *101*(4), 536–540.

37. Lopez-Salido, I.; Lim, D.C.; Kim, Y.D. Ag nanoparticles on highly ordered pyrolytic graphite (HOPG) surfaces studied using STM and XPS. *Surf. Sci.*, **2005**, *588*, 6–18.

38. Noborikawa, J.; Lau, J.; Ta, J.; Hu, S.; Scudiero, L.; Derakhshan, S.; Ha, S.; Haan, J.L. Palladium-copper electrocatalyst for promotion of oxidation of formate and ethanol in alkaline media. *Electrochim. Acta*, **2014**, *137*, 654–660.

39. Mårtensson, N.; Nyholm, R.; Calén, H.; Hedman, J.; Johansson, B. Electron-spectroscopic studies of the CuxPd1-x alloy system: Chemical-shift effects and valence-electron spectra. *Phys. Rev. B: Condens. Matter Mater. Phys.*, **1981**, *24*(4), 1725–1738.

40. Gabrielli, C.; Mocoteguy, P.; Perrot, H.; Zdunek, A.; Nieto-Sanz, D. Influence of the anode on the degradation of the additives in the damascene process for copper deposition. *J. Electrochem. Soc.*, **2007**, *154*(3), D163–D169.

41. Morimoto, A.; Okazaki, K.; Kuwabata, S.; Torimoto, T. presented in oart at ECS Meeting, Hawaii, October, **2012**. ECS Meeting Abstracts: http://ma.ecsdl.org/content/MA2012-02/53/3666.short. accessed October 2019.

42. Richter, K.; Birkner, A.; Mudring, A.V. Stabilizer-free metal nanoparticles and metal–metal oxide nanocomposites with long-term stability prepared by physical vapor deposition into ionic liquids. *Angew. Chem., Int. Ed.*, **2010**, *49*, 2431–2435.
43. Strunskus, T.; Kiene, M.; Willecke, R.; Thran, A.; Bechtolsheim, C.V.; Faupel, F. Chemistry, diffusion and cluster formation at metal-polymer interfaces. *Mater. Corros.*, **1998**, *49*, 180–188.
44. Kariuki, N.N.; Wang, X.; Mawdsley, J.R.; Ferrandon, M.S.; Niyogi, S.G., Vaughey, J.T.; Myers, D.J. Colloidal synthesis and characterization of carbon-supported Pd− Cu nanoparticle oxygen reduction electrocatalysts. *Chem. Mater.*, **2010**, *22*(14), 4144–4152.
45. Garzón-Manjón, A.; Meyer, H.; Grochla, D.; Löffler, T.; Schuhmann, W.; Ludwig, A.; Scheu, C. Controlling the amorphous and crystalline state of multinary alloy nanoparticles in an ionic liquid. *Nanomaterials*, **2018**, *8*(11), 903.

CHAPTER 3

Degradation of Shell Thickness-Tunable Au@Cu_2O Core-Shell Nanoparticles in Aqueous Solution

3.1 Introduction

Recent technological developments have made terahertz (THz) wave to be used in lots of fundamental studies and practical applications such as broadband communication, homeland security and medical imaging.[1-3] Development of THz wave source has accelerated in terms of higher output intensity, wider spectral generation and compact in size and at low cost. Huang *et al*. found a water film could generate both THz wave and X-ray under femtosecond laser excitation and the THz wave emission can be enhanced through dispersing ZnTe colloids in water.[4-5] The integration of the THz wave technology and nanomaterials is worthwhile. Thus, the colloidal aqueous dispersion is of interest for developing new source for THz wave.

As discussed in chapter 1, metal/semiconductor interface leads to terahertz (THz) wave emission applications. With the reports by Huang *et al*., metal@semiconductor core-shell nanoparticles (NPs), which consist of metal-semiconductor interface, also possibly enhance THz wave emission as like as ZnTe.[4-5]

Au@Cu_2O is hereby chosen because Au core is stable, and the Cu_2O shell recently becomes an attractive THz wave source.[6-10] With the enhancement of the localized surface plasmon resonance (LSPR) of Au, Au@Cu_2O core-shell NPs are expected to be useful in terahertz wave emission. The synthetic route of Au@Cu_2O core-shell NPs is relatively easy. It is because there is small lattice mismatches between the lattice planes of (111) for Au and (200) for Cu_2O, which leads the epitaxial growth of Cu_2O on the surface of Au cores.[11-12] This approach does not require any ligand to control the particles' sizes and it is beneficial to the THz wave emission. It is because the commonly used ligands in NPs syntheses are usually organic, which possibly absorb the THz wave emitted from the NPs.

However, the chemical stability of Au@Cu_2O core-shell NPs in water should be evaluated before applying them since Huang *et al.* found the degradation of ZnTe colloids after several tests of THz wave emission.[5] This chapter presents a facile synthesis method of synthesizing Au@Cu_2O core-shell NPs. The Cu_2O shell thickness was controllable from 2 to 40 nm by adjusting the concentration of Cu precursor during the synthesis. Characteristic UV-Vis absorption bands of Au@Cu_2O NPs dispersed in ethanol/water mixed solvent were monitored in 14 days, and to evaluate whether the Au@Cu_2O NPs in aqueous solution suit for the THz wave emission test.

3.2 Experimental

3.2.1 Materials

Anhydrous copper (II) chloride ($CuCl_2$, 95%, Wako, Japan), hydrogen tetrachloroaurate (III) trihydrate ($HAuCl_4 \cdot 3H_2O$, 99.5%, Kanto, Japan), trisodium citrate dihydrate (SC, 99.99%, Wako), sodium dodecyl sulfate (SDS, 97 %, Junsei, Japan), sodium hydroxide (NaOH, 97%, Junsei), hydroxylamine hydrochloride ($NH_2OH \cdot HCl$, 98%, Kanto), and ethanol (99.5%, Wako) were used as received. Water used in experiments was purified using a PureLabo system (Organo/ELGA, resistivity > 18.2 MΩ).

3.2.2 Synthesis of Au NPs

Spherical Au NPs were synthesized using the Turkevich method. Briefly, 500 mL of 0.5 mM $HAuCl_4$ (0.1030 g) aqueous solution was heated to boiling in a 1 L Erlenmeyer flask with stirring at 1000 rpm. A pre-heated 25 mL of SC solution (0.25 g, 1 wt.%) was added to the $HAuCl_4$ solution rapidly. The mixture was boiled for 15 min then cooled down to room temperature (25 °C) naturally prior to use.

3.2.3 Synthesis of Au@Cu_2O core-shell NPs

Figure 3.1 illustrates the steps of making Au@Cu_2O core-shell NPs. 25 mL of 0.1 M $CuCl_2$ aqueous solution, 25 mL of SDS aqueous solution (80 g/L), 50 mL of 1 mM Au NP solution, and 6.3 mL of 1 M NaOH solution were sequentially added into 164 mL of DI water with vigorous stirring, followed by ultrasonication for 1 min. Then, 5 mL of 0.2 M $NH_2OH{\cdot}HCl$ solution was injected into the solution, that was further stirred at 400 rpm for another 1 h for the formation of Au@Cu_2O core-shell NPs. Eventually, the solution was centrifuged at 10000 rpm for 5 min. After the supernatant was decanted, the precipitates were washed with ethanol three times using centrifugation (10000 rpm, 5 min).

2.2.4 Characterization

UV-Vis absorption spectra were measured using a JASCO V-630 spectrophotometer. The size distribution based on the dynamic light scattering (DLS) technique and zeta potentials of obtained NPs samples were obtained by using a zeta-potential and particle size analyzer (Photal Otsuka Electronics, ELSZ-1000ZS). The morphologies of core-shell NPs were observed using transmission electron microscope (TEM, JEOL JEM-2000FX, 200 kV) and scanning electron microscope (SEM, JEOL

JSM-6700F, 15 kV). The high-resolution transmission electron microscope (HRTEM) images were taken by using a high-resolution field-emission gun scanning TEM (STEM, JEM-ARM200F Cold, JEOL) operated at 200 kV. The X-ray diffraction (XRD) patterns were collected by using a Rigaku Miniflex II X-ray diffractometer with the Cu Kα radiation, λ = 1.5418 Å as the source.

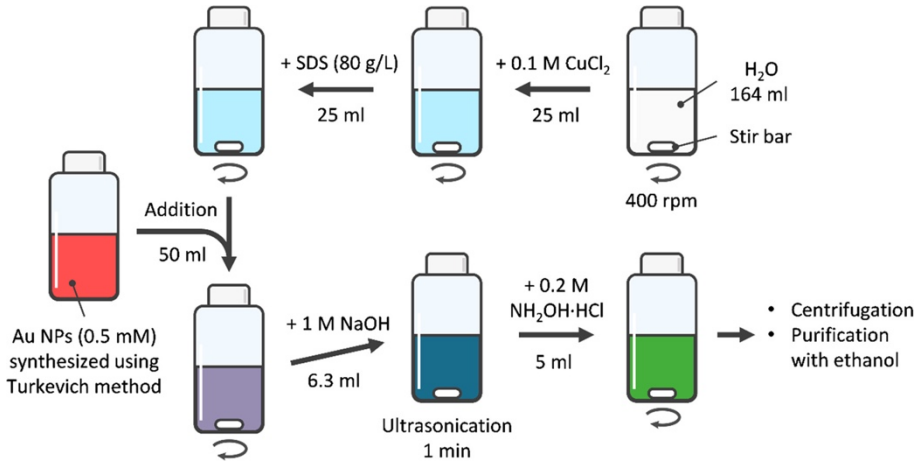


Figure 3.1 Procedure of synthesizing Au@Cu_2O core-shell NPs.

3.3 Results and Discussion

3.3.1 Formation of Au@Cu_2O core-shell NPs

Figure 3.2 shows TEM image, size distribution, and UV-Vis absorption spectrum of Au NPs that were used as the core. **Figure 3.3** is the visual image of solution for showing the colour change during the synthesis. Cu_2O was formed by reducing $Cu(OH)_2$ to Cu_2O with $NH_2OH \cdot HCl$. Generally, core-shell NPs with bimetallic heterostructures can only formed when two metals have lattice well-matched to each other.[13-14] The formation of Cu_2O shell on the Au NPs was owing to small lattice mismatch between Cu_2O and Au, so that Cu_2O could grow uniformly on the surface of Au NPs.

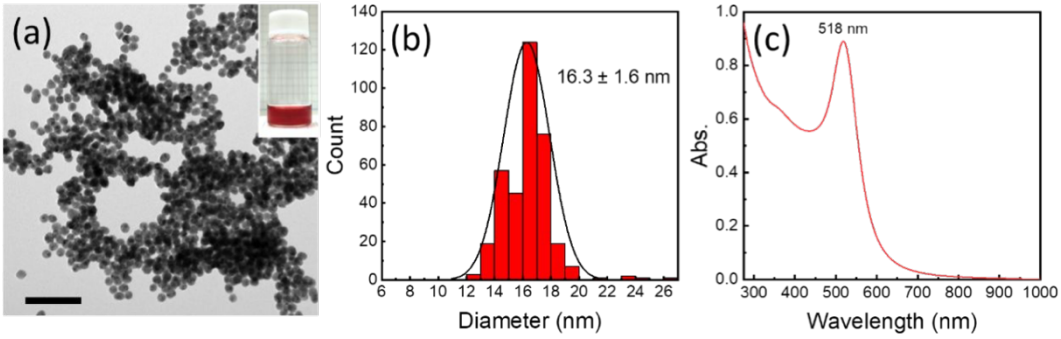


Figure 3.2 (a) TEM image with scale bar 100 nm. Inset is the photo of solution. (b) size distribution and (c) UV-Vis absorption spectrum as-synthesized Au NPs.



Figure 3.3 Color change in the synthesis of Au@Cu_2O NPs.

Analysis on a single Au@Cu_2O core-shell NP captured by high-angle annular dark-field STEM (HAADF-STEM) image (**Figure 3.4**a) shows the Cu_2O shell surrounded the central Au core. The bright-field TEM image (**Figure 3.4**b) indicates the diffraction contrast in the shell area, that is the polycrystalline Cu_2O shell. The HRTEM image (**Figure 3.4**c) was captured at the interface of the Au core and the Cu_2O shell. The interplanar spacing of Au core was 2.32 Å, matched with the *d*-spacing of Au (111) plane. It was parallel to the (111) lattice planes of the Cu_2O shells, which had interplanar spacing of 2.46 Å. The image shows the good epitaxial growth of Cu_2O on Au. Moreover, the spots in the fast Fourier transform (FFT) pattern (**Figure 3.4**d) were attributed to the (111), (200), and (311) reflections of cubic structured Cu_2O and also the (111) reflection of face-centered cubic structured Au.

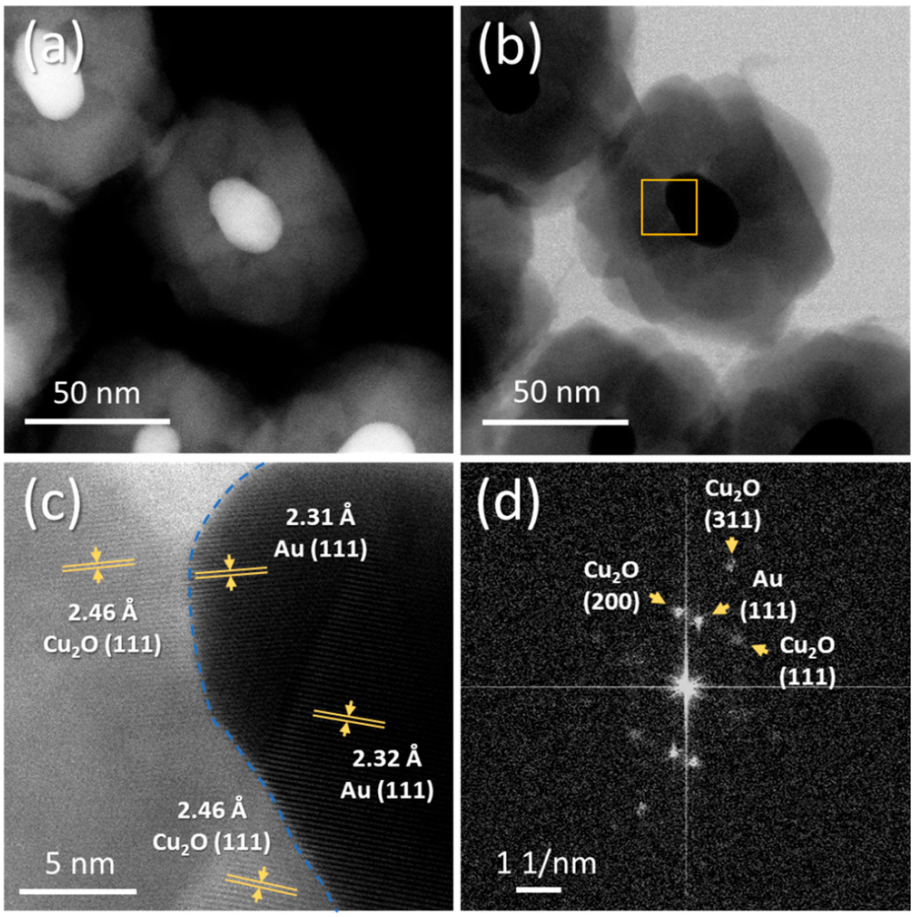


Figure 3.4 (a) HAADF-STEM and (b) TEM images of Au@Cu_2O core-shell NPs. (c) HRTEM image taken at the interface of Cu_2O shell and Au core labeled in (b). (d) Fast Fourier Transform (FFT) of the image in (c).

3.3.2 Tunable Cu_2O shell thickness

XRD patterns of Cu_2O and Au@Cu_2O NPs are shown in **Figure 3.5**. The diffraction peaks at 29.6°, 36.4°, 42.3°, 61.3°, 73.7°, and 77.6° were attributed to the (110), (111), (200), (220), (311), and (222) planes of Cu_2O. The crystalline size of Cu_2O was 38.5 nm, which was calculated using Scherrer's equation with taking the full width at half

maxima (FWHM) of the main peak located at 36.4°. The crystalline size of Cu_2O was close to the Cu_2O shell thickness measured from TEM image (35.1 ± 4.0 nm). XRD pattern of Au@Cu_2O matches with that of Cu_2O, but a small peak contributed by the Au core was found at 38.2°.

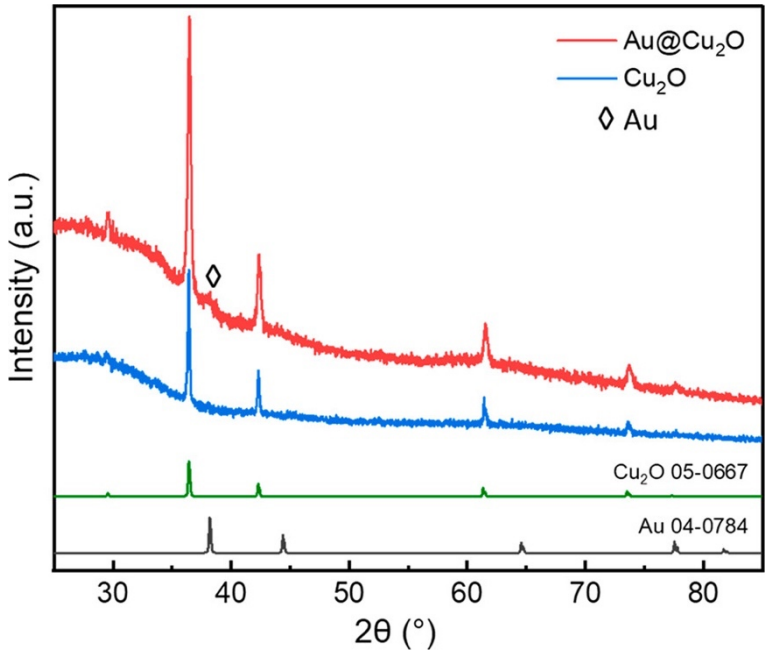


Figure 3.5 XRD patterns of as-synthesized Au@Cu_2O core-shell NPs and Cu_2O. Standard patterns of Cu_2O (JCPDS no. 05-0667) and Au (JCPDS no. 04-0836) for reference.

The shell thickness of Cu_2O can be controlled over the range of 2-35 nm by varying the concentration of $CuCl_2$ solution during the synthesis. When $CuCl_2$ was dissolved in the alkaline medium, $Cu(OH)_2$ colloids formed. These colloids were reduced by $NH_2OH{\cdot}HCl$ to form Cu_2O. The more $Cu(OH)_2$ colloids, the thicker Cu_2O shell can be obtained. **Figure 3.6**a-d shows the TEM images of Au@Cu_2O core-shell NPs synthesized using different concentration of $CuCl_2$ aqueous solution – 100, 10, 2, and 1 mM, respectively (named in order as Au@Cu_2O-100, Au@Cu_2O-10, Au@Cu_2O-2, and Au@Cu_2O-1). The shell thickness of Cu_2O increased with the concentration of $CuCl_2$ in the solution. The colours of the solution containing Au@Cu_2O NPs with different Cu_2O shell thicknesses were distinct. The Cu_2O shell thickness was determined by subtracting the overall diameter of the NP by the diameter of the Au core. The average shell thickness of Au@Cu_2O NPs were 2.1, 4.6, 16.6, and 35.1 nm with increasing the concentration of $CuCl_2$ solution (**Figure 3.6**e-h). Moreover, the Au core was fully encapsulated in all NPs in the Au@Cu_2O-100 sample and Au@Cu_2O-10. Alternatively, thin Cu_2O shells with irregular shapes were observed in Au@Cu_2O-2 and Au@Cu_2O-1 samples and even part of the surfaces of the Au cores were not encapsulated by Cu_2O.

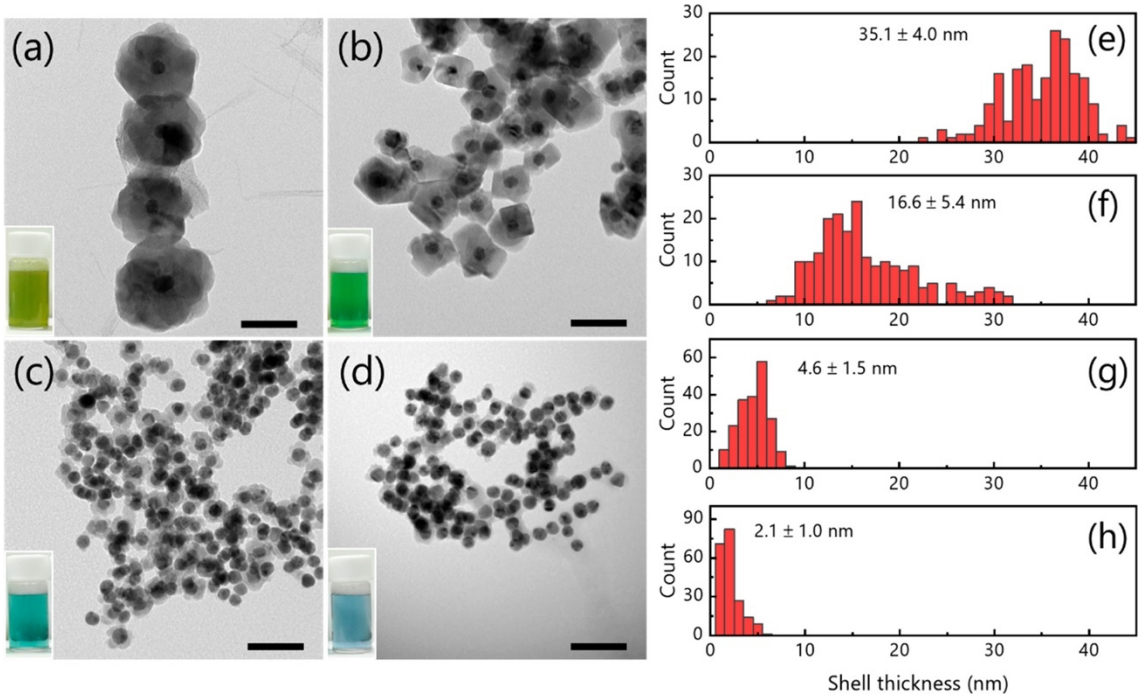


Figure 3.6 TEM images with scale bar 50 nm of as-synthesized Au@Cu_2O core-shell NPs named (a) Au@Cu_2O-100, (b) Au@Cu_2O-10, (c) Au@Cu_2O-2, and (d) Au@Cu_2O-1. The inset of each image shows the visual image of the solution with different Cu_2O shell thickness. (e-h) Size distributions of Cu_2O shell thickness correspond to (a-d).

3.3.3 Aggregations of Au@Cu_2O core-shell NPs

Although the visual images (**Figure 3.2** and insets of **Figure 3.6**) show no aggregation/precipitations appeared during the synthesis. Size distribution obtained from DLS (**Figure 3.7**) was larger than those of the individual particles shown in the corresponding TEM images, indicating the existence of aggregated clusters of Au@Cu_2O NPs. Also, the relatively small zeta potential (**Figure 3.8**) reveals that the Au@Cu_2O NPs were prone to aggregate with an extended storage time.

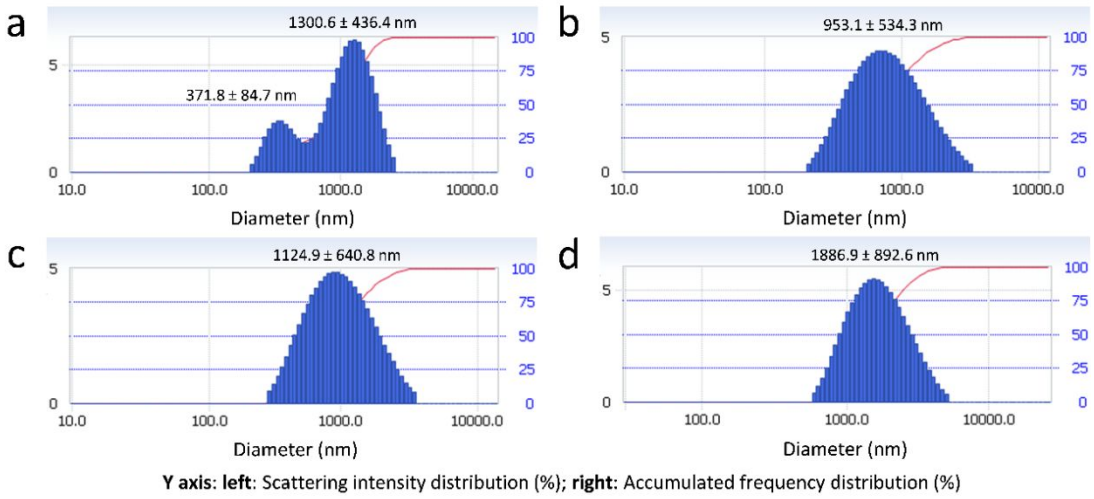


Figure 3.7 DLS results of as-synthesized Au@Cu_2O core-shell NPs: (a) Au@Cu_2O-100, (b) Au@Cu_2O-10, (c) Au@Cu_2O-2, (d) Au@Cu_2O-1 (Concentration: 0.1 mM (based on Au); Solvent: ethanol).

3.3.4 Optical properties of Au@Cu_2O core-shell NPs

The Au NPs had a surface plasmon resonance (SPR) absorption peak at 518 nm (**Figure 3.2**c). The SPR peak red-shifted when Cu_2O shell with different thickness formed on Au core from 518 nm to 574 nm (Au@Cu_2O-1), 641 nm (Au@Cu_2O-2), and 667 nm (Au@Cu_2O-10) (**Figure 3.8**). This was due to the increase in local dielectric constant resulted from the interfacial effect between the thicker Cu_2O shell and the Au core. The SPR absorption peak of Au NPs was not observed in the case of Au@Cu_2O-100, suggesting the Au core was fully encapsulated by Cu_2O shell. In other words, other three samples probably contain Au cores that were not completely encapsulated by Cu_2O shell and/or the Cu_2O shell was thin that the UV-Vis radiation could reach to the Au core in the measurement. Moreover, the absorption peaks at 381 nm and 455 nm were attributed to the interband transitions in Cu_2O and the scattering from the Cu_2O shell.[15] These absorption peaks had higher intensity with increasing Cu_2O shell thickness. In addition, Mie scattering also resulted in the higher absorbance at a wavelength below 500 nm for Au@Cu_2O-10 and Au@Cu_2O-100 samples.

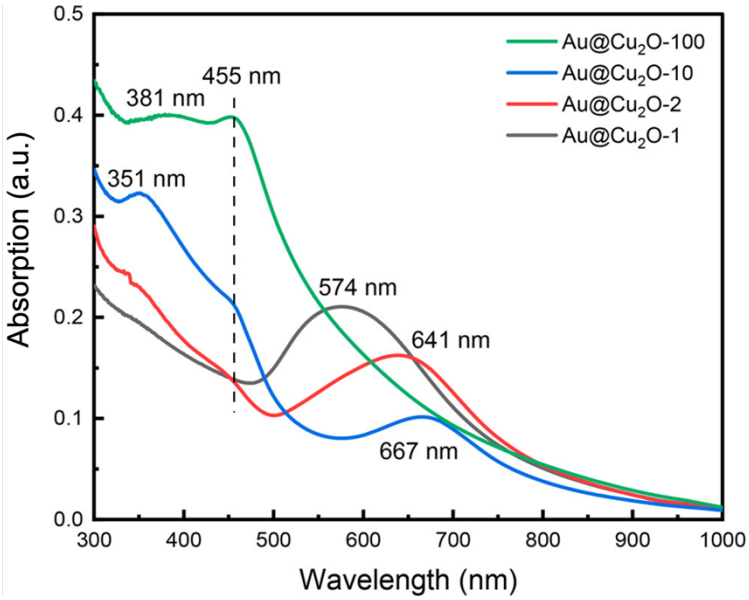
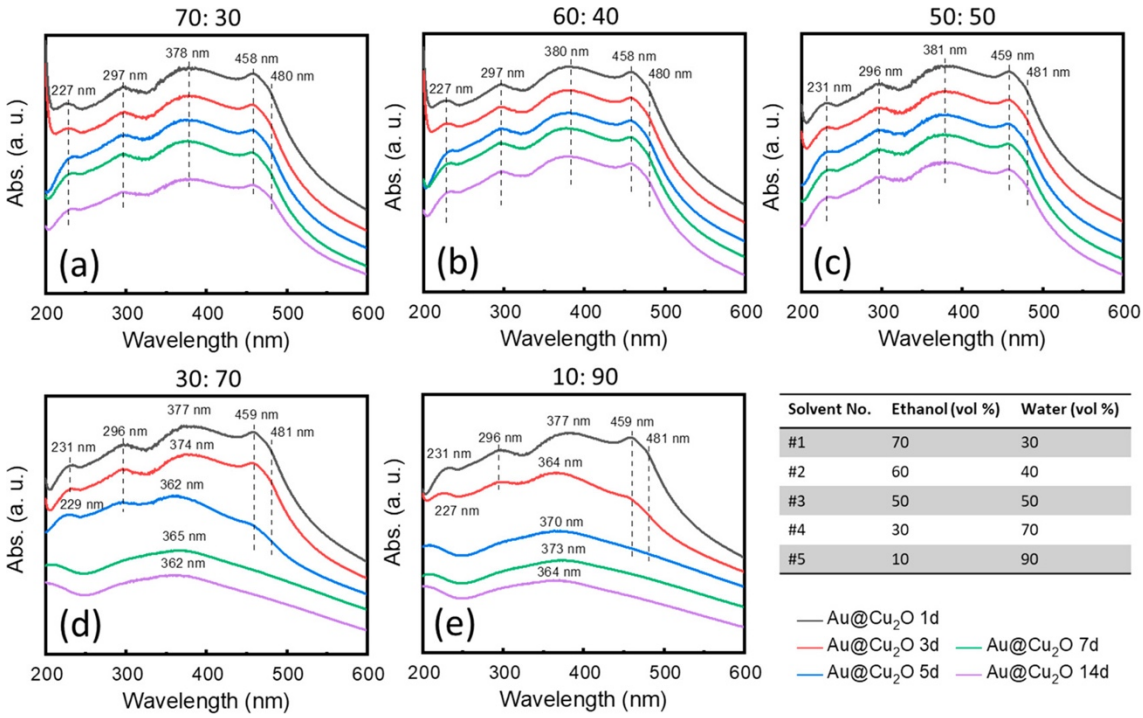


Figure 3.8 UV-Vis absorption spectra of as-synthesized Au@Cu_2O-100, Au@Cu_2O-10, Au@Cu_2O-2, and Au@Cu_2O-1 core-shell NPs with decreasing Cu_2O shell thickness.

3.3.5 Stability of Au@Cu_2O core-shell NPs in water/ethanol mixed solvent

Au@Cu_2O core-shell NPs were dispersed in aqueous solvent, ethanol/water mixed solvents with various compositions (ethanol/water vol/vol in mL) of 70:30 (#1), 60:40 (#2), 50:50 (#3), 30:70 (#4), and 10:90 (#5). These dispersions were kept at room temperature. **Figure 3.9** shows the Au@Cu_2O-100 NPs dispersed in ethanol/water mixed solvents had characteristic absorption peak at 230, 296, 380, 458, and 480 nm in all solvent compositions. In the solvents of < 50 vol % water content (#1, #2, and #3), all of the characteristic absorption peaks of Au@Cu_2O were preserved for 14 days without any changes (**Figure 3.9**a-c). In solvent #4, the characteristic absorption peak became weaker

after 5 days and disappeared after 7 days, leaving a broad absorption band with the maximum at about 360 nm (**Figure 3.9**d). In solvent #5, the characteristic absorption peaks almost disappeared after 5 days, leaving a broad absorption band with the maximum at about 370 nm (**Figure 3.9**e). The absence of absorption peaks was attributed to the structure of Au@Cu_2O core-shell NPs had changed, or some reactions were taken place during the storage.



Solvent No.	Ethanol (vol %)	Water (vol %)
#1	70	30
#2	60	40
#3	50	50
#4	30	70
#5	10	90

Figure 3.9 UV-Vis absorption spectra of Au@Cu_2O-100 core-shell NPs suspensions after synthesis for 1, 3, 5, 7, and 14 days stored in ethanol/water mixed solvents with different compositions (ethanol/water, vol %) of (a) 70:30 – #1, (b) 60:40 – #2, (c) 50:50 – #3, (d) 30:70 – #4, (e) 10:90 – #5.

TEM images of Au@Cu_2O-100 sample stored in solvent #4 – with ethanol/water ratio 30:70 – were taken time by time (**Figure 3.10**). The morphologies of the Au@Cu_2O-100 NPs changed from a spherical shape to an irregular core-shell structure with multiple Au cores in 5 days. Then the Cu_2O shell aggregated with neighbor shells in 14 days, resulted in large aggregates of Cu_2O attached to multiple Au cores. The selected-area electron diffraction (SAED) pattern in the inset of **Figure 3.10**c has the diffraction signals of both CuO and Au, indicating the phase transformation from Cu_2O to CuO occurred.

For comparison, UV-Vis absorption spectra of Cu_2O NPs stored in solvent #4 show the SPR absorption of Cu_2O NPs diminished along with the storage time (**Figure 3.11**). The corresponding TEM images and SAED pattern (**Figure 3.12**) of the Cu_2O NPs stored for 30 days show the formation of CuO aggregates. Both Cu_2O and CuO were typical p-type semiconductors but former has direct band gap (2.1 eV) and latter has indirect band gap (1.2 eV).[8] The phase transformation from Cu_2O and CuO would change the properties of the NPs, and therefore challenges are remained to utilize Au@Cu_2O core-shell NPs in practical use.

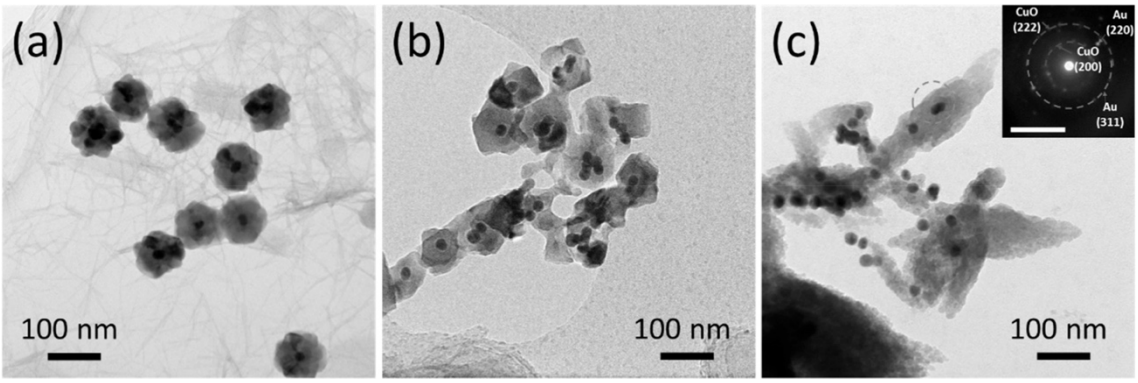


Figure 3.10 TEM images of (a) as-synthesized Au@Cu_2O core-shell NPs, (b) after 5 days, and (c) after 14 days in an ethanol/water mixed solvent with composition of 30:70 in vol% (#4). The inset in (c) is the SAED pattern of the region labeled by dashed circle in (c).

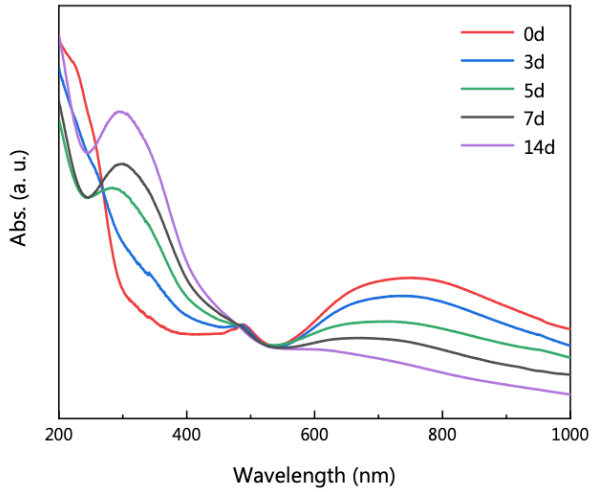


Figure 3.11 UV-Vis absorption spectra of Cu_2O NPs stored in ethanol/water mixed solvent with composition of 30:70 in vol% (solvent #4).

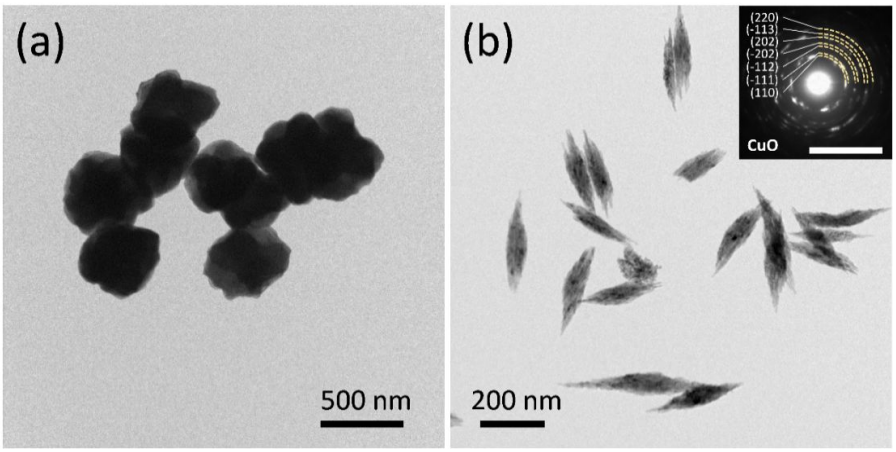


Figure 3.12 TEM images of (a) as-prepared Cu_2O particles and (b) Cu_2O particles dispersed in ethanol/water mixed solvent with composition of 30:70 in vol% for 30 days at room temperature.

3.4 Conclusion

Au@Cu_2O core-shell NPs with a tunable Cu_2O shell thickness of 2-40 nm were synthesized. The ethanol/water mixed solvent with high water content (>50 vol %) can deteriorate the chemical stability of the Au@Cu_2O core-shell NPs by oxidizing the Cu_2O shell to CuO. Although the Au@Cu_2O core-shell NPs can initially provide metal/semiconductor interface, the degradation leads the loss of unique properties of Cu_2O. The instability of Au@Cu_2O core-shell NPs in high water content solution brings the difficulties to apply them to the THz wave emission test mentioned in reference 5 because the THz wave emission set up requires NPs disperse in water.

3.5 References

1. Akyildiz, I.F.; Jornet, J.M.; Han, C. Terahertz band: Next frontier for wireless communications. *Phys. Commun*., **2014**, *12*, 16–32.
2. Liu, H.; Zhong, H.; Karpowicz, N.; Chen, Y.; Zhang, X. Terahertz Spectroscopy and Imaging for Defense and Security Applications. *Proc IEEE Inst. Electr. Electron Eng.*, **2007**, *95*(8), 1514–1527.
3. Fitzgerald, A.J.; Berry, E.; Zinovev, N.N.; Walker, G.C.; Smith, M.A.; Chamberlain, J.M. An introduction to medical imaging with coherent terahertz frequency radiation. *Phys. Med. Biol.*, **2002**, *47*, R67–R84.
4. Huang, H.; Nagashima, T.; Hsu, W.; Juodkazis, S.; Hatanaka, K. Dual THz Wave and X-ray Generation from a Water Film under Femtosecond Laser Excitation. *Nanomaterials*, **2018**, *8*(7), 523.
5. Huang, H.; Chau, Y.-t.R.; Yonezawa, T.; Nguyen, M.T.; Zhu, S.; Deng, D.; Nagashima, T.; Hatanaka, K. THz wave emission from ZnTe nano-colloidal aqueous dispersion irradiated by femtosecond laser. *Chem. Lett.*, **2020**, *49*(6), 597–600.
6. Lopez, J.; Café, A.; Husay, H. A.; Lopez, L.; Salvador, A.; Estacio, E.; Somintac, A. Terahertz emission from Cu_2O/PSi with Fabry-Perot mode at 800 nm. *Proc. Samahang Pisika ng Pilipinas* **2016**, *34*, SPP-2016-2A-06 2016.
7. Lu, X.; Yonezawa, T. Terahertz emission from Cu_xO/Au thin film. 2014 *MWP/APMP* **2014**, 164-165.
8. Lu, X.; Ishida, Y.; Mishina, T.; Nguyen, M. T.; Yonezawa, T. Enhanced Terahertz Emission from Cu_xO/Metal Thin Film Deposited on Columnar-Structured Porous Silicon. *Bull. Chem. Soc. Jpn.*, **2015**, *88*(10), 1385–1387.
9. Ramanandan, G. K. P.; Adam, A. J. L.; Ramakrishnan, G.; Petrik, P.; Hendrikx, R.;

Planken, P. C. M. Optical characterization of gold-cuprous oxide interfaces for terahertz emission applications. *Appl. Opt.* **2014**, *53*, 10, 1994-2000.

10. Ramakrishnan, G.; Ramanandan, G. K. P.; Adam, A. J. L.; Xu, M.; Kumar, N.; Hendrikx, R. W. A.; Planken, P. C. M. Enhanced terahertz emission by coherent optical absorption in ultrathin semiconductor films on metals. *Opt. Express* **2013**, *21*, 14, 16784-16798.
11. Rai, O.; Majhi, S.M.; Yu, Y.T.; Lee, J.H. Noble metal@metal oxide semiconductor core@shell nano-architectures as a new platform for gas sensor applications. *RSC Adv.*, **2015**, *5*(93), 76229–76248.
12. Chen, L.; Sun, H.; Zhao, Y.; Zhang, Y.; Wang, Y.; Liu, Y.; Zhang, X.; Jiang, Y.; Hua, Z.; Yang, J. Plasmonic-induced SERS enhancement of shell-dependent Ag@Cu_2O core-shell nanoparticles. *RSC Adv*, **2016**, *7*(27), 16553–16560.
13. Wang, Y.Q.; Nikitin, K.; McComb, D.W. Fabrication of Au-Cu_2O core-shell nanocube heterostructures. *Chem. Phys. Lett.*, **2008**, *456*(4-6), 202–205.
14. Kuo, C.-H.; Hua, T.-E.; Huang, M.H. Au Nanocrystal-Directed Growth of Au-Cu_2O Core-shell Heterostructures with Precise Morphological Control. *J. Am. Chem. Soc.*, **2009**, *131*(49), 17871–17878.
15. Mahmoud, M. A.; Qian, W.; El-Sayed, M. A. Following Charge Separation on the Nanoscale in Cu_2O–Au Nanoframe Hollow Nanoparticles. *Nano Lett.*, **2011**, *11*(8), 3285–3289.

CHAPTER 4

Relation between Oxidative Temperature and Intensity of THz Wave Emission of Copper Thin Films

4.1 Introduction

Studies of THz radiation are impelled by applications such as non-destructive examination[1-3], biological molecules detection[4-5] and broadband communication.[6-7] It is known that gallium arsenide (GaAs) is a promised THz source under ultrafast pulse laser irradiation.[8-10] The laser pulses accelerate charge carriers at the air/semiconductor interface, where the depletion field (also known as Schottky field) exists and develop a transient current as the source of THz radiation.[11-12] Although Cu_2O and Au@Cu_2O were suggested for enhancing THz wave emission of water in chapter 3, the application remains challenged due to the degradation of Cu_2O in aqueous solution. Therefore, aqueous-free thin film samples are proposed for evaluating the THz wave emission from Cu_2O and Au/Cu_2O interface in this chapter.

Several reports found the THz wave emission enhancement from Cu_2O, which was formed via oxidative annealing of Cu layer, on Au/Si substrate.[13-17] Ramakrishnan *et al.* demonstrated the THz wave emission intensity increased with the thickness of Cu_2O

layer. A 420nm-thick Cu_2O layer had the highest THz wave emission in their study. Such enhancement of THz radiation was due to more void spaces existed in a thicker layer, promoting laser absorption. They also found that Cu_2O films with thickness less than 100 nm, annealed at temperature of 250 °C for 3 h emitted almost no THz wave.[17] It is noted that the temperature for oxidizing a Cu film in air is an important factor since high temperature promotes the oxidation rate of Cu and influences the thickness, grain size and porosity of the oxide layer. We found different annealing temperatures (110 °C,[14-15] 220 °C,[16] 250 °C[17]) and annealing duration (2.5 h,[14-15] 3 h[16-17]) were used in different literatures for oxidizing the Cu film to Cu_2O as THz source, but there is no report regarding the effect of the oxidative annealing temperature of a Cu film at same annealing time to the THz wave emission intensity. The thickness of as-deposited Cu film in above mentioned literatures was also dissimilar to others.

This chapter reports the THz wave emission from annealed Cu film with respect to the annealing temperature on Si or Au/Si substrates. The Cu/Si or Cu/Au/Si structures were prepared by depositing metal films on Si substrate. The thicknesses of as-deposited Cu and Au films were controlled by precise magnetron sputtering deposition technique. These structures were oxidative annealed at temperature ranged from 80 to 300 °C for 2.5 h. Both structures had the highest THz wave emission intensity after annealing at

temperature of 80 °C for 2.5 h. THz wave emission decreased from Cu/Si or Cu/Au/Si structures by increasing the annealing temperature. The THz wave emission from annealed Cu film is owing to Cu_2O/Cu interface based on the findings of material characterization.

4.2 Experimental

4.2.1 Materials

Non-doped <100>-oriented Si wafers (ϕ50 mm, 280 μm-thick, ≥ 1000 Ω cm^{-1}, Global Top Chemical, Japan), Cu target (99.99% in purity, ϕ50 mm, Nilaco, Japan), Au target (99.99% in purity, ϕ50 mm, Tanaka Precious Metals, Japan) and ultra-high purity hydrofluoric acid (HF, concentration 48 %, Stella Chemifa, Japan) were used as received.

4.2.2 Preparation of oxidative annealed Cu/Si and Cu/Au/Si samples

Si wafers as the thin film substrates were cut into 1 cm^2 using a glass cutter. The wafers were immersed into acetone and washed with an ultrasonic bath for 5 min. The wafers were then put into 8% HF solution for 20 min to etch away the SiO_2 on the surface followed with UV-ozone cleaning prior to use.

Magnetron sputtering was used for metal film deposition. The Si wafer was placed in the sputtering chamber, positioned 60 mm away normal to the sputtered target surface. After 20 times of Ar (99.99% purity) purging and evacuation, the pressure of the chamber was set at 2 Pa with Ar as the carrying gas. 50 mA of current was firstly applied to the target and sputtering performed at the first 10 min was to etch away the oxides on the target surface. During the cleaning process, a mechanical shutter was used to cover the substrate to avoid depositing oxides on it. After that, sputtering current was set to 30 mA. Single layered Cu/Si was obtained via sputtering Cu for 25.5 min. For double layered Cu/Au/Si structure, Au was firstly sputtered for 6.5 min followed with sputtering Cu for 25.5 min. Samples were taken out from the sputtering chamber and were transferred to a muffle furnace for oxidative annealing process. Annealing temperature was set to 80, 110, 140, 170, 200, 250, 300 °C, respectively. The heating ramp rate was set to 0.5 °C min^{-1}. A thermocouple equipped with a data logger was insert nearby the sample to monitor the actual annealing temperature. The samples were kept in a desiccator prior to characterize.

4.2.3 Characterization

The crystal structure and oxidizing condition of samples before and after annealing were measured by X-ray diffractometer (XRD, Rigaku MiniFlex II, Cu Ka radiation, λ= 0.15418 nm, scanning range = 30 to 75°). Focus ion beam (FIB) was used to cut the cross-sections of Cu/Au/Si sample annealed at 110 °C, which were then observed under transmission electron microscope (TEM, JEOL JEM-2000FX, 200 kV).

4.2.4 THz wave emission measurement

Laser irradiation experiments for THz time-domain spectroscopy (TDS) were carried out in a usual manner. Femtosecond laser pulses (35 fs/transform-limited, 800 nm, 1 kHz, Mantis/Legend Elite HE USP, Coherent) were irradiated without focusing to the sample surface, which is held on a conventional mirror holder, with the incident angle of 45°. The incident laser energy was fixed at 0.14 mJ/pulse and the beam diameter was 8 mm. THz wave emission toward the reflection direction was transferred to a setup for electro-optic sampling with a <110>-oriented ZnTe single crystal (1-mm thick, Nippon Mining & Metals, Co. Ltd.). Measurements with lock-in detection were carried out with a chopper (3502, New Focus) and a lock-in amplifier (SR830, Stanford Research System), the effective laser repetition is 0.5 kHz. No apparent sample damages were recognizable

after the laser irradiation experiments. TDS signals were obtained, and THz wave emission spectra were calculated by discrete Fourier-transform (DFT) of the TDS signals. The optical path length from the sample surface to the ZnTe crystal is 70 cm. All the laser irradiation experiments were carried out in atmospheric pressure in air (23 °C with 40-50 % humidity). Sharp absorption lines observed in DFT spectra, at 0.55 THz for instance, are due to THz absorption by water components[18] in atmosphere.

4.3 Results and Discussion

4.3.1 Optical properties of prepared samples

Reflectance spectra of all samples prior to proceed THz wave emission test (**Figure 4.1**) reflected less than 10% of light at visible wavelengths. Variation of reflectance among samples was possibly due to the change in surface roughness due to annealing, or some dust particles were loaded on the sample surface. After annealing, samples appeared in different colors because Cu films at the surface had various oxidation degrees with respect to the annealing temperature. In overall, the absorption of 800 nm-wavelength femtosecond laser pulse occurred in all samples was expected.

4.3.2 Oxidation degree of Cu layer at different annealing temperatures

Figure 4.2 shows the XRD patterns (2θ range = 34 to 50°) of as-sputtered and annealed Cu/Si. The raw data were normalized by taking the intensity of Si (400) peak appeared at 2θ = 69° from the Si substrate as the highest point (not given in the figure) and the smallest value from the data as the lowest point. The as-sputtered Cu film had a broad peak located at 43.3° for the Cu (111) plane. The broad peak indicated that the crystalline size was small. The peak located at 36.4° in the pattern of (b) sample annealed at 80 °C represented the Cu_2O (111) plane. The XRD patterns clearly demonstrated that

oxidation of Cu to CuO involves two steps with increasing temperature:

1^{st} step: $4\ Cu + O_2 \rightarrow 2\ Cu_2O$

2^{nd} step: $2\ Cu_2O + O_2 \rightarrow 4\ CuO$

The formation of CuO requires more heat energy at the same annealing time under same ambient condition because CuO has greater enthalpy of fusion ($\Delta_f H^\circ_{Solid}$ = -156.06 kJ/mol) than Cu_2O does ($\Delta_f H^\circ_{Solid}$ = -170.71 kJ/mol).[19] The grains in Cu film also grew with raising temperature as the main peaks in the XRD had narrower full-width at half maxima (FDHM). The intensity of the Cu_2O (111) peak was increased relative to that of the Cu (111) peak by increasing the temperature from (b) 80 to (d) 140 °C. The intensities of the strongest peak of Cu and that of its oxides were used to estimate the relative content of Cu_2O (wt.%) in the film using the method by Hu *et al*.[20]:

$$\text{Relative content of } Cu_2O\ (\text{wt.}\%) = \frac{I_{Cu_2O}}{I_{Cu_2O} + I_{Cu}}$$

Table 4.1 lists the calculated Cu_2O content (wt.%) from the films annealed at 80, 110, and 140 °C. It should be noted that the as-deposited film contained lots of small grains which contributed to low and broad signals to the Cu and Cu_2O peaks in the XRD pattern of the as-sputtered and annealed films. Thus, the estimated Cu_2O contents listed in **Table 4.1** are approximated values. Raising the annealing temperature to (g) 250 °C resulted in both Cu_2O and CuO phases and only CuO phase existed at (h) 300 °C.[21-22] All

characteristic peaks became less broad as the annealing temperature increased due to the crystal growth under high temperature. On the other hand, the Cu film kept under ambient for 1 week (**Figure 4.3**) had the characteristic peak of Cu_2O (111) plane due to the oxidation behavior of Cu when it contacted with oxygen in the air.[23]

Table 4.1 The estimated amount of Cu_2O (wt.%) in the Cu film annealed at 80, 110 and 140 °C.

Condition	Cu_2O (wt.%)
80 °C, 2.5 h	47.0
110 °C, 2.5 h	49.0
140 °C, 2.5 h	52.6

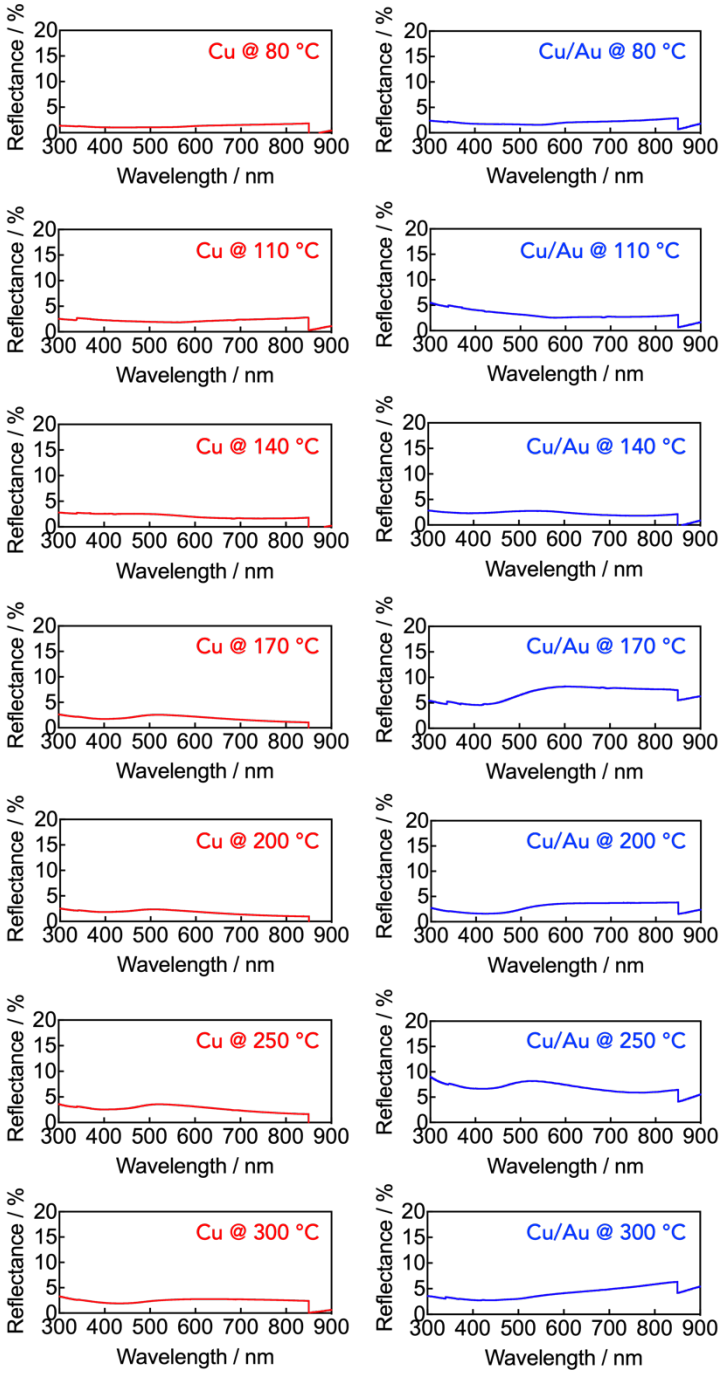


Figure 4.1 Reflectance spectra of Cu/Si and Cu/Au/Si samples at different annealing temperature.

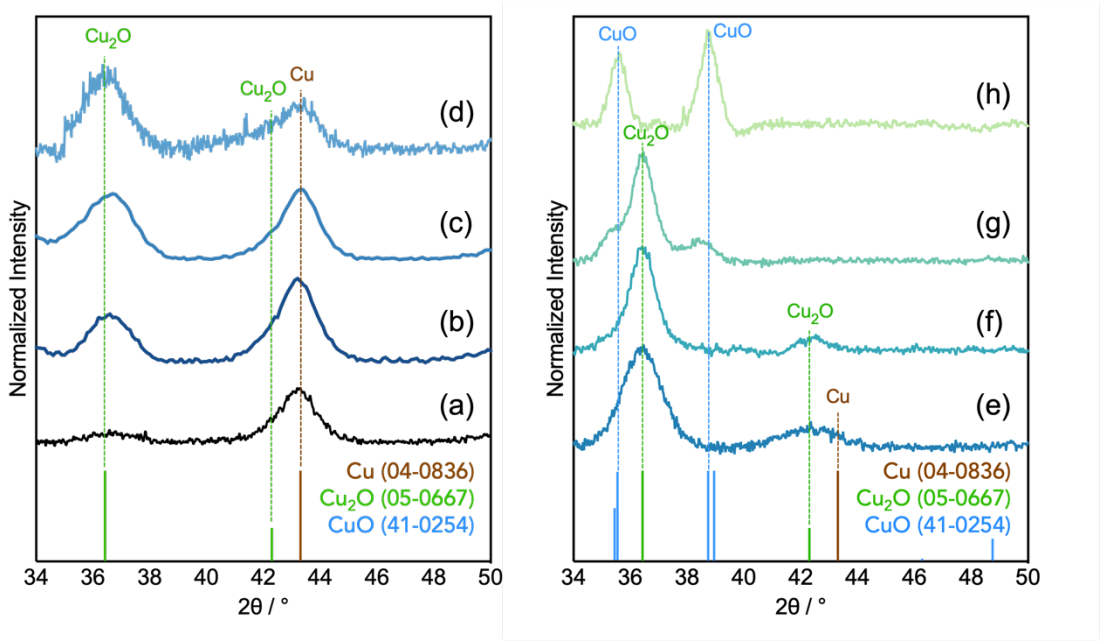


Figure 4.2 XRD patterns of Cu films at conditions of (a) as-sputtered, annealed at (b) 80, (c) 110, (d) 140, (e) 170, (f) 200, (g) 250 and (h) 300 °C.

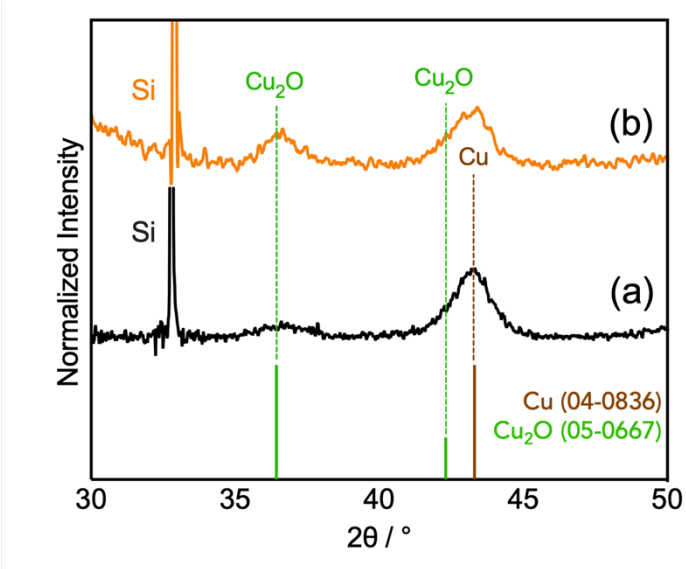


Figure 4.3 XRD patterns of (a) as-sputtered Cu film and (b) that being kept under ambient (25 °C) for one week.

4.3.3 Cu_2O in Cu layer

The cross-sectional image of Cu/Au double-layered structure on Si substrate annealed at 110 °C was captured by TEM (**Figure 4.4**a). Average thickness of Au layer was 54 nm and that of Cu layer was 80 nm. It should be noted that thicker Cu film was formed during the oxidative annealing. For instance, Ramanandan *et al.* reported that the thickness of Cu film was increased for 1.5 times when it was completely oxidized to Cu_2O from Cu at 220 °C for 3 h.[16] However, the film thicknesses in this study did not change much compared with the as-deposited film thickness reported by Xu *et al*. under the same film depositing condition.[14] Increase in thickness might have small significance under low temperature ($\leq$ 140 °C) conditions, which was agreed by the characteristic peaks in XRD patterns (**Figure 4.2**a-d) that did not have large variation in the grain sizes at $\leq$ 140 °C. A selected area electron diffraction (SAED) pattern (**Figure 4.4**c) was taken at the uppermost surface of the Cu layer (red circle (b) in **Figure 4.4**a). The diffraction rings were indexed as Cu_2O (111), (200), (220), and (311) planes (JCPDS No. 005-0667). Then, SAED pattern was taken at the area having both Cu and Au layers (red circle (d) in **Figure 4.4**a) and the diffraction rings of Cu (111) (JCPDS No. 004-0836) and Au (111), (200), (220) and (311) (JCPDS No. 041-0254) were observed (**Figure 4.4**e). The SAED results suggested that the Cu_2O was at the uppermost surface of Cu layer and the structure could

be denoted as "Cu_2O/Cu/Au" and it was the evidence of oxide layer migrates from the top to bottom of Cu film.

Electron energy loss spectroscopy (EELS) was performed to precisely determine the thickness of Cu_2O formed on the Cu layer after heating. **Figure 4.5**a-c shows cross-sectional TEM image of Cu/Au/Si heated at 80 °C. EELS spectra were taken throughout the region marked with the green line. The distance at the spectrum that contains oxygen peak at about 513 eV to the spectrum that without oxygen peak was defined as the thickness of Cu_2O (**Figure 4.5**d-e). The average thickness of Cu_2O was about 9 nm. Furthermore, the total thickness of Cu layer after annealing at 80 °C was 71 ± 2 nm. It can be considered that the as-deposited Cu layer would have thickness about 60 nm.

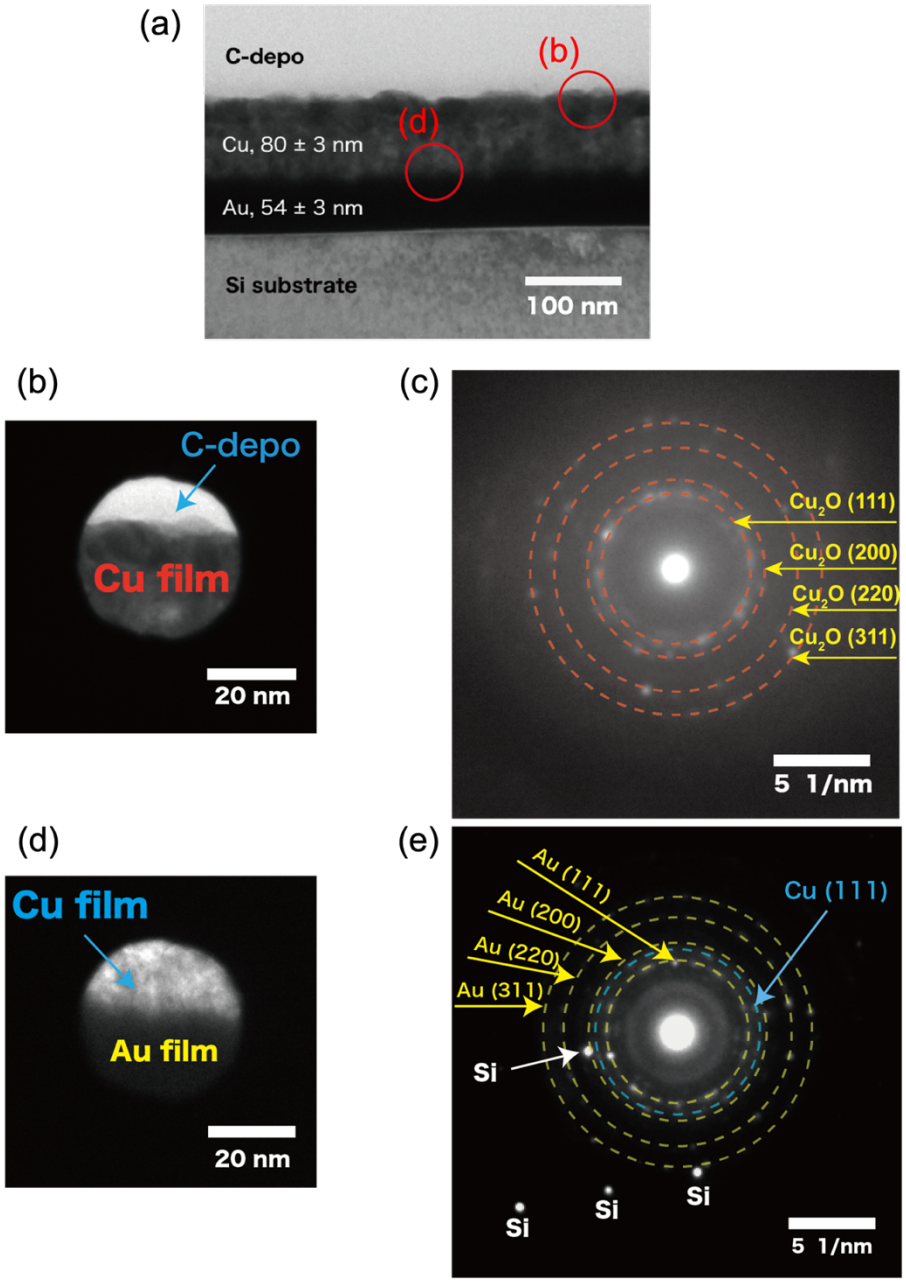


Figure 4.4 (a) TEM image of the cross-sectional Cu/Au/Si structure annealed at 110 °C for 2.5 h. (b) and (d) are selected area of taking diffraction patterns of (c) Cu film and (e) interface of Cu and Au films.

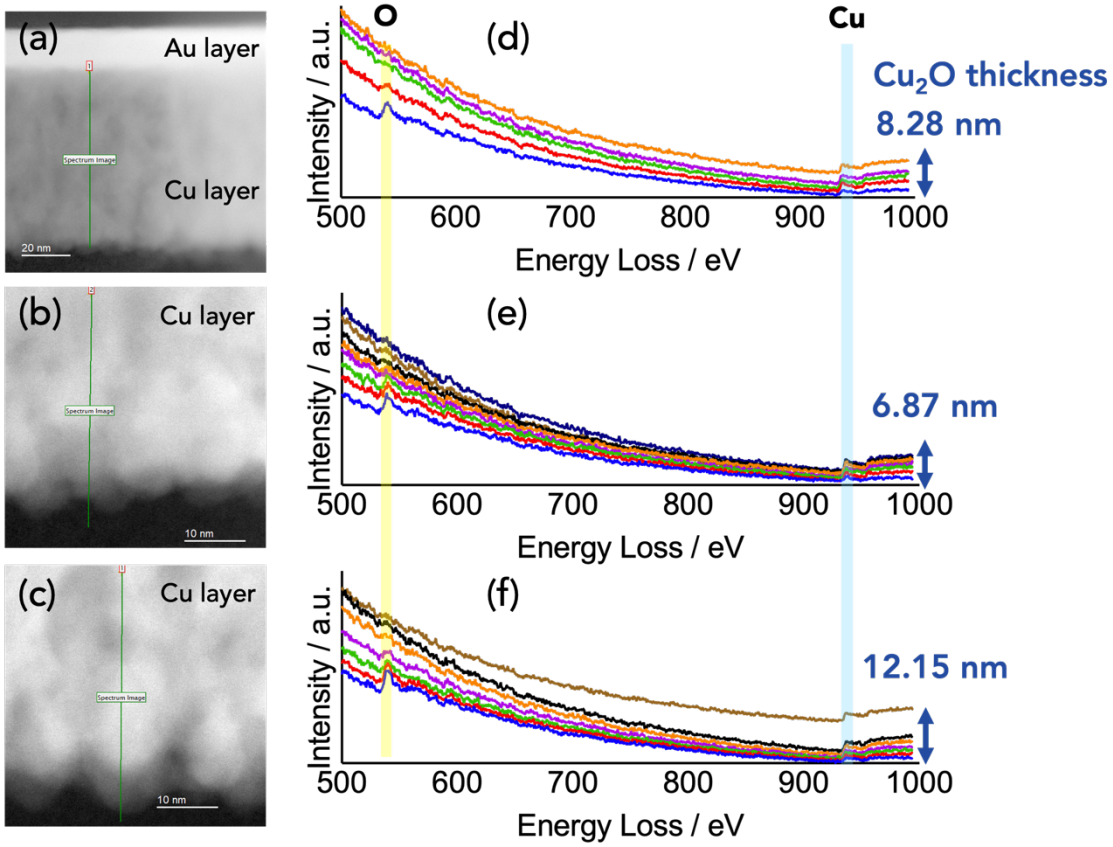


Figure 4.5 (a-c) TEM image of Cu/Au/Si heated at 80 °C taken at different regions. Green line indicates the scan region of (d-e) corresponding EELS spectra. Only spectra that can identify Cu_2O thickness are displayed in the EELS spectra.

4.3.4 Cu_2O/Cu interface as THz wave source

Figure 4.6 shows the TDS signals spectra measured from (a) bare Si wafer and (b) ZnTe <110> single crystals for comparison. Almost zero THz was emitted from a bare Si wafer via femtosecond laser excitation.

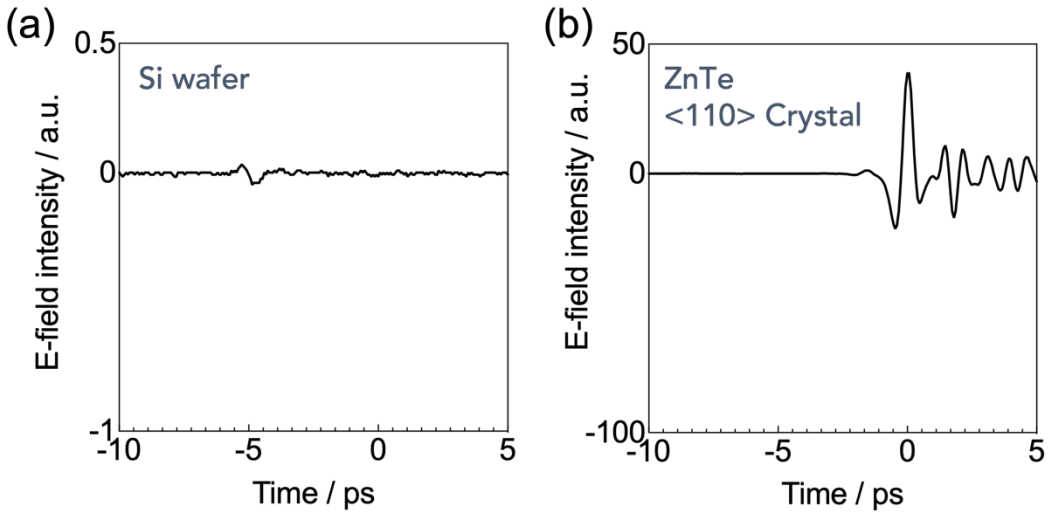


Figure 4.6 THz-TDS measurement of (a) bare Si wafer and (b) ZnTe <110> single crystal.

Figure 4.7 includes TDS signals and DFT spectra measured from Cu/Si structures treated with different annealing temperatures. Cu/Si annealed at 80 °C had the highest intensity of THz wave emission among samples. The intensity of the emission decreased steadily from samples treated at temperatures ranged from 110 to 140 °C. The emission was almost zero from samples treated at temperatures ≥ 170 °C. Similar

findings were given by Cu/Au/Si structures (**Figure 4.8**). In accordance with the XRD results, only samples that contain both Cu_2O and Cu emitted THz wave. THz wave emission was attributed to the Cu_2O/Cu interface in the samples annealed at 80, 110, 140 °C regardless to the existence of Au layer. It was because a depletion region was existed in the Cu_2O/Cu interface. A depletion region is formed when a metal with a lower work function (Φ_{Cu} = 4.7 eV[24]) was in contact with a p-type semiconductor that had a higher work function (Φ_{Cu_2O} = 4.84 eV[24,25]). An internal electric field was formed in the depletion region because of charge carriers (electrons and holes) are staying statically at the boundary of the region. When an ultrafast optical pulse irradiated samples, charge carriers interacted with the incident photon and moved to the depletion region. Those charge carriers accelerated within the internal electric field and generated a picosecond-scale transient current (also called drift current) – that is the source of THz wave (**Figure 4.9**).[26-27]

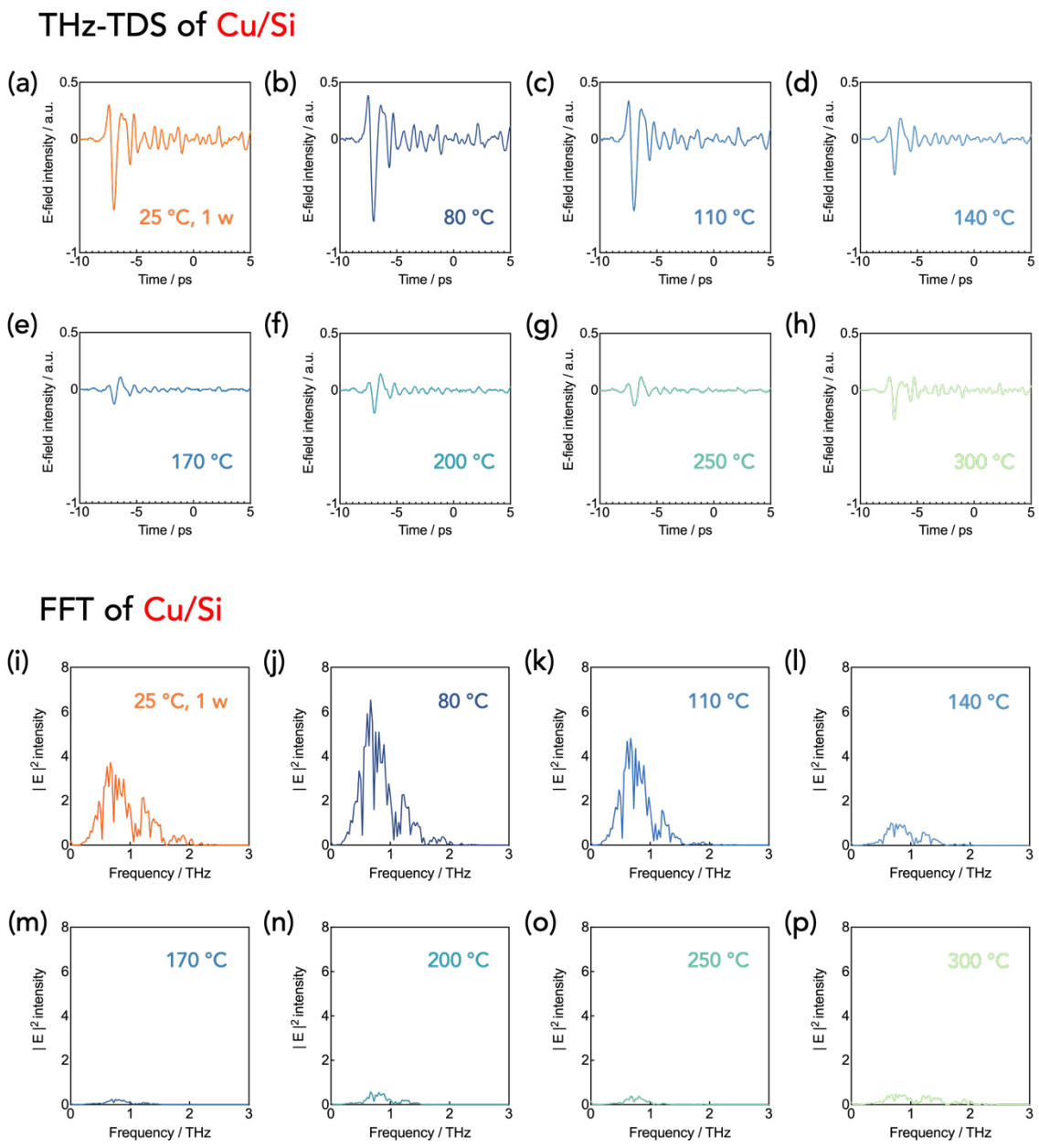


Figure 4.7 (a-h) THz-TDS and (i-p) corresponding FFT treated emission spectra of Cu/Si structures annealed at different temperatures.

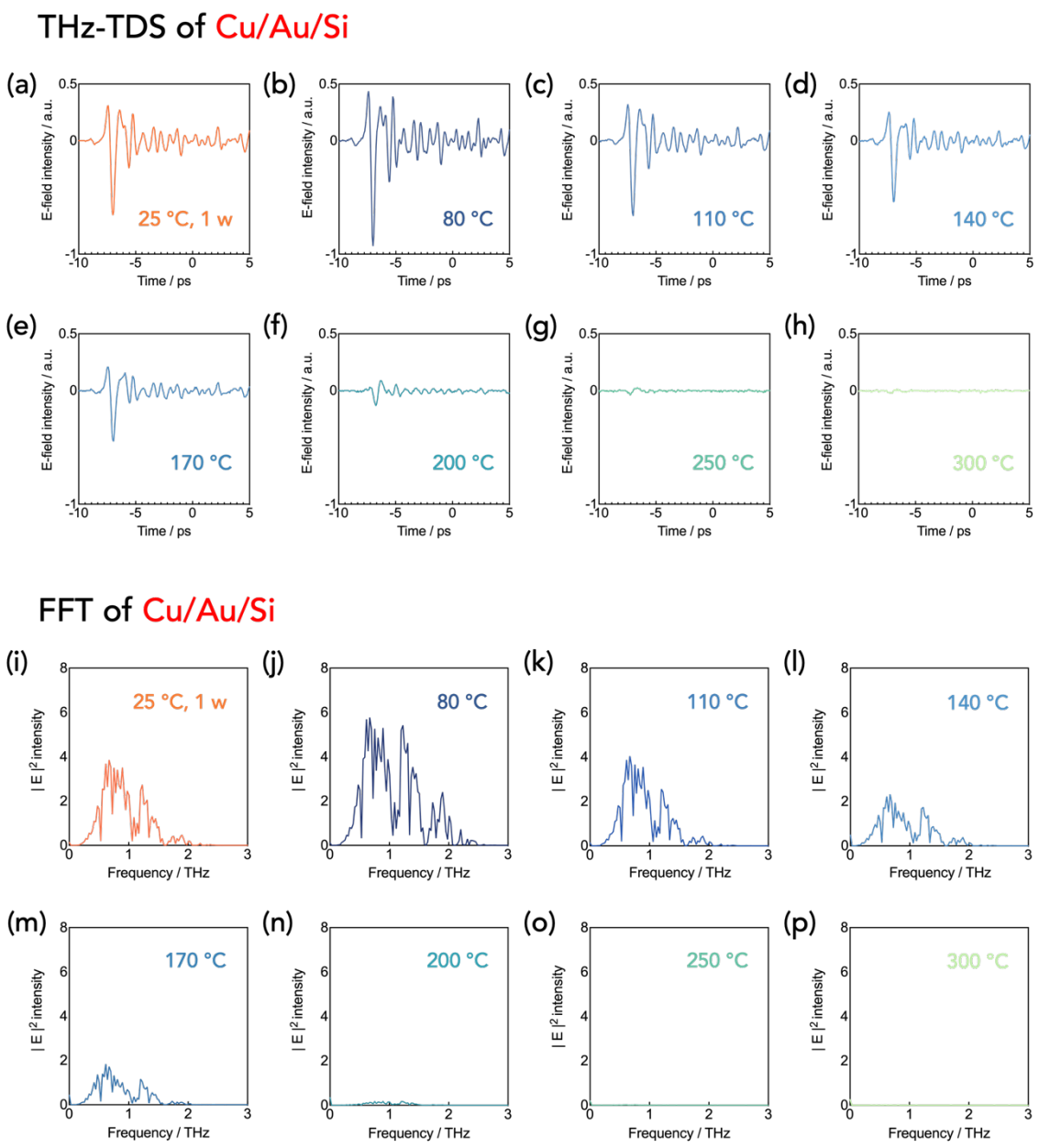


Figure 4.8 (a-h) THz-TDS and (i-p) corresponding FFT treated emission spectra of Cu/Au/Si structures annealed at different temperatures.

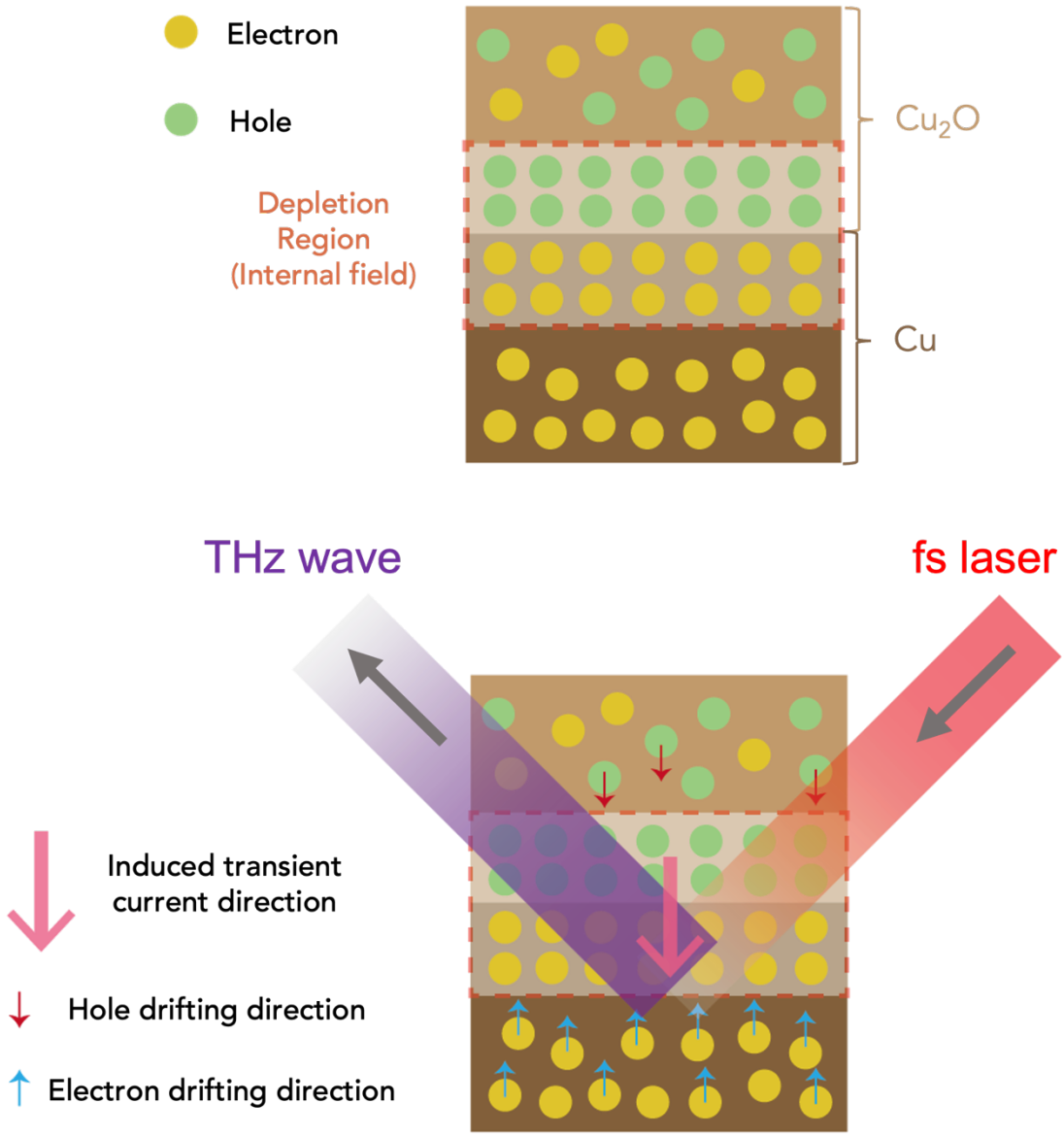


Figure 4.9 Scheme and mechanism of using Cu_2O/Cu interface as the THz wave source under femtosecond laser excitation. Mobility of the holes is approximately one order lower than that of electrons.

Since the flow of transient current is the ingredient of THz wave emission, the mobility of charge carriers is an important factor to the emission intensity. Figueiredo *et al*. had determined that the mobility of charge carriers decreases with increasing the annealing temperature.[28] More oxygen vacancies were created in the Cu layer at higher temperature. Those vacancies became obstacles for the movement of charge carriers. Electrons in Cu side have the highest mobility, but holes in Cu_2O side have less mobility when the oxidation degree increased. Therefore, THz wave intensity emitted from sample decreased with increasing the annealing temperature from 80 to 140 °C even these samples consisted of Cu_2O/Cu interface. In addition, TEM images of sample heated at higher temperature showed more cavities (**Figure 4.10**b-c). These cavities made poor connectivity between grains within the Cu layer, which also unfavorable for the flow of transient current. As a result, less THz wave was emitted.

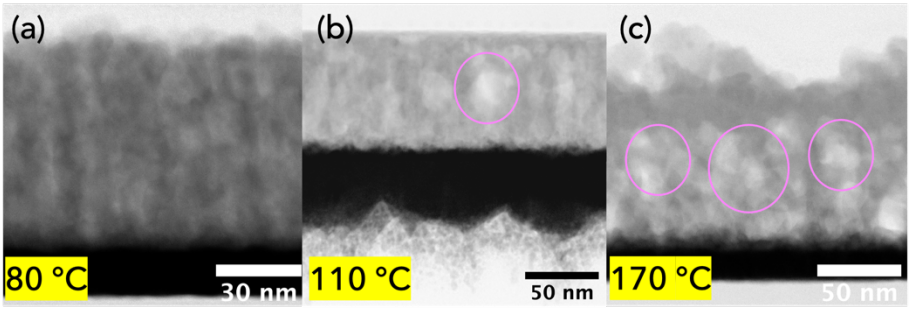


Figure 4.10 Cross-sectional TEM images of Cu/Au/Si heated at (a) 80 °C, (b) 110 °C, and (c) 170 °C. Pink circle indicates the cavities inside of the Cu layer.

4.3.5 Function of Au layer

Total THz wave emission intensities of both Cu/Si and Cu/Au/Si structures against the annealing temperature was summarized (**Figure 4.11**). At annealing temperature $\leq$ 170 °C, Cu/Au/Si structures generally emitted THz wave at higher intensity than Cu/Si. Cu/Au/Si structures annealed at 80 °C, that consisted of Cu_2O/Cu interface, had the highest THz wave emission even though some literatures claimed that the greatest THz emission from a Cu_2O/Au structure (without Cu to form Cu_2O/Cu interface).[14-17] There were two reasons to explain the phenomenon – (1) THz wave emitted from the Cu_2O/Cu interface propagated in all directions and the Au layer reflected the THz wave, therefore higher THz wave intensity was detected from Cu/Au/Si structures.[17] (2) The interaction of materials to the laser was increased with the sample thickness. An UV-vis measurement was carried out to evaluate the light absorption by single and double layer deposited on glass plate (**Figure 4.12**). It shows the absorption of Cu/Au heated at 80 °C had almost double value of absorbance compared with single layer. It might be due to some laser light was reflected at the Au layer surface.

Furthermore, less THz wave emission was detected from both annealed Cu/Si and Cu/Au/Si structures when the annealing temperature was at $\geq$ 200 °C. This is attributed to the lack of depletion region in those samples, which can also be explained

by the work function of materials. Work function of Cu_2O (Φ_{Cu_2O} = 4.84 eV[24]) is smaller than Au (Φ_{Au} = 5.1 eV[29]). An ohmic contact was formed in Cu_2O/Au [30]. Although CuO has a greater work function (Φ_{CuO} = 5.32 eV[24]) than Au, CuO is a semiconductor with indirect band gap. The combination of charge carriers may require higher excitation energy and thus not efficient enough to yield the transient current.[30,31] Therefore, almost zero-emission detected from samples annealed at $\geq$ 200 °C. On the other hand, diffusion also occurred in between Cu and Au layers during annealing.[15,16,32] When the Cu atoms diffused into the Au layer, the work function of the Au layer decreased. The work function of Au layer could be smaller than that of Cu_2O and depletion region was formed.[16] Thus, the THz wave emission intensity from the Cu/Au/Si structure was higher than that of the Cu/Si structure at an annealing temperature of 170 °C.

Nonetheless, both Cu/Au/Si structures kept in ambient for 1 week and annealed at 110 °C did not show significant enhancement in THz wave emission. The reason for the insignificant enhancement remains elusive. Other pieces of Cu/Si heated at 200, 250, and 300 °C were tested and a large variation of THz wave emission intensity was discovered (inset in **Figure 4.11**). The THz wave emission intensity from Cu/Si was higher than the Cu/Au/Si at $\geq$ 200 °C can be considered as experimental errors. The

results herewith found that the THz wave emission was enhanced by annealing samples at lower temperatures (80 °C), whereas the Cu_2O film thickness was in the range of less than 100 nm. The findings were different with the literature by Ramakrishnan *et al*.[17]. The main difference is attributed to the smaller the grain size and higher porosity of the Cu_2O layer formed by annealing at lower temperatures in this study. Contrastively, Ramakrishnan *et al*. annealed the Cu films at 250 °C to form Cu_2O on Au and found the Cu_2O films with a thickness less than 100 nm had almost zero THz emission.[17] At an annealing temperature of 250 °C and a Cu_2O film thickness less than 100 nm, samples in this study also emitted zero THz radiation.

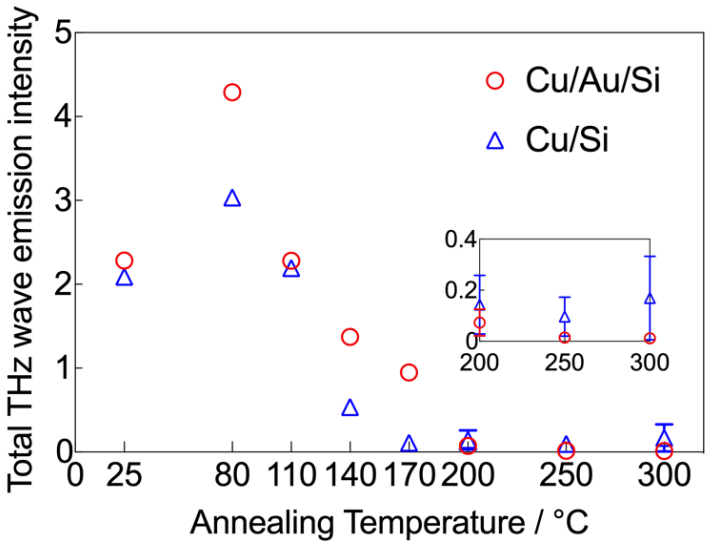


Figure 4.11 Total THz wave emission intensity of annealed Cu/Si and Cu/Au/Si structures against different annealing conditions.

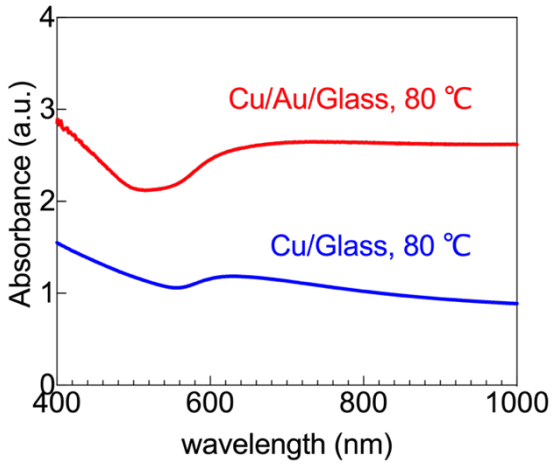


Figure 4.12 UV-Vis spectra of Cu/Au/Glass and Cu/Glass annealed at 80 °C. A bare glass slide was used as the baseline.

4.3.6 No THz wave emission from the inverted double-layered structure

The double-layered structure was inverted, i.e., Au/Cu/Si by depositing the Au layer on top of an annealed Cu layer. **Figure 4.13** shows the THz wave emission intensity from the Cu/Au/Si and Au/Cu/Si structures annealed at 110 °C for comparison. THz wave emission intensity from the Au/Cu/Si structure was weaker than that of Cu/Au/Si because of the incident laser power loss in the Au layer.[14] The uppermost Au layer also protected the Cu layer from further oxidation and made no Cu_2O/Cu interface, resulted in a reduction in THz wave emission. Hence, the inverted structure is not a sustainable THz source.

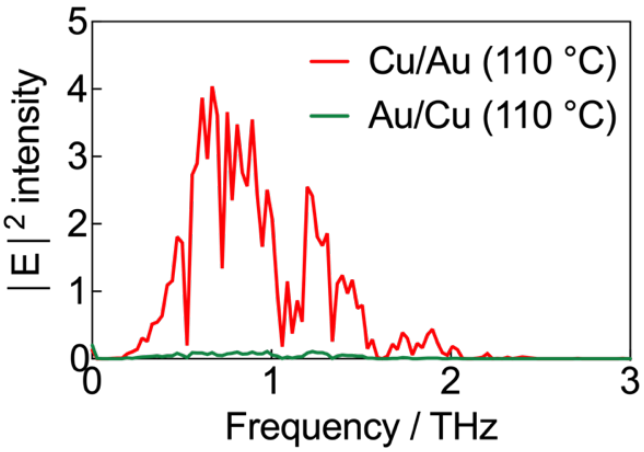


Figure 4.13 THz wave emission intensity from Cu/Au/Si and Au/Cu/Si structures annealed at 110 °C.

4.3.7 Suggestions of improving THz wave emission intensity

Intensities of THz wave emitted from samples in this study were still far lower than the normally used ZnTe <110>-single crystal with the same experimental settings. Since the resultant THz is proportional to the time derivative of the relative electron-hole motion, time profiles of THz wave reflect the transient current in the depletion region. Therefore, THz wave intensities can be enhanced by increasing the carrier density such as adopting a thicker film. So that the depletion region between metal and semiconductor can be expanded and more optical photons can be absorbed in the sample.[17,33] Semiconducting materials with narrower band gap is also recommended because smaller energy band gap can result in shorter recombination time of charge carriers so as to shorten the carrier lifetime.[34] Another approach is using higher laser powder and

shorten the laser pulse duration,[34] whereas more advanced technologies will be needed.

4.4 Conclusion

In summary, the THz wave emission was observed from the Cu_2O/Cu interface under femtosecond laser excitation. Although it was reported that the less than 100 nm thick Cu_2O layer annealed at 250 °C emitted almost no THz, this study found that Cu_2O/Cu interface formed by annealing 80 nm thick Cu layer at a temperature of 80 to 140 °C can enhance the THz wave emission. Especially at 80 °C, the Cu/Si gave the highest THz wave emission intensity. It was possibly due to the highly porous structure of the Cu_2O layer formed at low temperature, which can promote laser absorption. The THz wave emission was decreased at an annealing temperature of $\geq$ 200 °C. It was because the Cu layer did not have a Cu_2O/Cu interface and/or lack of porous structure from grain growth at that high annealing temperature. The Cu/Au/Si structures also had a similar THz wave emission trend with respect to the annealing temperatures. From that, Cu/Au/Si annealed at 80 °C showed an increase in THz wave emission by 41.4% compared with Cu/Si annealed at the same temperature. The Cu/Au/Si structures annealed at $\geq$ 200 °C also had almost zero THz wave emission because of the formation of ohmic contact at Cu_2O/Au and CuO/Au interfaces. Au/Cu/Si structure was also prepared and

annealed at 110 °C. The inverted structure had very low THz wave emission compared with Cu/Au/Si because of the dissipation of laser energy at the Au film and difficulty of the Cu film proceeding oxidation with the protection by Au film.

4.5 References

1. Jackson, J. B.; Mourou, M.; Whitaker, J. F.; Duling, I. N.; Williamson, S. L.; Menu, M; Mourou, G. A. Terahertz imaging for non-destructive evaluation of mural paintings. *Opt. Commun.* **2008**, *281*, 527-532.
2. Stoik, C. D.; Bohn, M. J.; Blackshire, J. L. Nondestructive evaluation of aircraft composites using transmissive terahertz time domain spectroscopy. *Opt. Express* **2008**, *16*, 21, 17039-17051.
3. Adam, A. J. L.; Planken, P. C. M.; Meloni, S.; Dik, J. TeraHertz imaging of hidden paint layers on canvas. *Opt. Express* **2009**, *17*, 5, 3407-3416.
4. Lee, D.; Kang, J.; Lee, J.; Kim, H.; Kim, C.; Hun Kim, J.; Lee, T.; Son, J.; Park, Q.; Seo, M. Highly sensitive and selective sugar detection by terahertz nano-antennas. *Sci. Rep.* **2015**, *5*, 15459.
5. Globus, T. R.; Woolard, D. L.; Khromova, T.; Crowe, T. W.; Bykhovskaia, M.; Gelmont, B. L.; Hesler, J.; Samuels, A. C. THz-Spectroscopy of Biological Molecules. *J. Biol. Phys.* **2003**, *29*,89-100.
6. Piesiewicz, R.; Kleine-Ostmann, T.; Krumbholz, N.; Mittleman, D.; Koch, M.; Schoebel, J.; Kurner, T. Short-Range Ultra-Broadband Terahertz Communications: Concepts and Perspectives. *IEEE Antennas Propag. Mag.* **2007**, *49*, 6, 24-39.
7. Heidemann, R.; Pfeiffer, T.; Jäger, D. Optoelectronically pulsed slot-line antennas. *Electron. Lett.* **1983**, *19*, 9, 316-317.
8. Mourou, G.; Stancampiano, C. V.; Antonetti, A.; Orszag, A. Picosecond microwave pulses generated with a subpicosecond laser-driven semiconductor switch. *Appl. Phys. Lett.* **1981**, *39*, 4, 295-296.
9. Rice, A.; Jin, Y.; Ma, X.F.; Zhang, X.-C.; Bliss, D.; Larkin, J.; Alexander, M.

Terahertz optical rectification from <110> zinc-blende crystals. *Appl. Phys. Lett.* **1994**, *64*, 11, 1324-1326.

10. Dakovski, G. L.; Kubera, B.; Shan, J. Localized terahertz generation via optical rectification in ZnTe. *J. Opt. Soc. Am. B* **2005**, *22*, 8, 1667-1670.
11. Zhang, X.-C.; Darrow, J. T.; Hu, B. B.; Auston, D. H.; Schmidt, M. T.; Tham, P.; Yang, E. S. Optically induced electromagnetic radiation from semiconductor surfaces. *Appl. Phys. Lett.* **1990**, *56*, 22, 2228-2230.
12. Chuang, S. L.; Schmitt-Rink, S.; Greene, B. I.; Saeta, P. N.; Levi, A. F. J. Optical rectification at semiconductor surfaces. *Phys. Rev. Lett.* **1992**, *68*, 1, 102-105.
13. Lopez, J.; Café, A.; Husay, H. A.; Lopez, L.; Salvador, A.; Estacio, E.; Somintac, A. Terahertz emission from Cu_2O/PSi with Fabry-Perot mode at 800 nm. *Proc. Samahang Pisika ng Pilipinas* **2016**, *34*, SPP-2016-2A-06 2016.
14. Lu, X.; Yonezawa, T. Terahertz emission from Cu_xO/Au thin film. 2014 *MWP/APMP* **2014**, 164-165.
15. Lu, X.; Ishida, Y.; Mishina, T.; Nguyen, M. T.; Yonezawa, T. Enhanced Terahertz Emission from Cu_xO/Metal Thin Film Deposited on Columnar-Structured Porous Silicon. *Bull. Chem. Soc. Jpn.* **2015**, *88*, 10, 1385-1387.
16. Ramanandan, G. K. P.; Adam, A. J. L.; Ramakrishnan, G.; Petrik, P.; Hendrikx, R.; Planken, P. C. M. Optical characterization of gold-cuprous oxide interfaces for terahertz emission applications. *Appl. Opt.* **2014**, *53*, 10, 1994-2000.
17. Ramakrishnan, G.; Ramanandan, G. K. P.; Adam, A. J. L.; Xu, M.; Kumar, N.; Hendrikx, R. W. A.; Planken, P. C. M. Enhanced terahertz emission by coherent optical absorption in ultrathin semiconductor films on metals. *Opt. Express* **2013**, *21*, 14, 16784-16798.

18. Exter, M. V.; Fattinger, Ch.; Grischkowsky, D. Terahertz time-domain spectroscopy of water vapor. *Opt. Lett.* **1989**, *14*, 20, 1128-1130.
19. Wang, L.S.; Wu, H.; Desai, S.R.; Lou, L. Electronic Structure of Small Copper Oxide Clusters: From Cu_2O to Cu_2O_4. *Phys. Rev. B: Cond. Matt.* **1996**, *53*, 12, 8028-8031.
20. Hu, L.; Huang, Y.; Zhang, F.; Chen, Q. CuO/Cu_2O composite hollow polyhedrons fabricated from metal–organic framework templates for lithium-ion battery anodes with a long cycling life. *Nanoscale* **2013**, *5*, 10, 4186-4190.
21. Kumar, V.; Masudy-Panah, S.; Tan, C. C.; Wong, T. K. S.; Chi, D. Z.; Dalapati G. K. Copper oxide based low cost thin film solar cells. *IEEE 5th Int. Nanoelectronics Conf. (INEC)* **2013**, 443-445.
22. Serin, N.; Serin, T.; Horzum, Ş.; Çelik, Y. Annealing effects on the properties of copper oxide thin films prepared by chemical deposition. *Semicond. Sci. Technol.* **2005**, *20*, 5, 398.
23. Platzman, I.; Brener, R.; Haick, H.; Tannenbaum, R. Oxidation of Polycrystalline Copper Thin Films at Ambient Conditions. *J. Phys. Chem. C* 2008, *112*, 4, 1101-1108.
24. Singh, B.; Mehta, B. R. Relationship between nature of metal-oxide contacts and resistive switching properties of copper oxide thin film based devices. *Thin Solid Films* **2014**, *569*, 35-43.
25. Bai, P.; Zhang, Y. H.; Guo, X. G.; Fu, Z. L.; Cao, J. C.; Shen, W. Z. Realization of the high-performance THz GaAs homojunction detector below the frequency of Reststrahlen band. *Appl. Phys. Lett.* **2018**, *113*, 24, 241102.
26. Adomavičius, R; Urbanowicz, A.; Molis, G.; Krotkus, A. Terahertz emission from *p*-InAs due to the instantaneous polarization. *Appl. Phys. Lett.* **2004**, *85*, 13, 2463.
27. Guo, Q.; Zhang, Y.; Lyu, Z.-H.; Zhang, D.-W.; Huang, Y.-D.; Meng, C.; Zhao, Z.-X.;

Yuan, J.-M. Terahertz emission and optical second harmonic generation from Si surfaces. Opt. Mater. Express **2019**, *9*, 5, 2376-2385.

28. Figueiredo, V.; Elangovan, E.; Gonçalves, G.; Barquinha, O.; Pereira, L.; Franco, N.; Alves, E.; Martins, R.; Fortunato, E. Effect of post-annealing on the properties of copper oxide thin films obtained from the oxidation of evaporated metallic copper. *Appl. Surf. Sci.* **2008**, *254*, 13, 3949-3954.
29. Eastman, D. E. Photoelectric Work Functions of Transition, Rare-Earth, and Noble Metals. *Phys. Rev. B* **1970**, *2*, 1, 1-2.
30. Gupta, R.; Misra, S. C. K.; Malhotra, B. D.; Beladakere, N. N.; Chandra, S. Metal/semiconductive polymer Schottky device. *Appl. Phys. Lett.* **1991**, 58, 1, 51-52.
31. Ping, A. T.; Khan, M. A.; Adesida, I. Ohmic contacts to n-type GaN using Pd/Al metallization. *J. Electron. Mater.* **1996**, *25*, 5, 819-824.
32. Tompkins, H. G.; Pinnel, M. R. Low-temperature diffusion of copper through gold. *J. Appl. Phys.* **1976**, *47*, 9, 3804-3812.
33. Adams, A. C.; Pruniaux, B. R. Gallium Arsenide Surface Film Evaluation by Ellipsometry Its Effect on Schottky Barriers. *J. Electrochem. Soc.* **1973***, 120*, 3, 408-414.
34. Khorshidi, M.; Zafari, S.; Dadashzadeh, G. Increase in terahertz radiation power of plasmonic photoconductive antennas by embedding buried three-stepped rods in electrodes. *Opt. Express* **2019**, *27*, 16, 22327.

CHAPTER 5

Mechanistic Studies of ZnTe Microspheres formed in a PVP-contained Polyol System and their THz Wave Emission Availability

5.1 Introduction

Zinc telluride (ZnTe) is an II-IV semiconductor with a direct band gap of ~2.26 eV under room temperature.[1-3] Various forms of ZnTe (solid crystals, colloids, thin films) are widely used as blue-green light-emitting diodes[4], electro-catalysts[2,5-7], electrode material for Li-ion batteries[8], bioimaging agents[9] and antimicrobial agents[10]. Particularly, <110>-directional ZnTe single crystal is used in THz wave generation and detection because of its electro-optic properties. Molecular beam epitaxy (MBE) and Bridgman-Stockbarger (BS) method are used to fabricate single crystals of ZnTe. However, MBE is a high-cost technique, and BS method usually requires high temperature (~1000 ºC).[11] In recent study, Huang *et al.* has confirmed the THz wave enhancement from water through adding polycrystalline-ZnTe colloids to the dispersion upon femtosecond laser pulse irradiation.[12] Even though they have found the ZnTe colloids were chemically unstable, which makes the colloids not 'durable' enough to be THz wave source, it is no doubt that the use of polycrystalline ZnTe particles as the THz

wave source has been inspired by their work. Apart from nano colloids used in ref. [12], recently ZnTe microspheres have drawn attention because of its photocatalytic activity on reduction of CO_2 and they are not easily deteriorated from the catalytic reaction.[13-18] As a result, these ZnTe microspheres are considered as a potential THz wave emitter under ultrafast laser irradiation.

Among approaches of making micro-structured ZnTe, solution chemistry-based methods (e.g., solvothermal method[15-18], chemical reduction method[19-25]) are convenient compared to the traditional thermal evaporation methods [26-28] which require high temperature condition. In chemical reduction methods, Te sources usually require extra preparation steps prior to use. Sodium hydrogen telluride (NaHTe) is a frequently used Te source for chemical syntheses in aqueous systems.[20-23] It is formed by mixing Te with sodium borohydride ($NaBH_4$) in aqueous phase. Preparation of NaHTe solution must be conducted under an oxygen-free environment. Especially, it oxidizes spontaneously and results in elemental Te easily during the injection step, making the synthesis becomes unmanageable.[29] Zhang *et al.* have introduced Sodium tellurite (Na_2TeO_3) is used as the Te source to overcome these tedious steps.[30] It is because other commonly used Te source (e.g., NaHTe) usually require an oxygen free environment, making the synthesis becomes unmanageable in some extent. On the other hand, Na_2TeO_3

is stable in air and can be dissolved in polar solvents to form a Te precursor solution under air.[30-32] As a result, the syntheses of ZnTe or other Te compounds should be more manageable using Na_2TeO_3 as the Te precursor. Moreover, ZnTe colloids synthesized from some wet chemical routes in certain pH conditions were unstable.[20] This causes difficulties to their practical usage, and thus a surfactant is desired to improve the stability of ZnTe colloids. Poly(N-vinyl-2-pyrrolidone) (PVP) is suggested as the surfactant, which can protect the ZnTe particles from deterioration. and structure-directing agent.[33-39] PVP is a hydrophilic polymer, so that the PVP-capped colloids are dispersible in aqueous solution.[40]

$TeO_3^{2-} + 3H_2O + 4e^- \rightarrow Te + 6OH^-$ (E_0 = -0.57 V) … (**Eq. 5.1**) [41]

$Te + 2e^- \rightarrow Te^{2-}$ (E_0 = -1.143 V) … (**Eq. 5.2**) [42]

The syntheses of ZnTe microspheres with diameter from sub-micron to few micrometers via solvothermal method have been reported.[15-18] Particularly, Ehsan *et al.* have conducted a set of time-dependent experiment to study the growth of ZnTe microspheres from the Zn^{2+} and TeO_3^{2-} ions in NaOH solution without any surfactant. They have proposed a formation scheme of ZnTe microspheres.[15] That is, large Te(0) spherical and rod-like crystals formed at first, then the Zn^{2+} deposited on the Te(0)

spheres/rods for the nucleation of ZnTe. The ZnTe nuclei was further growth via Ostwald ripening followed with the inward diffusion of Te(0) to form ZnTe.[15] On the other hand, Wu *et al.* and Li *et al.* have reported the syntheses of ZnTe microspheres in ethylene glycol (EG) with the usage of PVP as surfactant.[16-18] Particularly, Li *et al.* have studied the effect of PVP to the morphologies of ZnTe microspheres.[18] They have also discussed the formation of ZnTe microspheres, that involved two major steps: the first step was the reduction of TeO_3^{2-} ions to Te(0) (**Eq. 5.1**), which were further reduced to Te^{2-} ions (**Eq. 5.2**). These sequential reactions were based on the electrode potential values. The second step involved the nucleation and growth of ZnTe occurred via the combination of Te^{2-} ions and Zn^{2+} ions. Then, ZnTe microspheres were formed through the attachment of ZnTe nanocrystals to each other by sharing a common crystal orientation, which is also called 'directional attachment'.[18] Although the first step in this proposed scheme was consistent with the findings by Ehsan *et al.*[15], evidence regarding to the elemental Te formed at the first step and its morphologies was not given. In fact, the system is rather complicated when PVP is involved. It is because sizes and morphologies of Te are highly determined by the amount of PVP in the reaction system.[34,37-38] Based on the formation mechanism of ZnTe microspheres suggested by Ehsan *et al.*[15], sizes of ZnTe microspheres might be determined by the sizes of Te(0),

which also related to the Ostwald ripening. From this point of view, the effect of morphologies of Te formed at the early stage to the sizes and morphologies of ZnTe microspheres as final product is of interest.

This chapter consists of two sections: In the first part, the formation of ZnTe microspheres in EG via a hot injection method was studied. Different amount of PVP was used to synthesize ZnTe microspheres. The effect of PVP on ZnTe microspheres' morphologies and growth was discussed. The moderate parameters of obtaining homogeneous ZnTe microspheres was then suggested. The formation process of ZnTe microspheres in a PVP-contained system was systematically studied at 0.2–48 h time frames. The findings showed Te wires/rods became the sacrificial template for the growth of ZnTe microspheres in longer reaction time. The influence of using different ratio of solvents and complexing agent for precursors was also discussed. In the second part, equal-mass of different sized ZnTe microspheres were drop-casted on a Si wafer to test their THz wave emission ability. Moreover, a day-long laser irradiation test was conducted with the sample having the highest THz wave emission, for testing the 'durability' of ZnTe microspheres towards the THz wave emitting applications. Finally, comments were given for determining the possible mechanisms of THz wave emission from ZnTe microspheres.

5.2 Experimental

5.2.1 Materials

Non-doped <100>-oriented Si wafers (ϕ50 mm, 280 μm-thick, ≥ 1000 Ω cm^{-1}, Global Top Chemical, Japan), ultra-high purity hydrofluoric acid (HF, concentration 48 %, Stella Chemifa, Japan), $ZnCl_2$ (Kanto, Japan), $Zn(CH_3COO)_2$ (Kanto, Japan), Na_2TeO_3 (Wako, Japan), EG (Kanto, Japan), ethylenediamine (en, Wako, Japan), and PVP (K-90, M.W. = 1,200,000, Kanto, Japan) were used as received.

5.2.2 Preparation of precursor solution

0.20 mmol of Zn salt ($ZnCl_2$ or $Zn(CH_3COO)_2$) and 0.16 mmol of Na_2TeO_3 were placed in a mixture of 3 mL of EG and 0.64 mL of en. $Zn(CH_3COO)_2$ and Na_2TeO_3 were not dissolved well without en.[35] The function of en is complexing of Zn^{2+} as tris(ethylenediamine)zinc(II) ($[Zn(en)_3]^{2+}$)[43] and boosting the dissolution of salts by its strong polarity. The mixture was stirred at room temperature under a dark environment for 6 h to obtain a homogeneous transparent precursor solution.

5.2.3 Synthesis of ZnTe microspheres

Figure 5.1 illustrates the experimental setup of making ZnTe microspheres. 15 mL of EG was mixed with PVP in a three-necked round bottom flask equipped with a reflux system under stirring at 1,000 rpm. The flask was immersed into an oil bath and connected to the Schlenk line. After PVP completely dissolved, the solution was heated at 60 °C for 1 h to remove oxygen from the system. Vacuum-argon gas exchange was then carried out to make the system being under argon atmosphere. A thermocouple coupled with a data logger was immersed to the solvent throughout the reaction for temperature monitoring. Temperature of the oil bath was increased until the data logger shows the EG-PVP mixture had reached to 200 °C. Then, the precursor solution (total volume 3.64 mL) was injected rapidly to the hot EG-PVP mixture using a needle syringe. **Table 5.1** lists the parameters of experiments for each sample. After precursor injection, the transparent EG-PVP mixture became charcoal grey immediately and turned to silvery grey in an hour, which was originated by the formation of Te.[44] Eventually the mixture became reddish brown at 24 h. No further colour change was observed afterwards. The flask was then quenched to room temperature naturally under an Argon flow for 30 min after the reaction. Finally, the product was purified via centrifugation with ethanol for three times (5,000 rpm, 10 min), and dried in a vacuum oven prior to characterize.

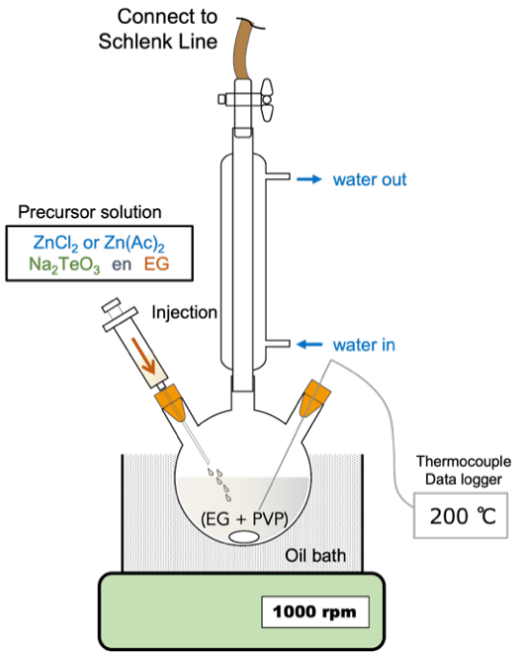


Figure 5.1 Schematic diagram of the experimental setup of making ZnTe microspheres.

Table 5.1 Parameters used in preparing each sample. (Reaction temperature: 200 °C and stirring speed = 1,000 rpm)

Sample code	PVP added	*t* = reaction time / h	Reaction temperature / °C
0PVP(*t*)	0 mg	0.2, 0.5, 48	200
259PVP(*t*)	259 mg	0.2, 0.5, 48	200
518PVP(*t*)	518 mg	0.2, 0.5, 1, 2, 6, 12, 24, 48	200 (48 h only: 160, 180)
1036PVP(*t*)	1036 mg	0.2, 0.5, 48	200

5.2.4 Characterization of ZnTe microspheres

Crystal structures and average crystallite sizes of samples were evaluated with the data taken by X-ray diffraction (XRD, Rigaku, MiniFlex II, Cu Ka radiation, λ = 1.5418 Å, scan speed = 0.5° min^{-1}, and scanning range = 20 to 60°). Morphologies of the ZnTe microspheres were observed using a scanning electron microscope (SEM, JSM-6701F, 15 kV, JEOL, Japan). The average size of ZnTe microspheres was obtained by measuring 150 particles from SEM images using ImageJ software (U.S. National Institutes of Health, USA). Aspect ratio of Te rods/wires was obtained based on measuring 150 rods/wires from SEM images. Since the diameter of Te rods were not homogeneous throughout the structure, the largest diameter was used to calculate the aspect ratio. Also, ZnTe microspheres may covered part of Te rods during their growth. Hence, the measured length of Te rods represented the uncovered part of Te rods. (i) AR of each Te rods, (ii) average AR of Te rods in sample, and (iii) its standard deviation were calculated by below equation:

(i) $$AR_{Sample} = \frac{Length\ of\ Te\ rods}{Maximum\ diameter\ of\ Te\ rods}$$

(ii) $$Average\ AR_{Sample} = \frac{AR_{Sample}}{Sample\ size}$$

(iii) $$AR_{Sample,SD} = \sqrt{\frac{\sum(AR_{Sample} - Average\ AR_{Sample})^2}{Sample\ size}}$$ where sample size = 150.

Diffraction pattern and high-resolution images of the ZnTe microspheres were captured

using a transmission electron microscope (TEM, JEOL-2010, 200 kV, JEOL, Japan), a scanning transmission electron microscopy (STEM, JEOL-JEM-ARM200F, 200 kV, JEOL, Japan), and a multi-beam ultra-high voltage electron microscope (HVEM, JEOL-JEM-ARM1300, 1250 kV, JEOL, Japan), respectively. Composition of fine structures in samples was obtained by point analysis and/or elemental mapping using an energy-dispersive X-ray spectroscope (EDS) coupled with SEM and/or STEM.

An ultra-microtome machine (ULTRACUT S, Reichert-Nissei, Leica AG, Austria) was used for sectioning the sample 518PVP(0.5h) for cross-sectional structure observation under TEM. Before using the ultra-microtome to cut the sample into slides, the sample was diluted in ethanol and embedded into a resin. The resin was prepared by mixing well 2 mL of Quetol-812 (Nisshin-EM, Japan), 1 mL of dodecenyl succinic anhydride (DDSA, Nisshin-EM) and 1.4 mL of methyl nadic anhydride (MNA, Nisshin-EM) to obtain a yellowish clear solution. Then, 0.1 mL of DMP-30 (Nisshin-EM) was added, and the solution turned to caramel colour. The resin was poured into a hexagonal pyramid-shaped capsule with 1 mL of volume followed with injecting sample dispersed in ethanol. The capsule was sealed tightly, and the resin was cured at 60 °C for 30 h inside a drying oven. After that, the cured resin embedded with sample was separated from the capsule and trimmed into 50 nm-thick specimens using the ultra-microtome with a

diamond blade. Finally, the trimmed specimens were collected and loaded on the collodion film of TEM grids prior to observe.

5.2.5 Preparation of ZnTe/Si

Pretreatment of Si wafers prior to use was carried out with procedures mentioned in chapter 4. Instead, the size of Si wafers was cut into 2.7 × 2.7 cm^2. Syntheses of different sized ZnTe microspheres were done using similar procedures mentioned in chapter 5. ZnTe microspheres with size larger than 1 μm (not mentioned in chapter 5) were obtained by increasing the concentration of Zn and Te precursors during the synthesis. The products were washed and dried into powder form. Syntheses were repeated for several times until each batch of ZnTe microspheres stocked up to about 90 mg. ZnTe microspheres powder was dispersed in ~ 1 mL of EG. The dispersion was sonicated until no precipitates were observed with naked eyes. Then, the dispersion was drop-casted onto Si wafer and dried for overnight in a vacuum oven with temperature set at 40 ºC. Cracks easily formed in the film if the drying temperature was higher than 40 ºC. Re-deposition of the film was proceeded when cracks were observed and/or Si wafer exposed to the surface, because Si wafer also contributes to THz wave emission under femtosecond laser irradiation.

5.2.6 THz wave emission measurement

Figure 5.2 shows a block diagram of the experimental setup. Each sample was placed on a circular sample holder with 40 mm of diameter. Femtosecond laser pulses (35 fs/transform-limited, 800 nm, 1 kHz, Mantis/Legend Elite HE USP, Coherent) were irradiated without focusing to the sample surface, which is held on a conventional mirror holder, with the incident angle of 45°. The incident laser energy was adjustable at 0.2, 0.3, 0.4, 0.5 mJ/pulse and, the beam diameter was 25.4 mm. THz wave emission toward the reflection direction was transferred to a setup for electro-optic sampling with a <110>-oriented ZnTe single crystal (1-mm thick, Nippon Mining & Metals, Co. Ltd.) by the off-axis parabolic mirror (OAPM). After the sample, a Teflon plate blocked the remaining light from optical parametric amplifier (OPA). Measurements with lock-in detection were carried out with a chopper (3502, New Focus) and a lock-in amplifier (SR830, Stanford Research System), the effective laser repetition is 0.5 kHz. No apparent sample damages were recognizable after the laser irradiation experiments. TDS signals were obtained, and THz wave emission spectra were calculated by discrete Fourier-transform (DFT) of the TDS signals. All the laser irradiation experiments were carried out in atmospheric pressure in air (23 °C with 40-50 % humidity).

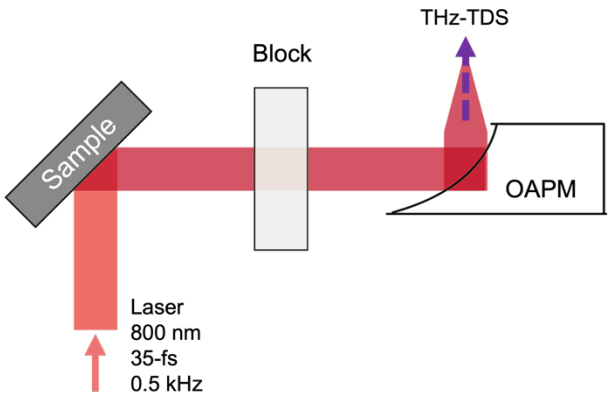


Figure 5.2 Block diagram of the experimental setup (top view).

5.3 Results and Discussion

5.3.1 Effect of PVP to ZnTe microspheres at reaction time of 48 h

Figure 5.3 shows SEM images and the size distributions of ZnTe microspheres synthesized using different amount of PVP. ZnTe microspheres in 0PVP(48h) had the largest size (972 ± 159 nm) among samples. The neck formation between particles was observed (**Figure 5.3**a). ZnTe microspheres were separated from each other and likely became monodispersed spheres by increasing the amount of PVP (**Figure 5.3**b-c). 518PVP(48h) yielded the smallest sized ZnTe microspheres in this study (634 ± 97 nm) . Further increasing the amount of PVP i.e., 1036PVP(48h) resulted in microspheres in larger size (811 ± 75 nm) than that in 518PVP(48h) (**Figure 5.3**d). These results suggested that the particle size was not reduced linearly with increasing amount of PVP, but the smallest ZnTe microspheres were yielded by a moderate amount of PVP. Rod structures observed in 0PVP(48h) and 259PVP(48h) were identified as Te rods by EDS elemental mapping (**Figure 5.4**c-e). **Figure 5.5** shows XRD patterns of samples presented in **Figure 5.3**. The diffraction peaks of all samples matched with the standard pattern of cubic (zincblende) structured ZnTe, with peaks at $2\theta = 25.26°$, 29.25°, 41.81°, 49.50° and 51.85°, corresponding to (111), (200), (220), (311) and (222) planes, respectively (JCPDS No. 15-0746). Average crystalline sizes from each diffraction peak of all samples are

listed in **Table 5.2**. Grain sizes in all directions (several ten nanometers) were smaller than the particle size (micrometers), suggesting that ZnTe microspheres were polycrystalline. Peaks at $2\theta = 27.5°$, 38.3° and 40.4° matched with the hexagonal structure Te reference (JCPDS No. 36-1452) in XRD patterns of 0PVP(48h) and 259PVP(48h). The XRD results were coherent with the Te rods observed in SEM-EDS (**Figure 5.4**). The formation rate of ZnTe microspheres in 0PVP(48h) and 259PVP(48h) were slower than that in 518PVP(48h) and 1036PVP(48h) because the latter did not contain unreacted Te. In other words, unreacted Zn^{2+} ions/$[Zn(en)_3]^{2+}$ complexes should be remained in both 0PVP(48h) and 259PVP(48h). However, no Zn or its oxide peak were observed in the XRD pattern. It was because Zn is not easily reduced by EG which has weak reducing power, so the unreacted ions/complexes were washed away from the centrifugation.

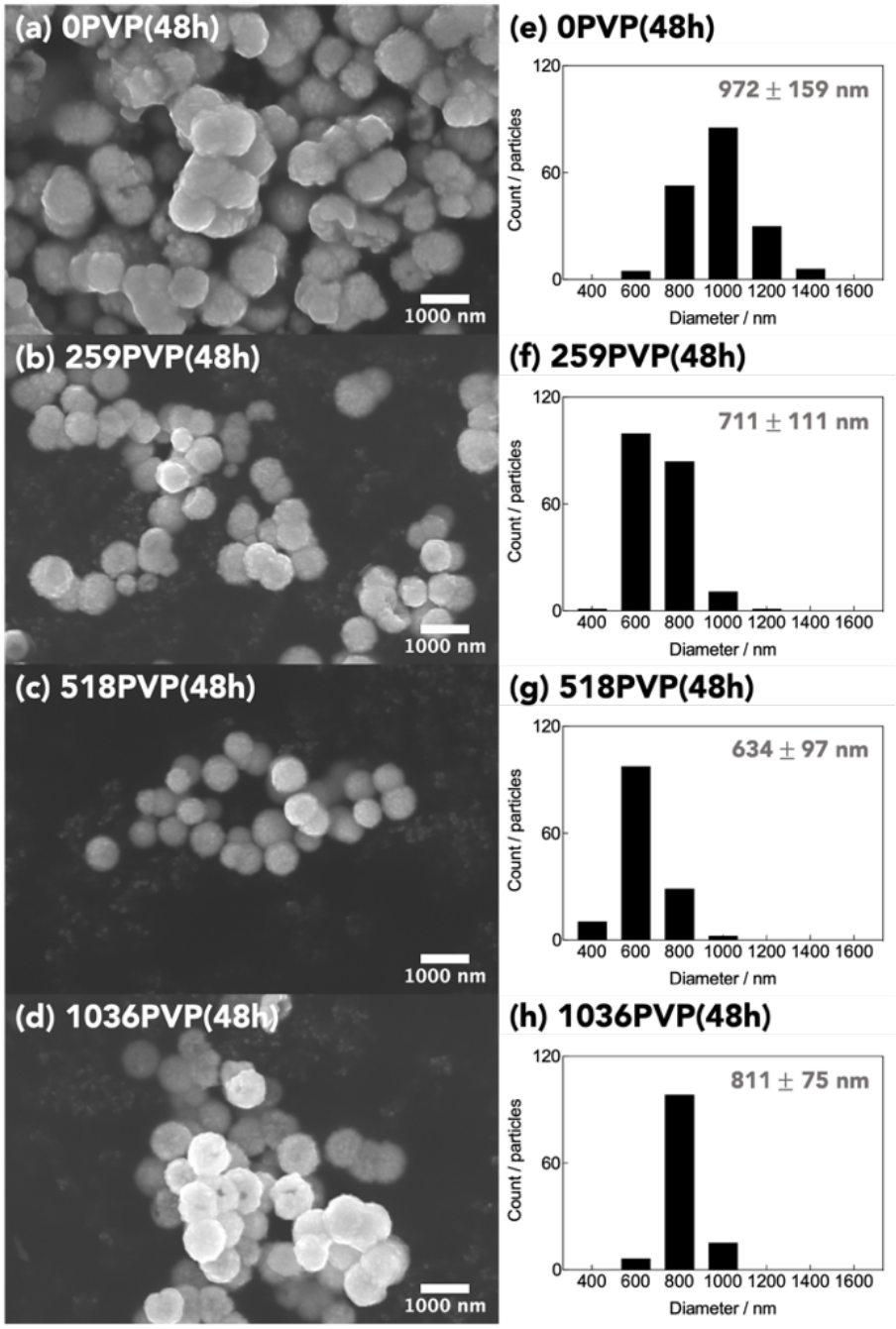


Figure 5.3 SEM images of ZnTe microspheres from samples (a) 0PVP(48h), (b) 259PVP(48h), (c) 518PVP(48h), (d) 1036PVP(48h), and (e-h) the corresponding size distributions.

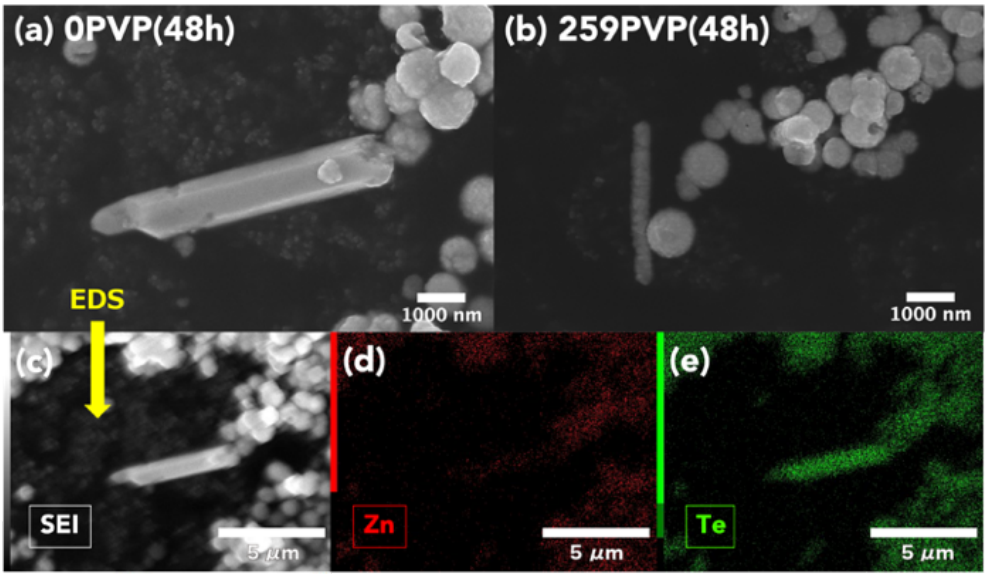


Figure 5.4 SEM images of rod structures in (a) 0PVP(48h) and (b) 259PVP(48h). (c) Region of sample 0PVP(48h) to perform EDS elemental mapping analysis of (d) Zn and (e) Te.

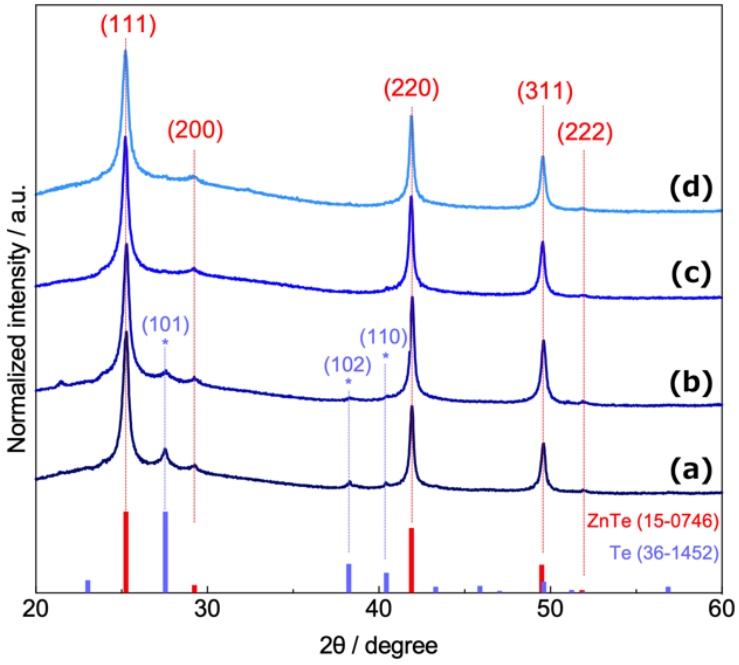


Figure 5.5 XRD patterns of sample (from bottom) (a) 0PVP(48h), (b) 259PVP(48h), (c) 518PVP(48h) (d) and 1036PVP(48h). Bar charts are reference patterns of ZnTe (Red, JCPDS No. 15-0746) and Te (Blue, JCPDS No. 36-1452).

Table 5.2 Average crystalline sizes calculated from XRD peaks of sample.

Peaks	0PVP(48h)	259PVP(48h)	518PVP(48h)	1036PVP(48h)
ZnTe (111)	15.9 nm	15.8 nm	16.2 nm	14.8 nm
ZnTe (220)	29.4 nm	31.6 nm	26.4 nm	26.5 nm
ZnTe (311)	24.1 nm	22.5 nm	22.5 nm	22.0 nm

5.3.2 Structure and composition of ZnTe microspheres

The detailed crystal structures of ZnTe microspheres were studied through sample 518PVP(48h). **Figure 5.6** is the SAED pattern taken at the edge of one of the ZnTe microspheres in 518PVP(48h). The SAED pattern showed rings with bright spots. The spaces between adjacent planes were calculated with diameter of each ring and they were compared with the JCPDS reference of ZnTe (**Table 5.3**). The results revealed the existence of (111), (200), (220), (311) planes of cubic (zinc-blende) ZnTe. The difference in lattice spacing between sample and the reference were constantly fall between 0.024 ± 0.001 Å, which was within the precision of the TEM-SAED analysis. The atomic resolution image of ZnTe microspheres taken by STEM (**Figure 5.7**). The STEM image showed the ZnTe microsphere consisted of ZnTe nanocrystals with (111), (200) and (220) planes (**Figure 5.7**c-e). These findings were coherent with XRD results (**Figure 5.5**).

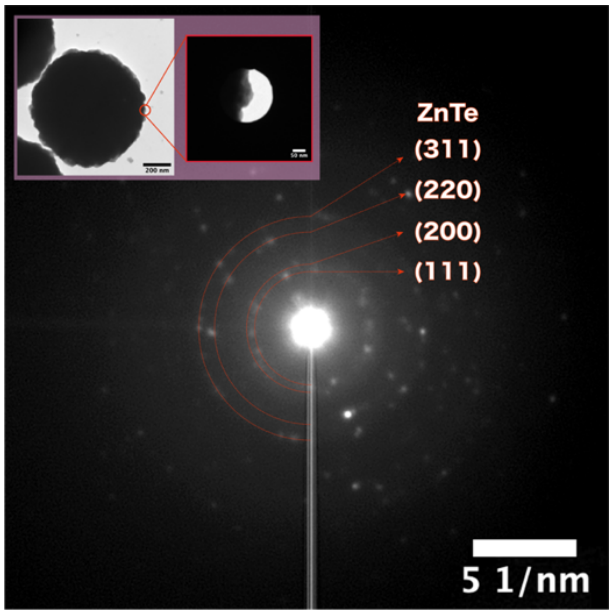


Figure 5.6 Selected area electron diffraction (SAED) pattern of the ZnTe microsphere. Inset are the TEM images showing the area where the SAED pattern was taken.

Table 5.3 Lattice spacing of different planes of cubic (zincblende) ZnTe. ***S***: measured from the SAED pattern of 518PVP(48h); ***R***: taken from JCPDS reference no. 15-0746.

Planes	***S*** / Å	***R*** / Å	***S*** – ***R*** / Å
(111)	3.548	3.523	0.025
(200)	3.076	3.051	0.025
(220)	2.183	2.159	0.024
(311)	1.866	1.840	0.026

Composition of ZnTe microspheres was also evaluated by STEM-EDS. The elemental mapping showed both Zn and Te were evenly distributed in the microspheres (**Figure 5.8**). The Zn-to-Te atomic ratio of a single ZnTe microsphere was 42 : 58. This was different from the SEM-EDS result that showed the average Zn-to-Te atomic ratio was 52 : 48 (**Figure 5.9**). The inconsistency of results from SEM-EDS and STEM-EDS might be due to the following reasons: (1) Difference in the interaction volume between two EDS detectors. (2) Compositional inhomogeneity among particles. (3) Some Zn-rich small particles (< 600 nm) existed around the ZnTe microspheres since a large region including several bunches of ZnTe microspheres was measured in the SEM-EDS mapping. We further performed SEM-EDS point analyses for another 27 ZnTe microspheres. Two-third of measured ZnTe microspheres had Zn less than 50%. Hence, it was not surprised to find a Te-rich microsphere under STEM-EDS. We could consider in overall the ZnTe microspheres were close to stoichiometry (**Figure 5.10**).

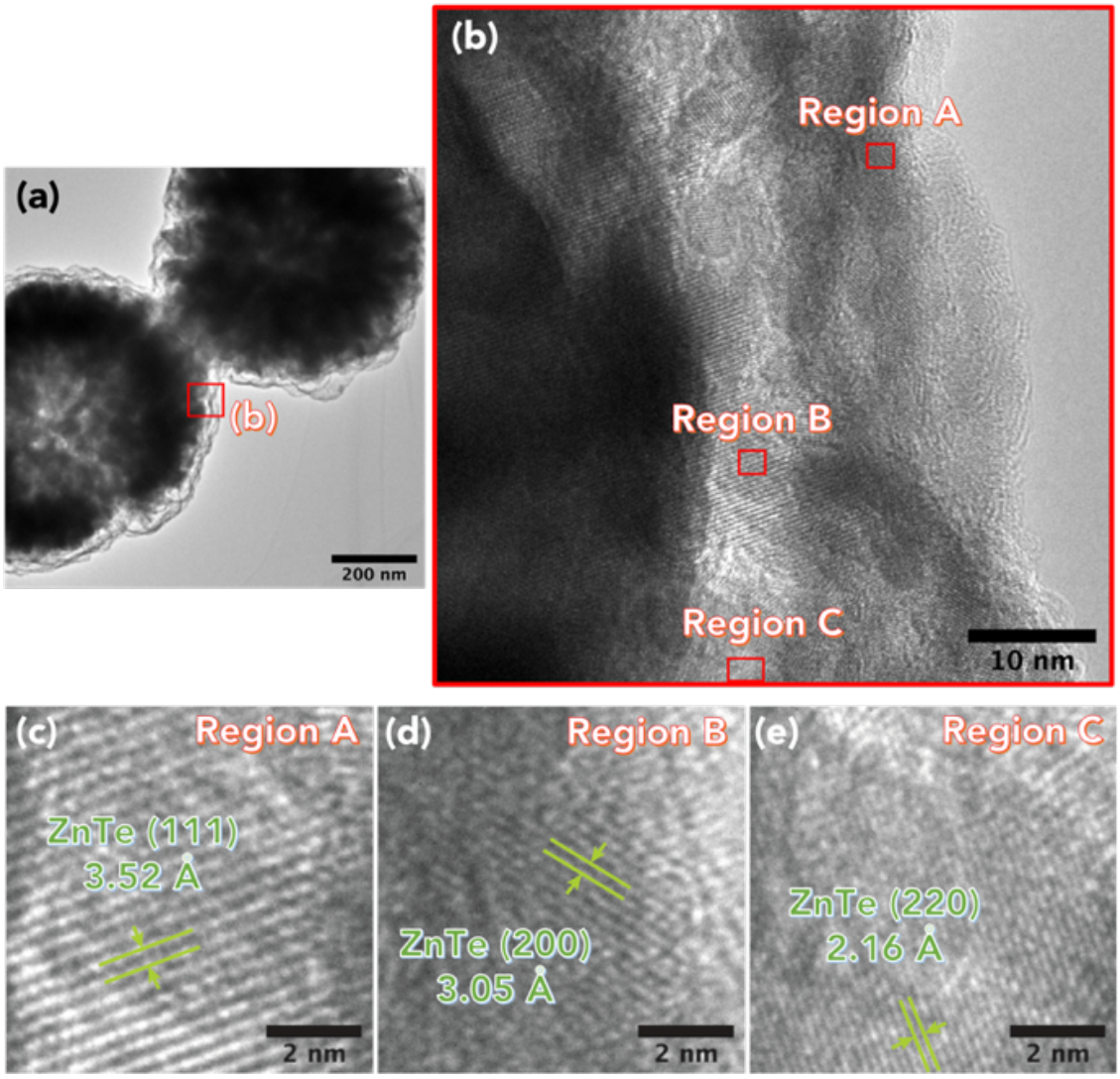


Figure 5.7 (a) TEM micrographs of ZnTe microspheres in 518PVP(48h) in low magnification. (b) High magnification image of the region selected by the red square in (a). (c-e) Enlarged regions in (b), indicating the lattice spacing of ZnTe in (111), (200), (220) planes respectively.

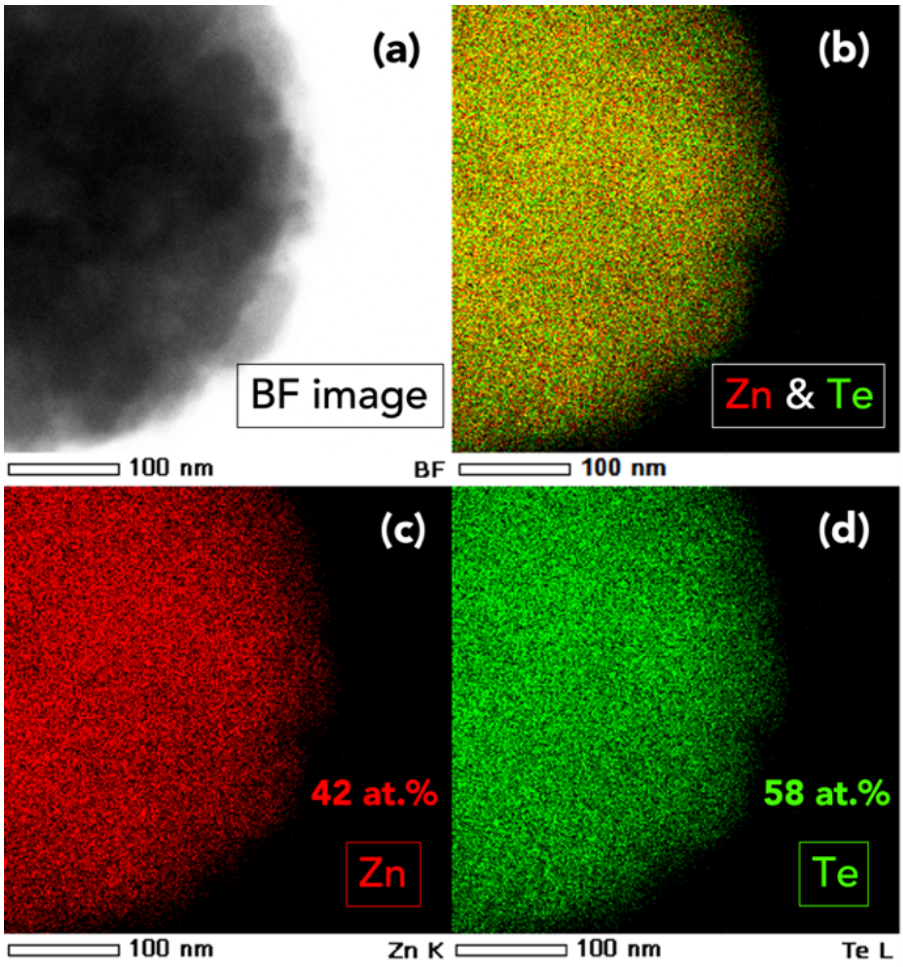


Figure 5.8 (a) STEM bright field image of a ZnTe microsphere in 518PVP(48h). (b) Overlay image of elemental mapping of (c) Zn (Kα line) and (d) Te (Lα line).

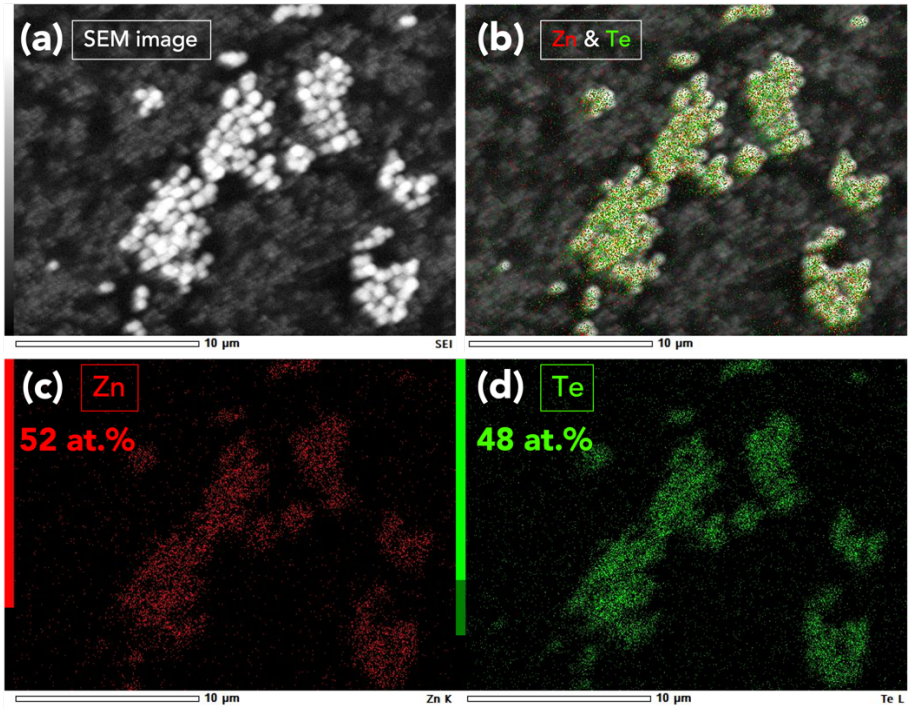


Figure 5.9 SEM image of ZnTe microspheres in 518PVP(48h). (b) Overlay image of elemental mapping of (c) Zn and (d) Te.

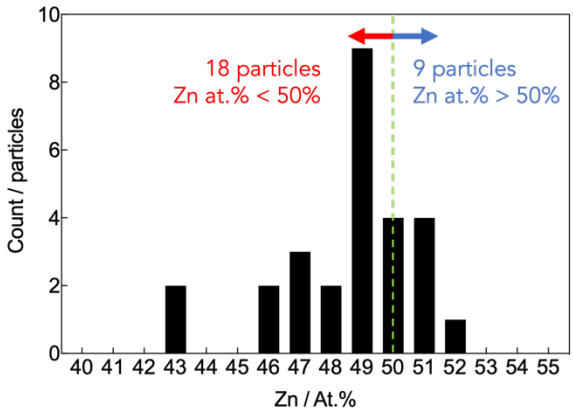


Figure 5.10 Zn content (at. %) among 27 ZnTe microspheres detected by SEM-EDS point analysis.

5.3.3 Relation of PVP amount to the growth of ZnTe microspheres

Initially, it was expected that the size reduction ZnTe microspheres with more PVP used (**Figure 5.3**e-g). However, the size of ZnTe microspheres in 1036PVP(48h) was larger than that in 518PVP(48h). It was considered that the size of ZnTe microspheres might be determined at the earlier time in the reaction. Therefore, syntheses of ZnTe microspheres were further conducted using different amount of PVP for 0.5 h and observed their change of sizes and morphologies under SEM.

Figure 5.11 shows the ZnTe microspheres had been already formed at 0.5 h with many Te rods regardless to the amount of PVP. Size of ZnTe microspheres in 0PVP(0.5h) and 1036PVP(0.5h) were larger than that in 259PVP(0.5h) and 518PVP(0.5h). **Figure 5.12** summarizes the length and diameter of Te rods formed among samples. Both length and diameter of Te rods synthesized without PVP were exceptionally longer than samples synthesized with PVP. It was because PVP is a structure-directing agent.[33-38,44] The selective adsorption of PVP on specific planes of Te crystal restricted the growth of the crystal in certain directions. As a result, 259PVP(0.5h), 518PVP(0.5h) and 1036PVP(0.5h) yielded shorter and thinner Te rods compared with 0PVP(0.5h).[48-50] Moreover, ZnTe microspheres were likely formed at two tips of Te rods when PVP was used in the reaction (**Figure 5.11**b-c). Several research reported that the Te rods grew along the [001]

direction.[37-38,44-46] The tips of Te rods, which were corresponding to the (001) facets, were found to have higher surface energy compared with those at other facets.[47-48] The higher the surface energy, the easier defects form. Therefore, Zn ions/complexes in the surrounding could migrate at those defects easily, forming ZnTe nuclei at two ends of the Te rod. In the case of without using PVP, ZnTe microspheres were not only grew at the tip of Te rod, but also formed at the side and surrounded the Te rods (**Figure 5.11**a). The result suggested that PVP were possibly adsorbed on the sides of Te rods, and they could restrict the ZnTe nucleate on the sides of Te rods. As the ZnTe microspheres were 'grabbing' the Te rods during their growth (**Figure 5.11**a) and almost no Te rods were observed at 48 h (**Figure 5.3**), the Te rods formed at 0.5 h were possibly used as a template for the nucleation and growth of ZnTe. Size of ZnTe microspheres in 0PVP(48h) were the largest (972 ± 159 nm) among samples because the Te rods formed at earlier stage had the largest diameter.

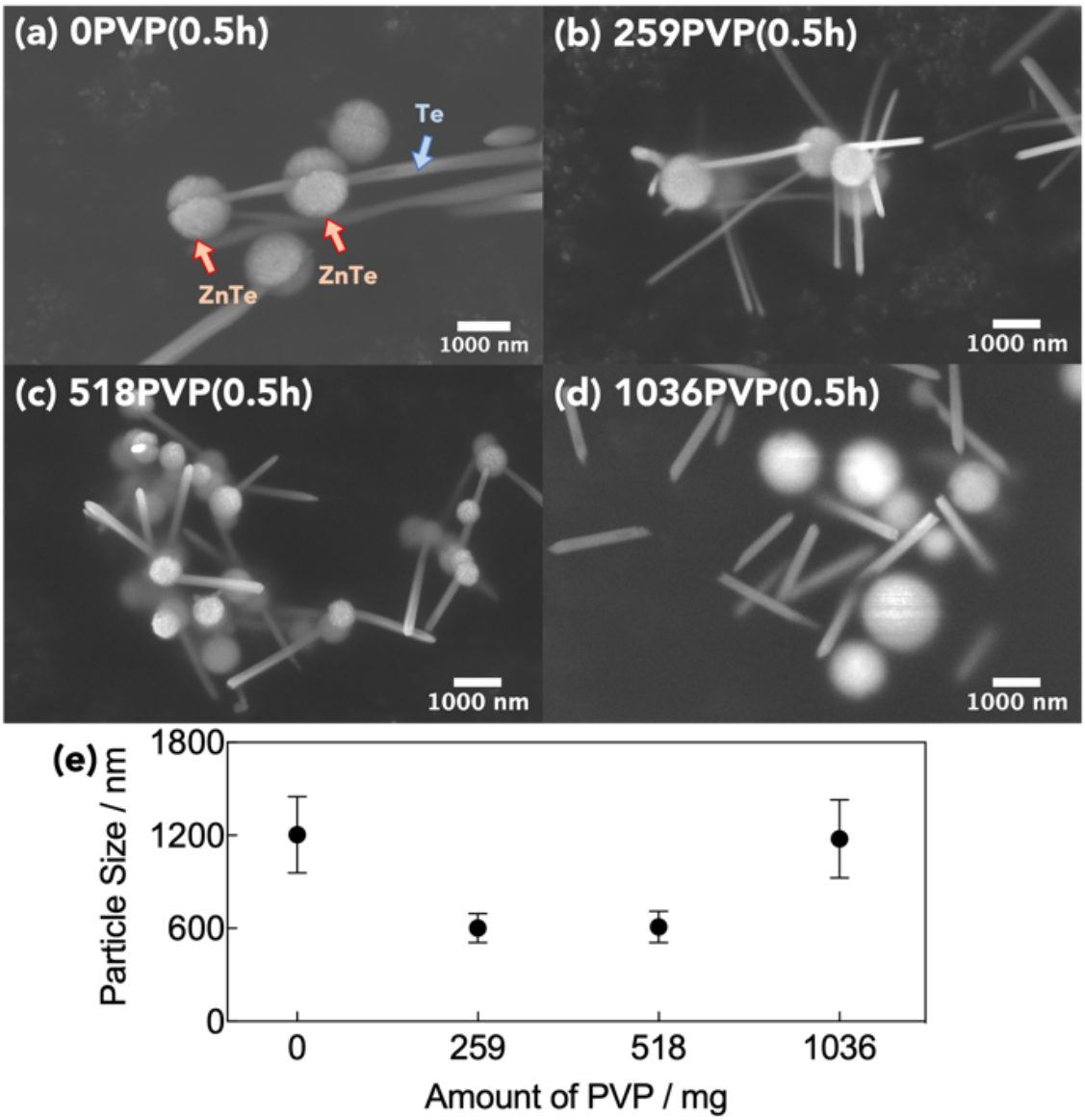


Figure 5.11 SEM images of samples (a) 0PVP(0.5h), (b) 259PVP(0.5h), (c) 518PVP(0.5h), (d) 1036PVP(0.5h). (e) Size of ZnTe microspheres against amount of PVP at reaction time of 0.5 h.

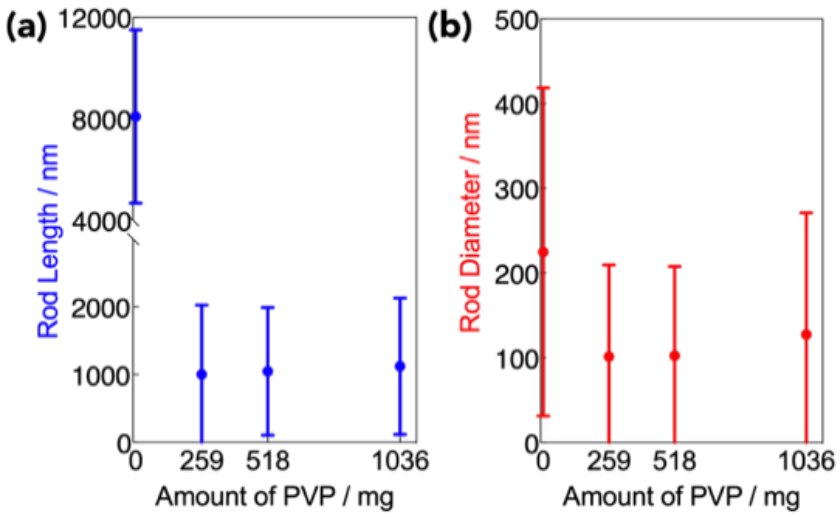


Figure 5.12 (a) Length and (b) diameter of Te rods in samples synthesized for 0.5 h using 0 mg, 259 mg, 518 mg, and 1036 mg of PVP, respectively.

On the other hand, separated ZnTe microspheres and Te rods were observed in 1036PVP(0.5h). The ZnTe microspheres appeared in 1036PVP(0.5h) had already reached to the size close to that in 1036PVP(48h), which revealed that part of the ZnTe nucleated and grew quickly at the first 0.5 h. The particle size was highly determined by the nucleation rate, which faster nucleation yields smaller particles with higher homogeneity.[49] To detailly explain the particle size of ZnTe microspheres against amount of PVP in the reaction, experiments were conducted for 0.2 h. **Figure 5.13** shows XRD results of samples synthesized at 0.2 h and 0.5 h. There were an obvious ZnTe (111) peak in 1036PVP(0.2h) and a very small ZnTe (111) peak in 259PVP(0.2h), whereas both 0PVP(0.2h) and 518PVP(0.2h) only had diffraction peaks matched with Te. The

nucleation and growth kinetics of ZnTe in the system of 1036PVP might be the fastest immediately after the precursor injection process. At 0.5 h, intensity of ZnTe peaks increased significantly in all samples, especially 259PVP and 518PVP (**Figure 5.13**e-h). The relative content of ZnTe existed in each sample was then estimated by calculating the ratio of ZnTe (111)/Te (101) peak intensities, with assuming the intensity of Te (101) peak as 1. Since there was no detectable ZnTe peak in 0PVP(0.2h) and 518PVP(0.2h), the intensities for these samples were set to 0. The total kinetics (nucleation kinetic and growth kinetic) of ZnTe could be postulated by comparing the ratio of peak intensities at 0.2 h and 0.5 h. It should be emphasized that this comparison could not provide information of whether nucleation or growth kinetic contributes more to the ZnTe (111) peak because the peak intensities increased and the FWHM narrowed simultaneously.

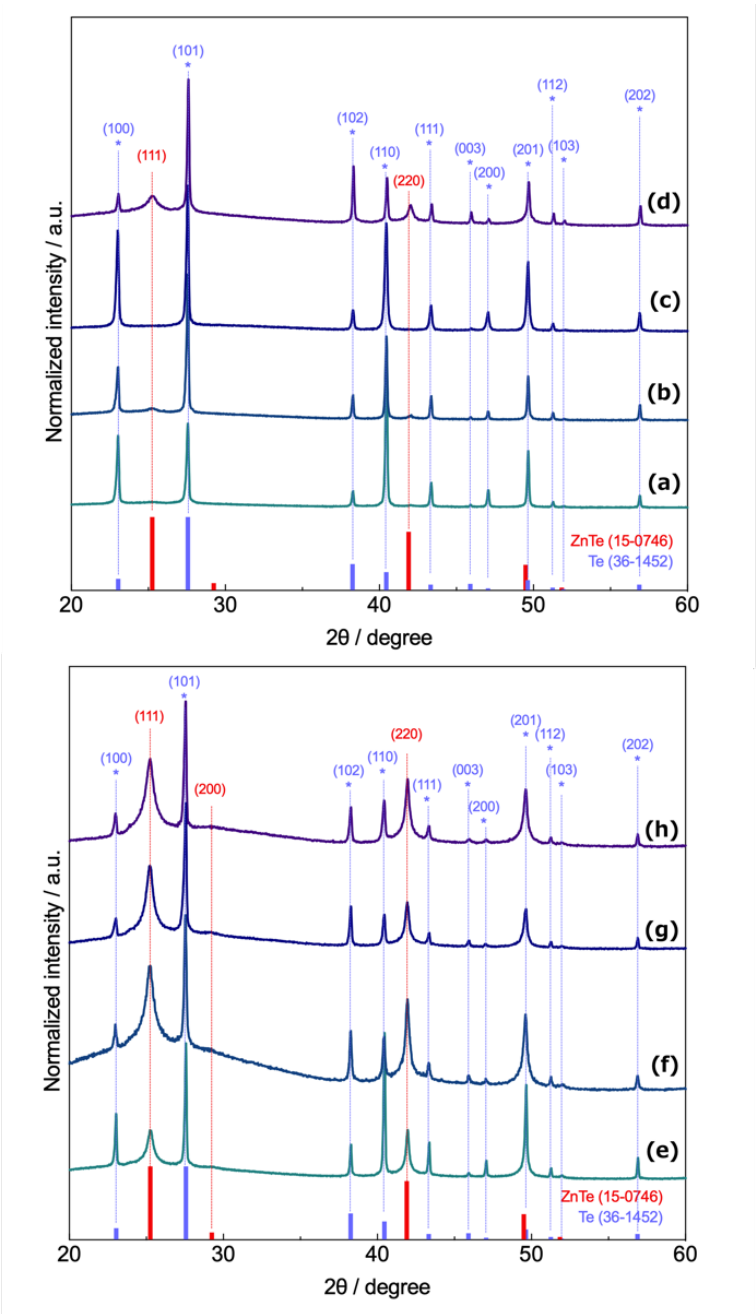


Figure 5.13 XRD patterns of sample (a) 0PVP(0.2h), (b) 259PVP(0.2h), (c) 518PVP(0.2h), (d) 1036PVP(0.2h), (e) 0PVP(0.5h), (f) 259PVP(0.5h), (g) 518PVP(0.5h), (h) 1036PVP(0.5h). Bar charts are reference patterns of ZnTe (JCPDS No. 15-0746) and Te (JCPDS No. 36-1452).

Table 5.4 Estimated relative content of ZnTe in samples synthesized at 0.2 h and 0.5 h based on XRD results in Figure 5.13.

	ZnTe@0.2 h	ZnTe@0.5 h	Increased ZnTe content
0PVP	0 %	32.7 %	32.7 %
259PVP	2.7 %	56.2 %	53.5 %
518PVP	0 %	51.9 %	51.9 %
1036PVP	11.1 %	55.9 %	44.8 %

Table 5.4 lists the estimated relative content of ZnTe in samples at 0.2 h and 0.5 h based on XRD results in **Figure 5.13**. The large particles formed in 0PVP(48h) were not only because of the largest Te rods acted as the sacrificial template for ZnTe grew, but also due to the slowest total kinetics. **Figure 5.14** shows the average particle size of ZnTe in 0PVP increased from 0.2 h to 0.5 h, then decreased from 0.5 h to 48 h, which were possibly caused by the redistribution and reassembly of ZnTe particles. This trend also revealed that the multiple nucleation sites of ZnTe were formed during the reaction until 48 h, causing a broad size distribution.[50] Although the total kinetics of ZnTe were the fastest in 1036PVP at 0.2 h as it had the most significant ZnTe (111) peak, the ZnTe content in 1036PVP from 0.2 h to 0.5 h did not increase as much as that in both 259PVP and 518PVP (**Table 5.4**). Multiple nucleation events were also occurred in 1036PVP (**Figure 5.14**d). As a result, ZnTe microspheres size in 1036PVP(48h) were smaller than

that in 0PVP(48h) but larger than that in 259PVP(48h) and 518PVP(48h). For 259PVP and 518PVP, both the ZnTe content (**Table 5.4**) and ZnTe microsphere sizes (**Figure 5.14**b-c) increased significantly in the time frame from 0.2 h to 0.5 h. Even though 259PVP had higher increased ZnTe content (53.5%) than 518PVP (51.9%) from the estimation in Table 3, Te rods were remained in 259PVP(48h) (**Figure 5.5**b). Also, ZnTe microsphere size in 259PVP changed more from 0.5 h to 48 h (**Figure 5.14**b) compared with 518PVP (**Figure 5.14**c). Therefore, the growth rate of ZnTe in 259PVP samples must be slower than that in 518PVP samples between 0.5 h to 48 h. In other words, 518PVP had the fastest total kinetics between 0.5 h to 48 h as 518PVP(48h) did not contain any Te (**Figure 5.5**c) and ZnTe particle sizes did not changed significantly after 0.5 h. Thus, the smallest-sized homogeneous ZnTe microspheres were yielded in 518PVP(48h).

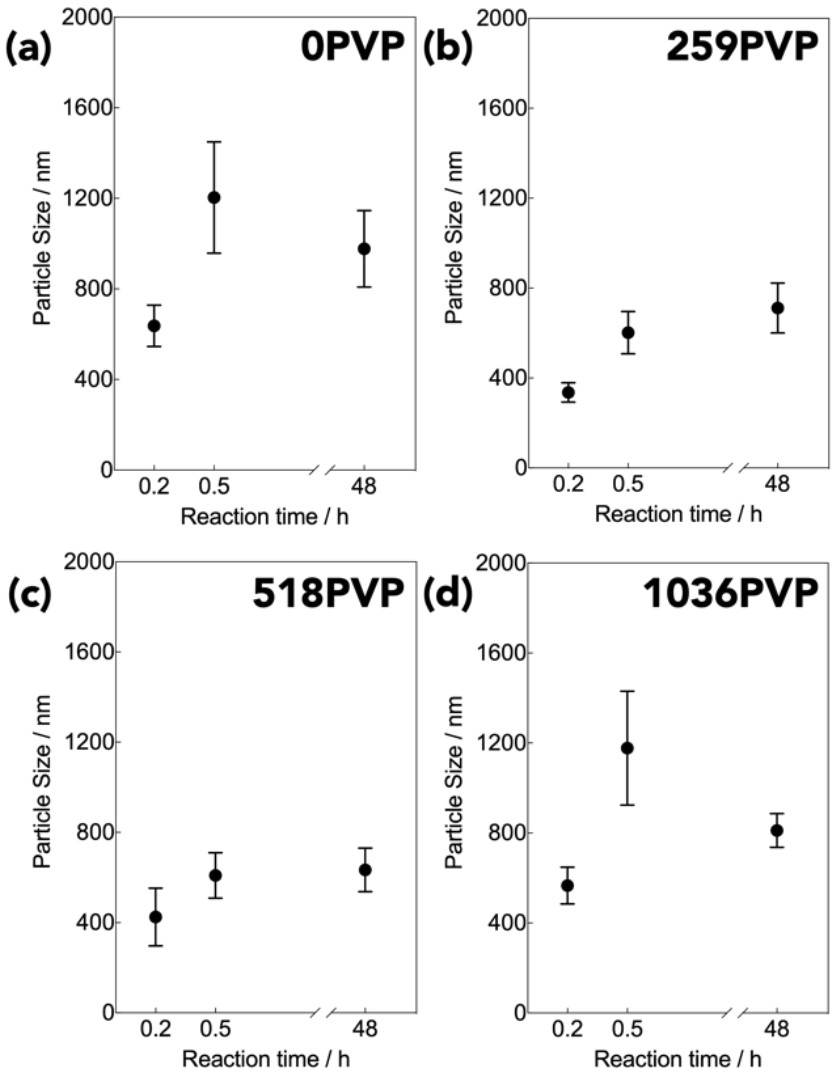


Figure 5.14 ZnTe particle sizes against reaction time of 0.2 h, 0.5 h and 48 h, respectively in sample (a) 0PVP, (b) 259PVP, (c) 518PVP and (d) 1036PVP.

Moreover, the formation kinetics of ZnTe microspheres could be further evaluated from the perspective of the nucleation and growth kinetics of Te(0) in each system. It was because the nucleation and growth of ZnTe required Te^{2-} ions, which were reduced from Te(0).[15,18] Experiments were conducted with only injecting Te precursor to the EG-PVP mixture. The growth of Te in 3 min were studied among samples. The crystallinity of Te was higher in 0PVP and 1036PVP than that in 259PVP and 518PVP (**Figure 5.15**). Te rods were mostly observed in the microscopic images of 0PVP (**Figure 5.16**a) and 1036PVP (**Figure 5.16**d). Contrastively, Te wires/rods with few nanometers in diameter with small particles surrounded them were found in 259PVP and 518PVP (**Figure 5.16**b-c). The EDS spectra revealed that small particles in **Figure 5.16**c had low Te content, and the SAED pattern suggested that these small particles were not well-crystalized (Inset of **Figure 5.17**a). These small particles might be the Te nuclei that could further growth into Te wires/rods in longer reaction time. The result demonstrated that amount of PVP could significantly affect the nucleation and crystal growth of Te rods, and particularly the growth of Te was slower in 259PVP and 518PVP for reaction time of 3 min. Therefore, the formation of Te^{2-} ions and the nucleation of ZnTe were happened at a later time in the 259PVP and 518PVP systems. Although Te nucleated and growth faster in 0PVP and 1036PVP in 3 min, the reaction kinetics of ZnTe for longer reaction time

were slower in these systems as discussed above. Thus, larger ZnTe microspheres were yielded in the products of 0PVP(48h) and 1036PVP(48h).

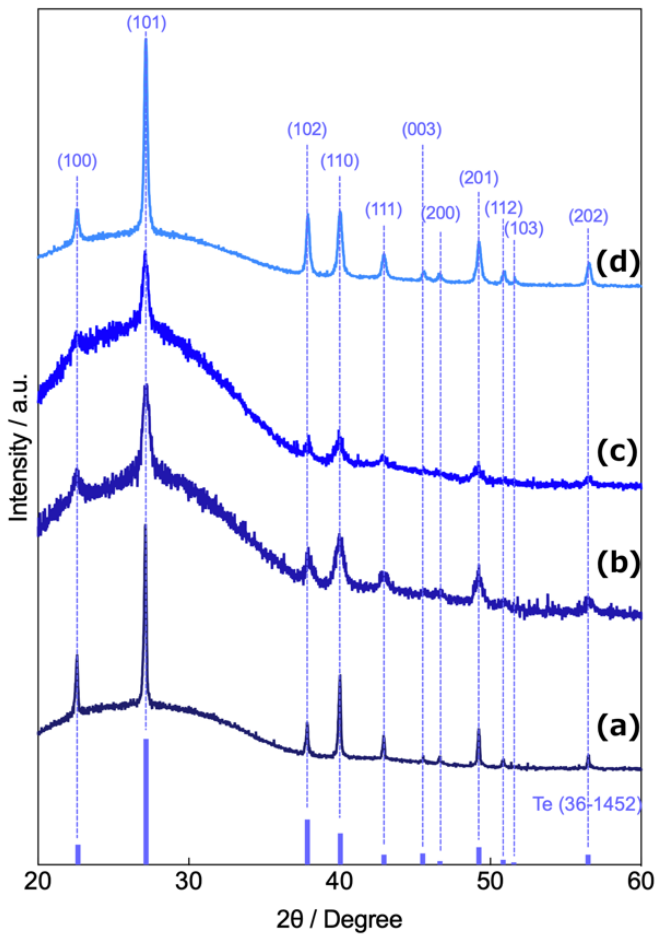


Figure 5.15 XRD patterns of Te formed at reaction time of 3 min in the systems (a) 0PVP, (b) 259PVP, (c) 518PVP, (d) 1036PVP. Bar chart is a reference pattern of Te (JCPDS No. 36-1452).

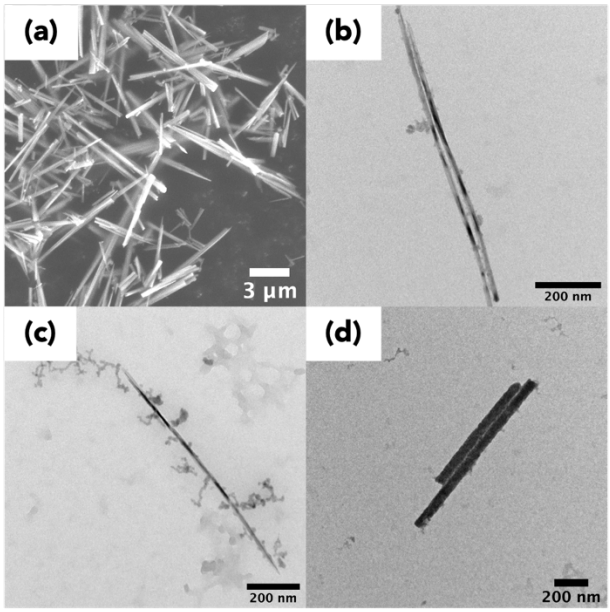


Figure 5.16 (a) SEM image of Te rods synthesized for 3 min with 0 mg of PVP. TEM images of Te rods synthesized for 3 min with (b) 259 mg, (c) 518 mg and (d) 1036 mg of PVP, respectively.

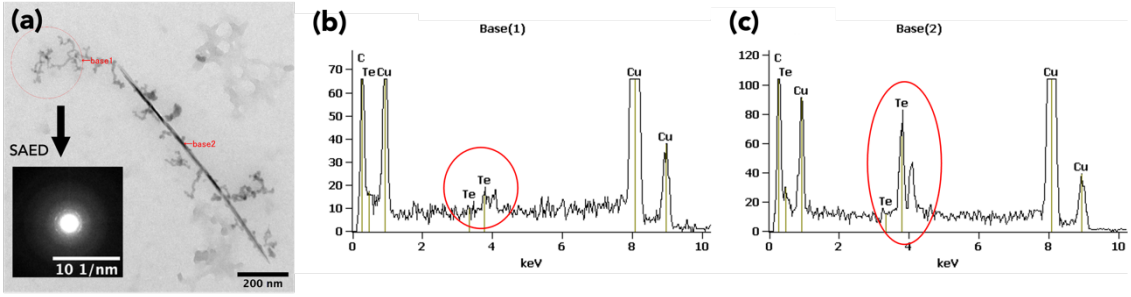


Figure 5.17 (a) Indicating the target sites ‘base1’ and ‘base2’ of taken EDS spectra in Figure 5.16c. Inset is the SAED pattern taken from area indicated with a red circle. EDS spectra of (b) ‘base1’ and (c) ‘base2’ indicated in (a).

5.3.4 Consideration of formation process of ZnTe microspheres

ZnTe microspheres in 518PVP(0.5h) were not simply contacted with the Te rods, but they were likely 'stabbed' by the rods (**Figure 5.11**c). This might be the origin of the hole on some microspheres (**Figure 5.3**). To further investigate the formation of ZnTe microspheres from Te rods as the template, samples were synthesized with using parameters of 518PVP but changing the reaction time. **Figure 5.18** and **Figure 5.19** show the XRD patterns and SEM images of samples synthesized from 0.2 h to 48 h, respectively. At 0.2 h, Te wires/rods and some particles were already formed (**Figure 5.19**a), which were in larger size compared with that formed in 3 min (**Figure 5.16**c). At 0.5 h, the intensity of ZnTe (111) characteristics peak increased significantly, yet Te was still the major substance in the product (**Figure 5.18**b). Particles linked to the Te rods were commonly found under SEM (**Figure 5.19**b). The average size of particles increased from 425 nm to 609 nm from 0.2 h to 0.5 h. STEM-EDS elemental mapping was performed for the particle-and-rod structured in 518PVP(0.5h) (**Figure 5.20**). The particle was a ZnTe microspheres, with a Te rod 'stabbing' it. At 1 h, 518PVP(1h) had a more significant ZnTe (111) characteristics peak (**Figure 5.18**c), and more spherical particles and less rods can be found under SEM (**Figure 5.19**c). **Figure 5.21** summarizes the dimensions of Te rods and sizes of ZnTe particles synthesized at 0.2, 0.5, 1 h based on the size measurement

with SEM images. The aspect ratio (AR) of Te rods formed at 0.2 h was 27.7 ± 15.0. The formation of thin Te rods might be owing to incomplete conversion from TeO_3^{2-} to Te(0). At 0.5 h, the AR of Te rods decreased to 9.9 ± 2.7, due to the increase in diameter and the decrease in length of Te rods simultaneously. The increase in diameter of Te rods could be assigned to that more TeO_3^{2-} ions had been reduced to Te(0) with longer reaction time, so that Te rods were able to growth wider. Meanwhile, nucleation and growth of ZnTe were likely occurred at the tips of Te rods, so the consumption of Te for the ZnTe formation yielded shorter Te rods. At 1 h, the diameter and length of Te rods further decreased (average AR = 9.2 ± 3.0) while ZnTe microsphere size increased. The dimensions of Te rods were not traceable anymore when the reaction time was prolonged to 2 h onwards (**Figure 5.19**d). XRD results also showed the ZnTe peak had narrower full width at half maxima (FWHM) and higher intensity than Te peak with longer reaction time. Simultaneously, Te peak had a wider FWHM and diminished completely as the reaction time reached to 24 h (**Figure 5.18**g). It can be concluded that the Te rods were consumed for the formation of ZnTe microspheres. This involved the dissolution of Te to form Te^{2-} with longer reaction time by the reducing ability of EG at high temperature, which subsequently combined with Zn^{2+} ions or $[Zn(en)_3]^{2+}$ complexes in the surrounding to form ZnTe nuclei. From the SEM image of 1036PVP(0.5h) (**Figure 5.11**d), the

separated ZnTe microspheres and Te rods suggested that one ZnTe microsphere was not necessary formed by one Te rod. We considered that the detachment of the ZnTe microsphere from the tip of Te rod was occurred when the ZnTe microsphere had finished the growth. Then, another ZnTe nucleus formed and grew at the tip of the remained Te rod again, forming another ZnTe microsphere.

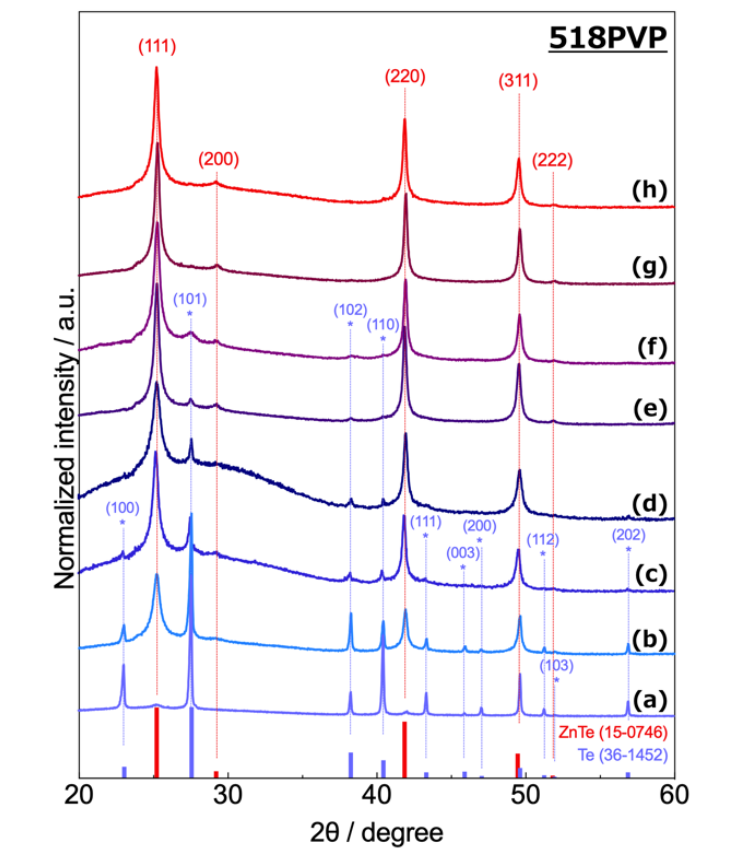


Figure 5.18 XRD patterns of samples 518PVP synthesized at (a) 0.2 h, (b) 0.5 h, (c) 1 h, (d) 2 h, (e) 6 h, (f) 12 h, (g) 24 h and (h) 48 h. Bar charts are reference patterns of ZnTe (JCPDS No. 15-0746) and Te (JCPDS No. 36-1452).

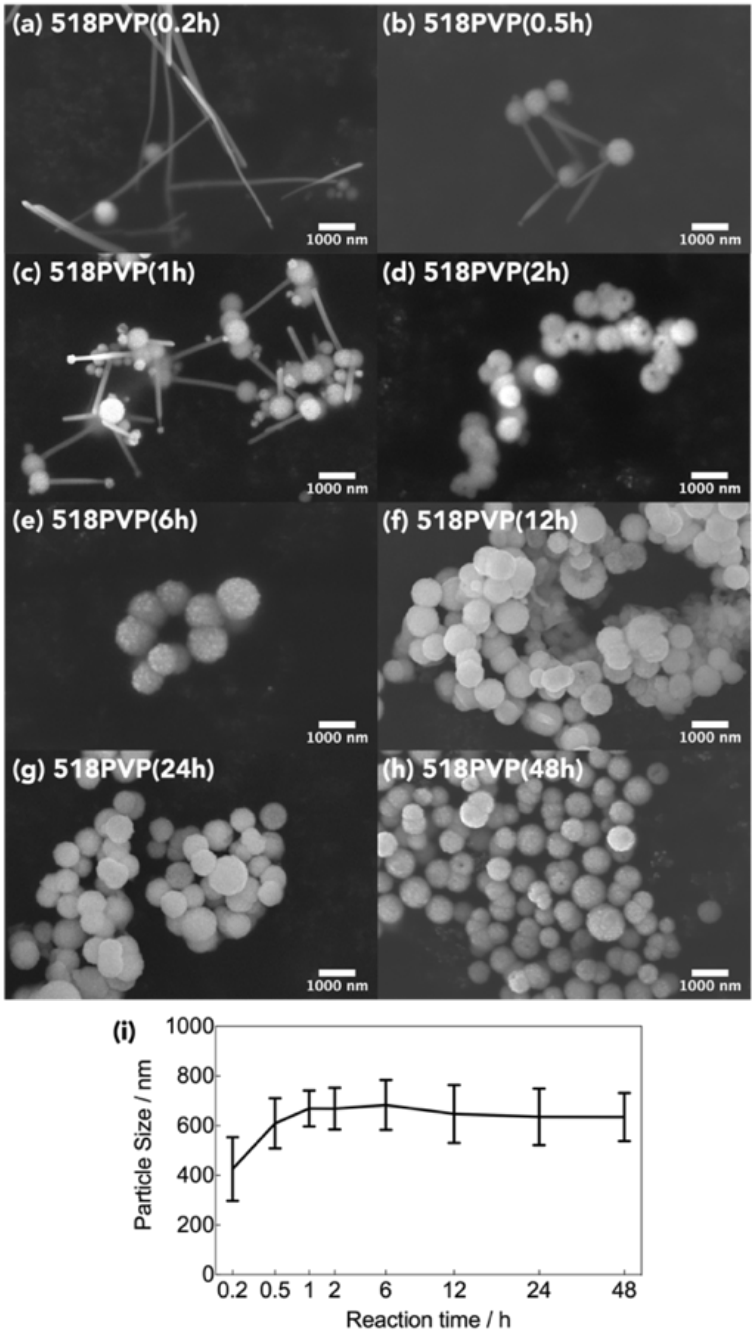


Figure 5.19 SEM images of samples 518PVP synthesized at (a) 0.2 h, (b) 0.5 h, (c) 1 h, (d) 2 h, (e) 6 h, (f) 12 h, (g) 24 h, and (h) 48 h. (i) Size of ZnTe microspheres against reaction time from 0.2 h to 48 h.

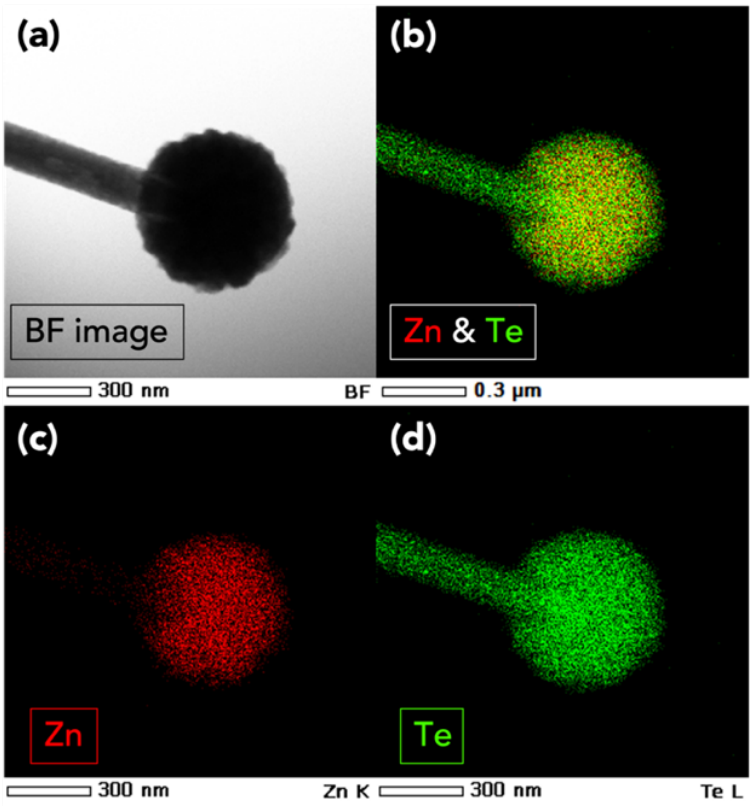


Figure 5.20 (a) STEM bright field image of a Te rod and ZnTe particle in 518PVP(0.5h). (b) Overlay image of elemental mapping of (c) Zn and (d) Te.

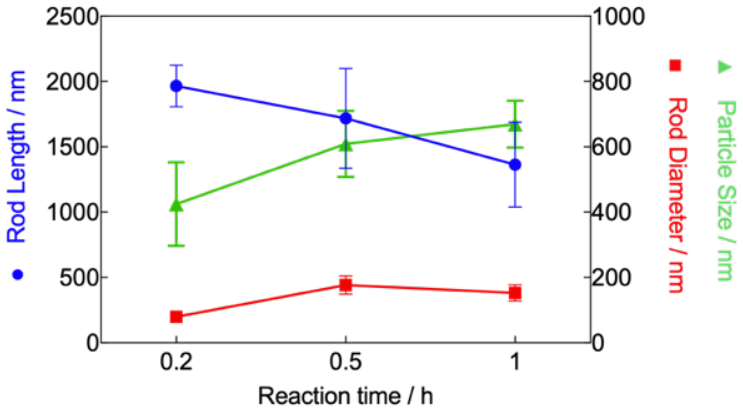


Figure 5.21 Te rod (dot) length, (square) diameter, (triangle) size of microspheres of samples 518PVP against reaction time from 0.2 h to 1 h.

The inner structures of ‘Te rod-stabbed’ ZnTe microspheres were of interest (**Figure 5.20**). HVEM images clearly showed that the tip of Te rod had reached to the center of ZnTe microspheres (**Figure 5.22**a). We made efforts to obtain atomic resolution image of the interface of Te rods and ZnTe microspheres, but a rapid destruction of Te rods was happened when they were focused by the electron beam at a higher magnification (**Figure 5.22**b-c). Generally, Te has a melting point at about 450 °C.[51] The thermal energy generated by the ablation of the intense accelerating electron beam to the Te rods under vacuum might be exceeded this temperature; nor the Coulomb explosion happened in the telluride compounds under an electron beam.[52] This caused the difficulties of taking high resolution images of the Te-ZnTe interface. Furthermore, a low contrast region was always found at the tip of Te rods compared with the region that far from the tip (**Figure 5.22**d-f). The difference in contrast was found regardless of whether the Te rods had ZnTe microspheres formed at their tips or not (**Figure 5.22**d-f). The low contrast region nearby the tips might be owing to the less Te content because the tips were junctions for supplying Te^{2-} ions for the nucleation and growth of ZnTe. Furthermore, TEM images of the ultra-microtome specimens clearly showed that the tips of Te rods were all-round encapsulated by the ZnTe particles (**Figure 5.22**g-i). Some Te rods were detached from the resin during the ultra-microtome processing and the

remained Te rods in the specimens also experienced rapid destruction under electron beam irradiation at 200 kV with magnification higher than 400 kx. It is believed that extra efforts are needed to prevent the destruction of Te during the TEM and/or HVEM observation for studying the atomic lattices of how the ZnTe nucleated and growth at the tips of Te rods. For example, using a cyro-TEM holder for better heat dissipation in the sample grid, which would be the future work of this study.

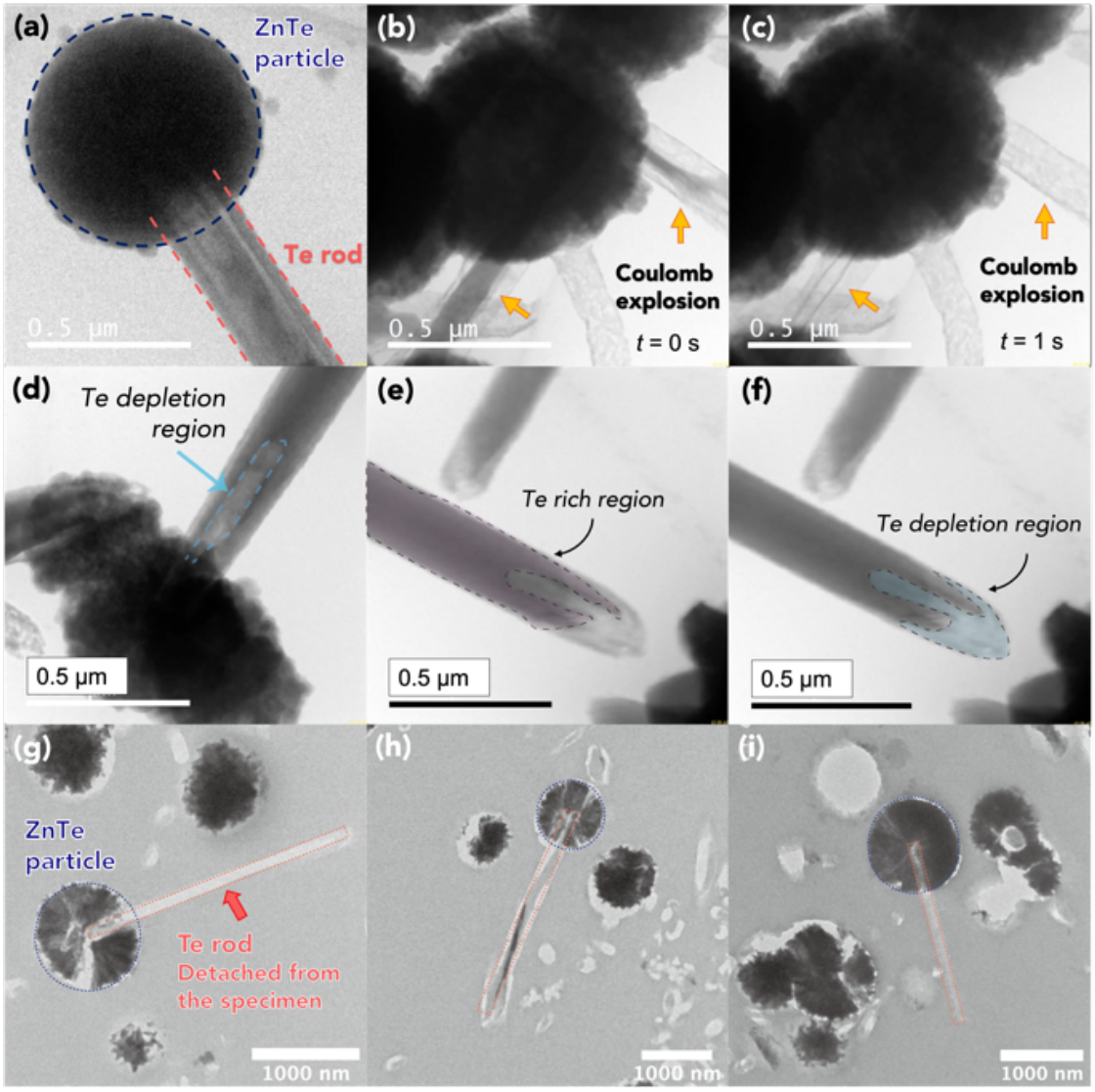


Figure 5.22 (a-f) HVEM micrographs of 518PVP(0.5h). (b-c) Rapid destruction occurred at Te rods (indicated with arrows) in a second. (d) Regions with different contrast on Te rods: (e) High contrast region and (f) low contrast region. (g-i) TEM micrographs of cross-sectional specimens fabricated with the ultra-microtome from the resin embedded 518PVP(0.5h) sample. Voids at the Te rods region is due to the detachment of Te rods from the specimen. Dashed lines are guides for the eyes.

In addition, ZnTe microsphere shown in **Figure 5.7**a and **Figure 5.23** had voids at its central region. Ehsan *et al*. claimed that the hollow structure was formed by oxygen gas released from ZnTe microspheres during the inward diffusion process of small-sized rods into the spheres.[15] Since no PVP were used in their study, ZnTe could nucleate and growth on any part of the Te rods. The growth of ZnTe subsequently resulted in small-sized rods, which were eventually 'digested' by the ZnTe microspheres.[15] Instead, the growth mechanism of ZnTe microspheres in PVP-contained EG solvent was concerned in this study. Firstly, TeO_3^{2-} ions were reduced to Te(0) in the form of rods. The Te rods were in hexagonal structure in principle. Due to the adsorption of PVP at sides of Te rods, and the lower surface energy of sides compared with the tips of Te rods, ZnTe preferably nucleated at the tips of Te rods. Secondly, ZnTe crystals started to growth and were like building blocks to construct the ZnTe microsphere, which was possibly driven by the oriented attachment.[18] Formation of voids in the ZnTe microsphere could be explained in three ways – (i) The ZnTe crystals would growth into larger size and small crystalline/amorphous ZnTe were formed simultaneously in longer reaction time. These early formed crystals blocked the further diffusion of Zn ions from outside to the inner part of the microspheres. Te^{2-} ions were continuously reduced by EG under high temperature. These Te^{2-} ions dissolved in the solvent and encountered with Zn^{2+} for the

further nucleation and growth of ZnTe, and left a cavity inside the ZnTe microspheres (**Figure 5.24**).[53-56] (ii) When both Zn and Te atoms diffused during the growth of ZnTe, the difference of diffusion rate resulted in voids and cavities in the ZnTe microsphere.[57-59] (iii) Hollow-structured Te tubes might be formed.[60-61] The 3D diagram (constructed through the FIB-SEM in **Figure A5.1**) showed that some Te rods had hollow structure and the hollow part could not supply any Te^{2-} ions to the center of the ZnTe microspheres, resulted in voids and cavities. Then, the ZnTe microsphere would detach from the Te rod in a vigorously stirred solution once the cavities were large enough to break the junction of Te rod and ZnTe microsphere. Therefore, ZnTe microspheres with voids were observed. This hypothesis of the detachment of ZnTe microspheres from Te rods was advocated by the hexagonal pore found in the cross-sectional image of some ZnTe microspheres, which was matched with the hexagonal structure of Te rods (**Figure 5.25**). The nucleation and growth for another ZnTe microsphere continuously occurred at the tips of the remained Te rods in the solution, which became smaller in sizes throughout the reaction. Eventually, all Te rods were consumed with longer reaction time and only ZnTe microspheres left as the final product.

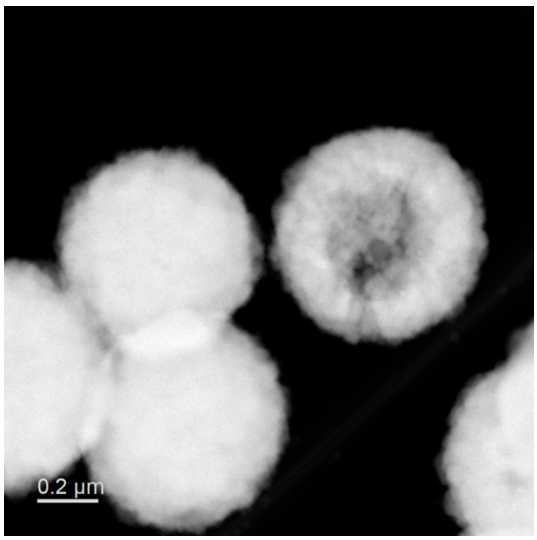


Figure 5.23 STEM-HAADF image of ZnTe microspheres in 518PVP(48h).

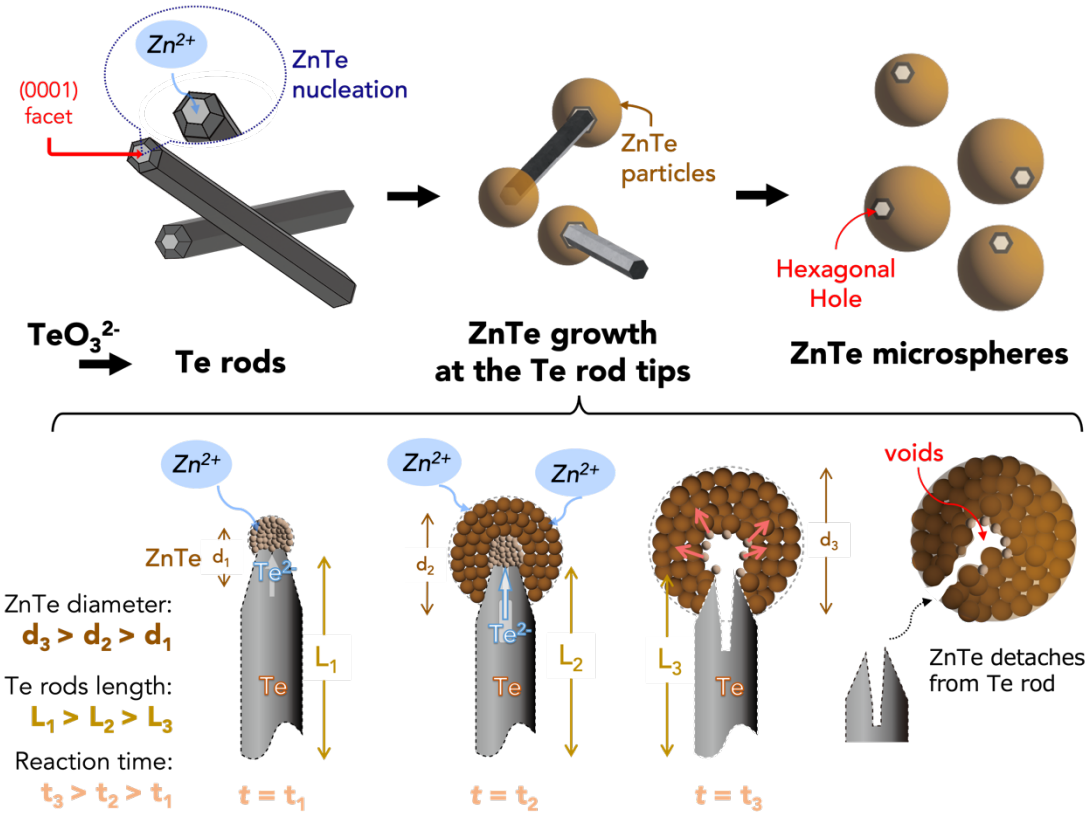


Figure 5.24 Schematic diagram of the formation process of ZnTe microspheres in PVP-contained EG.

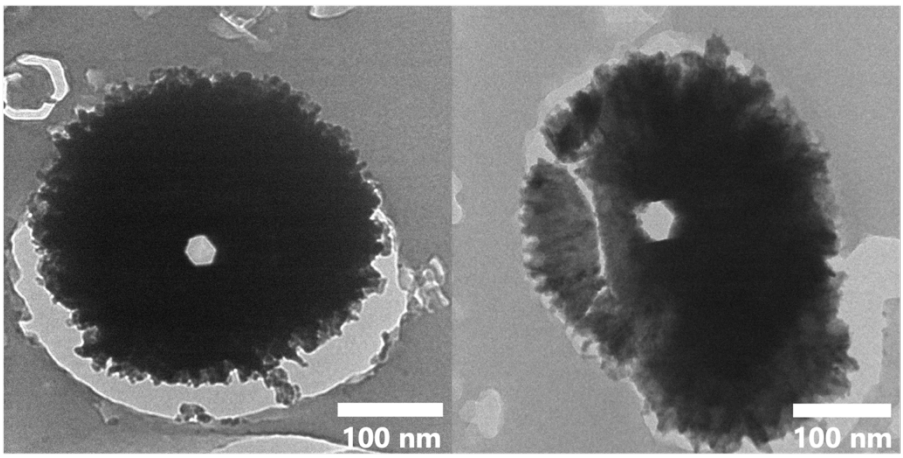


Figure 5.25 A hexagonal pore appeared at the central region of the cross-section of ZnTe microspheres.

5.3.5 Effect of reaction temperature to the microspheres' formation

Syntheses at temperature 160 and 180 ℃ were carried out (amount of PVP = 518 mg) and compared with that at 200 ℃. Reaction temperature higher than 200 ℃ was not selected because it is far too much from the boiling temperature of ethylene glycol (197 ℃). SEM images of obtained products are shown in **Figure 5.26.**

In case of 160 ℃, many Te rods were remained after reacted for 48 h (Figure 19a-b). At this temperature a part of Te was reduced to Te^{2-} by ethylene glycol. Small amount of ZnTe microspheres were obtained. The under-growing ZnTe microsphere at the tip of Te rods (**Figure 5.26**a) and ZnTe microspheres with sized ~2 μm were observed (**Figure 5.26**b). In case of 180 ℃, syntheses were carried out for 6 h and 48 h of reaction time respectively. At 6 h, different-sized ZnTe microspheres with many small-sized Te

rods were observed (**Figure 5.26**c-d). The sizes of ZnTe microspheres varied largely, the largest ZnTe microspheres had diameter exceeded 2 μm. At 48 h, ZnTe microspheres were mostly obtained (Figure 19e-f) with a little trace of Te. No ZnTe microsphere larger than 2 μm was found. The average size of obtained ZnTe microspheres was 1015 ± 121 nm, smaller than that obtained at 160 ℃ and larger than that obtained at 200 ℃ (634 ± 97 nm). This result suggests that more robust nucleation occurred at a higher temperature, which is related to the increase of the reducing power of ethylene glycol. At 160 ℃, robust nucleation of Te from TeO_3^{2-} (E_0 = -0.57 V vs SHE)[41] was not favorable, that yielded Te rods with inhomogeneous morphologies. It was even more difficult to further reduce Te to Te^{2-} (E_0 = -1.143 V vs SHE)[42] to form ZnTe. The most robust nucleation at 200 ℃ resulted in the smallest ZnTe microspheres. It is noted that at 180 ℃, many Te rods still remained at 6 h. The obtained ZnTe microspheres at 6 h were larger than that at 48 h. Redistribution and reassembly of ZnTe microspheres were happened from 6 h to 48 h, that involved the multiple nucleation events.

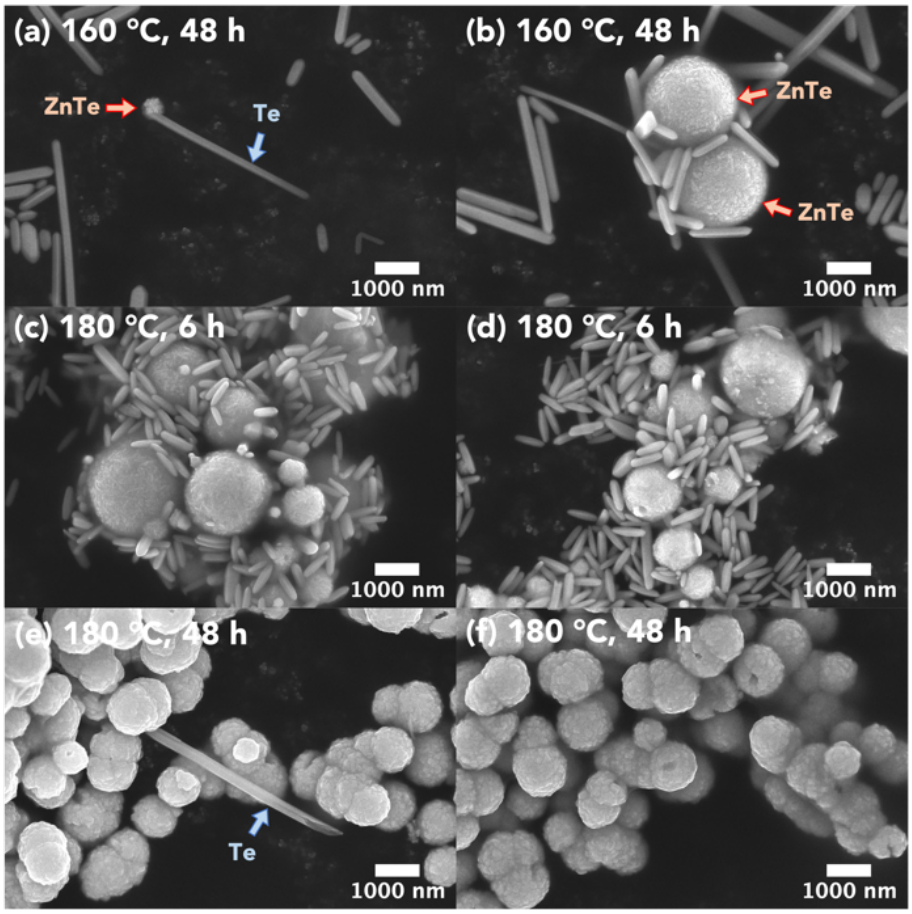


Figure 5.26 SEM images of products obtained at temperature (a-b) 160 ℃ for 48 h and 180 ℃ for (c-d) 6 h and (e-f) 48 h.

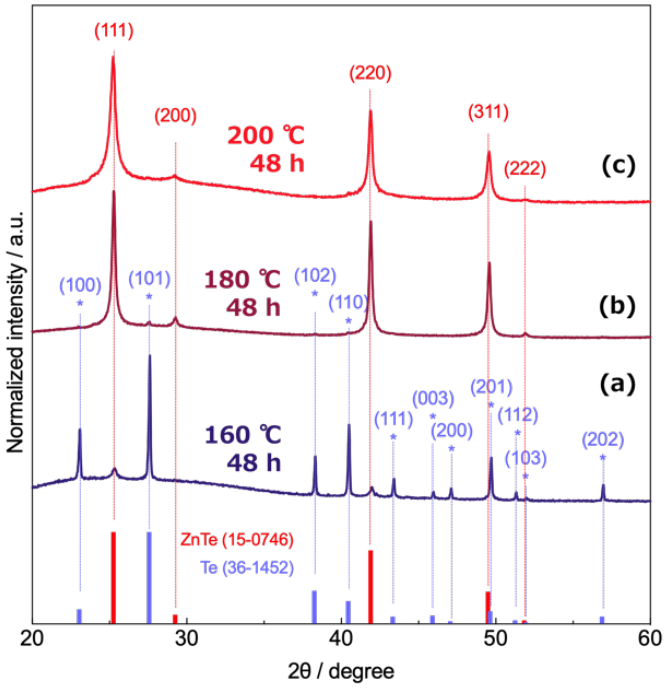


Figure 5.27 XRD patterns of products obtained at temperature (a) 160 ℃, (b) 180 ℃, and (c) 200 ℃ for 48 h.

Figure 5.27 show the XRD patterns of products synthesized at different temperatures for 48 h. The crystalline size calculated with full width at half maximum of ZnTe (111) obtained at 180 ℃ was 27.7 nm, larger than that obtained at 200 ℃ (16.2 nm). When synthesizing nano/micro particles using chemical reduction method, high reactive temperature increases the total reaction rate – nucleation and growth rates. The residual Te at 180 ℃ suggested that the formation of ZnTe did not complete. According to the XRD results, high temperature (200 ℃) was conducive to nucleation of ZnTe, whereas low temperature (180 ℃) was favorable for the growth of ZnTe crystals. Therefore, both

diameter of ZnTe microspheres and their crystalline size increase with decreasing the reaction temperature.

5.3.6 Effect of concentration of Na_2TeO_3 to the microspheres' morphologies

Syntheses were carried out using different amount of Na_2TeO_3 (0.16, 0.20 and 0.24 mmol) with fixed amount of $ZnCl_2$ (0.20 mmol) in the precursor solution (amount of PVP = 518 mg, reaction time = 48 h, temperature = 200 °C). The higher the concentration of Na_2TeO_3, the larger sized ZnTe microspheres were obtained. The particle sizes was 950 ± 114 nm for 0.20 mmol of Na_2TeO_3 (**Figure 5.28**a) and 1868 ± 395 nm for 0.24 mmol of Na_2TeO_3 (**Figure 5.28**b), which were larger than 634 ± 97 nm for 0.16 mmol of Na_2TeO_3. Residual Te rods were found in products obtained with equal or higher molar amount of Na_2TeO_3 compared with that of $ZnCl_2$. There were two reasons for obtaining larger-sized ZnTe microspheres with higher concentration of Na_2TeO_3 – (i) larger Te rods formed with more TeO_3^{2-} ions. When ZnTe nucleated and started to grow at Te rods' tips, a larger Te rod could supply more Te^{2-} ions for the growth of larger ZnTe microspheres before the microsphere detached from the rod. (ii) Dispersion of Te rods onto ZnTe microspheres' surfaces. These findings were consistent with the results by Ehsan *et al.* as they also obtained larger ZnTe microspheres when using higher

concentration of Na_2TeO_3.[15] Additionally, no obvious change in crystalline sizes of ZnTe was found with varying the concentration of Na_2TeO_3 according to XRD results (**Figure 5.28**c). This suggests that the crystalline size is more related to the reaction temperature than the Te to Zn molar ratios.

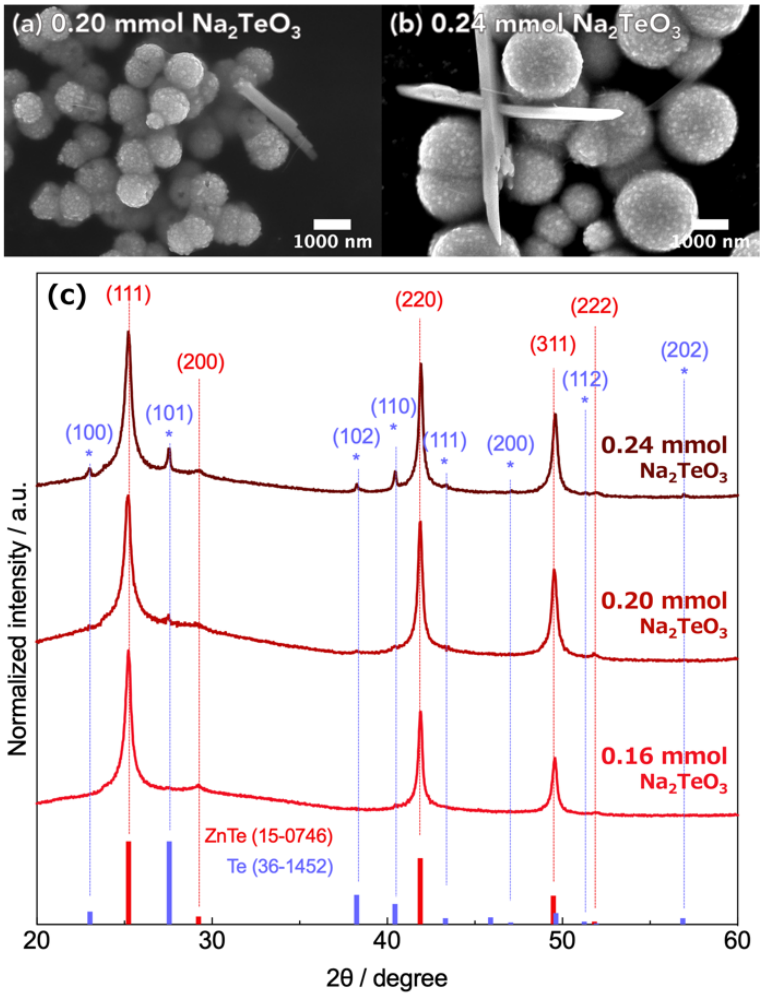


Figure 5.28 SEM images of 518PVP(48h) synthesized using (a) 0.20 mmol and (b) 0.24 mmol of Na_2TeO_3 in the precursor solution. (c) The corresponding XRD patterns. Bar charts are reference patterns of ZnTe (JCPDS No. 15-0746) and Te (JCPDS No. 36-1452). Amount of $ZnCl_2$ = 0.20 mmol, reaction temperature = 200 ℃.

5.3.7 $Zn(CH_3COO)_2$ as the Zn precursor

Sizes and morphologies of ZnTe microspheres synthesized using $Zn(CH_3COO)_2$ as the Zn source was used to compared with that using $ZnCl_2$. Although Wu *et al*. obtained ZnTe in different morphologies by using same content of PVP and solvents but different Zn precursors [16], ZnTe in spherical shape regardless the choice of precursors were obtained in this study. The average size of ZnTe microspheres synthesized with $Zn(CH_3COO)_2$ is 524 ± 61 nm, which was smaller than that synthesized using $ZnCl_2$ (**Figure 5.29**a). TEM image (**Figure 5.29**b-c) shows the ZnTe microspheres were polycrystalline. Smaller crystalline size of ZnTe was yielded by using $Zn(CH_3COO)_2$ (9.8 nm) compared with using $ZnCl_2$ (16.2 nm) through calculation with ZnTe (111) peak from XRD results (**Figure 5.29**d). The CH_3COO^- ions would be the key role of forming smaller ZnTe microspheres. Also, Te was not completely reduced at 48 h. The incomplete reaction might be due to some stable coordination phases formed when $Zn(CH_3COO)_2$ was used. The formation process of ZnTe microspheres that using $Zn(CH_3COO)_2$ as the precursor is worth studying in the future.

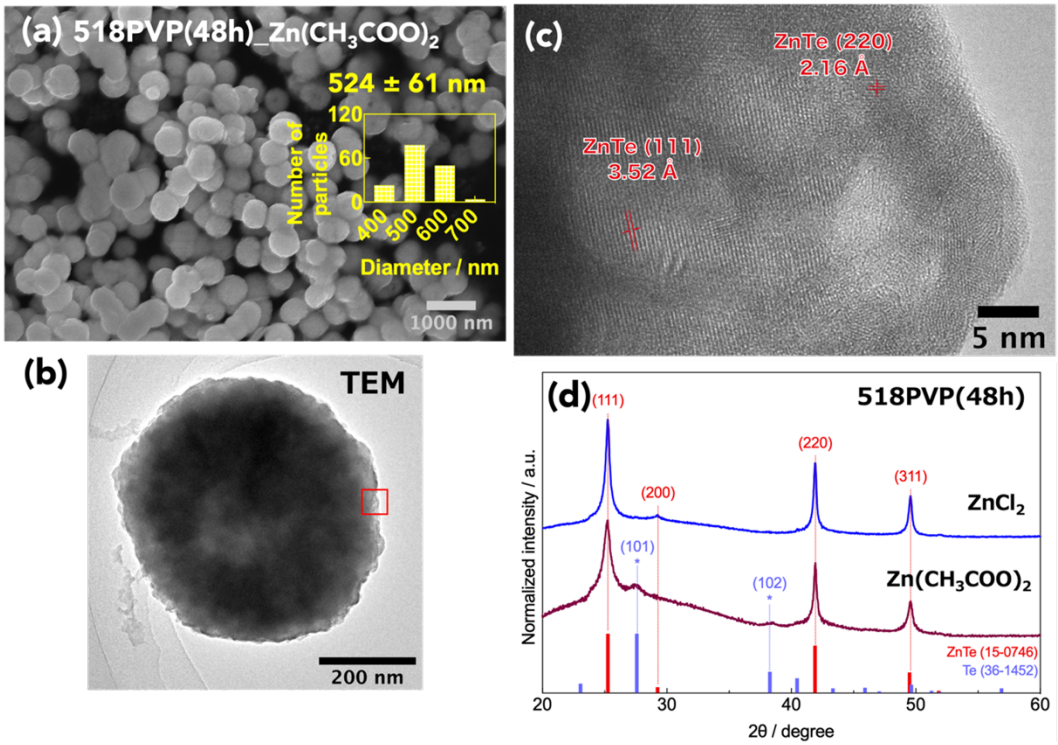


Figure 5.29 (a) SEM image (inset is the size distribution), TEM images (b) at low magnification and (c) at high magnification of the area marked in (b). (d) XRD pattern of the ZnTe microsphere sample 518PVP(48h) synthesized using $Zn(CH_3COO)_2$ (Amount of PVP = 518 mg, reaction time = 48 h, reaction temperature = 200 °C). XRD pattern of $ZnCl_2$ is attached for comparison. Bar charts are reference patterns of ZnTe (JCPDS No. 15-0746) and Te (JCPDS No. 36-1452).

5.3.8 Effect of en to the microspheres' morphologies

The importance of moderate amount of en for making ZnTe microspheres was also demonstrated. Same experimental parameters as synthesizing 518PVP(48h) to make ZnTe microspheres but doubled the amount of en in the precursor solution *i.e.*, EG = 2.36 mL and en = 1.28 mL. The size of ZnTe microspheres did not change significantly (669

± 72 nm) (**Figure 5.30**a). However, some small structures attached on the microspheres made the surface of particles looked rougher than that obtained using 0.64 mL of en. It was because en is a commonly used reducing agent [62-64], extra amount of en would affect the reaction kinetics, and thus alternated the size-homogeneity of ZnTe microspheres. TEM image (**Figure 5.30**b-c) shows the obtained ZnTe microspheres were polycrystalline. No residual Te was observed with additional en from the XRD result (**Figure 5.30**d). The findings suggested that using an appropriated amount of en in the precursor solution is the key factor for making homogeneous ZnTe particles with a smooth spherical morphology. This study hereby suggests using 0.64 mL of en can effectively yield the sized-homogeneous ZnTe microspheres.

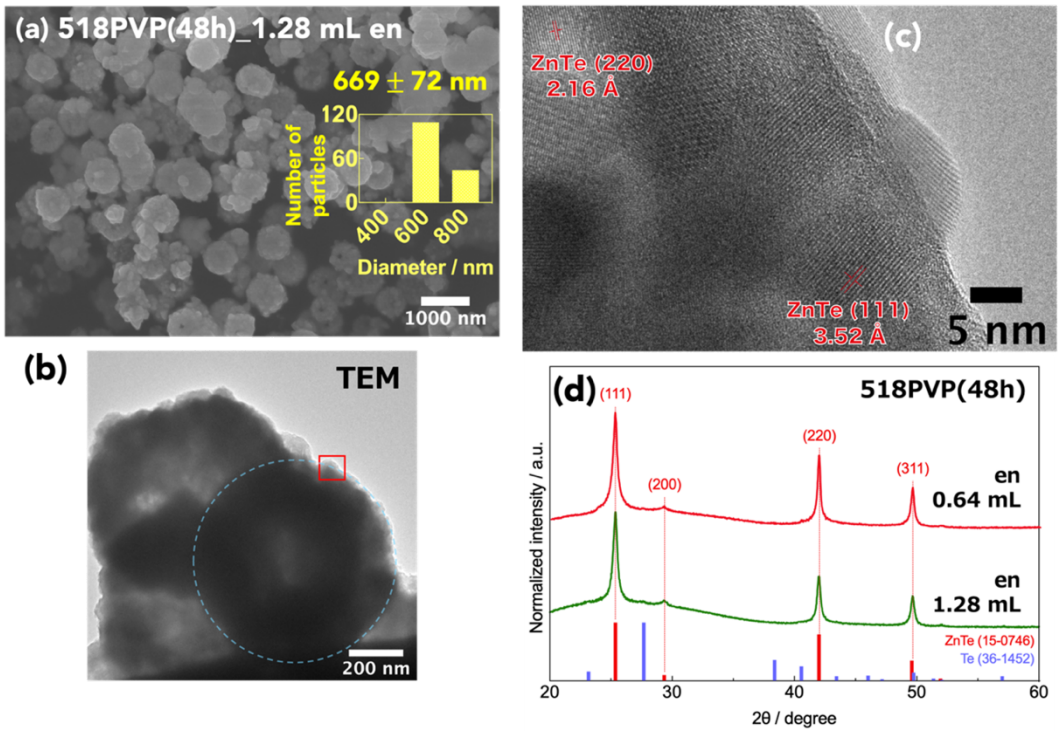


Figure 5.30 SEM image (inset is the size distribution), TEM images (b) at low magnification (dashed line is a guide for eyes to identify a ZnTe microsphere) and (c) at high magnification of the area marked in (b). (d) XRD pattern of the ZnTe microsphere sample 518PVP(48h) synthesized using doubled amount (1.28 mL) of en in the precursor solution (Amount of PVP = 518 mg, reaction time = 48 h, reaction temperature = 200 °C). XRD pattern of using 0.64 mL of en is attached for comparison. Bar charts are reference patterns of ZnTe (JCPDS No. 15-0746) and Te (JCPDS No. 36-1452).

5.3.9 ZnTe microspheres as THz wave source

Table 5.5 ZnTe microspheres used for THz emission test and their synthesis parameters.

Sample	Average size	PVP amount	Precursors	Loaded amount
ZnTe-0.7	746 ± 144 nm	518 mg	0.2 mmol of $ZnCl_2$ 0.16 mmol of Na_2TeO_3	83.8 mg
ZnTe-0.8	854 ± 141 nm	1036 mg		84.0 mg
ZnTe-1.0	1.0 ± 0.2 μm	0 mg		87.0 mg
ZnTe-1.6	1.6 ± 0.2 μm	518 mg	0.4 mmol of $ZnCl_2$ 0.32 mmol of Na_2TeO_3	87.2 mg
ZnTe-1.9	1.9 ± 0.5 μm	518 mg	0.6 mmol of $ZnCl_2$ 0.48 mmol of Na_2TeO_3	90 mg

Different sized-ZnTe microspheres were stocked up through repeating the syntheses. The diameters of ZnTe microspheres were remeasured from SEM images (**Figure A5.2**) after mixing the stocked-up microspheres (**Table 5.5**). ~90 mg of ZnTe microspheres were deposited on the Si wafer, confirmed by the initial and final weight of the Si wafer. XRD patterns of different sized-ZnTe microspheres loaded on Si wafer are given in **Figure 5.31**. No traceable Te was observed. Crystalline size of ZnTe microspheres in each sample was determined with (111) and (220) peaks in the data using X'Pert HighScore Plus (Malvern PANalytical, the Netherlands), also with the intensity ratio of (220) peak-to-(111) peak for each sample (**Table A5.1**). **Figure 5.32**a shows the

crystalline size calculated from each peak with respect to samples. Larger crystalline sizes are always given by (220) peaks than (111) peaks. Diffuse reflectance spectra (**Figure A5.3**) show all samples have reflectance less than 10% at 800 nm of laser excitation wavelength. It is assumed that the laser light can be absorbed by all samples. Reflectance had no tendency to the size differences. It should be noted that the reflectance is affected by surface roughness and film thickness, and the drop casting technique used in the experiment did not give an even-thickness film of ZnTe microspheres.

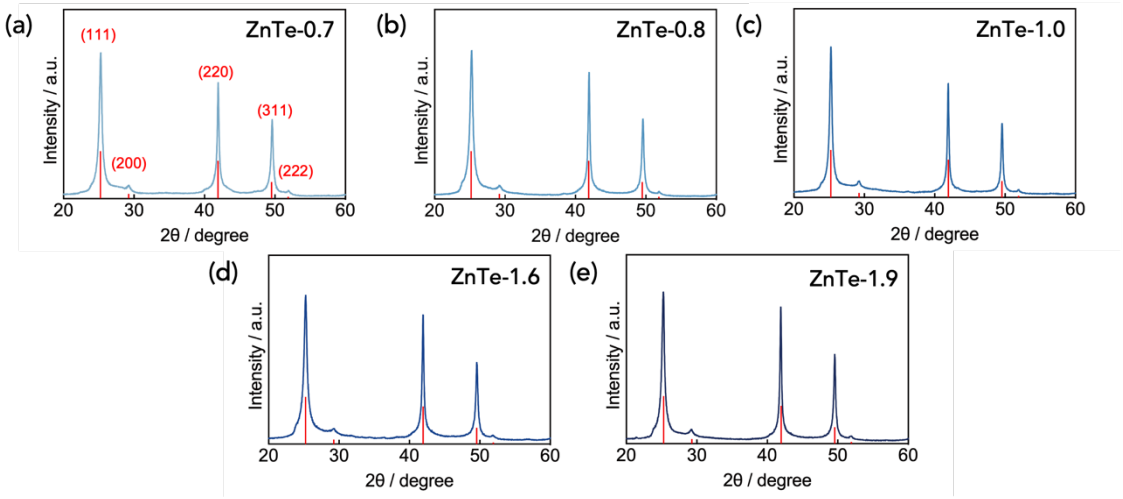


Figure 5.31 XRD patterns of (a) ZnTe-0.7, (b) ZnTe-0.8, (c) ZnTe-1.0, (d) ZnTe-1.6, and (e) ZnTe-1.9 loaded on Si wafer. Bar charts are reference pattern of ZnTe (JCPDS No. 15-0746).

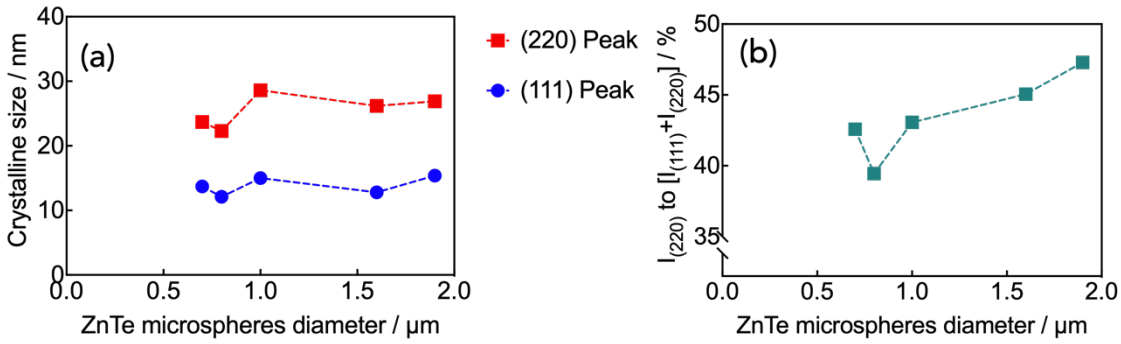


Figure 5.32 (a) Sizes of crystals with (111) and (220) faces with respect to the ZnTe microspheres' diameter. (b) Content of (220) crystals determined from XRD peak intensities.

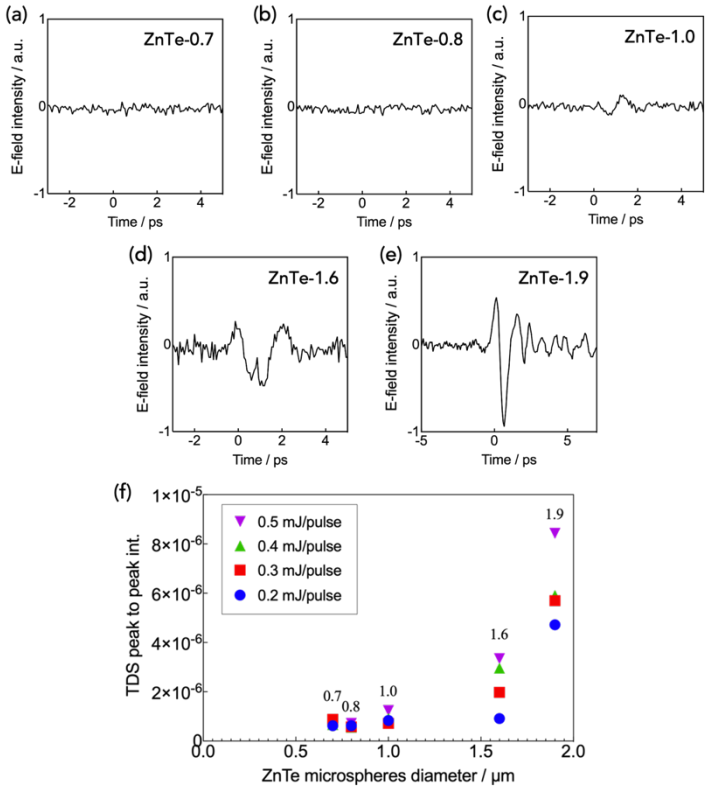


Figure 5.33 (a) THz-TDS of sample (a) ZnTe-0.7, (b) ZnTe-0.8, (c) ZnTe-1.0, (d) ZnTe-1.6, (e) ZnTe-1.9. Laser intensity is 0.4 mJ/pulse. (f) Summary of peak-to-peak intensities in TDS against average ZnTe microspheres' size with respect to different laser pulse intensity.

Figure 5.33 shows THz-TDS of all samples irradiated by laser with intensity 0.4 mJ/pulse. THz wave emission intensity increased with increasing average size of ZnTe microspheres. Regardless to the laser pulse intensity, ZnTe-0.7, ZnTe-0.8, and ZnTe-1.0 emitted relatively weak THz wave. Contrastively, ZnTe-1.6 and ZnTe-1.9 resulted in THz wave emission and that increased significantly with increasing laser intensity (**Figure 5.33**f), which is agreed by **Eq 1.2**. THz emission was not likely contributed by the surface depletion field of semiconductor. It was because the wavelength of laser was 800 nm (equivalent to a photon energy of 1.55 eV), that was not sufficient to proceed photoexcitation and excite the electron-hole pairs in ZnTe with larger band gap of 2.26 eV. On the other hand, photo-Dember effect on ZnTe is also considerably weak, because it usually occurs in narrow band gap semiconductors (e.g., InAs, InSb).[65] Therefore, the THz wave emission from all samples is considerably contributed by the optical rectification (OR).

Thickness of ZnTe microspheres deposited in each sample was estimated with the measurement using confocal laser scanning microscope. A scratch was made at the center of each ZnTe microspheres film so that the Si wafer substrate was exposed to the surface. Scanning were executed and a profile line of the scanned area showed the thickness of ZnTe microspheres film. Assume the ZnTe microspheres were well arranged

on the Si wafer. The thickness of ZnTe microspheres film and estimated number of layers of ZnTe microspheres were listed in **Table 5.6**. The result suggested that number of layers may not be the reason of THz wave emission, as well as particle sizes seem not affecting the THz wave emission. Therefore, it was considered that crystalline size could be the key factor of THz wave emission.

Table 5.6 Thickness of ZnTe microspheres film of each sample and the estimated number of layers of ZnTe microspheres loaded on Si wafer via dividing the thickness by the diameter of ZnTe microspheres.

Sample	Thickness	Number of layers
ZnTe-0.7	57 μm	~81
ZnTe-0.8	52 μm	~65
ZnTe-1.0	43 μm	~43
ZnTe-1.6	56 μm	~35
ZnTe-1.9	54 μm	~28

As discussed in chapter 1, orientation of crystals and the laser-incident angle are important factors to generate strong THz electric field through OR. Maximum THz electric field can be reached when the laser irradiates {110} crystal planes at a normal direction. Instead, Guo *et al.* has reported THz wave generated from <111>- oriented

ZnTe single crystal as well.[66] Therefore, crystals with (111) and (220) planes in the ZnTe microspheres were possibly contributed to the THz wave emission, even though it is difficult to quantify the contribution because of the random orientation of polycrystalline materials. Crystalline size might not relate to the THz wave emission because ZnTe-1.0 had the largest crystals, but it only emitted weak THz wave (**Figure 5.33**c). The amount of crystals with (220) plane to that with (111) plane, given by the XRD peaks of two planes, also had no tendency against the THz wave emission intensity. However, the THz wave emission was possibly enhanced when considering both factors together – moderate crystalline sizes and high ratio of peak intensities of (220) plane to (111) plane (> 80%).

One of the concerns is that induced polarizations in the optical rectification process in each nanocrystal of ZnTe microspheres would compensate each other because these crystals were highly random oriented, i.e. net polarization = 0. The morphologies of different sized ZnTe microspheres might give some ideas in explaining the THz wave emission in larger spheres. Larger ZnTe spheres tended to conjugate with neighbor particles and formed a bunch of microspheres with asymmetrical shape (**Figure 3.34**a) but smaller ZnTe spheres stayed individual and spherical (**Figure 3.34**d). Considering a bunch of microspheres in ZnTe-1.9 as a single particle, the induced polarization was non-

zero. It was because the ‘particle’ is non-symmetrical (**Figure 3.34**c). In case of single ZnTe microsphere in smaller sized, the induced polarization in either <110> and <111> oriented nanocrystals would have higher probability to be canceled out by each other since the particle is symmetrical (**Figure 3.34**f). As a result, more bunches of ZnTe microspheres in ZnTe-1.9 (pink circles in **Figure 3.34**b) might be favorable to the THz wave emission because of the non-zero induced polarization.

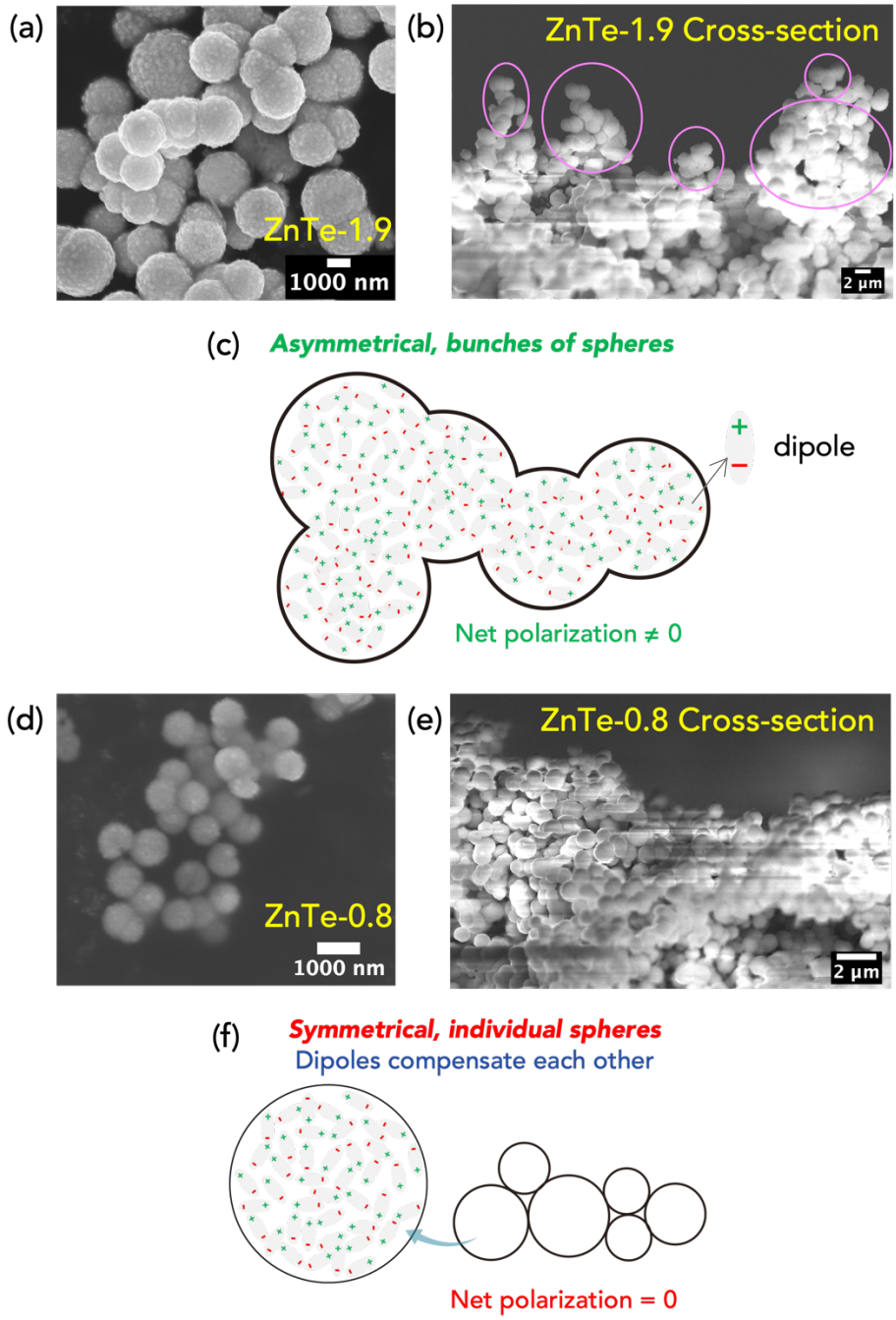


Figure 5.34 SEM image of stocked ZnTe microspheres before deposition on Si wafer for (a) ZnTe-1.9 and (d) ZnTe-0.8. Cross-sectional image of ZnTe microspheres layer deposited on Si wafer of (b) ZnTe-1.9 and (e) ZnTe-0.8. Pink circle indicates a bunch of ZnTe microspheres. Schematic diagram for explaining the induced dipoles in sample (c) ZnTe-1.9 and (f) ZnTe-0.8.

The intrinsic semiconductor properties such as dopants, carrier concentrations and stoichiometric compositions also affect the emission of THz wave, because these features affect the band gap of ZnTe.[67] The composition of ZnTe microspheres was not perfectly stoichiometric compared with single crystals. The more or less content of Zn and Te atoms, impurities during the syntheses, and/or oxidation of Zn atoms are also possibly affecting the centrosymmetry of ZnTe crystals, which highly determines the OR.

Moreover, PVP was involved in making ZnTe microspheres (except ZnTe-1.0). Although PVP considerably did not affect the THz wave emission, the existence of PVP was counted when the ZnTe microspheres were weighed and loaded on Si wafer. Therefore, the actual amount of ZnTe microspheres in all samples did not perfectly equal to each other, and samples with the smaller ZnTe microspheres possibly consisted of more PVP, due to the large surface area of smaller particles. This affected the number of ZnTe microspheres to be effectively irradiated by the laser pulse. Thus, weak/almost zero emission was found in ZnTe-0.7, ZnTe-0.8, and ZnTe-1.0.

Lastly, a day-long laser irradiation test was conducted using ZnTe-1.9 to test its stability with the laser intensity at 0.4 mJ/pulse. **Figure 5.35** shows ZnTe-1.9 constantly emitted THz wave for a day. Data points fell off from the average (shaded area) are considered as experimental error. Therefore, the ZnTe microspheres are considered as a stable THz wave source.

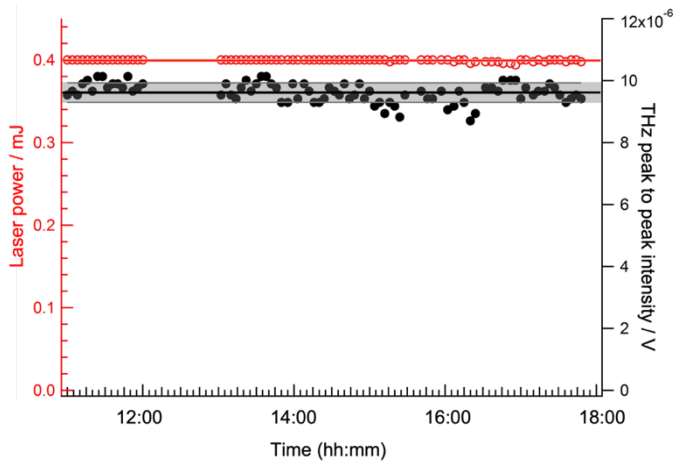


Figure 5.35 THz intensity (right y-axis) with respect to time with laser excitation at intensity 0.4 mJ/pulse (left y-axis). Total 80 data points were taken in between 10:00 am to 5:30 pm on 2022/05/04.

5.4 Conclusion

A hot injection method of preparation of ZnTe microspheres with size 600 – 1000 nm has been demonstrated. Amount of PVP used in the reaction determined the reaction kinetics of Te rods formed from TeO_3^{2-} ions at earlier stage, which were the template for ZnTe to grow, and therefore influencing the nucleation and growth rate of ZnTe microspheres in longer reaction time. Homogeneous, high-purity ZnTe microspheres with an average size of 634 nm have been synthesized with using 518 mg of PVP and reaction time of 48 h. All-round analyses on the formation process of ZnTe microspheres have been performed using various characterization techniques, and a formation scheme of ZnTe microspheres has been proposed. Some key points on further analyzing the ZnTe microspheres were issued – the problem of Coulomb explosion of Te rods during HVEM observation and elucidating the functionality of using $Zn(CH_3COO)_2$ as the precursor for making smaller-sized ZnTe microspheres.

On the other hand, THz wave emission was observed from the ZnTe microspheres sized $\geq$ 1.6 μm. Even though single crystal ZnTe is mostly used in THz generation in other studies, this study demonstrated polycrystalline ZnTe can also emit THz wave under laser irradiation. The THz emission was originated from OR. Larger ZnTe microspheres prone to emit THz wave significantly.

This research brings in-depth information regarding to the formation mechanism of ZnTe microspheres in a PVP-containing polyol system and first preliminarily demonstrated THz wave emission from polycrystalline ZnTe microspheres.

5.5 References

1. Wang, Q.; Wang, X.; Yu, Z.; Jiang, X.; Chen, J.; Tao, L.; Wang, M.; Shen, Y. Artificial photosynthesis of ethanol using type-II g-C_3N_4/ZnTe heterojunction in photoelectrochemical CO_2 reduction system. *Nano Energy*, **2019**, *60*, 827-835.
2. Wen, P.; Li, H.; Ma, X.; Lei, R.; Wang, X.; Geyer, S.M.; Qiu, Y. A colloidal ZnTe quantum dot-based photocathode with a metal-insulator-semiconductor structure towards solar-driven CO_2 reduction to tunable syngas. *J. Mater. Chem. A*, **2021**, *9*, 3589-3596.
3. Luo, S.; Shen, H.; He, X.; Zhang, Y.; Li, J.; Oron, D.; Lin, H. Facile *in situ* synthesis of dendrite-like ZnO/ZnTe core/shell nanorod heterostructures for sensitized solar cells. *J. Mater. Chem. C*, **2016**, *4*, 4740-4747.
4. Sato, K.; Hanafusa, M.; Noda, A.; Arakawa, A.; Uchida, M.; Asahi, T.; Oda, O. ZnTe pure green light-emitting diodes fabricated by thermal diffusion. *J. Cryst. Growth*, **2000**, *214/215*, 1080-1084.
5. Sadaqat, M.; Nisar, L.; Babar, N.-U.-A.; Hussain, F.; Ashiq, M.N.; Shah, A.; Ehsan, M.F.; Najam-Ul-Haq, M.; Joya, K.S. Zinc-telluride nanospheres as an efficient water oxidation electrocatalyst displaying a low overpotential for oxygen evolution. *J. Mater. Chem. A*, **2019**, *7*, 26410-26420.
6. Jang, J.-W.; Cho, S.; Magesh, G.; Jang, Y.J.; Kim, J.Y.; Kim, W.Y.; Seo, J.K.; Kim, S.; Lee, K.-H. Aqueous-Solution Route to Zinc Telluride Films for Application to CO_2 Reduction. *Angew. Chem. Int. Ed.*, **2014**, *53*, 5852-5857.
7. Won, D.H.; Chung, J.; Park, S.H.; Kim, E.-H.; Woo, S.I. Photoelectrochemical production of useful fuels from carbon dioxide on a polypyrrole-coated p-ZnTe photocathode under visible light irradiation. *J. Mater. Chem. A*, **2015**, *3*, 1089-1095.

8. Seo, J.-U.; Park, C.-M. ZnTe and ZnTe/C nanocomposite: a new electrode material for high-performance rechargeable Li-ion batteries. *J. Mater. Chem. A*, **2014**, *2*, 20075-20082.
9. Law, W.-C.; Yong, K.-T.; Roy, I.; Ding, H.; Hu, R.; Zhao, W.; Prasad, P.N. Aqueous-Phase Synthesis of Highly Luminescent CdTe/ZnTe Core/Shell Quantum Dots Optimized for Targeted Bioimaging. *Small*, **2009**, *5*, 1302-1310.
10. Ghosh, S.; Ghosh, D.; Bag, P.K.; Bhattacharya, S.C.; Saha, A. Aqueous synthesis of ZnTe/dendrimer nanocomposites and their antimicrobial activity: implications in therapeutics. *Nanoscale*, **2011**, *3*, 1139-1148.
11. Jin, M.; Yang, W.-H.; Wang, X.-H.; Li, R.-B.; Xu, Y.-D.; Xu, J.-Y. Growth and characterization of ZnTe single crystal via a novel Te flux vertical Bridgman method. *Rare Metals*, **2021**, *40*, 858-864.
12. Huang, H.; Chau, Y.R.; Yonezawa, T.; Ngueyn, M.T.; Zhu, S.; Deng, D.; Nagashima, T.; Hatanaka, K. THz Wave Emission from ZnTe Nano-colloidal Aqueous Dispersion Irradiated by Femtosecond Laser. *Chem Lett.*, **2020**, *49*, 597-600.
13. Wang, Y.; He, T. ZnTe-based nanocatalysts for CO_2 reduction. *Curr. Opin. Green Sustain. Chem.*, **2019**, *16*, 7-12.
14. Li, P.; He, T. Recent advances in zinc chalcogenide-based nanocatalysts for photocatalytic reduction of CO_2. *J. Mater. Chem. A*, **2021**, *9*, 23364-23381.
15. Ehsan, M.F.; Ashiq, M.N.; He, T. Hollow and mesoporous ZnTe microspheres: synthesis and visible-light photocatalytic reduction of carbon dioxide into methane. *RSC Adv.*, **2015**, *5*, 6186-6194.
16. Wu, X.; Zhou, S.; Lou, S.; Wang, Y.; Shi, X.; Gao, T.; Liu, Y. Solvothermal synthesis of ZnTe microspheres with enhanced light current. *Mater. Lett.*, **2012**, *83*, 4-7.

17. Wu, X.-P.; Gu, J.; Zhou, S.-M.; Li, X.-Y.; Wang, S.-L.; Jin, L.; Chen, H.; Shi, J.-J. Red bayberry-like ZnTe microstructures: Controlled synthesis, growth mechanism and enhanced photocatalytic performance. *J. Alloys Compd.*, **2015**, *627*, 166-173.
18. Li, S.; Xu, Y.; Zhang, K.; Zhong, B.; Yan, J. Controllable preparation and rapid photoelectric response of homogeneous ZnTe microspheres. *New J. Chem.*, **2022**, *46*, 3777-3785.
19. Zhang, J.; Sun, K.; Kumbhar, A.; Fang, J. Shape-Control of ZnTe Nanocrystal Growth in Organic Solution. *J. Phys. Chem. C*, **2008**, *112*, 5454-5458.
20. Xu, S.; Wang, C.; Xu, Q.; Zhang, H.; Li, R.; Shao, H.; Lei, W.; Cui, Y. Key Roles of Solution pH and Ligands in the Synthesis of Aqueous ZnTe Nanoparticles. *Chem. Mater.*, **2010**, *22*, 5838-5844.
21. Dunpall, R.; Mlowe, S.; Revaprasadu, N. Evidence of oriented attachment in the growth of functionalized ZnTe nanoparticles for potential applications in bio-imaging. *New J. Chem.*, **2014**, *38*, 6002-6007.
22. Cheng, T.; Li, D.; Li, J.; Ren, B.; Wang, G.; Cheng, J. Aqueous synthesis of high-fluorescence ZnTe quantum dots. *J. Mater. Sci. Mater. Electron.*, **2015**, *36*, 4062-4068.
23. Patra, S.K.; Bhushan, B.; Priyam, A. Water-soluble, luminescent ZnTe quantum dots: supersaturation-controlled synthesis and self-assembly into nanoballs, nanonecklaces and nanowires. *Dalton Trans.*, **2016**, *45*, 3918-3926.
24. Zhang, J.; Jin, S.; Fry, H.C.; Peng, S.; Shevchenko, E.; Wiederrecht, G.P.; Rajh, T. Synthesis and Characterization of Wurtzite ZnTe Nanorods with Controllable Aspect Ratios. *J. Am. Chem. Soc.*, **2011**, *133*, 15324-15327.
25. Meng, Q., Jiang, C.; Mao, S.X. Temperature-dependent growth of zinc-blende-

structured ZnTe nanostructures. *J. Cryst. Growth*, **2008**, *310*, 4481-4486.

26. Rao, G.K.; Bangera, K.V.; Shivakumar, G.K. The effect of substrate temperature on the structural, optical and electrical properties of vacuum deposited ZnTe thin films. *Vacuum*, **2009**, *83*, 1485-1488.
27. Bacaksiz, E.; Aksu, S.; Ozer, N.; Tomakin, M.; Özçelik, A. The influence of substrate temperature on the morphology, optical and electrical properties of thermal-evaporated ZnTe Thin Films. *Appl. Surf. Sci.*, **2009**, *256*, 1566-1572.
28. Ko, H.; Park, S.; An, S.; Lee, C. Intense near-infrared emission from undoped ZnTe nanostructures synthesized by thermal evaporation. *J. Alloys Compd.*, **2013**, *580*, 316-320.
29. Wang, Y.; Yang, M.; Ren, Y.; Fan, J. Ratiometric determination of hydrogen peroxide based on the size-dependent green and red fluorescence of CdTe quantum dots capped with 3-mercaptopropionic acid. *Microchim. Acta.*, **2019**, *186*, 277-285.
30. Zhang, C.; Yan, J.; Liu, C.; Ji, X.; He, Z. One-Pot Synthesis of DNA-CdTe:Zn^{2+} Nanocrystals Using Na_2TeO_3 as the Te source. *ACS Appl. Mater. Interfaces*, **2014**, *6*, 3189-3194.
31. Sheng, Z.; Han, H.; Hu, X.; Chi, C. One-step growth of high luminescence CdTe quantum dots with low cytotoxicity in ambient atmospheric conditions. *Dalton Trans.*, **2010**, *39*, 7017-7020.
32. Wang, Y.; Liu, S. ONE-POT SYNTHESIS OF HIGHLY LUMINESCENT CdTe QUANTUM DOTS USING SODIUM TELLURITE AS TELLURIUM SOURCE IN AQUEOUS SOLUTION. *J. Chil. Chem. Soc.*, **2012**, *57*, 1109-1112.
33. Safo, I.A.; Werheid, M.; Dosche, C.; Oezaslan, M. The role of polyvinylpyrrolidone (PVP) as a capping and structure-directing agent in the formation of Pt nanocubes.

Nanoscale Adv., **2019**, *1*, 3095-3106.

34. Liu, Z.; Li, S.; Yang, Y.; Hu, Z.; Peng, S.; Liang, J.; Qian, Y. Shape-controlled synthesis and growth mechanism of one-dimensional nanostructures of trigonal tellurium. *New J. Chem.*, **2003**, *27*, 1748-1752.
35. Safdar, M.; Wang, Z.; Mirza, M.; Butt, F.K.; Wang, Y.; Sun, L.; He, J. Telluride-based nanorods and nanosheets: synthesis, evolution and properties. *J. Mater. Chem. A*, **2013**, *1*, 1427-1432.
36. Wang, K.; Liang, H.-W.; Tao, W.-T.; Yu, S.-H. Templating synthesis of uniform Bi_2Te_3 nanowires with high aspect ratio in triethylene glycol (TEG) and their thermoelectric performance. *J. Mater. Chem.*, **2011**, *21*, 15057-15062.
37. Zhang, B.; Hou, W.; Ye, X.; Fu, S.; Xie, Y. 1D Tellurium Nanostructures: Photothermally Assisted Morphology-Controlled Synthesis and Applications in Preparing Functional Nanoscale Materials. *Adv. Funct. Mater.*, **2007**, *17*, 486-492.
38. Qian, H.-S.; Yu, S.-H.; Gong, J.-Y.; Luo, L.-B.; Fei, L.-f. High-Quality Luminescent Tellurium Nanowires of Several Nanometers in Diameter and High Aspect Ratio Synthesized by a Poly (Vinyl Pyrrolidone)-Assisted Hydrothermal Process. *Langmuir*, **2006**, *22*, 3830-3835.
39. Qi, X.; Balankura, T.; Zhou, Y.; Fichthorn, K.A. How Structure-Directing Agents Control Nanocrystal Shape: Polyvinylpyrrolidone-Mediated Growth of Ag Nanocubes. *Nano Lett.*, **2015**, *15*, 7711-7717.
40. Oh, S.-D.; So, B.-K.; Choi, S.-H.; Gopalan, A.; Lee, K.-P.; Yoon, K.R.; Choi, I.S. Dispersing of Ag, Pd, and Pt-Ru alloy nanoparticles on single-walled carbon nanotubes by γ-irradiation. *Mater. Lett.*, **2005**, *59*, 1121-1124.
41. Butz, Z.J.; Hendricks, A.; Borgognoni, K.; Ackerson, C.J. Identification of a TeO_3^{2-}

reductase/mycothione reductase from Rhodococcus erythropolis PR4. *FEMS Microbiol. Ecol.*, **2021**, *97*, fiaa220.

42. Li, Y.; Wang, Z.; Ding, Y. A Novel Chemical Route to ZnTe Semiconductor Nanorods. *Inorg. Chem.*, **1999**, *38*, 4737-4740.
43. Chen, M.; Xie, Y.; Chen, H.; Qiao, Z.; Qian, Y. Preparation and Characterization of Metal Sulfides in Ethylenediamine under Ambient Conditions through a γ-Irradiation Route. *J. Colloid Interface Sci.*, **2001**, *237*, 47-53.
44. Saxena, M.; Bera, A.K.; Venkatesh, R. Wet chemical assisted synthesis of self assembled tellurium nanostructures with enhanced stability. *Mater. Lett.*, **2021**, *301*, 130330.
45. Liang, F.; Qian, H. Synthesis of tellurium nanowires and their transport property. *Mater. Chem. Phys.*, **2009**, *113*, 523-526.
46. Tang, Z.; Wang, Y.; Sun, K.; Kotov, N. Spontaneous Transformation of Stabilizer-Depleted Binary Semiconductor Nanoparticles into Selenium and Tellurium Nanowires. *Adv. Mater.*, **2005**, *17*, 358-363.
47. Tran, R.; Xu, Z.; Radhakrishnan, B.; Winston, D.; Sun, W.; Persson, K.A.; Ong, S.P. Surface energies of elemental crystals. *Sci. Data*, **2016**, *3*, 160080-160093.
48. Jain, A.; Ong, S.P.; Hautier, G.; Chen, W.; Richards, W.D.; Dacek, S.; Cholia, S.; Gunter, D.; Skinner, D.; Ceder, G.; Persson, K.A. Commentary: The Materials Project: A materials genome approach to accelerating materials innovation. *APL Mater.*, **2013**, *1*, 011002.
49. Shevchenko, E.V.; Talapin, D.V.; Schnablegger, H.; Kornowski, A.; Festin, Ö.; Svedlindh, P.; Haase, M.; Weller, H. Study of Nucleation and Growth in the Organometallic Synthesis of Magnetic Alloy Nanocrystals: The Role of Nucleation

Rate in Size Control of $CoPt_3$ Nanocrystals. *J. Am. Chem. Soc.*, **2003**, *125*, 9090-9101.

50. Naik, A.N.; Patra, S.; Sen, D.; Goswami, A. Evaluating the mechanism of nucleation and growth of silver nanoparticles in a polymer membrane under continuous precursor supply: tuning of multiple to single nucleation pathway. *Phys. Chem. Chem. Phys.*, **2019**, *21*, 4193-4199.
51. Kracek, F.C. The melting point of tellurium. *J. Am. Chem. Soc.*, **1941**, *63*, 1989-1990.
52. Zhang, G.; Chen, J. A multifaceted application of designed coulomb explosion occurring on oxidized topological crystalline insulator SnTe. *CrystEngComm*, **2022**, *24*, 571-578.
53. Yu, J.; Guo, H.; Davis, S.A.; Mann, S. Fabrication of Hollow Inorganic Microspheres by Chemically Induced Self-Transformation. *Adv. Funct. Mater.*, **2006**, *16*, 2035-2041.
54. Ding, J.; Liu, X.; Wang, M.; Liu, Q.; Sun, T.; Jiang, G.; Tang, Y. Controlled synthesis of $CeVO_4$ hierarchical hollow microspheres with tunable hollowness and their efficient photocatalytic activity. *CrystEngComm*, **2018**, *20*, 4499-4505.
55. Alp, E.; Araz, E.C.; Buluç, A.F.; Güner, Y.; Deger, Y.; Esgin, H.; Dermenci, K.B.; Kazmanli, M.K.; Turan, S.; Genç, A. Mesoporous nanocrystalline ZnO microspheres by ethylene glycol mediated thermal decomposition. *Adv Powder Technol.*, **2018**, *29*, 3455-3461.
56. Guo, R.; Bao, Y.; Kang, Q.; Liu, C.; Zhang, W.; Zhu, Q. Solvent-controlled synthesis and photocatalytic activity of hollow TiO_2 microspheres prepared by the solvothermal method. *Colloids Surf. A Physicochem. Eng. Asp.*, **2022**, *633*, 127931.
57. Tu, K.N.; Gösele, U. Hollow nanostructures based on the Kirkendall effect: Design

and stability considerations. *Appl. Phys. Lett.*, **2005**, *86*, 093111-3.

58. Fan, H.J. Knez, M.; Scholz, R.; Hesse, D.; Nielsch, K.; Zacharias, M.; Gösele, U. Influence of Surface Diffusion on the Formation of Hollow Nanostructures Induced by the Kirkendall Effect: The Basic Concept. *Nano Lett.*, **2007**, *7*, 993-997.
59. Anderson, B.D.; Tracy, J.B. Nanoparticle conversion chemistry: Kirkendall effect, galvanic exchange, and anion exchange. *Nanoscale*, **2014**, *6*, 12195-12216.
60. Mayers, B.; Xia, Y. Formation of Tellurium Nanotubes Through Concentration Depletion at the Surfaces of Seeds. *Adv. Mater.*, **2002**, *14*, 279-282.
61. Pei, J.; Chen, G.; Jia, D.; Yu, Y.; Sun, J.; Qiu, Z.; Yu, Y. Construction of hollow tellurium hierarchical architecture via a trisodium citrate assisted self- sacrificed template eroding mechanism. *RSC Adv.*, **2014**, *4*, 36257-36261.
62. Yoon, J.-H.; Chae, W.-S.; Im, S.-J.; Kim, Y.-R. Mild synthesis of ultra-small CdSe quantum dots in ethylenediamine solution. *Mater. Lett.*, **2005**, *59*, 1430-1433.
63. Che, J.; Shen, L.; Xiao, Y. A new approach to fabricate graphene nanosheets in organic medium: combination of reduction and dispersion. *J. Mater. Chem.*, **2010**, *20*, 1722-1727.
64. Xu, W.; Li, Z.; Wu, H.; Qu, X.; Niu, J. Investigation on Three Dimensional Hybrid Organic–Inorganic β-ZnTe$(en)_{0.5}$ Flowerlike Structures and Corresponding Mesoporous PbTe Flowerlike Microcrystals. *J. Inorg. Organomet. Polym. Mater.*, **2020**, *30*, 2736-2743.
65. Gu, P.; Tani, M.; Kono, S.; Sakai, K.; Zhang, X.-C. Study of terahertz radiation from InAs and InSb. *J. Appl. Phys.*, **2002**, *91*(9), 5533.
66. Guo, Q.; Kume, Y.; Fukuhara, Y.; Tanaka, T.; Nishino, M.; Ogawa, H.; Hiratsuka, M.; Tani, N.; Hangyo, M. Observation of ultra-broadband terahertz emission from ZnTe

films grown by metaloganic vapor epitaxy. *Solid State Commun.*, **2007**, *141*(4), 188-191.

67. Wilke, I. Terahertz emission from narrow band gap semiconductors. *IEEE Trans Terahertz Sci Technol*, **2007**, *6772*, 67720N.

5.6 Supporting Information

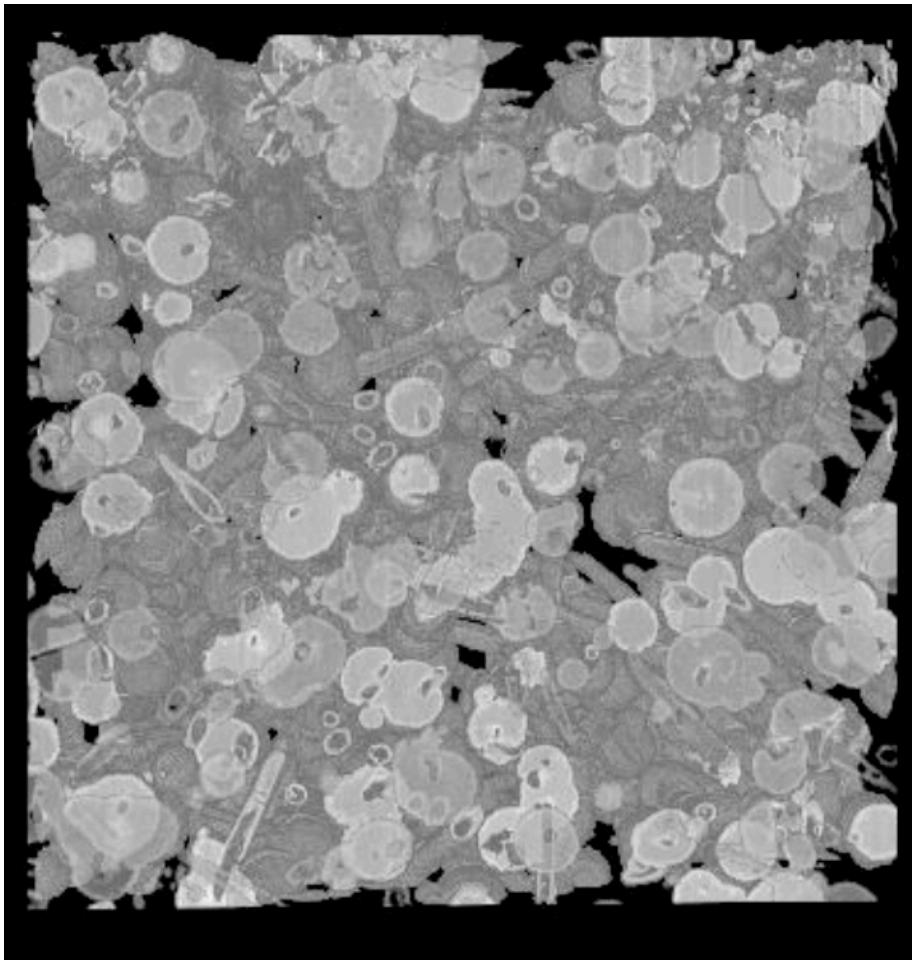


Figure A5.1 3D diagram constructed by overlapping cross-sectional images of sample 518PVP(0.5h) using FIB-SEM.

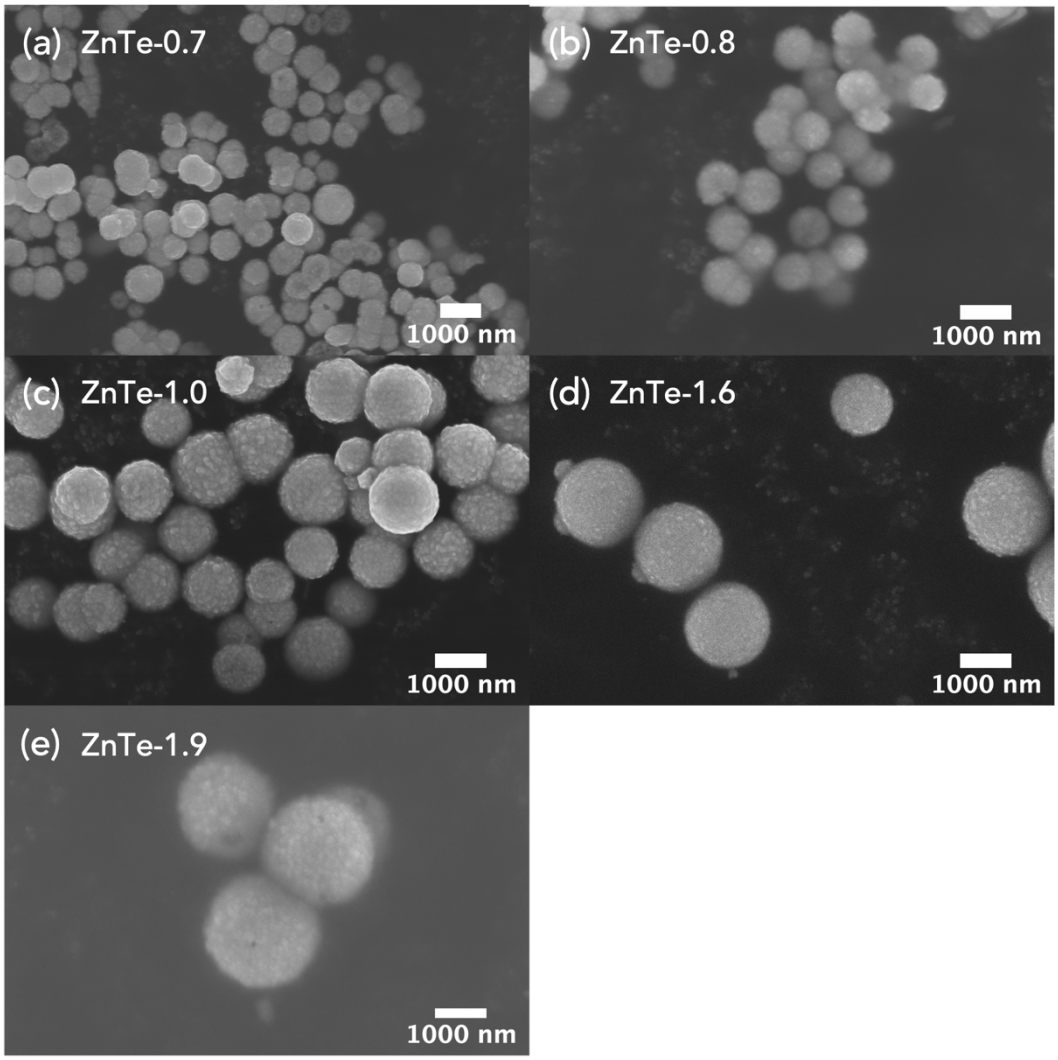


Figure A5.2 SEM images of (a) ZnTe-0.7 (746 ± 144 nm), (b) ZnTe-0.8 (854 ± 141 nm), (c) ZnTe-1.0 (1.0 ± 0.2 μm), (d) ZnTe-1.6 (1.6 ± 0.2 μm), and (e) ZnTe-1.9 (1.9 ± 0.5 μm).

Table A5.1 Crystalline size calculated with (111) and (220) peaks; peak intensity of (220) to sum of peak intensities of (111) and (220), using X'Pert HighScore Plus (Malvern PANalytical, the Netherlands).

Sample	Crystalline size (111)	Crystalline size (220)	$\frac{I_{(220)}}{I_{(111)} + I_{(220)}}$
ZnTe-0.7	13.7 nm	23.7 nm	42.6%
ZnTe-0.8	12.1 nm	22.3 nm	39.5%
ZnTe-1.0	15.0 nm	28.6 nm	43.1%
ZnTe-1.6	12.8 nm	26.2 nm	45.1%
ZnTe-1.9	15.4 nm	26.9 nm	47.3%

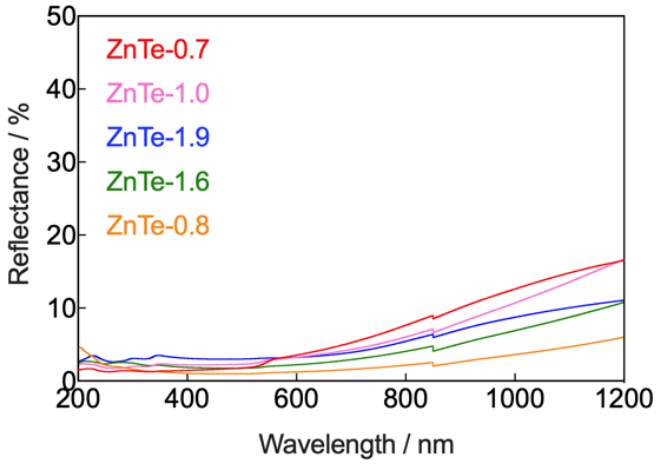


Figure A5.3 Diffuse reflectance spectra of ZnTe microspheres loaded on Si wafer.

CHAPTER 6

General Conclusion

This dissertation focuses on synthesizing nano/micro materials using sputter deposition (top-down) and chemical reduction (bottom-up) approaches and investigating their optical response under ultrafast laser pulse irradiation. Potential applications of different forms of Cu-based materials and ZnTe were listed. Approaches – either top-down or bottom-up? of synthesizing nano/materials were discussed. Besides, with the development of laser technologies, the interaction between ultrafast laser pulse and different nano/micro materials (nonlinear optics, semiconductors, water, etc.) is of interest. The mechanisms (optical rectification, Schottky junctions, etc.) of EM wave in X-ray and THz regime emitted through such interaction were given. In particular, the broadband THz pulse emission from Cu-oxides thin film and from polycrystalline ZnTe microspheres were reported.

Chapter 2 presents the use of single sputter deposition for synthesizing monometallic Cu NPs dispersion and double target co-sputter deposition for synthesizing bimetallic Cu-Pd alloy NPs dispersion in the liquid PEG. The optical properties, particle sizes, structures, compositions, stability in the solution of NPs were characterized using

UV-Vis, TEM, STEM-EDS, XRD, and XPS. Both Cu and Cu-Pd NPs had size less than 5 nm and dispersed in PEG without aggregation. UV-Vis spectrum of monometallic Cu NPs dispersion showed an absorption peak at 570 nm, which was originated from Cu NPs. Cu-Pd alloy NPs dispersion did not show such characteristic peak in UV-vis region, indicating alloy formation instead of the mixture of Cu and Pd NPs. Growth in size of Cu NPs in 1 week and the oxidation progress of Cu NPs in PEG were monitored. Characterizations were diversely carried out to distinguish the composition of Cu-Pd alloy NPs, which were synthesized through different combinations of sputtering current. Results proved that using double target sputter deposition by alternating sputtering current could vary compositions of alloy NPs. The sputtered Cu-Pd alloy NPs had low crystallinity. Degradation of Cu-Pd alloy NPs during storage for 4 days because the Cu atoms in Cu-Pd alloy NPs prone to dissolute into the PEG.

Chapter 3 studies the stability of Au@Cu_2O core-shell NPs synthesized by wet-chemical route and stored in water/ethanol mixed solvents. 16 nm-sized Au NPs were synthesized using Turkevich method. Cu_2O shells grew on Au NPs epitaxially because of the small lattice mismatch between Au and Cu_2O. The thickness of Cu_2O shell was tunable from 2 to 40 nm through increasing $CuCl_2$ concentration during syntheses. Absorption peak in UV-Vis spectra of Au@Cu_2O core-shell NPs has red shifted with

thicker Cu_2O shells. The stability of Au@Cu_2O core-shell NPs was poor in the solvents that contain > 50 vol % water content. At day 5 of storage, the Cu_2O shell of individual core-shell NP prone to aggregate with the neighbor shells, and the Au cores left from the shell. Meanwhile, the characteristic absorption peak of Cu_2O was no more appeared. It was because the water promoted oxidation of Cu_2O to CuO, which also degraded the unique optical properties of the original Au@Cu_2O. This study shows the Au@Cu_2O core-shell NPs dispersed in aqueous solvents was not an appropriate candidate for THz wave emission test due to their instability.

Chapter 4 presents THz wave emission from semiconductor/metal interface using aqueous free Cu and Cu/Au thin film samples followed with oxidative annealing (80 to 300 ºC, 2.5 h) to obtain Cu oxides as the semiconductor layer. THz wave emission intensity with respect to the oxidation temperature for annealing Cu layer, and the function of Au layer were discussed. Film thickness of Cu was 80 nm and that of Au was 50 nm. Si wafer was used as the substrate. Samples were irradiated by femtosecond laser (35 fs, 800 nm). THz wave emitted from samples were monitored by time-domain spectroscopy in reflection mode. Results showed that Cu_2O/Cu interface was the key feature of THz wave emission. Samples annealed at 80 °C had THz wave emission at the highest intensity compared with that annealed at other temperatures due to enhancement

of laser absorption by porous structures formed at low oxidative temperature. Cu/Au/Si had higher THz wave emission intensity compared with Cu/Si in general because Au film acted as a reflector of THz wave and/or enhance the laser absorption of Cu_2O/Cu interface through Fabry-Pérot effect.

Chapter 5 presents mechanistic studies of ZnTe microspheres formed in a PVP-contained polyol system. ZnTe microspheres were synthesized at 200 °C via a hot injection method in a polyol system with adding 0, 259, 518, and 1036 mg of PVP. A retrospective study was conducted to evaluate the formation process of ZnTe microspheres by conducting experiments from 0.2 h to 48 h. Nucleation and growth of ZnTe at the tips of Te rods in a PVP-contained polyol system were observed in sample reacted less than 1 h. More ZnTe microspheres and less Te rods were observed when the reaction was proceeded for longer time, suggesting that Te rods were the sacrificial template for the growth of ZnTe. Amount of PVP is the key factor of controlling dimensions of Te rods formed at the initial stage as well as the sizes of ZnTe microspheres by influencing the nucleation and growth rate of ZnTe. The obtained ZnTe microspheres at 48 h consisted of voids, which were originated by the detachment of ZnTe microspheres from Te rods after their growth. Furthermore, the possibility of ZnTe microspheres as THz wave source was discussed. Although the ZnTe microspheres were polycrystalline, THz

wave emission was observed. The larger ZnTe microspheres (> 1.0 μm) were prone to generate THz wave in higher intensity, which possibly originated from the nonlinear effect by ZnTe and the surface depletion field between ZnTe and air.

Discussion in this dissertation has brought up to date knowledges on different approaches to synthesize nano/micro materials and the optical response of these materials to the ultrafast laser pulses. The findings are significant to the development of THz wave technologies and further widen the availability of nano/micro materials for broadband THz pulse technologies.

LIST OF JOURNAL PUBLICATIONS

1. **Yuen-ting Rachel Chau**, Lianlian Deng, Mai Thanh Nguyen, Tetsu Yonezawa. "Monitor and Growth and Oxidation of Cu-nanoparticles in PEG after Sputtering" *MRS Advances*, **2019**, *4*, 5-6, 305-309.

2. **Yuen-ting Rachel Chau**, Mai Thanh Nguyen, Mingbei Zhu, Arnaud Romier, Tomoharu Tokunaga, Tetsu Yonezawa. "Synthesis of composition-tunable Pd-Cu alloy nanoparticles by double target sputtering" *New Journal of Chemistry*, **2020**, *44*, 12, 4704-4712.

3. Shilei Zhu, Dan Deng, Mai Thanh Nguyen, **Yuen-ting Rachel Chau**, Cheng-Yen Wen, Tetsu Yonezawa. "Synthesis of Au@Cu_2O Core-Shell Nanoparticles with Tunable Shell Thickness and Their Degradation Mechanism in Aqueous Solutions" *Langmuir*, **2020**, *36*, 13, 3386-3392.

4. **Yuen-ting Rachel Chau**, Hsin-hui Huang, Mai Thanh Nguyen, Koji Hatanaka, Tetsu Yonezawa. "THZ wave emission from the Cu_2O/Cu interface under femtosecond laser irradiation" *Applied Physics Express*, **2020**, *14*, 1, 012006.

5. **Yuen-ting Rachel Chau**, Mai Thanh Nguyen, Tomoharu Tokunaga, Tetsu Yonezawa. "Mechanistic consideration of ZnTe microspheres formation in a PVP-contained polyol system via hot injection method" (Accepted on Feb 02, 2023)

OTHER PUBLICATIONS

1. Lianlian Deng, Mai Thanh Nguyen, Jingming Shi, **Yuen-ting Rachel Chau**, Tomoharu Tokunaga, Masaki Kudo, Syo Matsumura, Naoyuki Hashimoto, Tetsu Yonezawa. "Highly correlated size and composition of Pt/Au alloy nanoparticles via magnetron sputtering onto liquid" *Langmuir*, **2020**, *36*, 12, 3004-3015.

2. Hsin-hui Huang[#], **Yuen-ting Rachel Chau**[#], Tetsu Yonezawa, Mai Thanh Nguyen, Shilei Zhu, Dan Deng, Takeshi Nagashima, Koji Hatanaka. "THz wave emission from ZnTe nano-colloidal aqueous dispersion irradiated by femtosecond laser" *Chemistry Letters*, **2020**, *49*, 6, 597-600.

3. Mingbei Zhu, Mai Thanh Nguyen, **Yuen-ting Rachel Chau**, Lianlian Deng, Tetsu Yonezawa. "Pt/Ag Solid Solution Alloy Nanoparticles in Miscibility Gaps Synthesized by Cosputtering onto Liquid Polymers" *Langmuir*, **2021**, *37*, 19, 6096-6105.

LIST OF CONFERENCES

1. "Growth and oxidation of Cu-nanoparticles Sputtered in PEG"

   H30 Joint Winter Presentation of ISIJ-JIMS on 10-11 Jan 2019 in Muroran, Japan

2. "Synthesis of Pd and Pd/Cu nanoparticles via sputtering deposition"

   R1 Joint Summer Session of ISIJ-JIMS on 5 Jul 2019 in Kitami, Japan

3. "Synthesis of Pd-Cu alloy nanoparticles by double target sputtering"

   China-Japan-Korea The 3rd A3 Foresight Symposium on 9-12 Oct 2019 in Shanghai, China

4. "Synthesis of Pd-Cu alloy nanoparticles by sputtering onto PEG"

   Joint Symposium on Materials Chemistry and Physics on 13 Dec 2019 in Sapporo, Japan

5. "THz radiation from Cu_2O/Cu interface under fs-laser excitation"

   A3 Foresight & 5 Star Alliance Joint Workshop on Organic/Inorganic Hybrid Nano Materials and Bio Imaging on 2-3 Dec 2020 (Online)

6. "Femtosecond Laser Excited THz wave from Cu/Cu_2O Interface"

   The 72nd Division Meeting, Division of Colloid and Surface Chemistry on 21 Sep 2021 (Online)

7. “Formation Mechanism of ZnTe Micro-Particles in Ethylene Glycol”

   The Chemical Society of Japan, Hokkaido Division 2022 Summer Symposium (Kakiken) on 23 Jul 2022 (Online)

8. “Formation Scheme of ZnTe Microspheres via Hot Injection Method”

   The 73rd Divisional Meeting of Division of Colloid and Surface Chemistry (International Symposium) on 20 Sep 2022 (Online)

   【Oral Presentation Award for Young Scientist】

9. “Monitor the Growth of ZnTe Microspheres in a PVP-contained Polyol System”

   The 103rd CSJ Annual Meeting on 22-25 Mar 2023 in Noda-shi, Chiba, Japan